Contributions to the hydrology and hydrogeology of the Nubian Sandstone Aquifer of Northern Chad

Thesis presented at the

FACULTY OF SCIENCES

CENTER FOR HYDROGEOLOGY AND GEOTHERMICS

(CHYN)

UNIVERSITY OF NEUCHÂTEL, SWITZERLAND

For the degree of

DOCTOR OF SCIENCES

Presented by

Marie-Louise A. Vogt

Accepted on the recommendation of

Prof. Philip Brunner

Prof. Daniel Hunkeler

Prof. Hon. François Zwahlen

Dr. Sebastián Pera

Dr. Pedro Martínez Santos

Defended on

January 28th, 2019

UNIVERSITÉ DE NEUCHÂTEL

Faculté des Sciences
Secrétariat-décanat de Faculté
Rue Emile-Argand 11
2000 Neuchâtel – Suisse
Tél : + 41 (0)32 718 21 00
E-mail : secretariat.sciences@unine.ch

IMPRIMATUR POUR THESE DE DOCTORAT

La Faculté des sciences de l'Université de Neuchâtel autorise l'impression de la présente thèse soutenue par

Madame Marie-Louise VOGT

Titre:

"Contributions to the hydrology and hydrogeology of the Nubian Sandstone Aquifer of Northern Chad"

sur le rapport des membres du jury composé comme suit:

- Prof. Philip Brunner, directeur de thèse, Université de Neuchâtel, Suisse
- Prof. Daniel Hunkeler, co-directeur de thèse, Université de Neuchâtel, Suisse
- Prof. émérite François Zwahlen, Université de Neuchâtel, Suisse
- Dr Sebastián Pera, IST-SUPSI, Canobbio, Suisse
- Prof. Pedro Martínez Santos, Universidad Complutense de Madrid, Espagne

Neuchâtel, le 6 mai 2019

Le Doyen, Prof. P. Felber

Acknowledgments

My thanks go to Prof. Philip Brunner and Prof. Daniel Hunkeler for giving me the opportunity to work on the Nubian Sandstone Aquifer System for my PhD for the last four years. Thanks for having shared your experience, for your supervision and for the several discussions that guided this thesis. Special thanks go to Prof.Hon. François Zwahlen with whom I mostly shared the passion of the hydrogeology of Chad.

The field campaigns and the analysis of water probes were performed in the framework of the project ResEau - Cartographie des Ressources en Eau de la République du Tchad. We thank the Ministry of Water and the Ministry of Higher Education of Chad (Ismaël Moussa Mohamed, Dr. Moussa Isseini, Dr. Hamza Brahim, Dr. Abderamane Hamit, Bagamla Lamtouin) for facilitating the work in the field and for sharing information. We thank Nouradine Haroun, Issa Aware and Alphonse Vajois for the sampling of water probes and the collection of hydrogeological data in the Tibesti Mountains and Akoina Moursal and Miradj Habib for the sampling of water probes in 2016 in the Ennedi Mountains. Our thanks also go out to the staff of the ResEau project (Dr. Yves Haeberlin, Marc-André Bünzli, Olivier Sénégas, Amira Kraiem) and Dr. Sebastina Pera, for their involvement in the preparation and implementation of the sampling campaigns. We would also like to thank Prof. Stephan Kröpelin and co-workers (University of Köln) for providing water samples.

I'm also grateful for the technical advices of Dr. Daniel Käser and Dr. Julien Straubhaar for the development of the R code, and Dr. Joshua Larsen for the insightful discussions on remote sensing. Many thanks also go to Vincent Gruber for the analysis of the water probes, and to Fabien Gremaud for the support in the development of the conceptual model of the Tibesti Mountains.

Finally, I would like to express my gratitude to my parents. Undoubtedly, without their support all along my life, I would not be here today. A special thanks also go to my husband, Maher Salha, and its everlasting energy. As well as to Jocelyne Bonfiglio-Baumann for giving me a family in Neuchâtel.

Abstract

This thesis investigates the geology, meteorology, hydrology and groundwater hydrochemistry of the Nubian Sandstone Aquifer System (NSAS) of Northern Chad, with the aim of developing a conceptual model for the organization of the groundwater flow system. The NSAS is one of the largest aquifers of the world, shared between Libya, Egypt, Sudan and Chad. Given the aridity of the region, groundwater corresponds to a precious water resource for these countries.

The Chad sector of the NSAS is one the least known parts of the aquifer system. Key challenges in this project were the difficult access to the area and the lack of monitoring data for groundwater and meteorology. However, the region of Northern Chad, corresponding to the southern margin of the Kufra basin, one of the major sub-basins of the NSAS, is characterized by higher precipitation rates. Potential recharge occurring in this region might have regional implications on the aquifer system, as suggested by previous authors.

Fieldwork was undertaken between 2013 and 2016, covering a total area of approximately 100,000 km^2. The overall objectives of the field campaigns were to acquire data on the geology and sedimentology of the reservoir, the groundwater flow organization and on the hydrochemical (major ions, stable isotopes) composition of groundwater. Given the few available ground-based climatic data, the meteorological and hydrological dynamics were investigated by the use of remote sensing data (RFE2.0, LandSat8OLI).

The hydrochemical composition of groundwater and results from remote sensing data (precipitation and actual evapotranspiration) indicate that in the Ennedi and Tibesti Mountains of Northern Chad there is potential for diffuse and concentrated recharge. Recharge potentially occurs during few high-intensity precipitation events concentrated during the summer rainy season (mid July – mid September), but appears to occur every year.

Apart from these recharged zones, a large depressional area extents in between these mountainous regions. This zone is explicitly recognized as a major structural entity marking the directions of the Hercynian tectonic phase. The main zones of discharge of the NSAS of Northern Chad are located within these Central Lowlands. The hydrochemical composition of groundwater within the discharge zones of Northern Chad is comparable to compositions of other discharge zones of the NSAS.

The conceptual model resulting from the hydraulic heads measured in the field are similar to the model developed eighty years ago by previous authors. The groundwater flow organization and the stable isotopic ratios indicate that the main discharge zones (Ounianga lakes, Faya-Largeau) are supplied by a groundwater flow originating from a recharge zone active during the previous pluvial periods of the Late Pleistocene to mid-Holocene.

Finally, this study demonstrates the crucial role of wadis in redistributing surface water within the mountainous regions of Northern Chad. By the use of LandSat images, this study identifies the most active wadis where there is high potential for concentrated recharge. This renewable resource could be better managed in order to improve the access to water for the local population.

Keywords

Nubian Sandstone Aquifer System, Kufra basin, Northern Chad, arid climate, recharge, wadis, hydrology, hydrogeology, remote sensing, stable isotopes and hydrochemistry, conceptual groundwater flow model.

Résumé

Cette thèse étudie la géologie, la météorologie, l'hydrologie et la géochimie des eaux souterraines de l'Aquifère des Grès de Nubie (NSAS) du Nord du Tchad, avec l'objectif de développer un modèle conceptuel de l'organisation des écoulements souterrains. L'Aquifère des Grès de Nubie est l'un des plus grands aquifères au monde, partagé entre la Libye, l'Egypte, le Soudan et le Tchad. La région se caractérise par son aridité, par conséquence l'eau souterraine est une ressource précieuse pour ces pays.

Le secteur tchadien de l'Aquifère des Grès de Nubie est l'une des zones les moins connues du système. Les majeurs défis de ce projet ont été la difficulté d'accès à la zone d'investigation, ainsi que le manque de données de surveillance sur les eaux souterraines et la météorologie. Pourtant, la région du Nord du Tchad, correspondant à la marge sud du bassin de Kufra, l'un des principaux sous bassin du NSAS, est caractérisée par des taux de précipitation plus importantes. La recharge s'opérant dans cette région pourrait également avoir des implications sur le système aquifère régional, comme déjà suggéré par d'autres chercheurs.

Des campagnes de terrain ont été entreprises entre 2013 et 2016, couvrant une superficie approximative de 100,000 km^2. Les objectifs de ces campagnes de terrain étaient d'acquérir des données sur la géologie et la sédimentologie du réservoir, sur l'organisation des écoulements souterrains et sur l'hydrochimie (ions majeurs, isotopes stables) des eaux souterraines. Pour palier au manque de données climatiques, la dynamique météorologique et hydrologique a été investiguée en utilisant des données satellitaires (RFE2.0, LandSat8OLI).

La composition hydrochimique des eaux souterraines ainsi que les résultats de l'analyse d'images satellitaires (précipitation, évapotranspiration) indiquent que les montagnes de l'Ennedi et du Tibesti correspondent à des zones à fort potentiel de recharge diffuse et concentrée. La recharge s'opère potentiellement annuellement, au courant de quelques averses concentrées durant la saison pluvieuse (mi-juillet à mi-septembre).

Au de-là des zones de recharge, une large dépression s'étend entre ces zones montagneuses. Cette dépression est explicitement reconnue comme étant une entité structurelle majeure marquant les directions de la phase tectonique de l'Hercynien. Les principales zones de décharge du NSAS du Nord du Tchad se trouvent le long de cette dépression. La composition hydrochimique des eaux souterraines

dans ces zones de décharge est comparable à la composition des eaux souterraines dans d'autres zones de décharge du NSAS.

Le schéma conceptuel qui résulte des mesures de terrain de charges hydrauliques est similaire au schéma développé par les chercheurs il y a quatre-vingt années. L'organisation des écoulements souterrains et la composition isotopique indiquent que les zones de décharge (Lacs d'Ounianga, Faya-Largeau) sont approvisionnées par un écoulement en provenance de zones ou la recharge s'est principalement opérée durant les époques pluviales passées de la fin du Pléistocène à l'Holocène moyen.

Enfin, cette étude démontre le rôle crucial qui jouent les ouadis dans la redistribution d'eau de surface pour les régions montagneuses du Nord du Tchad. Grâce à l'imagerie satellitaire, cette étudie identifie les ouadis les plus actifs de l'Ennedi, ou il y a un fort potentiel de recharge concentrée. Cette ressource renouvelable pourrait être mieux gérée est ainsi garantir un meilleur accès à l'eau pour les populations locales.

Mots clés

Aquifère des Grès de Nubie, basin de Koufra, Nord Tchad, climat aride, recharge, ouadis, hydrologie, hydrogéologie, imagerie satellitaire, isotopes stables et hydrochimie, modèle conceptuel des écoulements souterrains.

Contents

Chapter 1 – Introduction

Chapter 2 – Review of the geology of the Kufra basin of Northern Chad

Chapter 3 – Mineralogical and textural analysis of the sedimentary sequence of the Kufra basin of Northern Chad

Chapter 4 – Hydrology and hydrogeology of the Tibesti Mountains and the Kufra basin of Northern Chad

Chapter 5 – Rainfall and surface water dynamics

Chapter 6 – Potential and actual evapotranspiration

Chapter 7 – Hydrochemistry and stable isotopes

Chapter 8 – Synthesis of the results and conceptual groundwater model

Appendices

Chapter 1

Introduction

1.1. The Nubian Sandstone Aquifer System - overview and current challenges

The Nubian Sandstone Aquifer System (NSAS) is one of the largest aquifer of the world. Its geographical extent reaches 2.2 Million km^2 (CEDARE, 2002) and is shared between Libya, Egypt, Sudan and Chad (Figure 1.1). The thickness of the sedimentary cover varies between less than 500 m to > 4,500 m (Bellini and Massa, 1980; El-Mehdi et al., 2004) in the central and northern part of the Kufra basin.

The current climate is arid to hyper-arid: potential evapotranspiration is exceeding precipitation by a factor of 10 to 300, depending on location (mean annual rainfall < 5 mmy^{-1}). Groundwater is the only permanent water resource for the region, besides the Nile River at the eastern margins (Figure 1.1). Groundwater reserves have been estimated at 150,000 km^3 for the NSAS (Thorweihe and Heinl, 2002), but a considerable amount of this reserve is located at depths from which it is unprofitable or infrastructurally difficult to extract.

Since the early 1960s, groundwater has been intensively extracted from the Kufra oases in Libya (Great Man Made River) and from the New Valley in Egypt (Baharyia, Farafra, Dakhla and Kharga oases), raising concerns about the transboundary impact of such extractions and the possible disappearance of the remaining oases ecosystems. In 1991, the four countries sharing this vast groundwater resource created the Joint Authority for the Study and Development of the NSAS (JASAD-NSAS) and promoted actions to enhance the understanding of the functioning of the groundwater system. The main motivations driving these investigations were: (1) the need to develop a strategy for a sustainable use of the groundwater resources, (2) to ensure an equitable use within the aquifer-sharing countries and (3) to estimate the transboundary impact due to the large groundwater extractions in Libya and Egypt.

The NSAS is subdivided in several sub-basins, the Kufra and Dakhla basins being the major ones. The Kufra basin covers a total surface of 400,000 km^2, extending from Northern Chad to Southern (Kufra oases) and Central Libya, holding estimated groundwater resources amounting at 25'000 km^3 (Said and El-Mehdi, 2000). It constitutes the geological and hydrogeological system investigated in this study. More specifically, this study focuses on the southern part of the Kufra basin included within the Chadian territories, one of the least investigated parts of the NSAS.

In Chad, the presence of such a vast aquifer system is seen as an exploitable resource for human and economic development. The current use of surface and groundwater in the Northern region of Chad amounts at 113 Mm^3 (HCNE et al., 2003) for an estimated population of 400'000 inhabitants (INSEED, 2018). Approximately 6% of the use is dedicated to pastoralism, the remaining to agricultural use. In view of a future sustainable extraction, it is fundamental to improve the current understanding of the system dynamics, and develop insights concerning the hydrology, the geology and the large-scale organization of the groundwater system.

1.2. The functioning of the NSAS – a historical review of research developments

The hydrogeological investigation of the NSAS began with the first field-based water table elevation measurements performed by Ball (1927) and Sandford (1935). Early researchers (Ball, 1927; Sandford, 1935; Hellström, 1940; Murray, 1952) described the NSAS as a regional artesian aquifer system, composed of a very large unconfined and recharged area (south of 25°N), and a confined leaky system north of the Post-Nubian limit (Figure 1.1). These first authors identified the mountains of Northern Chad (Ennedi, Erdis, Tibesti) as acting as effective barriers to the passage of the monsoonal rains, causing precipitations rates between 25 to 100 mmy^{-1}, significantly higher compared to the regional average. These authors indicated that groundwater was originating from some unknown "intake beds" located in the south of the NSAS (between Chad and Sudan), flowing over a distance of 1,700 km towards the N-NE and discharging in northern Egypt (Figure 1.1). This first conceptual flow model also showed that part of the groundwater originating from these mountains was flowing towards the south, therefore supplying the lakes of Ounianga Kebir and Ounianga Serir (Figure 1.2), as well as the more southern margin of the system (oases of Faya-Largeau) in Chad.

Given the large area concerned by recharge, the low hydraulic gradients and flow velocities, they concluded that the system would require less than 10 mmy^{-1} of modern recharge to maintain steady-state (Hellström, 1940; Heinl and Brinkmann, 1989). This concept of unconfined-confined system in steady state is referred in literature as to the *allochtonous theory* (= a recharged and *in-equilibrium* regional unconfined-confined system).

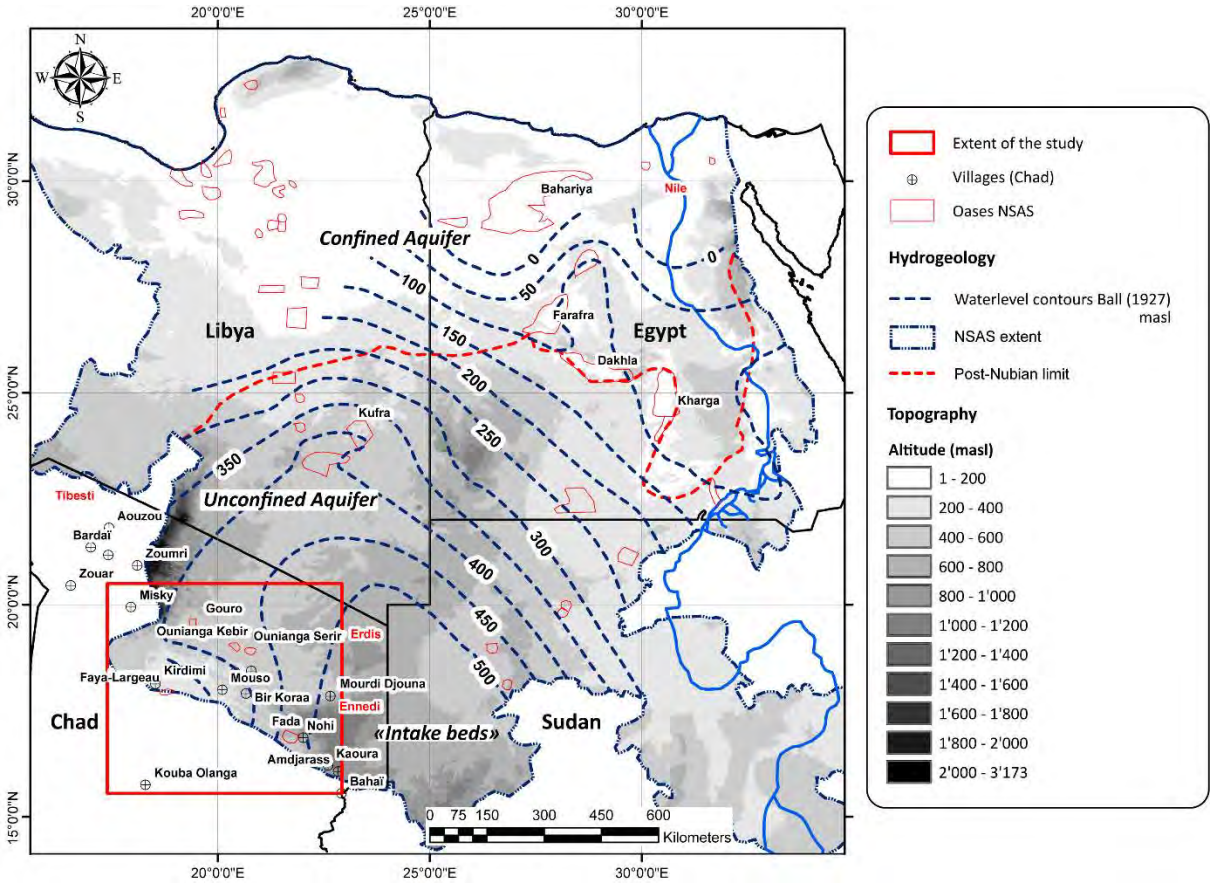

Figure 1.1: Map showing the extent of the Nubian Sandstone Aquifer System (NSAS), after Voss and Soliman (2014). The transboundary aquifer system crosses the borders of Libya, Egypt, Sudan and Chad. The locations of the oases (compiled after Voss and Soliman, 2014) are also shown, as well as the main villages in the Chad. Blue dashed lines indicate the water level measured and interpreted by Ball (1927) (compiled after Gossel et al., 2004). The Post-Nubian limit indicates the limit of the unconfined-confined aquifer (red dashed line). Altitudes are from SRTM (90 m altitude resolution). The red square shows the region under investigation.

The development of age-dating approaches based on ^{14}C (Münnich and Vogel, 1963; Klitzsch et al., 1976; Edmunds and Wright, 1979; Sonntag et al., 1982; Swailem et al., 1983; Muller and Haynes, 1984) and of numerical modelling (Heinl and Holländer, 1984; Brinkmann et al., 1987; Heinl and Brinkmann, 1989), challenged the concept of the allochtonous theory. Age gradients along the assumed flow lines proposed by Ball (1927) could not be observed. Moreover, comparatively young ages of 20,000 to 50,000 years were found for groundwater in the Egyptian depressions, which could not be explained with the allochtonous theory. To overcome the conceptual inconsistency of the allochtonous theory, new conceptual models were suggested (e.g. Pallas, 1980; Sonntag et al., 1982; Sonntag, 1984; Sonntag, 1986). Numerical modelling later confirmed that the observed hydraulic gradients are the result of the slow emptying of a very large aquifer system having experienced considerable amounts of recharge over large areas during the humid pluvial periods of the Pleistocene to Holocene.

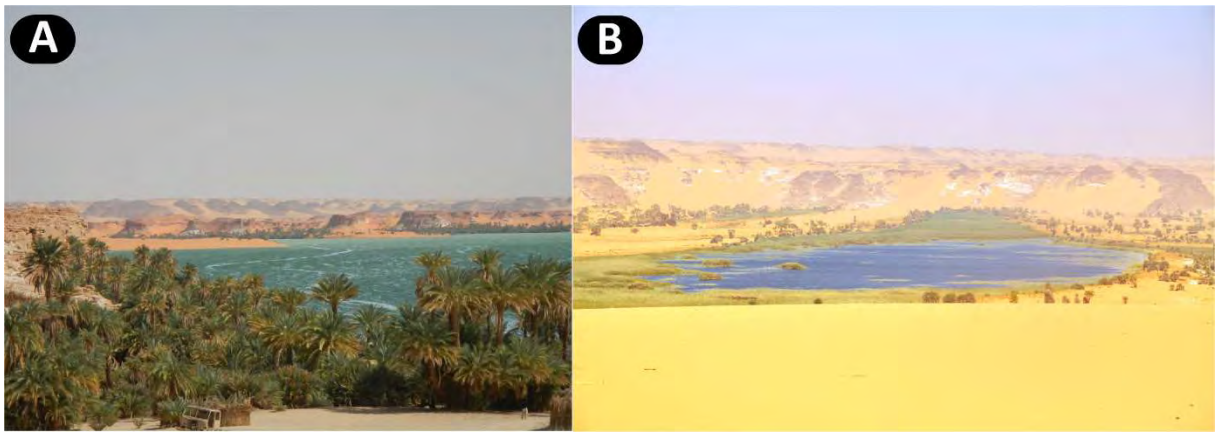

Figure 1.2: View of the Lakes of Ounianga (photos from the field). A) Ounianga Kebir, B) Ounianga Serir.

During the past periods of humid and semi-humid conditions, an increased importance of sub-regional flows over the regional flow described by the allochtonous theory is the reason advocated to explain the variability of groundwater ages. Authors developing numerical models of the region concluded that an equilibrium state could be maintained in the least up to 8,000 yrs BP, longer in specific areas of the system (Heinl and Holländer, 1984; Brinkmann et al., 1987; Heinl and Brinkmann, 1989). The concept of recharge during the past more favorable climatic setting provoking an increased influence of local groundwater systems over the regional groundwater flow, is referred in the literature as to the *autochtonous theory*.

The geographical and temporal distribution of paleohydrological deposits indicated a time lag between the decline in precipitation and the decline in the extent of the lacustrine and palustrine deposits from mid- to late-Holocene. This was interpreted by Lézine et al. (2011) as the inertial response of a large fully saturated aquifer system. Vasseur et al. (2015) mathematically expressed the transient state of a large aquifer system, such as the NSAS, subject to a "sudden" change in recharge regime. Given the specific hydraulic properties and the large horizontal and vertical extent, they concluded that such a system would need several millennia before reaching a new equilibrium state. Vasseur et al. (2015) argued that, the presence of hydraulic flows converging towards specific outlets, such as the Ounianga Lakes, play a major role in maintaining higher hydraulic gradients, even if no significant recharge occurred for the last 3,000 to 4,000 years.

Modelling approaches concluded that modern recharge could occur in the Mountains of Northern Chad, but that current recharge rates are several orders of magnitude inferior to discharge rates occurring in the depressions and oases (Gossel et al., 2004; Sefelnasr et al., 2015; Voss and Soliman, 2014). However, Vasseur et al. (2015) also concluded that, in the current climatic setting and without an upstream-unconfined sector (south of 25°N, Figure 1.1) receiving some amounts of modern recharge, the oases would already have dried out. Similarly, Ahmad (1983) concluded that the present

hydraulic heads could not be maintained without the current rates of recharge. And finally, Mohamed et al. (2017) concluded that the groundwater flow in the northern Kufra basin originates from the more elevated zone of the southern Kufra basin, potentially recharged.

1.3. Why Northern Chad?

The previous review showed that despite the many studies carried out, important questions remain. In fact, the current state of the art does not provide enough information on the hydrogeological functioning of the system in order to develop a solid and quantitative basis for sustainable water resource management. This is particularly true for the Chad extent of the NSAS, which has only rarely been the object of scientific research.

In order to fill these critical knowledge gaps, the Chadian government started in 2012 a partnership with the Swiss Confederation to promote water resources management. The project was called « ResEau - Cartographie des Ressources en Eau de la République du Tchad" (https://reseau-tchad.org). The goals were : (1) to increase knowledge on Chad's surface and groundwater through mapping and the acquisition of geographical information data, (2) to build capacities in the country through the formation of ministerial agents and young students in hydrogeology and GIS (master HydroSIG) and (3) to improve access to bibliographic and geographical data through the construction of the Centre de l'Information Géographique (CDIG), hosted by the Ministry of Water. Between 2012 and 2016, the ResEau project focused on the Eastern and Northern Chad regions, producing several hydrogeological maps based on remote sensing.

In this context, a range of field studies (Figure 1.3) was undertaken with the following objectives: (1) to collect information on groundwater, by measuring water table depths and select localities for water sampling, (2) to acquire information on the aquifer properties through geological and stratigraphic observations and sampling of characteristic rock formations, (3) and to geographically locate water occurrences or hydro(geo)logical significant features (enneris or wadis, presence of diatomites).

The information provided by the fieldwork (hydraulic heads measurements, hydrogeological observation, water and rock samples) represents a novel dataset for such a remote and inaccessible region. During these field campaigns, 223 water samples (from 185 different water points, resampled locations in different years), and 135 rock samples (Figure 1.4) were obtained, in an area covering approximately 100,000 km^2. Some of this information was used to produce the hydrogeological maps (e.g. MEH, 2015; MEH, 2016). However, more investigations were required to understand the large-scale groundwater flow organization of the NSAS of Northern Chad.

Figure 1.3: Pictures from the field. A) Training the use of a GPS in preparation of fieldwork; B) In-situ analysis of water samples; C) Inspection of water points, often crowded with people and camels; D) Getting stuck in dune sands is a daily business.

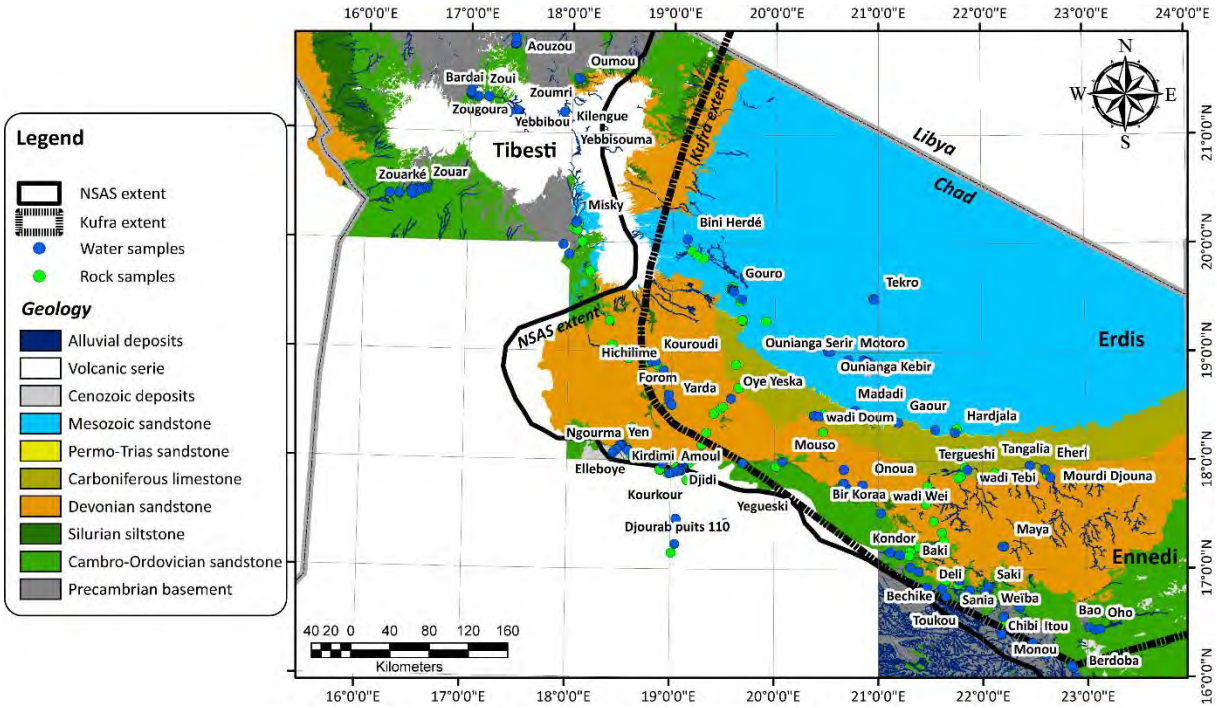

Figure 1.4.: Area covered by the field campaigns. The limit of the NSAS are from Voss and Soliman (2014). The Kufra basin extent is from Heron et al. (2009). Rock and water sampling locations are indicated as green and blue dots. Geological layers are from the SIRE database.

1.4. Main questions specific to Northern Chad's NSAS extent

1.4.1. Aim of this study

The aim of this study is to characterize the large-scale organization of surface hydrology and the groundwater flow system of the NSAS in Northern Chad. Hereafter, the specific questions and the different aspects investigated in this study are provided.

1.4.2. Geology and groundwater

Several geological and hydrogeological studies have been carried out for the Kufra basin (e.g. Sandford, 1935; Wolff, 1964; Williams, 1966; Goudarzi, 1970; Wright et al., 1982; Mahamoud, 1986; Lüning et al., 1999; Albert and Elgargoti, 2010). However, only few studies have been performed for the Chadian extent, and whenever geological and/or hydrogeological synthesis were presented, they were only sporadically supported by field studies.

Our first goal was therefore to review the existing literature regarding the geological history of the Kufra basin and to link it to the observations provided by the field and by the set of geological data (boundaries of the geological formations, faults) produced by the ResEau project. The geological phases that occurred in this region have resulted in stratigraphic discontinuities, variable thicknesses of geological formations, uplifted and subsided zones and several generations of fault directions, having a potential implication on the groundwater flow system. Thus, the main questions driving this

review were: (1) what are the main structural phases that shaped the Kufra basin? and (2) what implication do they have on the groundwater system?

1.4.3. Stratigraphy and groundwater

Sonntag (1986) describes the NSAS as a multilayer aquifer system composed of an upper unconfined aquifer and one or more confined aquifers underneath. The sedimentary sequence is composed of several sandstone layers of varying thicknesses, interbedded with clays and marls, spanning from the Cambro-Ordovician to the Upper Cretaceous. Pallas (1980) recognized that the Carboniferous formation, a marine sequence of up to 400 m thickness with low hydraulic conductivity, could separate the lower aquifer seated in the Cambro-Ordovician to Upper Devonian formations, from the upper aquifer seated in the Mesozoic formations. However, the presence of numerous faults, fractures and structural discontinuities and the large ratio of the lateral extent to the basin depth (ratios 100 to 1,000) increases the hydraulic conductivity over the entire area (vertical and horizontal, Sonntag, 1984).

In Northern Chad, the Paleozoic sequence outcrops at the surface, allowing investigating this lower section of the sedimentary sequence, otherwise positioned at great depths. Macroscopic observation from the field and the analysis of the rock samples had to be compiled in order to present a comprehensive view of the sedimentological sequence of the Kufra basin of Northern Chad and provide some estimates on the hydraulic properties and thicknesses of the different rock formations. The main questions driving this investigation were: (1) what is the aquifer's structure (multilayered)? (2) are there distinctive structural or sedimentological features, which can explain the location of discharge points such as springs and lakes? and (3) how thick and how efficiently low conductive layers, such as the Carboniferous formations, act as confining layers?

1.4.4. Hydraulic heads distribution

To the best of our knowledge, the only water table measurements carried out in the region of Northern Chad were performed eighty years ago by Ball (1927) and Sandford (1935). These measurements have been the dataset used so far in all the modeling approaches (e.g. Heinl and Brinkmann, 1989; Gossel et al., 2004).

Our fieldwork enabled to collect a denser and up to date dataset of water table measurements. The spatial distribution of hydraulic heads had to be interpreted on a large scale, in order to represent the groundwater system. In particular, elevated hydraulic heads are indicators of recharge. Lower hydraulic heads are indicators of zones of discharge. As previously introduced, the current conceptual flow model of the NSAS indicates that the system is in a transient state, not having yet reached a new equilibrium expressing the actual boundary conditions. Questions were therefore stated as follows: (1)

where are the zones of recharge and the zones of discharge? and (2) is the groundwater flow system, as observed today, the result of modern or past recharge?

1.4.5. Dynamics of recharge zones

For a sustainable management of the water resource, it is fundamental to characterize the spatial and temporal dynamics of recharge, particularly in arid environments. Within the framework of the JASAD activities, the Chad Water Authority recognized one of the main concerns to be the need to better characterize the mechanisms, dynamics and rates of modern recharge occurring in the Ennedi Mountains.

Unfortunately, there are only very few meteorological and hydrological data for the remote region of Northern Chad. Hydrological investigations were lastly conducted in the Tibesti Mountains between 1960's and 1980' by the *"Geographisches Institutes der Freien Universität Berlin"* and in the Ennedi Mountains between 1957 and 1959 by the *"Office de la Recherche Scientifique et Technique d'Outre-Mer"*. More recently, Mohamed et al. (2016) provided some estimate of recharge for the NSAS by the use of the GRACE satellite products, indicating that there is evidence that the southern Kufra extent is supplying the northern sector. However, no detailed study of precipitation and hydrological dynamics was previously performed for the NSAS of Northern Chad.

The improved accessibility to high-resolution remote sensing data provides the information needed to understand the large-scale climatic and hydrological dynamics. Therefore, the key questions addressed are: (1) what are the spatial and temporal dynamics of climatic forcing (precipitation and evapotranspiration)? (2) what are the temporal and spatial dynamics of "potential recharge"? (3) what are the main processes of surface water redistribution in the Ennedi Mountains? (4) and what is the relative importance between diffuse and concentrated recharge?

1.4.6. Dynamics of discharge zones

The NSAS of Northern Chad includes several important discharge points, also corresponding to the most populated sites. The Ounianga Lakes (Kebir and Serir), the southern slopes of the Ennedi Mountains and the oases of Faya Largeau, the West Palm Groves and Gouro are the most important in terms of human settlements.

In the arid climate of Northern Chad, these discharge zones constitute the main zones of water losses from the system. Evapotranspiration is the driving sink. As indicated by previous authors, the current recharge rates might be several orders of magnitude inferior to the discharge rates from oases. However, an estimation of actual evapotranspiration has never been carried out, these statements

being mostly the result from modelling approaches. Only a few estimates or measurements of potential evapotranspiration and pan evaporation were performed.

The lack of ground-based climatic data is challenging, but there are approaches based on remote sensing data, which allow overcoming these difficulties to a certain extent. Even if absolute values are uncertain and even if it is challenging to construct a complete time series, the dynamics of evapotranspiration in the discharge zones and along wadis can be investigated. Therefore, the main questions investigated are: (1) can we establish a temporal dynamics of groundwater fluctuations and phreatic evaporation in the discharge zones (e.g. Ounianga Kebir, Ounianga Serir, Gouro, Bedo, West Palm Groves and Faya-Largeau)? (2) are these fluctuations directly influenced by climatic forcing or rather the result of long-term dynamics of the aquifer system? (3) how much water is lost through evapotranspiration?

1.4.7. Large scale configuration of the groundwater system

The hydrochemical and stable isotopic signatures of groundwater provide valuable information on the origin of groundwater and relevant hydrogeological processes. Several authors working in the arid climate of Northern Africa have used the stable isotopic signature of groundwater to identify the zones experiencing modern recharge. Hydrochemical and stable isotopic signatures of groundwater of the NSAS in Northern Chad has not been previously characterized on a regional scale. Only a few examples of chemical analysis of groundwater are found within the reports of the Chadian Authorities or of international consultants, achieved in the framework of drilling programs. Stable isotopes were only very rarely analyzed.

The collection of water samples in the field and their analysis (major ions and stable isotopes) consist in a novel dataset, which had to be interpreted. The characterization of the hydrochemical and stable isotopic composition of groundwater in Northern Chad provides clues to link discharge zones to recharge zones, therefore to develop the conceptual model of the groundwater flow system. Thus, questions were addressed as follows: (1) what is the regional groundwater flow configuration? (2) what is the origin of groundwater discharging in the main oases (e.g. Ounianga Lakes, oases of Faya-Largeau)? and (3) how well does the hydrochemical composition of groundwater in the discharge zones correlate to the signature of groundwater in other parts of the NSAS?

1.5. Structure of the thesis

Chapter 2 is a synthesis of the available geological information of the Kufra basin and more specifically of the sector included within the Chadian territories. It presents the major geological phases (literature

review), the stratigraphic sequence composing the sedimentary basin (field-based) and discusses the most prominent structural features and their influence on the groundwater flow configuration.

Chapter 3 includes mineralogical, textural and geochemical observations and analytical results of rock samples collected in Northern Chad. It discusses the thicknesses of the geological formations, the range of hydraulic conductivities and transmissivities of the NSAS of Northern Chad, comparing observations and results from this investigation with studies from authors investigating other parts of the Kufra basin.

Chapter 4 introduces groundwater to the geological setting. The inspected water points from the regions of the Tibesti Mountains, Ennedi Mountains and central lowlands are described in terms of their relationship to an alluvial system or to a specific stratigraphic sequence. Considerations on the hydraulic properties of the different rock formations, based on mineralogy, intergranular porosities, geological macro structures observed in the field and groundwater occurrences related to specific sedimentary layers, are developed. Hydraulic heads and the observed groundwater flow directions are presented. The chapter also introduces the use of paleohydrological deposits as to confirm flow directions and infer hypothesis on the general behavior of the aquifer system. Hydrogeological profiles are presented.

Chapter 5 analyzes the patterns and intensity of precipitation interesting the region of Northern Chad by the use of the African Rainfall Estimates Algorithm Version 2 (RFE 2.0), a 10 km - resolution spatially distributed set of precipitation data. The analysis is undertaken for the Tibesti and Ennedi Mountains and the central lowlands. It then presents the observations extracted from applying the Normalized Difference Water Index to LandSat8OLI images (observation years 2013 to 2016). This analysis provides useful information on the dynamics of runoff (intensity, frequency) in response to rainfall. These data by themselves are not sufficient to quantify recharge, but provide a first order assessment of the precipitation rates and geographical differences within regions, allow identifying the most favorable zones for recharge and provide information for statistical analysis of precipitation rates.

Chapter 6 focuses on evapotranspiration. First, mean yearly estimates of potential evapotranspiration are elaborated. These results are compared to estimates found in the literature for the region under consideration. The spatially distributed actual evapotranspiration maps prepared from LandSat8OLI images (observation years 2013 to 2016) are then presented. The temporal and spatial distribution of actual evapotranspiration is discussed in terms of response to precipitation and/or groundwater dynamics. Estimates of total losses of evapotranspiration from the NSAS are presented.

Chapter 7 presents the hydrochemical (major ions and stable isotopes) characteristics of groundwater from the Tibesti Mountains, and surface and groundwater from the Nubian Sandstone Aquifer System

of Northern Chad (southern Tibesti, Ennedi Mountains and central lowlands). Their stable isotopic and hydrochemical signature are interpreted in terms of the origin of groundwater. The distinctive signature of groundwater recharged during the current period compared to groundwater recharged in past humid periods, is used to map the zones experiencing recharge and to further discuss its relationship to the NSAS regional aquifer system.

Finally, Chapter 8 synthetizes the key points elaborated in the previous chapters, presents a preliminary surface water balance and develops the conceptual flow model, integrating the results previously presented.

Chapter 2

Review of the geology of the Kufra basin of Northern Chad

2.1. Introduction

2.1.1. Introduction and aim

The Chadian area of the Kufra basin remains up to now one the least investigated regions of the NSAS. Only few studies have been performed for the Chadian extent, and whenever geological and/or hydrogeological synthesis were presented, they were only sporadically supported by field studies. However, several geological and hydrogeological studies were performed in other parts of the Kufra basin (e.g. Sandford, 1935; Wolff, 1964; Williams, 1966; Goudarzi, 1970; Wright et al., 1982; Mahamoud, 1986; Lüning et al., 1999; Albert and Elgargoti, 2010).

A review of the geology of the Kufra basin was presented in 1999 by Lüning et al., with the aim of evaluating the petroleum potential. However, no review was previously performed from the Chad perspective, focusing on the water resource. The objective of this chapter is to synthetize the available geological information of the Kufra basin and more specifically of the areas included within the Chadian territories. This chapter presents the major geological phases (structural and sedimentological), based on the current literature, the stratigraphic sequence composing the sedimentary basin (based on fieldwork) and discusses the most prominent structural features. The review provides the background information to which we refer to in the following chapters.

The review and analysis described in this chapter focuses on the following questions: (1) what are the main structural phases that shaped the Kufra basin? and (2) what implication do they have on the groundwater system? These questions are further analyzed in Chapters 3 and 4.

2.1.2. Note of terminology

In this and the following chapters, we refer to the Kufra basin to describe the geological basin, and to the Nubian Sandstone Aquifer System (NSAS) to describe the aquifer seated in the sedimentary sequence composing the Kufra geological basin. The Lake Chad geological basin is neighboring the Kufra basin towards the south. At the same time, the hydrological basin of the Lake Chad covers a large extent of the NSAS (see Chapter 4). When no other indications are added, the term Lake Chad basin is

used to describe the geological basin. When describing the Lake Chad hydrological basin, the indication "hydrological basin" is added.

2.1.3. Outline of the chapter

The chapter first presents a synthesis of the major geological phases having shaped the Kufra basin (section 2.2), based on literature review. A brief methodological section (section 2.3) is then presented.

Section 2.4.1 describes the stratigraphic sedimentary sequence (Paleozoic and Mesozoic) found in Northern Chad. To complete the description, a reconstructed litho-stratigraphic log and photos of the geological formations from the field are presented. The thicknesses of the geological formations are estimated from several geological cross-sections performed during our study, for which a selection is presented in section 2.4.2. Section 2.4.3 analyzes the fault directions on a regional scale and of selected localities of Northern Chad, localities which are later investigated in other chapters.

The discussion (section 2.5) synthetizes the geological information presented in this chapter, identifying the major geological phases. The discussion also focuses on the implication of the morphology and of the structural features issued by geological processes, to the groundwater flow configuration of the NSAS of Northern Chad.

2.2. Area of investigation

2.2.1. Boundaries of the Kufra basin

The Kufra basin is one of the major geological sub-basins of the NSAS, extending between Northern Chad and Central and Southern Libya over an area of 400,000 km^2 (Figure 2.1). The boundaries of the basin are defined by the zones of high basement elevation. The Kufra and Dakhla sub-basins are divided by the Calanscio Arch to the North (Jebel az-Zalmah, Le Heron and Howard, 2012) and the Jebel Oweinat Massif (Jebel Asba) to the East. The Kufra and Northern Sudan Platform are divided by the Oweinat-Howar Uplift in Northern Sudan, according to Mohamed et al. (2016). However, the region extending from the Ouaddaï in Chad towards the Oweinat Massif, also corresponds to a zone of basement uplift, identified as the Ennedi-Oweinat Uplift by Williams (1966).

The western limit of the Kufra basin, and of the NSAS, is defined by the Tibesti Mountains (Jebel Eghei, Jebel Nuqay). Towards the South, the extent of the Kufra basin and of the NSAS, is defined by the limit of the Paleozoic sedimentary cover, bounded to the Cenozoic sediments of the Lake Chad basin in the region of Faya-Largeau, and to the uplifted Precambrian basement of the Ouaddaï, south of the Ennedi Mountains (Lestang, 1965; Mahamoud, 1986; Klitzsch and Wycisk, 1987). The limit is marked by the Tibesti lineament (Guiraud et al., 2000). The NSAS is bounded to the Sirte basin towards the North-West.

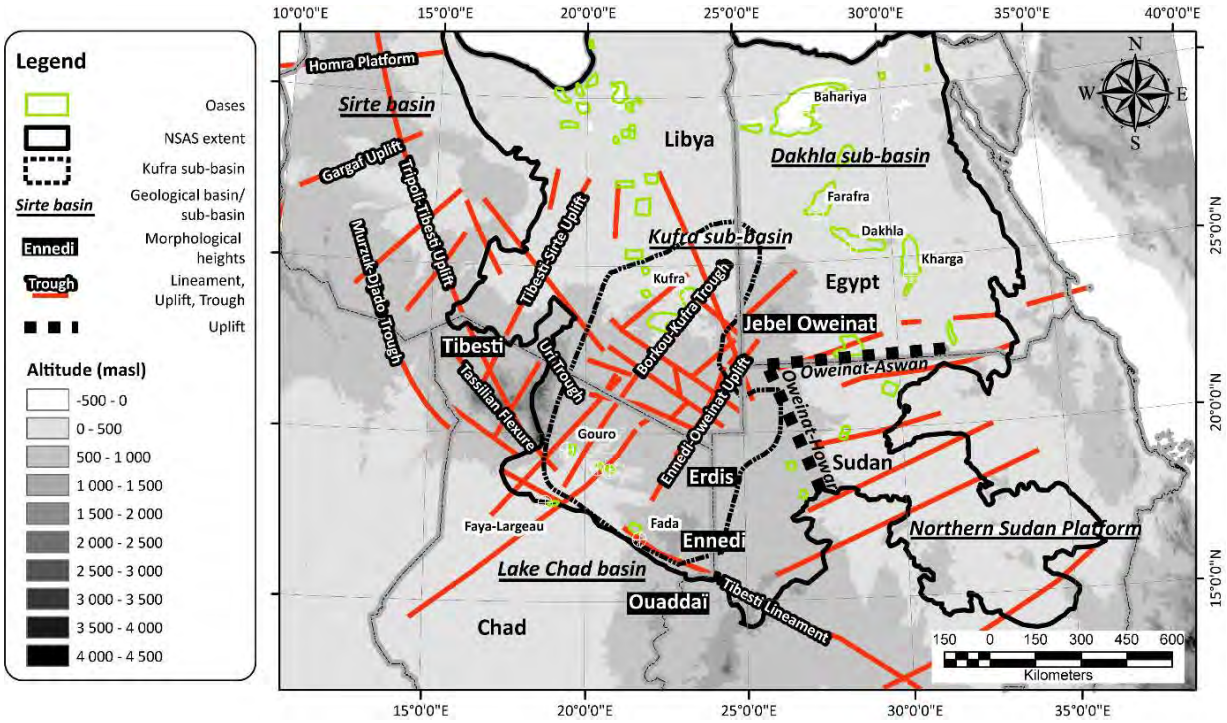

Figure 2.1: Map of the NSAS extent (from Voss and Soliman, 2014) and neighboring geological basins (Sirte and Lake Chad basins). The extent of the Kufra sub-basin is from Heron et al. (2009). The Kufra sub-basin is limited to the east by the Oweinat-Howar Uplift (Mohamed et al., 2016) or the Ennedi-Oweinat Uplift. The Northern Sudan Platform are divided from the Dakhla sub-basin by the Oweinat-Aswan Uplift (Mohamed et al., 2016). The location of oases are from Voss and Soliman (2014). Lineaments, uplifts and troughs are from Williams (1966), Guiraud et al.(2000), Elsheikh et al. (2011), Deniel et al. (2015). Main morphological heights (Tibesti, Ennedi, Erdis, Jebel Oweinat) of Northern Chad and Southern Libya are also indicated.

2.2.2. Geological phases of the Kufra basin

The Kufra basin is a NNE-SSW synclinal sedimentary basin (Figure 2.2). The basin is composed of Paleozoic and Mesozoic strata of > 4,500 m thickness in central and northern Libya (Bellini and Massa, 1980; Hesse et al., 1987; El-Mehdi et al., 2004; Herzog et al., 2008). The geological layers dip at a low angle from the basement heights towards the center of the basin. From its southern borders (in Northern Chad) moving northwards, the older formations (Paleozoic) gradually disappear under the younger formations (Mesozoic), forming a typical cuestas morphology northerly prograding.

The Kufra basin lies on a cratonic Precambrian basement (Bellini and Massa, 1980; Lüning et al., 1999), named the enigmatic Sahara Metacraton (Abdelsalam et al., 2002 **;** Begg et al., 2009). Several tectonic phases have characterized this region and more extensively Northern Africa during the Late Precambrian – Phanerozoic (Craig et al., 2008): (1) the Pan-African Orogeny; (2) the Infracambrian extension; (3) the Cambrian to Carboniferous alternating extension and compression; (4) the Late Carboniferous (Hercynian) intraplate uplift; (5) the Late Triassic – early Jurassic and the Early Cretaceous rifting; (6) the Mid Cretaceous "Austrian" and Late Cretaceous – Tertiary "Alpine" compression; (7) the Neogene to Recent uplift and volcanic activity.

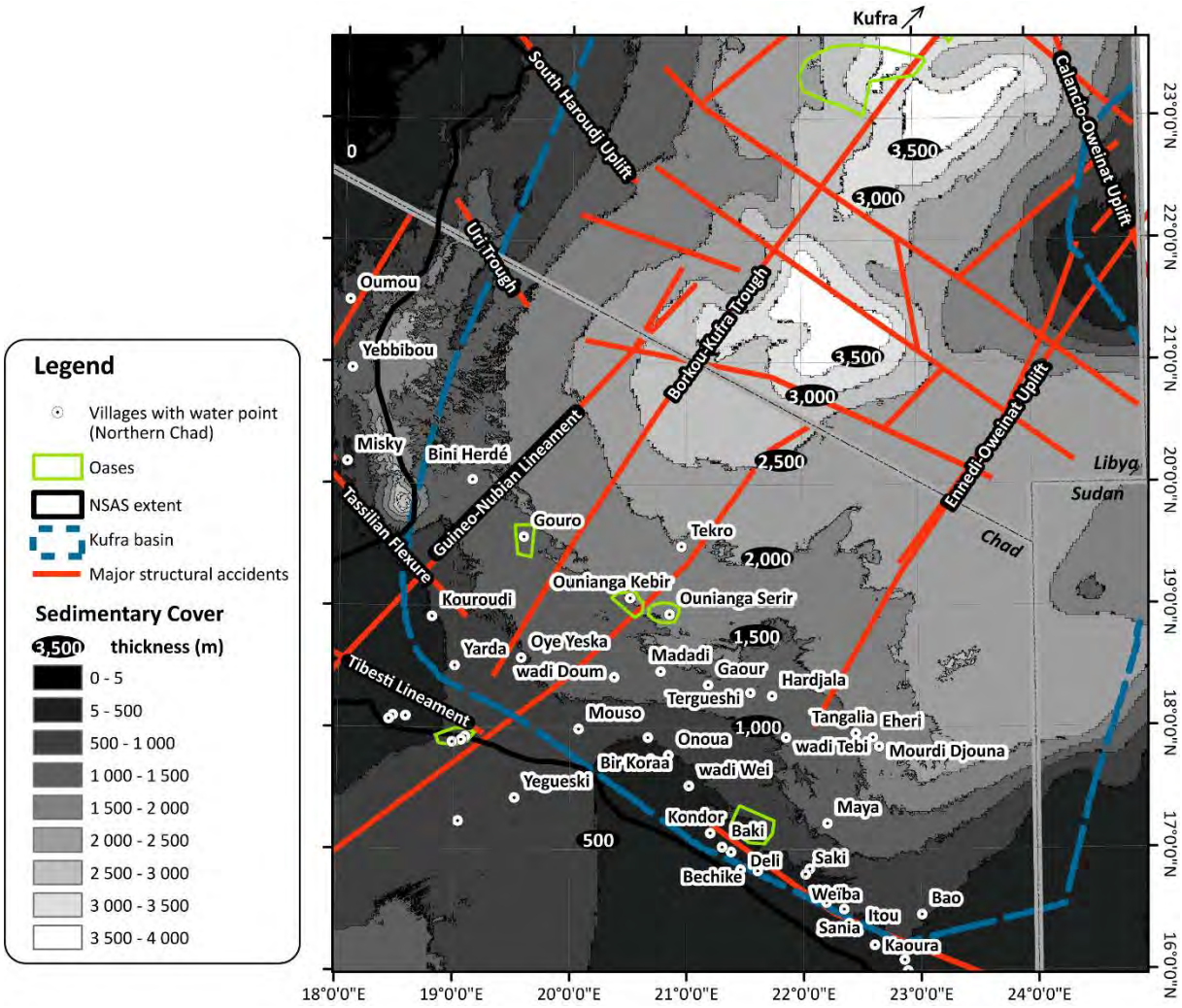

Figure 2.2: Map of the major structural features described in the text. Major structural accidents are from Williams (1966), Guiraud et al. (2000) and Deniel et al. (2015). Thickness of the sedimentary cover was extracted by data of basement elevation from Mahamoud (1986) and SRTM digital elevation model (Jarvis et al., 2008). Are also shown the oases locations, the extent of the Kufra basin (from Heron et al., 2009) and the extent of the Nubian Sandstone Aquifer System (from Voss and Soliman, 2014).

2.2.2.1. The Precambrian

Deep discontinuities have shaped the basement's structure during the Pan-African orogeny. These major structural accidents have replayed in several occasions in further geological times (Schandelmeier et al., 1987**;** Guiraud et al., 2000**;** Abdelsalam et al., 2002**;** Coward and Ries, 2003**;** Guiraud et al., 2005). The WNW-ESE Tibesti Lineament and SW-NE Guineo-Nubian Lineament correspond to two main Pan-African structures.

The Infracambrian extension resulted from regional subsidence and local intracratonic rifting (en echelon pull apart basins, Le Heron et al., 2009). Over-thickening of the Paleozoic and Mesozoic formations (3.5 to 4 km) observed in the south and in the northeast of the Kufra oases (Figure 2.2) are

interpreted as infracambrian weakness structures having experienced increased sagging during the Paleozoic and Early Cretaceous (Lüning et al., 1999).

Variable thicknesses of the Paleozoic formations around the flanks of the Kufra basin are interpreted as the result of extensional/transtensional and compressional/transpressional events during the Paleozoic (Craig et al., 2008).

2.2.2.2. The Lower Paleozoic (Cambrian to Silurian)

The Cambro-Ordovician was characterized by a general fluvio-continental environment from Chad to Mali and up to the extreme north of the Sahara (total surface of 1 M km^2), during which large volumes of sandstone were deposited (Lestang, 1965; Lüning et al., 1999; Le Heron and Howard, 2012). The sediment influx was originating from the south and south-west (continental exposed lands at 15-20°E, 15-18°N, Guiraud et al., 2005), following the main graben trends towards the NE (Beuf, 1971). In Libya (Murzuk basin, Heron and Craig, 2008), the Cambrian succession is named Hassaouna Formation, the terms Ash Shabiyat and Hawaz are used to indicate Lower and Middle Ordovician, respectively.

The development of a large icecap over much of Africa and South America during the Late Ordovician (Hirnantian, Upper Ordovician), has deeply incised the topography and morphology of the Cambro-Ordovician continental platform (Wacrenier, 1958; Beuf, 1971; Lüning et al., 1999; Le Heron and Howard, 2012). Glacially related deposits or erosional features recognized to be of the Late Ordovician are found in Jebel Arkenu (NE Libya) and Jebel Eghei (Northern Chad). Heron and Craig (2008) postulated that the NE-SW depressional zone running from Faya-Largeau to the Kufra oasis, was an inter-stream ice thick during the Hirnantian glaciation. Upper Ordovician glacial deposits are termed Memouniat Formation in the Kufra Basin.

The retreat of the inlandsis was followed by a period of glacio eustatic sea-level rise during the Early Silurian (Wacrenier, 1958; Lüning et al., 1999; Le Heron et al., 2010 ; Le Heron and Howard, 2012). In Libya, the Lower Silurian is named Tannezuft Formation and the Upper Silurian Akakus Formation.

NW to NNW directions dominate the early Paleozoic evolution (Caledonian phase). The South Harudj and Tripoli-Tibesti Uplifts, and their associated Dor el Gussa – Uri and Murzuk-Djado Troughs (Williams, 1966; Craig et al., 2008, Figure 2.2) compose the horst and graben structure of the early Paleozoic, initiating the development of many individual Paleozoic sedimentary basins (e.g. Illizi, Berkine, Murzuk and Kufra basins, Gindre et al., 2012). The southern Calanscio-Oweinat Uplift (southern Libya, Figure 2.2) is also associated with this phase.

2.2.2.3. The Upper Paleozoic (Devonian to Carboniferous)

Beuf (1971) estimates the deposition of the Lower Devonian fluvial-estuarine sandstone to be as extensive as the Cambro-Ordovician sandstone (approx. 1 M km^2). The massive early Devonian Tadrart formation (term used in Libya) shows cross-bedding structures of a fluvio-continental environment, with a north-eastward direction of the paleocurrent dispersals (SE-NW for Beuf, 1971). The region evolves to a more estuarine environment during the Late Devonian and a frankly marine environment during the Carboniferous (Gerard, 1958; Wacrenier, 1958; Capot-Rey, 1961; Kusnir and Schneider, 1993; Lüning et al., 1999; Le Heron and Howard, 2012).

The Hercynian tectonic phase, and its associated NE to NNE-trending uplifts and troughs, is considered as the phase which shaped mostly the Kufra and Murzuk basins (Williams, 1966**;** Lüning et al., 1999). The Tibesti-Sirte Uplift, the Borkou-Kufra Trough (Figure 2.2, Williams, 1966) and the Uplift of the Jebel Oweinat Massif (Bellini and Massa, 1980) are related to this phase. In the Tibesti Mountains, the Precambrian basement was flexured and most of the Paleozoic sequence strongly eroded (Gerard, 1958; Kusnir and Schneider, 1993; Deniel et al., 2015).

2.2.2.4. The Mesozoic

The Mesozoic formations of the Kufra basin were deposited in a predominantly continental fluvio-lacustrine environment (Wacrenier, 1958; Lestang, 1965; Coward and Ries, 2003).

An extensional phase with associated rifting characterized the Late Triassic – early Jurassic and the Early Cretaceous times. NE and ENE-trending graben structures observed in North-West Sudan (Schandelmeier et al., 1997; Elsheikh et al., 2011, Figure 2.2) and in the Western Desert of Libya (Craig et al., 2008) were attributed to this phase.

The Mid Cretaceous “Austrian” and Late Cretaceous – Tertiary “Alpine” compression was the result of intraplate stress associated to the Africa-Europe collision, inverting the Early Cretaceous rifting and reactivating the preexisting structural features, particularly the inherited NW to NNW Caledonian directions. During the Eocene, the area of the Jebel Oweinat was reactivated, accompanied with ring intrusions (Hallet, 2002).

2.2.2.5. The Cenozoic

The last rifting phase led to the development of the East African Rift, Gulf of Aden and Red Sea Rift system during the Oligo-Miocene (Craig et al., 2008). In Eastern Chad (Ouaddaï), NNW directions were interpreted as the result of Tertiary rifting (Oursingbé and Tang, 2011). Magmatic and volcanic activity and associated regional uplifts are widespread (Craig et al., 2008; Swezey, 2009) in Northern, Central (Harouj volcanic field) and Southern Libya/Northern Chad (Tibesti Volcanic Complex).

The Tibesti Volcanic Complex, an intercalation of basalts ("série noire") and rhyolites ("série claire"), capped by deposits of trachy-andésites, dates from the mid-Eocene to the Holocene (Dalloni et al., 1934; Gerard, 1958; Williams, 1966; Vincent, 1970; Beuf, 1971; Kusnir and Schneider, 1993; Deniel et al., 2015). Present-day volcanic activity is restricted to the Soborom solfatara field and the fumaroles of Pic Toussidé.

Tertiary uplifts, potentially reaching their maximum intensity during the Oligocene (Albert and Elgargoti, 2010), are seen to be responsible for the tilting and the basin margins exposure (e.g. southern Illizi, southern Ghadames and western Murzuk basins, Craig et al., 2008). The uplift of the southern region of the Kufra basin triggers the development of a watershed between the northern-directed rivers aiming at the Mediterranean sea (Mediterranean hydrological basin), and the southern-directed rivers aiming at the Paleo-Lake Chad (Lake Chad hydrological basin, Figure 2.5, Albert and Elgargoti, 2010).

From the Miocene (6.2-6.5 Ma, Lebatard et al., 2010) to the Holocene, the region of the Lake Chad basin experiences large deposits of fluvio-lacustrine sediments, attesting for a prolonged favorable climatic setting (Mega-Lake Chad maximum at 8,000-9,000 yrs. BP, see Chapter 4). During the quaternary, climatic oscillations were however recurrent, as indicated by several intercalations of fluvio-lacustrine deposits, alluviums, eolian sands and laterites.

2.3. Methods

2.3.1. Fieldwork

Three field campaigns, with a geological component, were undertaken between 2013 and 2015 in the framework of the ResEau project (https://reseau-tchad.org, see location of rocks samples in Figure 1.4). Most of the observations describing the Paleozoic sequence (Cambro-Ordovician to Carboniferous) were collected in the Ennedi Mountains (field campaign in February 2013), where this part of the sequence outcrops above ground level. The Upper Paleozoic (Devonian to Carboniferous) and Mesozoic sequence were investigated by tracing a transect between Faya-Largeau and the Ounianga Lakes (field campaign in January 2014). The third field campaign (in January 2015) covered these same formations in the surroundings of the Tibesti Mountains, and completed the information on the Cenozoic and Quaternary deposits. The identification of these formations in the field is largely based on the geological map of Wolff (1964) and on descriptions of the geological formations from Dalloni et al. (1934), Gerard (1958), Wacrenier (1958), Capot-Rey (1961), Lestang (1965), Williams (1966), Vincent (1970), Beuf (1971), Kusnir and Schneider (1993), Lüning et al. (1999) and Albert and Elgargoti (2010).

2.3.2. Data used in the chapter

In addition to the literature cited in the text, the figures and the analysis presented in this chapter are based on the following data: (1) hydrogeological maps (scale 1:500'000 and 1:200'000) and the SIRE database, including shapefiles data of geological information produced by the project ResEau; (2) SRTM (Shuttle Radar Topography Mission) version 4.1 (Jarvis et al., 2008); (3) basement elevation model (masl) from Mahamoud (1986); (4) log profiles and geological information included in BRGM (1991).

The structural analysis presented in section 2.4.3 are based on the structural information (faults directions) provided in the SIRE database. Rose diagrams of faults were prepared using the ArcMap (ArcGIS Desktop 10.5) extension Polar Plots and Circular Statistics (Jenness, 2014).

Estimated thicknesses of geological formations were derived by geological cross-sections (examples are given in section 2.4.2) adapted from the basement elevation model from Mahamoud (1986), SRTM, the geological map from Wolff (1964) and geological shapefiles from the SIRE database. Note that the modelled basement elevation from Mahamoud (1986) shows increased depths in the region of the Ennedi Mountains which are not representing the expected thicknesses of the sedimentary cover based on our fieldwork observation and derived by cross-sections (based on maps of Wollf , 1964, and MEH, 2015, 2016). For example, increased thicknesses of the sedimentary cover are indicated in areas were the Precambrian basement outcrops at the surface (Figure 2.6, cross-section 1, between Kaoura and Amdjarass).

The estimated thicknesses were also compared to the stratigraphical sequence described in Gerard (1958), Wacrenier (1958), Lestang (1965), Hesse et al. (1987), Kusnir and Schneider (1993), Lüning et al. (1999), Le Heron and Howard (2012), Gindre et al. (2012) and MEH (2015). Technical reports from the Chadian Water Authority in the frame of drilling and water points construction programs (Gombert, 1993**;** BURGEAP, 1996**;** BURGEAP, 1999a**;** BURGEAP, 1999b**;** BURGEAP, 2001a**;** BURGEAP, 2001b) were also consulted.

2.4. Results

2.4.1. The sedimentary sequence of the Kufra basin of Northern Chad

The Paleozoic and Mesozoic sequences of the Kufra basin are characterized by a generally fluvio-continental environment having deposited massive amounts of sediments (see section 2.2.2). The monotonous continental sedimentation was interrupted by a period of icecap coverage (Late Ordovician) followed by the installation of a circum-polar marine environment (Early Silurian) and by

a wide marine transgression during the Carboniferous. For reference, Figure 1.4 (Chapter 1) and Figure 2.5 show the distribution of the geological formations.

Estimated thicknesses, derived from cross-sections, of the Paleozoic formations (Cambro-Ordovician to Carboniferous) generally range from 1,050 to 1,350 m, while thicknesses of the Mesozoic formations (Madadi, Soeka, Lakes and Ounianga) range between 650 to 750 m (Figures 2.3 and 2.4). In the region investigated, approximately 250 m of Upper Cretaceous (Chieun and Tekro formations) end the sedimentary sequence.

2.4.1.1. The Lower Paleozoic (Cambrian to Silurian)

In Northern Chad, the Cambro-Ordovician sequence is composed of a cyclic massive continental sandstone, intercalated with silty layers, recognizable by its typical erosional features named “cheminée de fée” (Figure 2.3B). It overlies a peneplained Precambrian basement, as attested by the horizontal plane marking the contact (Figure 2.3A). At a mesoscale, the contact is identified by horizons of centimeters to meters-thick massive indurated crusts and soft laminated kaolinite and iron oxides, sealing cobbles and pebbles mainly of quartz and quartzite.

Glacial-originated structures and deposits resulting from the Late Ordovician inlandsis, are found in several localities at the southern flanks of the Ennedi massif and in the region of Faya-Largeau: glacial sculptured valleys (Figure 2.3C), diamictites, meter-length alignments, in relief because of secondary filling, and pressure-fractures, overprinting fluvio-estuarine cross-bedding structures of the Cambro-Ordovician sandstone (Figure 2.3D).

The deeply incised valleys are filled with Silurian transgressive shales and silty shales with occasional fine to very fine-grained sandstone beds, frequently exhibiting hummocky cross-stratifications. Silurian deposits are discontinuous in Northern Chad, from south of the Ennedi Mountains to the region of Faya-Largeau. In the region of Fada (southern Ennedi Mountains), the Silurian deposits form a wide platform. Towards the south of the plain, it is frequent to observe a sedimentary inversion coupled to differential erosion, showing the Cambro-Ordovician sandstone outcropping above the Silurian plain (Figure 2.3E).

Estimated thicknesses of the Cambro-Ordovician to Silurian sequence vary between 50 to 450 m. The observed Silurian formation’s thickness generally varies between 50 and 80 m.

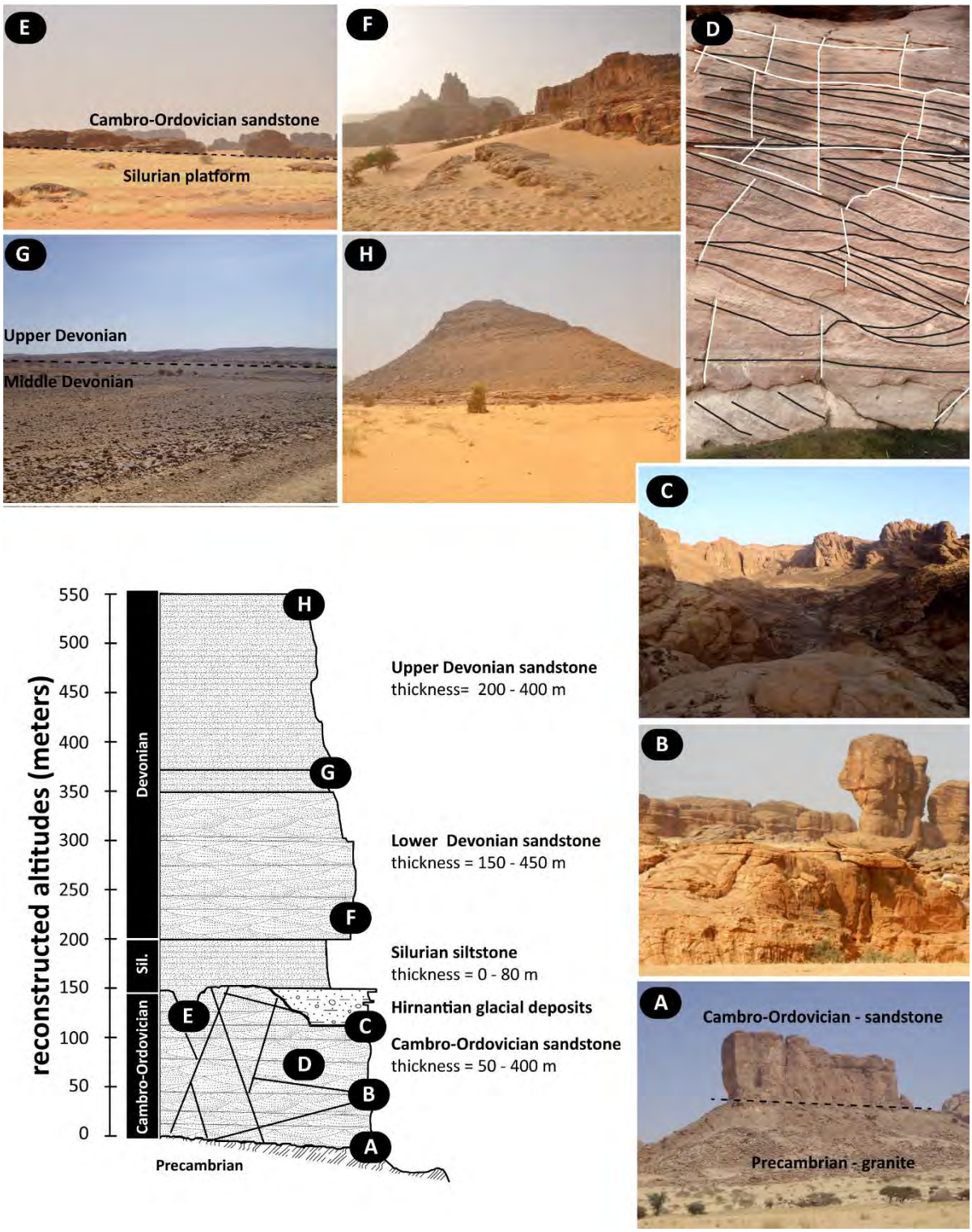

Figure 2.3: Reconstructed lithostratigraphic log (thicknesses are estimated from geological cross-sections) and photos from the field (their stratigraphic location are indicated on the log and their location on a map are indicated on Figures 2.5 and 2.6): Cambro-Ordovician to Upper Devonian. A) A recurrent morphology found in the eastern part of the Ennedi mountains, showing the contact between the magmato-metamorphic Precambrian basement and the Cambro-Ordovician sandstone; B)"Cheminée de fée" erosion features (Nabar); C) Glacial-sculptured valley (Archeï); D) Pressure-fractures (white line), overprinting fluvio-estuarine cross-bedding structures of the Cambro-Ordovician sandstone (black line), Archeï; E) At the southern limit of the Fada plain, Cambro-Ordovician sandstone outcropping above the Silurian; F) The Lower Devonian sandstone from the southern slopes of the Ennedi Mountains; G) The Middle Devonian platform (North of Fada); H) A typical morphology of the Upper Devonian (Ellichi).

2.4.1.2. The Upper Paleozoic (Devonian to Carboniferous)

In Northern Chad, the Devonian formations form a thick sedimentary sequence corresponding to the highest elevations of the Ennedi Mountains and covering a wide region north of Faya-Largeau. The Lower Devonian is composed of a red colored, fine-grained and occasionally medium-grained sandstone, showing cross-bedding structures of a river-estuarine environment. This lower sequence is morphologically and texturally very similar to the Cambro-Ordovician sandstone (Figure 2.3F). It is also intensively fractured, showing a characteristic sandstone rectangular hydrographic texture.

The Middle Devonian develops as a platform between the Lower and the Upper Devonian, composed of a psammitic platy sandstone (Figure 2.3G). The Upper Devonian is composed of a fine-grained, parallel-laminated to cross-stratified micaceous sandstone, and interbeds of siltstone/sandstone (Figure 2.3H), with frequent bioturbation and ripple marks figures, typical of shallow marine to lagoonal environments. Higher contents of sheet-like minerals (micas, clays) are also evident by the hydrographic system developing as a dense dendritic network.

Estimated thicknesses vary from 150 to 450 m for the Lower Devonian formation and from 200 to 400 m for the Middle and Upper Devonian.

The Carboniferous formation is well recognizable by the ~ 50 km-wide Mourdi depression (Figure 2.4A). In proximity to the contact with the Upper Devonian sandstone, the Carboniferous layers are composed of a relatively coarse continental sandstone, with ferruginous cement and iron oxides spherical concretions, and frequent ripple marks figures, indicating a shallow marine environment. The middle and upper part of the Carboniferous sequence is composed by an intercalation of sheet fine-grained sandstone, marls and blue limestone, indicating a deeper depositional environment.

The total thickness of the Carboniferous formation decreases from the East (north of the Ennedi Mountains, 250-350 m) towards the West, where it disappears at the foothill of the Tibesti Mountains.

2.4.1.3. The Mesozoic sequence

The age attributed to each individual Mesozoic formation in Northern Chad is still uncertain. The Madadi formation is indicated as Permo-Trias, but could theoretically be of Upper Carboniferous (Williams, 1966). Based on field observations from Lestang (1965) and similarities with the Murzuk basin's formations, Williams (1966) attribute the Soeka and Lakes formations to the Jurassic, the Ounianga formation to the Lower Cretaceous, the Chieun and Tekro formations to the Upper Cretaceous.

In Northern Chad, the Madadi Permo-Trias formation forms an escarpment north of the Mourdi depression, composed of fluvial sandstone and lacustrine siltstone (Figure 2.4B). Thicknesses are

approximately 50 m of a medium to coarse sandstone. The Soeka formation terminates with a 30 m thick red clay strata (Figure 2.4C). The Lakes formation, composed of sandy clays and medium-coarse sandstone, forms a platform of 20 km wide onto which are found the Lakes of Ounianga Kebir and Serir, and the oases of Gouro (Figure 2.4D). Estimated thicknesses of the Soeka and Lakes formations vary between 150 and 400 m.

North of the Ounianga Lakes and Gouro oases, the Ounianga formation forms a cuesta, composed of a pink sandstone intercalated with platy fine sandstone. The formation shows a fan-shaped morphology at its bottom (Figure 2.4E), becoming brittle-massive at higher stratigraphic levels (Figure 2.4F).

The Chieun formation, composed of varicolored silty shales with lenses of limnic limestone and chert nodules, forms a platform overlying the Ounianga formation. The observed sequence terminates with the Tekro formation, which forms a cuesta with a fan-shape morphology, composed of clays and violet argillites intercalated with sandstone (Figure 2.4G and 2.4H).

Estimated thicknesses of the Ounianga formation vary from 250 to 400 m. In the region investigated, approximately 250 m of Upper Cretaceous (Chieun and Tekro formations) end the sedimentary sequence.

2.4.1.4. Tertiary and Quaternary deposits

In Northern Chad, the “Continental Terminal” (Eocene-Miocene) is composed of fluvio-lacustrine deposits, generally clays and argillaceous sandstone, locally terminating with a ferrugineous carapace. These deposits are widely but sparsely distributed, and are found overlying unconformably Paleozoic or Mesozoic formations.

Holocene lacustrine deposits (diatomites, Figure 2.4I) have been widely observed in Northern Chad and elsewhere in the Kufra basin (Pachur and Altmann, 2007; Herrmann et al., 2009). Numerous examples of diatomite deposits are found in the Tibesti (altitudes 600 – 2,500 masl), in the Ennedi (altitudes 600 – 1,400 masl), in the Erdis (altitudes 600 – 800 masl), and in the depressional zone, comprising the oases of Faya-Largeau, Ounianga and Kufra (< 600 masl altitudes, Pachur and Altmann, 2007).

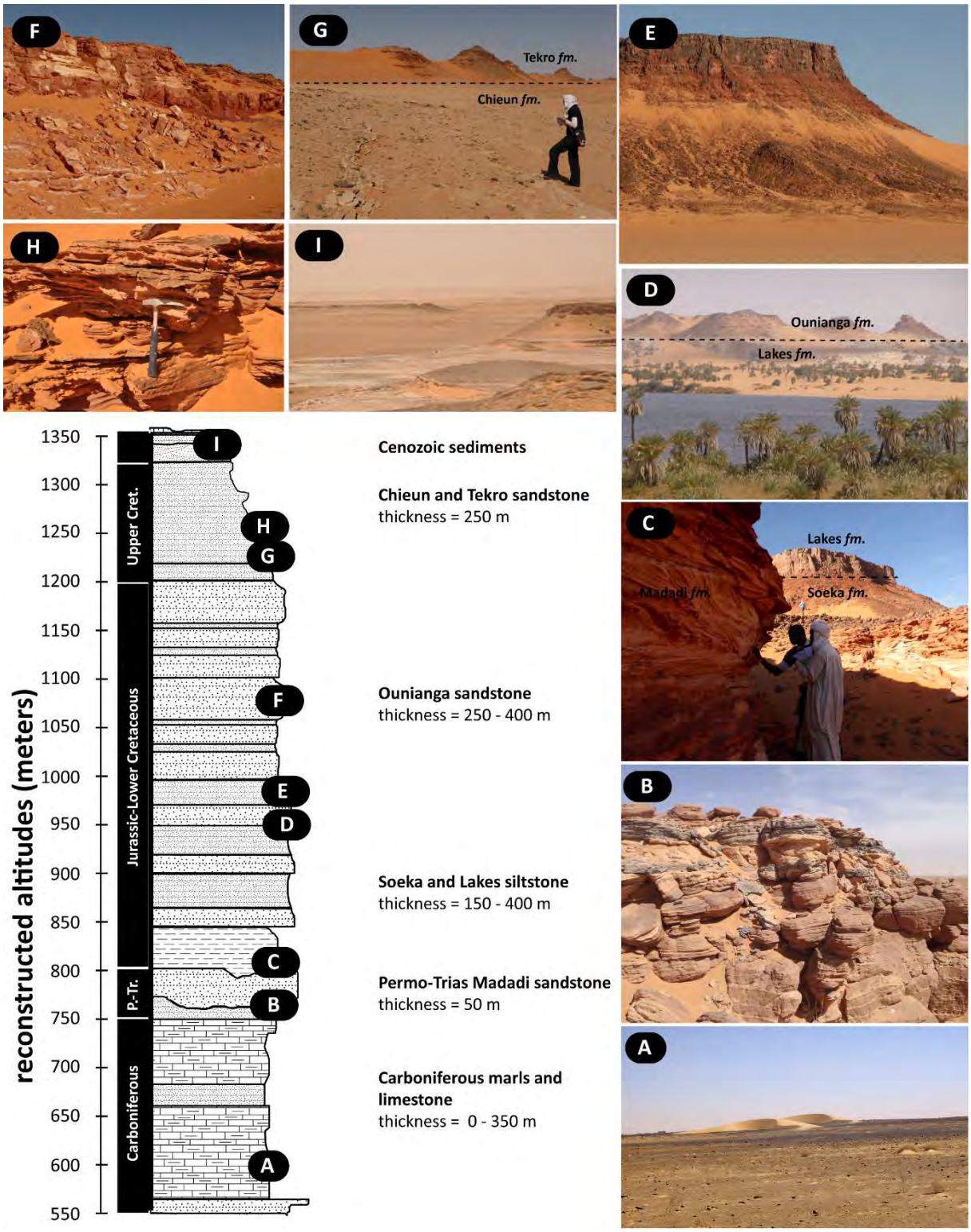

Figure 2.4: Reconstructed lithostratigraphic log (thicknesses are estimated from geological cross-sections) and photos from the field (their stratigraphic location are indicated on the log and their location on a map are indicated on Figures 2.5 and 2.6): Carboniferous to Tertiary-Quaternary. A) The Mourdi depression, showing a blue color indicating the presence of micritic limestone; B) Permo-Trias sandstone observed in Hardjalla; C) The illustration shows on the left, an outcrop of the Permo-Trias Madadi formation, and on the right the 30 m thick red clay strata and the silty sandstone of the Lakes formations; D) View of Lake Yoa (Ounianga Kebir) showing in the background, the contact between the Lakes formation and the Ounianga formation; E) The Ounianga formation (Lower section, escarpment north of Gouro); F) The Ounianga formation (upper section, north of the escarpment of Ounianga Kebir); G) The contact between the Chieun and the Tekro formation (Tekro); H) Outcrop view of the Tekro formation (Tekro); I) Lacustrine deposits (between Gouro and Ounianga Kebir).

2.4.2. Basement structure

Figure 2.5 are two schematic geological cross sections WNW-ESE.

Cross-section 1 is located close to the southern margin of the Paleozoic sandstone. The profile shows a deeper zone east of Faya-Largeau (basement elevation -500 masl, Borkou-Kufra Trough), and uplifted areas towards the west (Tibesti Uplift) and towards the east (Ennedi-Oweinat Uplift). The sedimentary cover thickness varies from west to east, from 150 m at the foothill of the Tibesti Mountains, to 800 m east of Faya-Largeau, to 150 m at the foothill of the Ennedi Mountains, and 250 m within the Ennedi Mountains.

Cross-section 2 cuts across the Paleozoic and Mesozoic formations, between Gouro (at the foothill of the Tibesti Mountains), the group of lakes of Ounianga, Mourdi Djouna, and terminating in the Ennedi Mountains. The figure shows the basin's structure characterized by the uplifted areas of the Tibesti and Ennedi Mountains (Tibesti and Ennedi-Oweinat Uplift), and a more thick and depressional zone in the center (Borkou-Kufra Trough). The group of lakes of Ounianga are located in a zone of lowlands, also corresponding to the thickest sedimentary cover.

According to the basement elevation map from Mahamoud (1986, Figure 2.2), the basement deepens and the sedimentary cover thickens from the southern margins towards the NE (see cross-sections of Chapter 4). In southern Libya, the thickness of the sedimentary cover varies from 2,200-2,300 m at the borders (foothills of the Ennedi and Tibesti Mountains) to 3,650 m, where the collapsed structure of thick sedimentary cover was interpreted as the result of increased sagging of inherited Infracambrian weaknesses (Lüning et al., 1999).

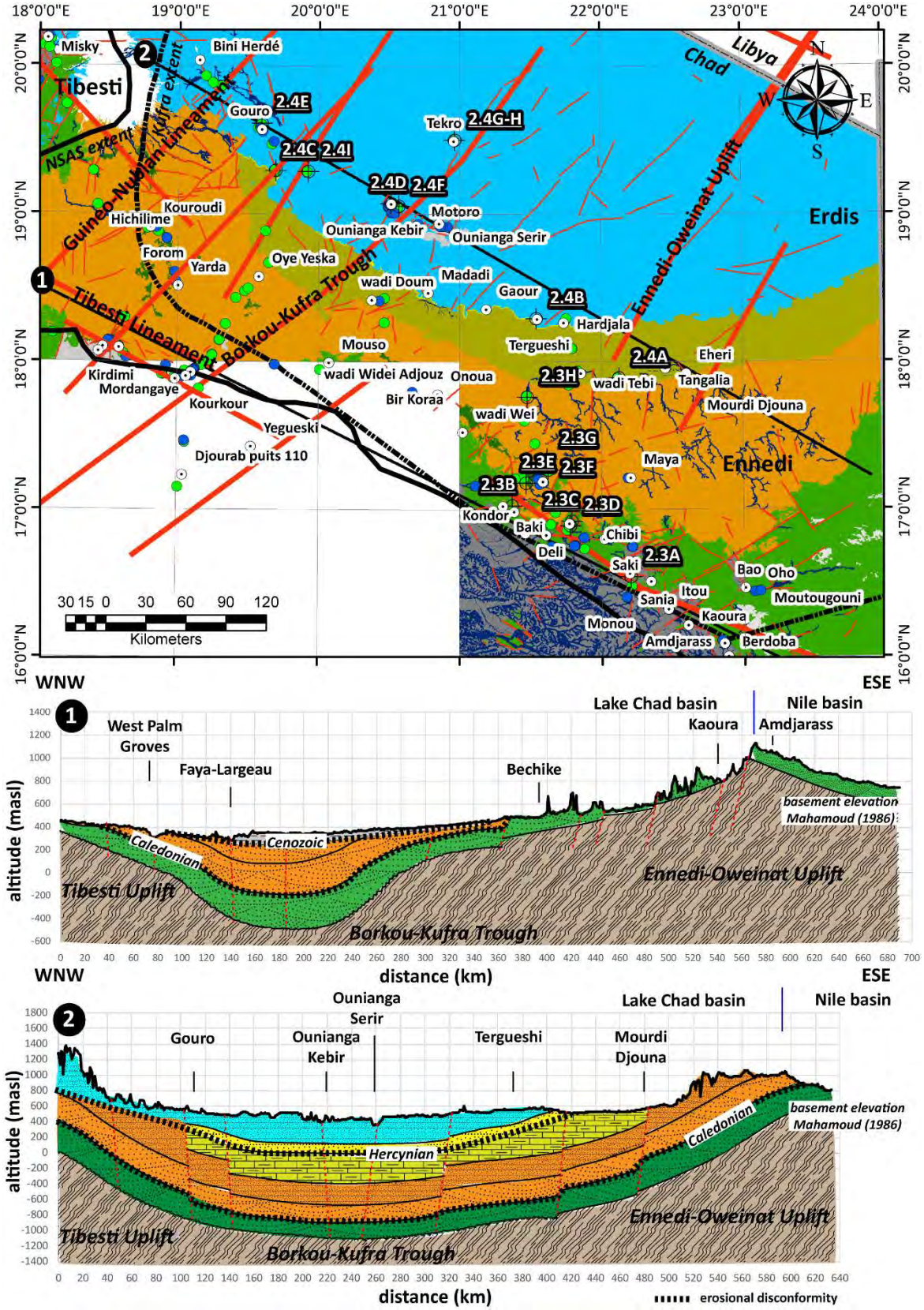

Figure 2.5: Geological map and cross-sections (WNW-ESE). The complete legend is presented in Figure 2.6. To simplify the representation of the cross-sections and given the uncertainty on the extent of the Silurian deposits (discontinuous, increased thickness), the Cambro-Ordovician sandstone and the Silurian siltstone are represented in the same unit named "Cambro-Ordovician". The basement elevation of the cross-sections was adapted from Mahamoud (1986). Topography was extracted from SRTM. Geological interpretation is based on geological shapefiles from the SIRE database.

2.4.3. Structural directions

Table 2.1 synthetizes the "observed" (extracted from the SIRE database) fault directions for several localities of Northern Chad. Figure 2.6 shows the described directions for four of these localities. A rose diagram of fault directions for the entire region comprising the Tibesti Mountains, the Ennedi Mountains and the central lowlands (defined as the region of lower altitude extending in between these two mountain chains) is also presented.

Table 2.1: Synthesis of structural directions "observed" (from SIRE database) in different regions of the NSAS of Northern Chad. Data were compared to the description in BRGM (1991).

Region	Structural directions	Observations
Ennedi Mountains (Figure 2.5A)	N120°	Mark the alignment of the Silurian platform from Fada to Bir Koraa and the limit between the Paleozoic formations and the Precambrian basement.
	N150-170°	Mark the eastern topographic heights of the mountain chain, separating the Lake Chad and the Nile hydrological basins.
	N0-10° N60-70°	Other observed directions.
Ounianga Lakes (Figure 2.5B)	N30-40°	Represented by a long discontinuity traversing the group of lakes of Ouianga Kebir and by smaller and repeated faults north of the group of lakes of Ounianga Serir.
	N120°	Represented by the direction of the limits of the sedimentary formations, south of the Ounianga Lakes.
	N90-100°	Dextral strike slip movement in Ounianga Kebir (lake Yoa, BRGM, 1991), posterior to N30-40° in Ounianga Serir.
	N10-20° N50-60°	Other observed directions.
Oases of Gouro (Figure 2.5C)	N150-180° N30-40° N50-60° N90-110°	Directions N90-110° are posterior. N50-60° can be followed southerly up to Yarda-Kouroudi.
Oasis of Faya-Largeau	N35-40°	Densely represented from West to East of the Faya-Largeau's Palm Grove. The northern part of the Palm Grove stretches along these directions.
	N70°	The southern part of the Palm Grove follows this direction.
	N0-10° N170°	Represented from west to east of the oasis.
	N110° N140°	Mainly located in the central part of the oasis.
West Palm Groves (Figure 2.5D)	N30-40°	Northern alignment of the Palm Groves (Kirdimi-Yen).
	N60°	Southern alignment of the Palm Groves (Yen-Aïn Galaka).
	N150° N0-10° N120°	Other observed directions.

Faults of directions N30-40° are numerous in the central lowlands (between Mouso and Tekro) and are seen as an important direction in the region surrounding the Ounianga Lakes, the oases of Gouro, Faya-Largeau and the West Palm Groves (Table 2.1, Figure 2.6B-C-D).

Directions N110-120° mark the contact of the sedimentary sequence of the Kufra basin with the Cenozoic deposits of the Lake Chad basin and with the uplifted Precambrian basement (Ouaddaï). The topographic breaks (platforms, cliffs) which indicate the change of the sedimentary layers, align along these same directions (Figure 2.6A-B-C-D).

Faults of directions N40-70° are also numerous and represented in the whole region (Figure 2.6A-B-C-D). In Faya-Largeau and the West Palm Groves (Figure 2.6D), these directions mark the southern alignment of the Palm Groves.

Directions N150-180° are densely represented south of the Tibesti Mountains (between Emi Koussi and Faya-Largeau) and in the Ennedi Mountains, where they mark the topographic heights separating the Lake Chad and Nile hydrological basins (Figure 2.6A-C-D).

Directions N90-100° are particularly represented in the Gouro and Ounianga oases (Figure 2.6B-C). In Gouro, directions N150-180° and N50-60° cross-cut directions N90-100°. BRGM (1991) describe the directions N90-100° as a dextral strike-slip movement, cross-cutting directions N30-40°.

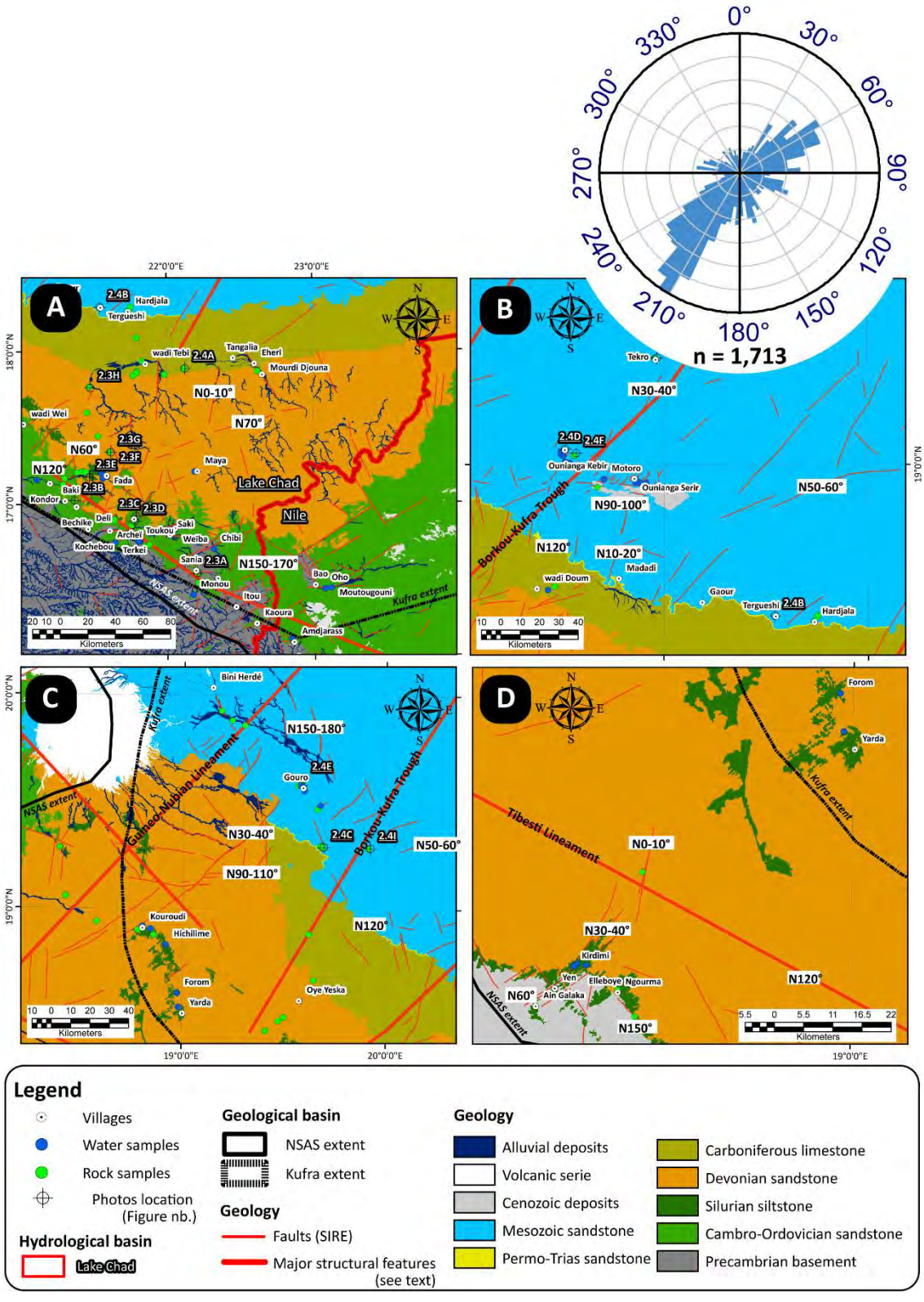

Figure 2.6: Geological maps of selected zones of the NSAS of Northern Chad. The rose diagram of faults (n: number of counts) is shown on the top-right. A) Geological map of the Ennedi Mountains, B) Geological map of the area surrounding the Ounianga Lakes, C) Geological map of the zone surrounding the Gouro oases, and D) Geological map of the West Palm Groves. Locations of water samples, rock samples, photos presented in Figures 2.3 and 2.4 are shown, as well as the hydrological and geological basins extents (the NSAS extent is from Voss and Soliman, 2014, the Kufra basin extent is from Heron et al., 2009). Faults (from the SIRE database) and major structural accidents (from Williams, 1966, Guiraud et al, 2000, Elsheikh et al., 2011, Deniel et al., 2015) are indicated. Geological background is from the SIRE database.

2.5. Discussion

2.5.1. Identification of major structural phases

The Kufra basin of Northern Chad lies within an area characterized by a long geological history. As previously introduced, many tectonic phases have successively occurred, often re-activating weakness lines of the basement inherited from the Pan-African orogeny (e.g. the SW-NE Guinean-Nubian Lineament or the WNW-ESE Tibesti Lineament**,** Guiraud et al., 2000): Caledonian, Hercynian, Triassic-Lower Jurassic, Lower and mid Cretaceous, and Cenozoic phases (Guiraud et al., 2005; Lüning et al., 1999).

Faults of directions N30-40°, N110-120°, N40-70°, N150-180° and N90-100° have been recurrently observed over the whole region of Northern Chad, comprising the Tibesti Mountains, the Ennedi Mountains and the central lowlands. N110-120° parallel the Tibesti Lineament (Figure 2.2, Guiraud et al., 2000), recognized as an inherited direction from the Pan-African Orogeny. N150-180° parallel the Tripoli-Tibesti Uplift and the Uri Trough, attributed to the Caledonian phase (Williams, 1966), but later reactivated. N30-40° parallel the Borkou-Kufra Trough and the Ennedi-Oweinat Uplift, attributed to the Hercynian tectonic phase (see section 2.2). Directions N40-70° were observed in Sudan (Elsheikh et al., 2011) and attributed to the Late Triassic – early Cretaceous extensional phase. N30-40° and N40-70° are also largely predominant in other parts of Northern Chad and Southern Libya (Deniel et al., 2015).

Estimated thicknesses from previous studies (Wacrenier, 1958; Hesse et al., 1987; Lüning et al., 1999; MEH, 2015; MEH, 2016) indicate higher variabilities and increased thicknesses for the Paleozoic formations (500 to 3,700 m) than for the Mesozoic formations (150 to 1,400 m, see Chapter 3). The observed variabilities of the Paleozoic formations thicknesses within the Kufra basin are potentially the result of the combined effect of the Hirnantian glaciation, the Caledonian and Hercynian tectonic phases.

The basement is considerably lowered in the region East of Faya-Largeau (-500 masl, Figure 2.5A). Depths of the basement in Faya-Largeau were determined by refraction seismic methods to be at 800 m bgl (Organisation Commune des Régions Sahariennes, 1962). Depths of the basement measured in boreholes are in agreement with the model of the basement structure of Mahamoud (1986). Thicknesses of the lacustrine deposits overlying the Paleozoic sandstones were determined to vary between 20 to 70 m (boreholes F1, F2, F3 and F4, BRGM, 1991). According to Wolff (1964), the Paleozoic formations in Faya-Largeau are composed of Cambro-Ordovician to Lower Devonian sandstones. This would indicate an increased thickness of these formations, compared to what is observed in the rest of the region of Northern Chad.

Heron and Craig (2008) postulated that the NE-SW depressional zone running from Faya-Largeau to the Kufra oasis, was an inter-stream ice thick during the Hirnantian glaciation. After the retreat of the glacial cover, the lower elevation would consequently be characterized by higher rates of sedimentation. As an example, thicknesses of up to 300 m of Lower Silurian Tannezuft Formation and Upper Silurian Akakus Formations were observed in Jabal az-Zalmah (Gindre et al., 2012). In Northern Chad, the outcrops of Silurian formations are discontinuous (Caledonian disconformity), with thicknesses of up to 50-80 m. However, in deeper parts of the basin, increased thicknesses could be expected (i.e. east of Faya-Largeau), as previously introduced.

Previous authors have already recognized the Hercynian phase as one of the main events having shaped the Kufra and Murzuk basins (Williams, 1966**;** Lüning et al., 1999). For example, Klitzsch (1966) postulated that the denudation of the Precambrian basement in the Tibesti Mountains is the result of the Hercynian orogeny.

The Kufra basin's elongation towards the NNE to NE and the main structural directions (Tibesti-Sirte Uplift, Borkou-Kufra Trough, Ennedi-Oweinat Uplift) are attributable to the Hercynian phase (Williams, 1966). Erosional disconformities are observed in the proximity of the Tibesti Mountains, where the Mesozoic formations rest directly on the Upper Devonian formations. The Carboniferous marine is absent from this zone (Figure 2.6B). In the Lake Chad basin, the Mesozoic formations rest directly on the Precambrian basement (Schneider, 1989), also attributable to the Hercynian phase. The Paleozoic sedimentary cover's thickness increases from the limit with the Cenozoic sediments of the Lake Chad basin and the Precambrian basement of the Ouaddaï, towards the NNE to NE.

Mesozoic and Cenozoic phases have potentially been important in reactivating pre-existing high zones. The uplifted Precambrian basement in the region of the Ennedi Mountains, for example, might be the result of several epirogenic movements, as already recognized by previous authors for the Tibesti Mountains (Dalloni et al., 1934; Klitzsch, 1966; Vincent, 1970; Deniel et al., 2015).

In Sudan, Elsheikh et al. (2011) relate faults of directions N40-70° to the Late Triassic – early Cretaceous extensional phase. These directions are widely observed in Northern Chad and Southern Libya as well (Deniel et al., 2015).

Directions N150-180° are densely represented south of the Tibesti Mountains (between Emi Koussi and Faya-Largeau) and in the Ennedi Mountains, where they mark the topographic heights separating the Lake Chad and Nile hydrological basins. These directions, paralleling the Tripoli-Tibesti Uplift and the Uri Trough (Caledonian, Williams, 1966), might have been reactivated during the Mid Cretaceous "Austrian", the Late Cretaceous – Tertiary "Alpine", the Oligo-Miocene tectonic phases and/or during the Tibesti volcanic activity, associated to regional uplifts during the mid-Eocene to Holocene.

2.5.2. Tectonic accidents and role of hydrogeology

The structure of the Kufra basin in Northern Chad is marked by the basement uplift in the regions corresponding to the Ennedi and Tibesti Mountains and by a subsided zone between these two mountain chains, resulting from several tectonic and depositional phases. The topography parallels the structure of the basin. The topography has a major influence on the patterns of precipitation and therefore on the potential for recharge, as presented in Chapter 5.

In the Ennedi and Tibesti Mountains, the Paleozoic sandstone rest on the uplifted Precambrian basement. In particular, the Cambro-Ordovician sandstone (and the Lower Devonian sandstone) shows intense fracturing, at a meso and macro scale. In the Ennedi Mountains, dissolution figures were observed in Bachiquele, syn-sedimentary folding and fractures were observed in Terkeï and glacially-related erosional features (e.g. pressure-fractures) were observed in Archeï. These features increase the hydraulic conductivity of the consolidated sandstone and provide preferential paths for infiltration and recharge of the aquifers through open fractures, sinks and along wadis. The most important perennial water points in the Ennedi Mountains are the gueltas of Archeï and Bachiquele (see Chapter 4). Both are the result of several upstream springs (up to 30 for Bachiquele) discharging from the Paleozoic sandstone along major faults, collecting into ponds in the wadi's alluvial system.

The central subsided zone of the basin was defined by Mohamed et al. (2016) as corresponding to the Pelusium Mega shear zone, or to the Borkou-Kufra Trough of Williams (1966). This zone was identified as characterized by increased fracturing and therefore higher hydraulic conductivities are to be expected. Most of the discharge zone of the NSAS (see Chapter 4) are located along this depressional zone (e.g. Ounianga Lakes, Faya-Largeau).

The Lakes of Ounianga are located at the intersection of several fault directions, in a zone of increased sediment's cover thickness. As concluded by Voss and Soliman (2014), in the thickest part of the basin, artesian flow might be an important part of the groundwater supply to the oases. The presence of deep fractures would allow the leakage from the deeper parts of the aquifer to the more shallow ones.

Artesian flow is the major supply to the oases of Faya-Largeau and of the West Palm Groves. The aquifer is confined by a layer of argillaceous lacustrine deposits (see Chapter 3 and 4), but leakage through fractures enable the groundwater to discharge at the ground surface as artesian springs (Kirdimi, Aïn Galaka).

2.6. Concluding remarks

This chapter provides a synthesis and interpretation of the major structural features of the Kufra basin based on the available geological information and on fieldwork performed in Northern Chad. The information included in this chapter provide the background geological information to which the following chapters refer.

The analysis of the geological history of the Kufra basin has shown that the basin was shaped in several tectonic phases. As a result, stratigraphic discontinuities (Silurian – Caledonian, Carboniferous – Hercynian), variable thicknesses of geological formations (Paleozoic), uplifted and subsided zones, and several generations of fault directions characterize the basin. These geological features have implications on the topography, on the rainfall patterns (i.e. the recharge rates) and on the groundwater flow patterns (increased transmissivities, artesian flow).

As observed by this study, the basement elevation model presented by Mahamoud (1986) do not always represent correctly what is observed from surface geology. Increased thickness of the sedimentary cover in a zone where the Precambrian basement is outcropping have been observed. A better representation of the basement structure is essential to estimate transmissivities. Geophysical surveys, such as seismic and gravimetry should be performed. Additionally, deep boreholes would enable to directly verify assumptions, such as the increased thickness of the Paleozoic formations expected to occur in the deepest part of the basin. Petroleum Exploration Companies performed deep boreholes, but the information is generally not publicly shared.

Chapter 3

Mineralogical and textural analysis of the sedimentary sequence of the Kufra basin of Northern Chad

3.1. Introduction and content of the chapter

3.1.1. Introduction

Sonntag (1986) describes the NSAS as a multilayer aquifer system of large vertical and horizontal extension, composed of an upper unconfined aquifer and one or more confined aquifers underneath. Pallas (1980) recognizes that the Carboniferous formation, a marine sequence of up to 400 m thickness with a low hydraulic conductivity, could separate the lower aquifer (Cambro-Ordovician to Upper Devonian) from the upper aquifer (Mesozoic). Sonntag (1986) however also concludes that the aquifers are hydraulically connected over the entire area through numerous faults, fractures and structural discontinuities.

This chapter describes the mineralogical, textural and geochemical characteristics of the sedimentary sequence of the Kufra basin in Northern Chad, with the aim of qualitatively characterize the aquifer's structure. MEH (2015; 2016) provides the characterization of the geological units for their "aquifer's potential". The present investigation presents re-verified thicknesses of the geological formations (presented in Chapter 2) and draws considerations on the hydraulic conductivities and transmissivities of the aquifer system. The main questions driving this investigation were: (1) what is the aquifer's structure (multilayered)? (2) are there distinctive structural or sedimentological features, which can explain the location of discharge points such as springs and lakes? and (3) how thick and how efficiently low conductive layers, such as the Carboniferous formations, act as confining layers? These questions are further discussed in Chapter 4.

3.1.2. Content of the chapter

This chapter is structured as follows. The next section (section 3.2) provides information on the sampling and analytical methodology. The mineralogical, textural and geochemical characteristics of the sampled rocks are then described (section 3.3). Mineralogical and textural observations included in this section result from the verification of two data sets (University of Geneva and De Halle &

Schmidt Geneva Mineral Service, see section 3.2.3), compiled in the framework of the ResEau project. A selection of photos of samples characteristic for the correspondent geological formation are presented with a simplified litho-stratigraphic log to show their stratigraphic position (see Chapter 2).

The discussion (section 3.4) first focuses on the comparison between the thicknesses of the geological formations of the NSAS of Northern Chad (see Chapter 2) and the thicknesses observed by other authors investigating the Kufra basin. Estimations of hydraulic conductivities found in the literature are then presented and applied to the sedimentary sequence of the NSAS of Northern Chad. Estimates of transmissivities compared to values from the literature conclude the chapter.

3.2. Rock sampling and analysis

3.2.1. Sampling

Three field campaigns with a geological component were undertaken between 2013 and 2015 (see Chapter 2). A total of 153 rock samples were collected from different locations and representing different geological layers. In the field, rock samples were described for their macroscopic characteristic and, based on the geological map 1:2'000'000 from Gerard (1958) and 1:1'500'000 from Wolff (1964), were attributed to a geological formation (see Annex 1).

The rock samples and their attribution to a specific formation and age were then re-verified against the geological maps of Wolff (1964) and the more recent hydrogeological maps of MEH (2015) and MEH (2016). Whenever a discrepancy was encountered, the final choice to attribute the sample to a specific age was made based on mineralogical considerations (e.g. compaction figures).

3.2.2. Mineralogical and textural analysis

79 thin sections were prepared and analyzed for mineralogical determination and textural description (Annex 1). 11 thin sections were prepared by the University of Geneva and analyzed with QEMSCAN. QEMSCAN is based on a SEM technology equipped with EDS units, enabling a high-resolution mineralogical mapping by the acquisition of EDS spectra compared against a corresponding database. 68 thin sections were prepared and analyzed by classical optical microscopy by De Haller & Schmidt Geneva Mineral Service. In the framework of the study presented in his chapter, all the thin sections were re-verified by using an optical microscope.

3.2.3. Geochemical analysis

45 rock samples were analyzed for their major and traces composition by X-ray fluorescence (Philips PW2400) at the University of Lausanne, Switzerland. Calibration was performed by the use of 19 known rock compositions. Major elements were determined on crushed rock melted pastilles while trace elements were determined on crushed rock pressed pastilles. Uncertainties are generally less than 0.4

wt% for major elements and 10 ppm for trace elements. Annex 2 presents the results of rock samples analysis.

3.3. Results

3.3.1. Mineralogical observations of the sedimentary sequence

The following descriptions are based on the field observation and on the re-verified rock samples analysis (optical microscope). The mineralogical observations are described as a temporal sequence, from the bottom (Cambro-Ordovician) to the top of the sedimentary sequence (Tertiary and Quaternary). Figures 3.1 and 3.2 show photos of a selected number of characteristic samples and their stratigraphic position reported onto the reconstructed litho-stratigraphic log (presented in Chapter 2). Ranges of intergranular porosities are also indicated (see section 3.3.2).

3.3.1.1. The Lower Paleozoic (Cambrian to Silurian)

The Cambro-Ordovician sandstone is composed of 69% of quartz and quartzites grains, cemented by silica in pellicular overgrowth on the quartz grains (Figure 3.1A). Iron oxides (goethite) have partially replaced the pellicular silica, giving an oxidized surface coating and a red-brown color to the sandstone. Pyrite has been observed, indicating a diagenetic process under reduced conditions.

Glacially-related deposits from the late Ordovician are variably represented by fine-grained laminated tillites and quartzitic conglomerates (Figure 3.1B), cemented by silica in pellicular overgrowth, partially replaced by iron oxides (goethite).

The Silurian formation is a ferrugineous siltstone and siltic/argillaceous sandstone of mostly white color (Figure 3.1C), composed of very fine-grained quartz (< 0.26 mm, 53%), muscovite and Ti-oxides in a silty (quartz, kaolinite) matrix, with late Fe-oxides impregnations.

3.3.1.2. The Upper Paleozoic (Devonian to Carboniferous)

Lower Devonian rocks collected south of the Ennedi Mountains and in the areas north and west of Faya-Largeau are generally composed by a medium to coarse quartzitic sandstone, locally evolving to a fine-grained or a microconglomeratic quartzitic sandstone (Figure 3.1D). Levels of fine to medium-grained quartzwacke have also been recognized. The medium to coarse sandstone and the quartwacke are composed of quartz and quartzite grains (50-90% vol) with variable amounts of a matrix composed of clays and iron oxides. They are cemented by silica in pellicular overgrowth and partially replaced by iron oxides (goethite). Some samples have a higher content of vermiforme/sheet kaolinite and pyrophyllite (up to 7% vol) in replacement of detrital muscovites, and associated low contents of siderite. The more silty samples are composed of 60-68% vol of fine quartz (< 0.85 mm) cemented by iron oxides.

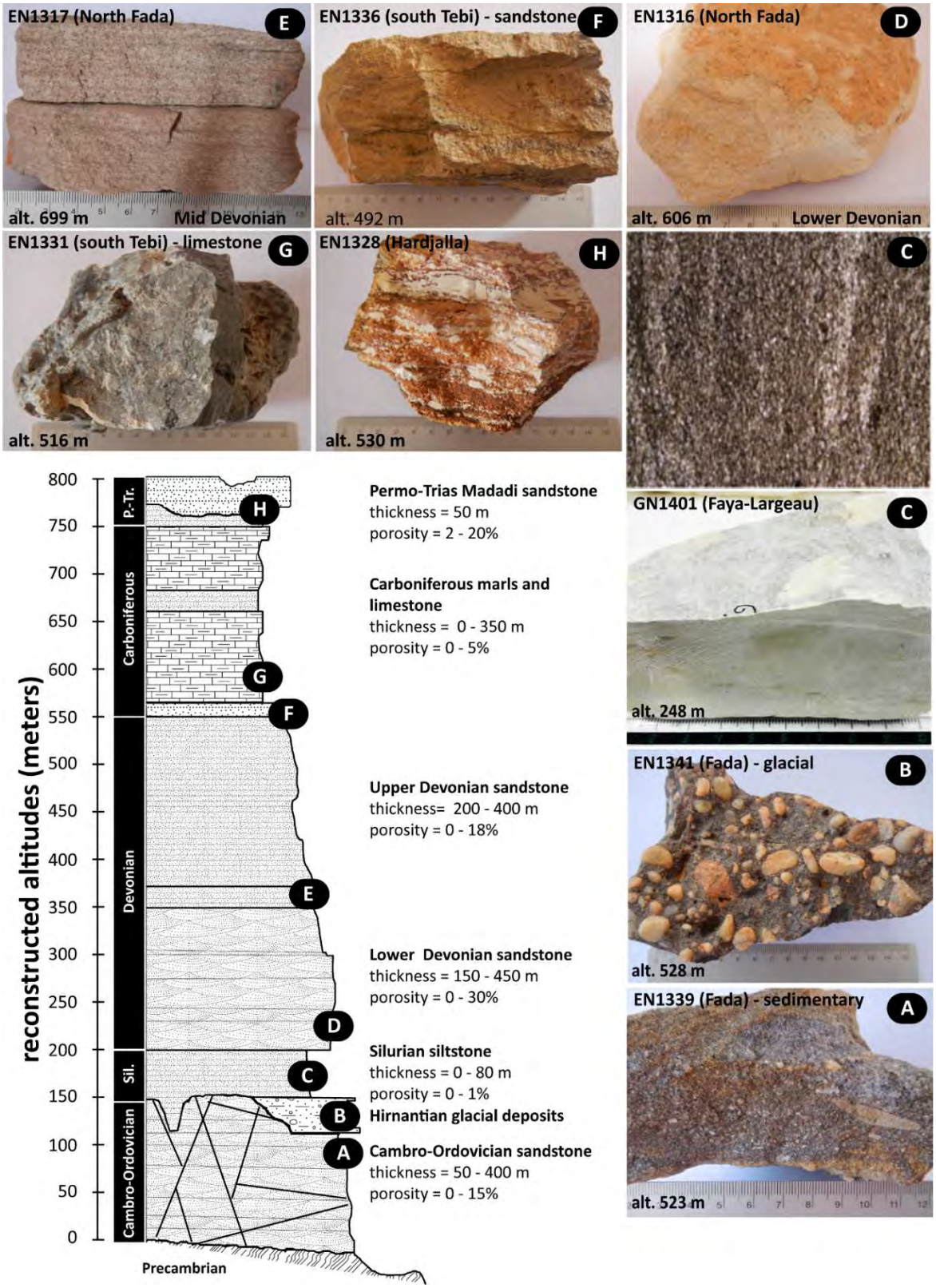

Figure 3.1: Selected number of rock samples characteristic of the correspondent geological formation. Their approximate stratigraphic position is reported on the synthetic litho-stratigraphic log. A) Cambro-Ordovician sandstone (sample ID: EN1339, collected in Fada, altitude 523 masl), B) Glacial conglomate (EN1341, Fada, 528 masl), C) Macroscopic and microscopic view of the Silurian siltstone (GN1401, Faya-Largeau, 248 masl), D) Lower Devonian sandstone (EN1316, north of Fada, 606 masl), E) Mid-Devonian sandstone (EN1317, north of Fada, 699 masl), F) Lower Carboniferous sandstone (EN1336, south of Tebi, 492 masl), G) Carboniferous limestone (EN1331, south Tebi, 516 masl), H) Permo-Trias Madadi sandstone (EN1328, Hardjalla, 530 masl).

The psammitic platy sandstone corresponding to the Middle Devonian platform (Figure 3.1E), is composed of 67% vol quartz and up to 13% kaolinite and pyrophyllite, and higher contents of trace minerals (zircon, rutile, apatite, illite, siderite).

The Upper Devonian samples are composed of a fine quartzitc sandstone and quartzwacke (44-82% vol quartz and a variable amount of a silty matrix), cemented by silica in pellicular overgrowth and partially replaced by iron oxides (goethite). Bioturbation figures are frequently observed, generally associated with iron oxides accumulations. Close to the Carboniferous formation (Mourdi Djouna), the Upper Devonian sandstone is characterized by a higher content of K-feldspar in the main mineralogical assemblage (quartz 79% vol, K-feldspar 1% vol, kaolinite 1% vol, chlorite 1% vol). Also, high contents of siderite have been observed (5% vol), as well as traces of illite.

On the southern margin of the Mourdi depression, the bottom sequence of the Carboniferous formation is composed of a fine to coarse-grained quartzo-feldspathic sandstone (quartz 78-81% vol, albite and K-feldspar 4-7% vol) containing traces of calcite, illite (up to 1% vol), clays (kaolinite and smectite, chlorite and pyrophyllite) and Fe-Ti oxides (Figure 3.1F). It intercalates with a quartzo-feldspathic limestone (quartz 46% vol, calcite 37 % vol, K-feldspar and albite 4% vol) containing 1-5% vol illite and up to 2% vol kaolinite and rutile.

In the middle Carboniferous section, the sandstone contains up to 5% vol of a complex mineralogical assemblage including Ba- and Ca-sulphates, clays, Fe-Ti oxides, pyrite and accessories. The limestone is micritic (65% vol calcite) with quartz clasts (10% vol, < 0.2 mm), showing microfractures and stylolites composed of calcite and late iron oxides (goethite, Figure 3.1G). Close to the contact with the Permo-Trias formation (SE of Gouro), the formation is a fine-grained sandstone composed of quartz (65% vol), cemented by silica, marking the effect of compaction, calcite and poikilitic gypsum (up to 35% vol).

3.3.1.3. The Mesozoic sequence

The Permo-Trias fine to coarse-grained sandstone (Hardjalla, Figure 3.1H) is composed of quartz (76-81% vol) and occasionally andesine (2% vol). The medium-grained sandstone contains varying quantities of siderite (up to 14% vol) and chlorite (up to 5% vol), or clays (kaolinite and smectite 11% vol) and pyrophyllite (2% vol). Traces of illite are found in all samples, and Fe-Ti oxides only occasionally. In the region SE of Gouro, the Permo-Trias samples are composed of quartz (20-73% vol) with a siltic matrix, cemented by silica in pellicular overgrowth and late iron oxides (hematite).

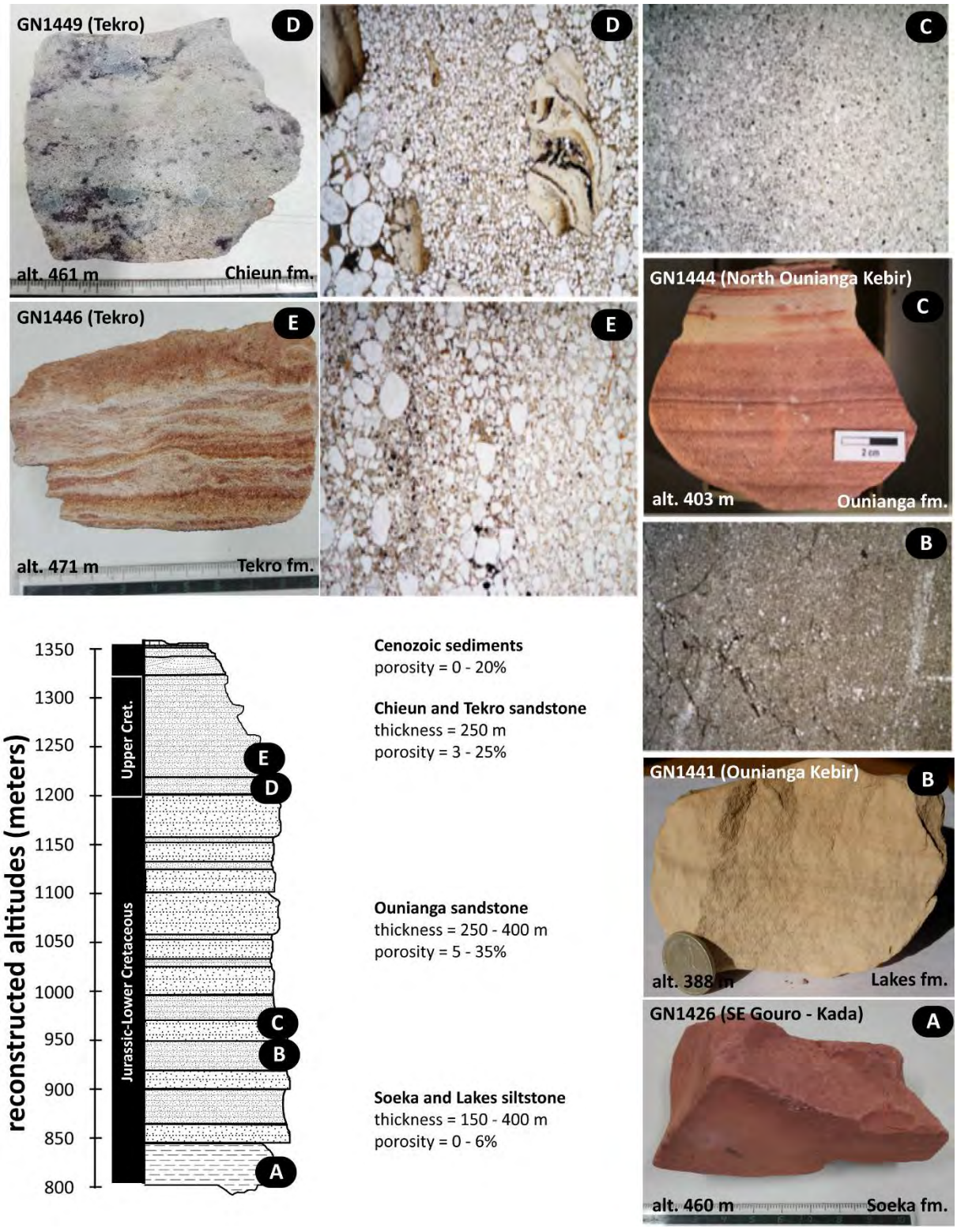

Figure 3.2: Selected number of rock samples characteristic of the correspondent geological formation. Their approximate stratigraphic position are reported on the synthetic litho-stratigraphic log. A) Soeka red argillite (sample ID: GN1426, collected in Kada, South-East of Gouro, altitude 460 masl), B) Macroscopic and microscopic view of the Lakes formation fine sandstone (GN1441, Ounianga Kebir, 388 masl), C) Macroscopic and microscopic view of the Ounianga formation sandstone (GN1444, North of Ounianga Kebir, 403 masl), D) Macroscopic and microscopic view of the Chieun formation sandstone (GN1449, Tekro, 461 masl), E) Macroscopic and microscopic view of the Tekro formation sandstone (GN1446, Tekro, 471 masl)

The Soeka formation is composed of a dark red argillite (Figure 3.2A).

The Lakes formation (Figure 3.2B) is a very fine white to light brown quartzwacke composed of quartz (75% vol, < 0.17 mm) in a a siltic matrix (up to 22% vol, quartz and kaolinite). They are cemented by a coarse kaolinite, partially replaced by illite.

The Ounianga Formation (Figure 3.2C) is a fine quartzitic sandstone composed of quartz (75-90% vol), cemented by silica and late iron oxides (goethite), intercalated with more siltic layers (quartzwacke) having a higher content of a kaolinitic matrix and an early cement. Figures of bioturbation are frequently observed.

The sample corresponding to the Chieun platform (Figure 3.2D) is a white argillaceous quartzitic sandstone composed of quartz/quartzites (73% vol) and clasts of siltite/argillite (10% vol), in a clay matrix, cemented by silica in pellicular overgrowth. Illite is in replacement of the clays, and late iron oxides are also observed.

3.3.1.4. Tertiary and Quaternary deposits

The Tertiary deposits, named “Continental Terminal”, are variably represented by fine to coarse quarzitic sandstone, micro conglomerates and breccia, quartzwacke, siltstones and argillaceous sandstone. The determination of the Eocene-Miocene rocks can be sometimes difficult because of their mineralogical and textural variability and because they are found sparsely distributed and unconformably overlying all formations. Nevertheless, mineralogically these samples show no presence of compaction figures and generally no silica cement in pellicular overgrowth, but a cement composed of iron oxides (goethite) and in some cases kaolinite or siderite.

Volcanic rocks are generally restricted to the Tibesti mountainous area, but volcanic clasts can be also found in the sediments of the Continental Terminal.

Numerous examples of quaternary diatomite and other lake-related deposits are found in localized depressions (Lakes formation platform, Faya-Largeau and West Palm Groves, see also Chapter 4).

3.3.2. Porosity estimation

The textural analysis of the rock samples can provide some indication on the intergranular porosity. These estimates do not represent effective porosity, for which specific tests should be accomplished. They neither represent total porosity, which would necessitate the integration of porosities issued by post-diagenetic processes (dissolution, precipitation, fracturing).

Table 3.1 presents the estimates of intergranular porosities, sorted by age of formations (see also Figures 3.1 and 3.2). Porosities estimates from Albert and Elgargoti (2010) are indicated for

comparison. The estimations from Albert and Elgargoti (2010), corresponding to one value per geological formation, are in general good agreement with the estimates of maximum intergranular porosity, provided in this work (Table 3.1). The variability (min-max) of the porosity estimates is the result of sampling and analysis of different layers of sandstone and siltstone interlayers, representing a geological unit (or formation), and of the variability of the rocks found in the large area covered by the sampling.

Table 3.1: Intergranular porosity estimation (min and max, % vol) sorted by geological formation.

Geological formation *in () number of samples*		**Intergranular porosity (%)**		
		min	**max**	**Albert and Elgargoti (2010)**
Cenozoic	volcanic (3)	0	1	
	sedimentary (17)	0	20	
Upper Cretaceous	Tekro (3)	8	25	25
	Chieun (1)	3	3	
Jurassic-Lower Cretaceous	Ounianga (7)	5	35	25
	Soeka & Lakes (6)	0	6	
Permo-Trias	Madadi (4)	2	20	22
Carboniferous	middle-top (6)	0	5	
	bottom (1)	15	15	20
Devonian	mid-upper (6)	0	18	16
	lower (16)	0	30	14
Silurian	(3)	0	1	
Cambro-Ordovician	glacial (3)	0	10	
	fluvial (2)	0	15	12
Precambrian basement	(2)	0	2	

For most of the Paleozoic and Mesozoic rocks, intergranular porosity is reduced by cemented silica in pellicular overgrowth and posterior partial replacement by iron oxides (goethite), illite and siderite. In some cases high amounts of diagenetic kaolinite and chlorite (or pyrophyllite) were also detected.

Intergranular porosities of the Paleozoic formations (Figure 3.1) vary between 0% for the silty interlayers to 15-30% for the massive fluvial sandstone layers (Cambro-Ordovician and Lower Devonian sandstone). The Cambro-Ordovician sandstone, the Upper Devonian micaceous sandstone and the lower Carboniferous sandstone have lower estimated porosities than the Lower Devonian sandstone. The mid to upper section of the Carboniferous, composed of limestone and marls, have maximum porosities of 5%.

The Mesozoic sandstone layers have generally higher intergranular porosities (25 – 35%) than the Paleozoic sandstone layers. The Permo-Trias Madadi formation, the Cretaceous Ounianga, Chieun and

Tekro formations have intergranular porosities varying between 2 and 35% (Figure 3.1). The Soeka and Lakes formations have maximum porosities of 6% (Figure 3.2).

Siltstones, argillaceous sandstone, coarse sandstone, micro conglomerates and breccia, of variable intergranular porosities (0-20%), represent the Cenozoic sedimentary rocks.

3.3.3. Geochemical composition

The Paleozoic and Mesozoic rocks of the Kufra basin of Northern Chad are mostly composed of a pure sandstone, with SiO_2 contents varying between 85 and 96 wt%, up to 9 wt% Al_2O_3, up to 9 wt% Fe_2O_3, up to 0.24 wt% of CaO, and MgO and Na_2O < 0.1 wt% (Figure 3.3).

The only marked compositional exception within the Paleozoic and Mesozoic formations, is the mid to upper section of the Carboniferous layer, composed of sheet fine-grained sandstone intercalated with marls and blue limestone (8 – 56 wt% SiO_2, 19 – 49 wt% CaO, 16 – 39 wt% LOI, 1 – 3 wt% Al_2O_3, < 1 wt% Fe_2O_3). Higher concentrations of MgO, Na_2O, Mn, Ba, and Sr are also associated to these rocks.

Figure 3.3 (next page): Rock samples composition of major elements (complete analysis are shown in Annex 1). Mean values are shown as blue dots. The measured variability is shown as the extent between the dotted lines. The results are shown as a stratigraphic sequence (from bottom to top): Cam-Or (Cambro-Ordovician), Sil (Silurian), Dev inf (Lower Devonian), Dev sup (Upper Devonian), Carb (Carboniferous), Perm-Tr (Permian and Triassic, Madadi formation), Ju-Cr inf (Jurassic - Lower Cretaceous, Soeka, Lakes and Ounianga formations), Cr sup (Upper Cretaceous, Chieun and Tekro formations), Te-Qu (Tertiary and Quaternary).

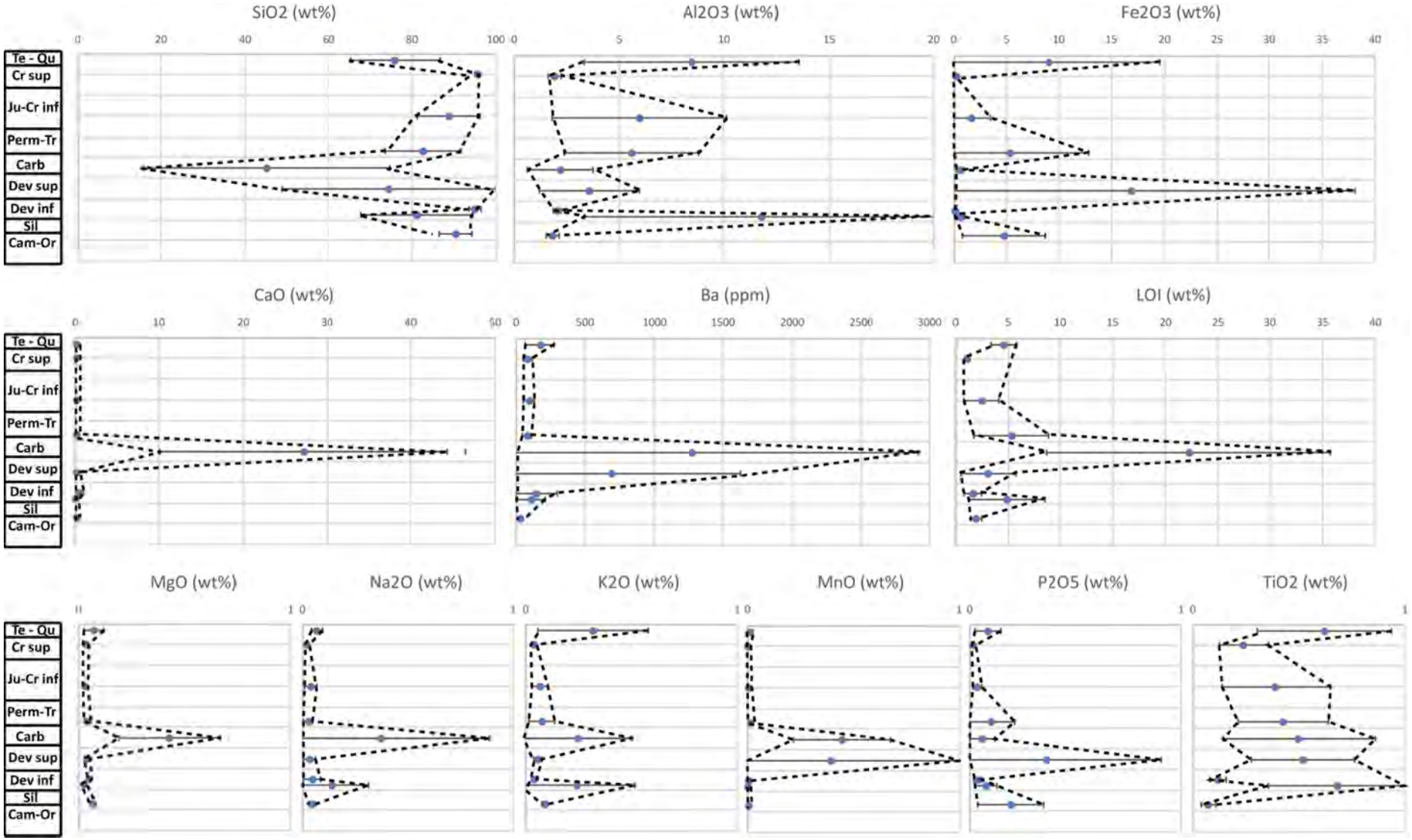
SiO2 (wt%)
Al2O3 (wt%)
Fe2O3 (wt%)
CaO (wt%)
Ba (ppm)
LOI (wt%)
MgO (wt%)
Na2O (wt%)
K2O (wt%)
MnO (wt%)
P2O5 (wt%)
TiO2 (wt%)
Te - Qu
Cr sup
Ju-Cr inf
Perm-Tr
Carb
Dev sup
Dev inf
Sil
Cam-Or

3.4. Discussion

3.4.1. Thickness of the sedimentary sequence of the Kufra basin of Northern Chad

Estimated thicknesses of the Paleozoic formations (Cambro-Ordovician to Carboniferous) generally range from 1,050 to 1,350 m, while thicknesses of the Mesozoic formations (Madadi, Soeka, Lakes and Ounianga) range between 650 to 750 m. In the region investigated, approximately 250 m of Upper Cretaceous (Chieun and Tekro formations) end the sedimentary sequence (Figures 3.1 and 3.2). Table 3.2 compares our estimates with thickness estimates presented by other authors investigating the Kufra basin (Hesse et al., 1987; Lüning et al., 1999; MEH 2015 and 2016).

Table 3.2: Average thickness of geological formations of the Kufra basin provided in this work compared to estimates found in the literature (Hesse et al., 1987; Lüning et al., 1999; MEH, 2015 and 2016).

	Reference	Geological formation	Thickness (m)
Average geological formations thickness (m)	our work	Paleozoic	1050 - 1350
		Mesozoic	850 - 950
	Hesse et al. 1987	Paleozoic	1840 - 1975 (Tibesti) - (central lowlands)
		Mesozoic	740 - 1475 (Tibesti) - (central lowlands)
	Lüning et al. 1999	Paleozoic	1380 - 3710 (Kufra)
		Mesozoic	150 - 1000 (Kufra)
	MEH 2015, 2016	Paleozoic	500 - 780 (Ennedi)
		Mesozoic	410 - 770 (Tibesti)-(central lowlands)

Compared to the thicknesses provided by Lüning et al. (1999), who compiles a large amount of information collected by previous authors in the Kufra basin of Libya, the Paleozoic sequence has reduced thicknesses in Northern Chad (1,050-3,050 for Northern Chad, 1,380-3,710 m in Kufra). This might indicate, as discussed in Chapter 2, that the Paleozoic sequence could be expected to be thicker in the deeper parts of the Kufra basin (i.e. east of Faya-Largeau, Kufra and Ounianga).

3.4.2. Ranges of hydraulic conductivities and role of fractures

Values of hydraulic conductivities of the NSAS found in the literature generally range between 10^{-4} to 10^{-5} ms^{-1} (Table 3.2). Sefelnasr (2007) provides estimates of hydraulic conductivity, resulting from the parametrization of hydrogeological modelling, ranging from 10^{-4} ms^{-1} to 10^{-7} ms^{-1} (Table 3.3). Voss and Soliman (2014) indicate a difference of three orders of magnitude between horizontal (10^{-5} ms^{-1}) and vertical hydraulic conductivities (10^{-8} ms^{-1} south of 25°N).

Table 3.3: Values of hydraulic conductivities found in the literature (Sonntag, 1986; Hesse et al., 1987; Sefelnasr, 2007; Voss and Soliman, 2014).

	Reference	Observation (aquifer, location)	Hydraulic conductivity (ms^{-1})
Average hydraulic conductivity (ms^{-1})	Sonntag 1986	NSAS	$1x10^{-5}$
	Hesse et al. 1987	Mesozoic (Kufra)	$1x10^{-4}$ to $6x10^{-5}$
	Sefelnasr 2007	NSAS	$6x10^{-5}$
	Voss and Soliman 2014	Horizonatal (KH)	$1x10^{-2}$ to $1x10^{-6}$ $1.5x10^{-5}$ (north 25°N) $2.2x10^{-5}$ (south 25°N) $7x10^{-5}$ (Kufra)
		Vertical (Kv)	$1.05x10^{-9}$ (north 25°N) $2.35x10^{-8}$ (south 25°N)

Based on the synthesis of thousands of measurements in the laboratory and in the field, Domenico and Schwartz (1998) indicate ranges of values of hydraulic conductivities between 10^{-6} to 10^{-13} ms^{-1} for similar sedimentary rocks as found in the Kufra basin (limestone, sandstone, siltstone, shale). The values applied by the previous modelers (e.g. Sefelnasr, 2007; Voss and Soliman, 2014) seem somehow high compared to estimates provided in Domenico and Schwartz (1998).

However, as suggested by Sonntag (1984), the presence of numerous faults, fractures and structural discontinuities and the large ratio of the lateral extent to the basin depth (ratios 100 to 1,000) increases the overall hydraulic conductivities. As discussed in Chapter 2, the Cambro-Ordovician sandstone (and the Lower Devonian sandstone) in the Ennedi Mountains, shows intense fracturing at a meso and macro scale. The fracturing increases the hydraulic conductivity of the consolidated sandstone and provides preferential paths for infiltration and recharge through open fractures, sinks and along wadis**.** The central subsided zone of the basin was defined by Mohamed et al. (2016) as corresponding to the Pelusium Mega shear zone, or to the Borkou-Kufra Trough of Williams (1966). This zone was identified as characterized by increased fracturing and therefore higher hydraulic conductivities are to be expected.

3.4.3. Implications to the aquifer's configuration

This study provides a certain detail on the range of thicknesses, the mineralogical, textural and geochemical characteristics of the sedimentary sequence of the Kufra basin of Northern Chad.

The sedimentary sequence of the Kufra basin corresponds to the deposition of massive amounts of continental sandstone (between 1,900 and 2,400 m thickness in Northern Chad, Table 3.4), characterized by variable intergranular porosities (up to 35% for the sandstone layers, 0% for the silty interlayers). The Paleozoic and Mesozoic formations generally show signs of compaction, quartz recrystallization, secondary iron oxides precipitation and mineral replacements by clays (kaolinite, pyrophyllite, illite), reducing the consolidated sediment's intergranular porosity.

Table 3.4: Thickness and intergranular porosity characteristics of the geological formation of the Kufra basin of Northern Chad. Ranges of hydraulic conductivity from Sefelnasr (2007), resulting from parametrization of hydrogeological modelling of the NSAS, and from Domenico and Schwartz (1998), resulting from thousands of measurements in the field and in laboratory of comparable rock formations, are indicated for comparison.

Geological formation	Thickness (m)	Intergranular porosity (%)	Hydraulic conductivity (ms^{-1})	
	our work		Domenico and Schwartz (1998)	Sefelnasr (2007)
Chieun and Tekro	250	3-25	$1x10^{-6}$ to $1x10^{-10}$	$1x10^{-4}$
Ounianga	250-400	0-35	$1x10^{-6}$ to $1x10^{-10}$	$1x10^{-5}$
Soeka and Lakes	150-400	0-6	$1x10^{-8}$ to $1x10^{-11}$	
Permo-Trias Madadi	50	2-22	$1x10^{-6}$ to $1x10^{-10}$	
Carboniferous	0-350	0-5	limestone $1x10^{-6}$ to $1x10^{-9}$ shale $1x10^{-9}$ to $1x10^{-13}$	$1x10^{-7}$
Mid and Upper Devonian	200-400	0-18	$1x10^{-7}$ to $1x10^{-10}$	$1x10^{-5}$
Lower Devonian	150-450	0-30	$1x10^{-6}$ to $1x10^{-10}$	$1x10^{-5}$
Silurian	50-80	0-1	$1x10^{-8}$ to $1x10^{-11}$	$1x10^{-7}$
Cambro-Ordovician	50-400	0-15	$1x10^{-6}$ to $1x10^{-10}$	$1x10^{-6}$

The study of the sedimentary sequence of the Kufra basin of Northern Chad shows that the multilayer aquifer system is potentially composed of three major and one minor aquifer formations (Table 3.4): (1) Cambro-Ordovician (50-400 m), (2) Devonian (350-850 m), (3) Permo-Trias (Madadi, 50 m) and (4) Cretaceous (Ounianga, Chieun and Tekro, 500-650 m).

These aquifer formations are interlayered with (1) the Silurian siltstone (up to 80 m thickness), (2) the Carboniferous marls and limestone (up to 350 m thickness), (3) the Soeka and Lakes formations argillite and fine sandstone (up to 400 m thickness) and (4) the Cenozoic sediments (up to 70 m thickness in Faya-Largeau, BRGM, 1991), characterized by reduced intergranular porosities (up to 6%) and lower hydraulic conductivities. The differential erosion of the intercalation of the sandstone and the more argillaceous deposits resulted in the typical "cuesta" morphology, characteristic of the region. The sandstone layers are marked by cliffs and the more argillaceous deposits by platforms (see Chapter 2).

Based on the thickness variability of the geological formations (extracted from the field observations and geological cross-sections, see Chapter 2) and applying the range of hydraulic conductivities values provided in Table 3.4 (Domenico and Schwarz, 1998), transmissivities of the NSAS of Northern Chad are estimated between $1.94*10^{-3}$ and $9.70*10^{-8}$ m^2s^{-1} (Table 3.5). These values correspond to the deepest parts of the basin (e.g. Tekro) within the area inspected in this study.

Table 3.5: Estimated transmissivities of the NSAS of Northern Chad (our study) based on estimates of thicknesses of geological formation (from field observation and geological cross-sections, see Chapter 2) and from the literature (Wright et al., 1982; Ahmad, 1983; Hesse et al., 1987; Sefelnasr, 2007; Vasseur et al., 2015).

	Reference	Aquifer, locality	Transmissivity (m^2s^{-1})
Average transmissivity (m^2s^{-1})	our study		$1.94x10^{-3}$ to $9.70x10^{-8}$
	Wright et al. 1982	NSAS	$2x10^{-2}$ to $8x10^{-3}$
	Ahmad 1983	Kufra	$2x10^{-2}$ to $4x10^{-2}$
		Sarir, West Sarir, Jalo, Tazerbo	$1x10^{-2}$ to $5x10^{-2}$
	Hesse et al. 1987	Mesozoic	$1x10^{-2}$ to $9x10^{-3}$
	Sefelnasr 2007	NSAS	$1x10^{-2}$
	Vasseur et al. 2015	NSAS	$6x10^{-3}$

Values of transmissivities from the literature (Wright et al., 1982; Ahmad, 1983; Hesse et al., 1987; Sefelnasr, 2007; Vasseur et al., 2015) are higher than estimated in this study. As previously seen, these authors base their estimates on higher values of hydraulic conductivities than values provided by Domenico and Schwarz (1998) for comparable rock formations.

3.5. Concluding remarks

The mineralogical and textural characterization of the sedimentary sequence of the Kufra basin of Northern Chad provide information on the aquifer's structure, potentially composed of four aquifer layers (Cambro-Ordovician, Devonian, Permo-Trias and Cretaceous), subdivided by low conductive layers (Silurian, Carboniferous, Jurassic and Cenozoic). The Kufra basin of Northern Chad is, however, densely fractured, increasing the connectivity between aquifers. As will be presented in Chapter 4, the combined presence of low conductive layers and fractures are seen to be the distinctive features which characterize most of the localities where springs and lakes are found (e.g. Fada, Madadi, Hardjalla, Tegueshi, Ounianga, Faya-Largeau).

The study of the sedimentary sequence of the Kufra basin of Northern Chad is only in its exploratory phase. This investigation provides some ranges of geochemical, mineralogical and textural characterization of the rocks composing the sedimentary sequence. However, sedimentary formations have thicknesses, mineralogy and textures that may vary greatly, both laterally and vertically. The results of this study are therefore only a first indication of the possible variabilities of thicknesses of the sedimentary sequence. A more detailed sedimentological study would be needed.

Hydraulic conductivities should be better characterized. Estimates of hydraulic conductivities should represent all conductive features such as porous media and fractures. In order to capture the different components and their relative importance, several methods should be undertaken (e.g. aquifer test, modelling, fracture orientation, apertures, density and roughness).

Chapter 4

Hydrology and hydrogeology of the Tibesti Mountains and the Kufra basin of Northern Chad

4.1. Introduction

4.1.1. Introduction and aim

The aim of this chapter is to present the geological analysis (litho-stratigraphic sequence presented in Chapters 2 and 3) complemented with hydrogeological information obtained during the fieldwork (hydraulic heads measurements). Both types of data are used to improve the conceptual understanding of the groundwater flow.

During our fieldwork, we inspected, measured and sampled 185 water points in an area of 100,000 km^2 (approximately 2 water points every 1,000 km^2). The densities of the water points and of human settlements are higher along the major wadis or enneris (synonyms meaning intermittent river courses) of the Ennedi and Tibesti Mountains and within the major discharge zones (oases of Faya-Largeau, West Palm Groves, Gouro and Ounianga), located in the depressional area extending between these two mountain chains. Anthropogenic discharge might be considered negligible and the groundwater system proximal to its natural state.

To the best of our knowledge, the only water table measurements carried out in the region of Northern Chad were performed eighty years ago by Ball (1927) and Sandford (1935). These measurements have been the basis for the previous modeling approaches (e.g. Heinl and Brinkmann, 1989; Gossel et al., 2004).

Our fieldwork enabled to develop a denser and up to date dataset of water table measurements. Given the groundwater flow patterns, questions investigated in this chapter are: (1) where are the zones of recharge and the zones of discharge? and (2) is the groundwater flow system, as observed today, the result of modern or past recharge?

4.1.2. Outline of the chapter

The chapter is structured as follows. Section 4.1.3 describes some general concepts of wadi hydrology illustrated with the example of the Zouarké catchment (later described in the chapter). A brief synthesis of the paleoclimatic variability is included in section 4.1.4. The morphological and hydrological settings are introduced in section 4.2.

After a methodological section (section 4.3), the water points sampled in the Tibesti Mountains are described in terms of their relationship to an alluvial system or to a geological layer (section 4.4.1). The Tibesti Mountains were only marginally investigated in the present study. Moreover, the region inspected do not have a direct linkage to the NSAS of Northern Chad. However, the characterization of the groundwater's hydrochemical and stable isotopic signature within this mountainous region is useful for the interpretation of the groundwater's signature within the NSAS (see Chapter 7). Therefore, we included in this chapter a section describing the inspected localities and the hydrological and hydrogeological context of the Tibesti Mountains. Chapter 7 refers to this information.

Sections 4.4.2 and 4.4.3 present the hydrogeological system of the NSAS (Ennedi Mountains and central lowlands), indicating the most productive geological formations, the possible connections between aquifers and the groundwater flow directions. This information is inferred from the measured hydraulic heads, the topography (extracted from the Shuttle Radar Topography Mission, SRTM) and the occurrence of diatomite deposits (SIRE database and from Pachur and Altmann, 2006).

The chapter concludes with a discussion (section 4.5) which synthetizes the key hydrogeological aspects of the Nubian Sandstone Aquifer System of Northern Chad.

4.1.3. Wadi Hydrology

In arid areas, an effective mechanism of recharge is concentrated recharge through fractures, ponding or along wadi courses (Lloyd, 1986; Johnston, 1987; Gee and Hillel, 1988; Stephens, 1994; Wood and Sanford, 1995; Edmunds, 2005; Scanlon et al., 2006). Wadi hydrology is an important component of the hydrogeological systems in the mountainous regions of the Tibesti and Ennedi of Northern Chad. Figure 4.1 presents a schematic view of the processes of precipitation, runoff, accumulation and infiltration (Sen, 2008) occurring in the catchment of a wadi system found in the project area (Zoaurké catchment, Tibesti Mountains).

Wadis are dry watercourses for most of the year (Figure 4.1A). During the rainy season, high-intensity precipitation will provoke runoff, floods or flash floods along the wadis, eroding the banks in the upstream and transporting large amounts of sediments downstream. The upstream of a wadi system is located at higher altitudes within a mountainous area, often characterized by higher amounts of

rainfall than the downstream areas. The outlet of the wadi is located in the downstream area, characterized by lower slopes and increased alluvial sediment's thickness.

During the flooding, sheet flow (q_{sh}) in the upstream zone will converge towards the main channel (q_c, Figure 4.1B). In low-lying areas within the main channel, the soil might become saturated: infiltration and seepage (q_i) will eventually provide recharge to the alluvial aquifer and the surrounding rock system (Figure 4.1C). The evaporation of surface water accumulating in the low-lying zones will also eventually concentrate salt deposits (sebkhas). Along the wadi course, several intermediate low-lying areas might occur before reaching the outlet. Eventually, recharge in the upstream areas of a wadi system will continue feeding the main channel even during the dry season (q_{inflow}, Figure 4.1D), securing the annual water supply.

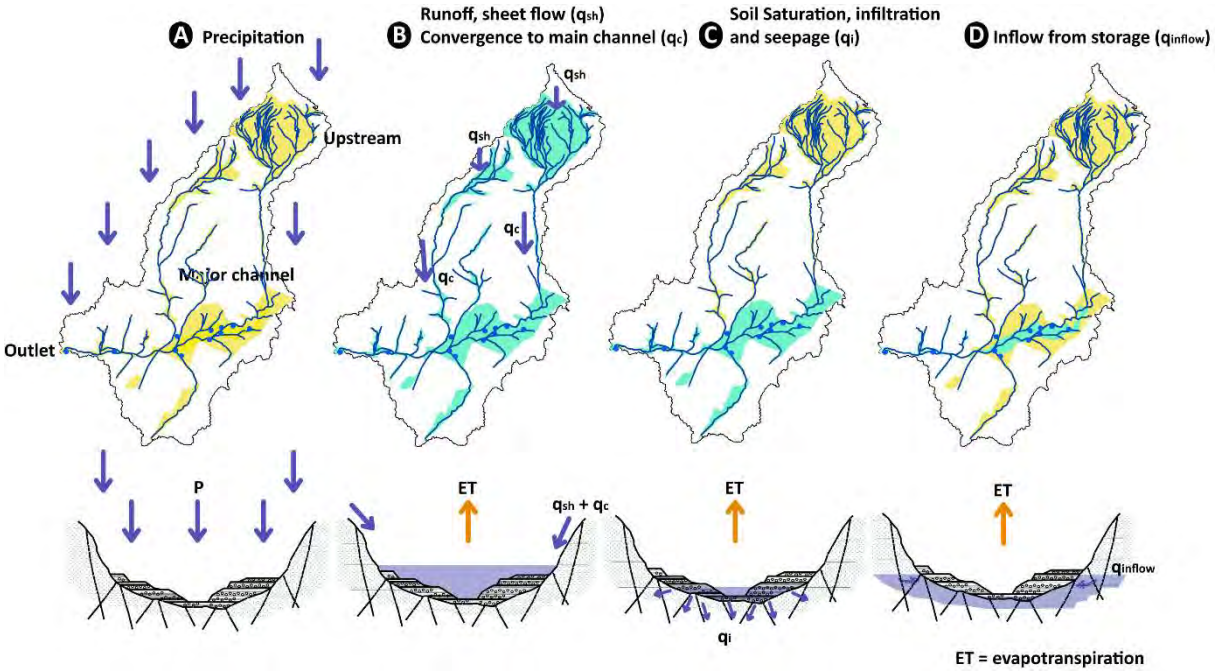

Figure 4.1: Schematic representation of wadi hydrology processes. The example is applied to the catchment of wadi Zouarké, in the Tibesti Mountains (see later in the chapter). Dry conditions are indicated by a yellow color (A, C and D), while flooded/humid conditions are indicated by a blue color (B, C and D).

4.1.4. Paleoclimatic changes

Wadis were probably permanent river courses in the past pluvial periods, feeding several intermediate lakes and terminating in the Holocene Mega-Lake Chad. Paleohydrological deposits such as diatomites have been widely observed in Northern Chad and elsewhere in the Kufra basin (Pachur and Altmann, 2007; Herrmann et al., 2009), testifying to the extensive development of an interior lacustrine environment.

The reconstruction of the late Pleistocene - Holocene Sahara paleoclimate (Gasse, 2000; Hoelzmann et al., 2001; Kröpelin et al., 2008), indicate the following climatic oscillation: (1) A great pluvial epoch between 50,000 and 20,000 yrs. BP, (2) Cold and dry semi-arid conditions between 20,000 and 14,000 yrs. BP, coincident with the last glacial maximum (18,000 yrs. BP, Wisconsin/Weichsel), (3) A cold but humid period between 14,000 and 10,000 yrs. BP, (4) A moist, lacustrine period between 10,000 and 8,000 yrs. BP (Mega-Lake Chad maximum at 8,000-9,000 yrs. BP), (5) A second moist, lacustrine period between 7,000 and 4,000 yrs. BP. The region has since then experienced increased arid conditions, with significant climatic fluctuations at a decadal scale (Edmunds et al., 1999).

During the last lacustrine period, the lake's levels at Ounianga were 40 m higher than nowadays (at 6,160 yrs. BP, Kröpelin et al., 2008). The Tibesti Mountains was a major area of recharge (Lézine et al., 2011). Radiocarbon dates from numerous sources in the Tibesti Mountains (Pachur, 1973, 1975) indicate humid conditions between 7,500 and 4,500 yrs. BP. Kröpelin et al. (2008) found specimens of *Erica arborea* in the sediments of Lake Yoa (Ounianga Kebir), dated at 4,300 yrs. B.P. This species is generally found at altitudes above 2,900 masl in the Tibesti Mountains, indicating a past connection between the Tibesti high altitudes and the lakes of Ounianga Kebir. As stated by Lézine et al. (2011), the region has experienced a favorable climatic setting up to 4,000 – 4,500 yrs. BP.

During the past periods of humid and semi-humid conditions, considerable amounts of precipitation would have infiltrated, leading to higher hydraulic heads and gradients. With the evolution towards an arid climate, the hydraulic heads and gradients decreased, the hydrological activity became intermittent and most of the zones of accumulation (lakes, ponds, oases) dried-out. Sub-regional flows eventually switched off, and a regional flow became predominant (Tóth, 2009). However, given the geometrical properties, storage coefficients and transmissivities of the NSAS, the time required for the system to adjust to a new boundary condition, determined by the change of the climate and of the recharge rates, is potentially of the order of several thousand years (Vasseur et al., 2015).

4.2. Morphological and hydrological setting

The structure of the Kufra basin and the topography in Northern Chad are marked by the basement uplift in the regions corresponding to the Ennedi and Tibesti Mountains (Chapter 2). The two mountain chains reach altitudes of 1,300 masl (Ennedi Mountains) and 3,440 masl (Tibesti Mountains). In between these two mountains, the region lies in a zone of lowlands (altitude < 500 masl) and of increased sedimentary thickness (see Chapter 2).

The ridges of the Tibesti and Ennedi Mountains mark the limits of the main hydrological basins: towards the north, the Mediterranean hydrological basin, towards the south, the Lake Chad hydrological basin and towards the east, the Nile hydrological basin (Figure 4.2).

The highest ridges of the Tibesti Mountains volcanic complex follow an east-west direction. They separate the river courses flowing towards the north (Mediterranean hydrological basin) from the river courses flowing towards the south (Lake Chad hydrological basin). In the southeast, ridges of direction N150° separate the Tibesti South-East from the Tibesti South sub-basins.

The highest ridges of the eastern Ennedi Mountains follow directions N-S and WSW-ENE. They separate the wadis flowing towards the east (Nile hydrological basin) from the wadis flowing towards the west (Lake Chad hydrological basin). From West to East, ridges also separate the wadis flowing towards the north (Mourdi sub-basin) from the wadis flowing towards the south (Djourab/Mortcha sub-basin).

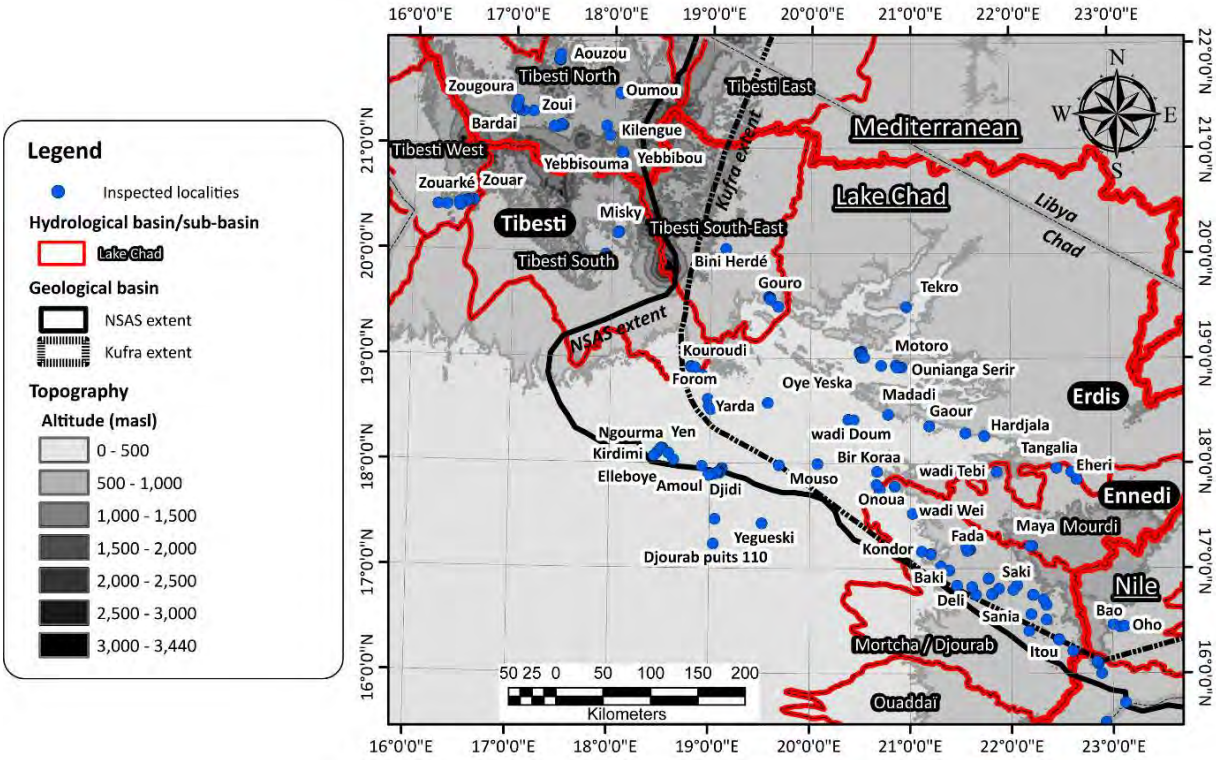

Figure 4.2: Map indicating the topography (from SRTM) and the subdivisions of hydrological basins and sub-basins (from the SIRE database), described in the text. The inspected localities are also indicated. The Kufra basin extent is from Heron et al. (2009) and the NSAS extent is from Voss and Soliman (2014).

The major enneris of the Tibesti Mountains are: (1) enneri Zoaurké flowing towards the south-west (Tibesti West sub-basin), (2) enneris Yao (not investigated) and Misky flowing towards the south and southeast (Tibesti South sub-basin), (3) enneris Zoumri-Bardangué and Yebbigué flowing towards the north (Tibesti North sub-basins).

The major wadis of the Ennedi Mountains are: (1) wadis Bao and Howar (Nile hydrological basin), flowing towards the east and south, (2) wadi Haouach (Lake Chad hydrological basin), flowing towards the south, (3) wadis Dougouro, Kordi and Béméché (Mourdi sub-basin), flowing towards the north, and (4) wadi Sala (Djourab/Mortcha sub-basin), flowing towards the SW and NW. Wadi Sala is composed of several wadis (wadis Sini-Chili, Nohi, Archeï, Ndou) originating at higher elevations within the Ennedi Mountains.

The region comprised between the foothill of the Tibesti Mountains (Aïn Galaka, Yen, Ngourma grouped under the term "West Palm Groves"), West of Kondor (western Ennedi Montains) and south of Tekro and the Ouninaga Lakes, lies is in a depression (below 500 masl). Elevations increase towards the Tibesti Mountains, the Ennedi Mountains and towards the Chad-Libya border.

In the region of the Chad-Libya border, the zone lying between the Tibesti and the Erdis plateaus is located at higher elevations compared to the southern (oases of Ounianga) and northern (Kufra oases) regions. E-W ridges (same directions as observed for the Tibesti Mountains) separate the Mediterranean hydrological basin to the north from the Lake Chad hydrological basin to the south.

4.3. Methods

4.3.1. Fieldwork measurements and verification

The hydraulic heads presented in this chapter were collected during several field campaigns: 1. Ennedi in February 2013; 2. Ennedi-Ounianga in July-August 2013; 3. Grès de Nubie (Faya-Largeau to Ounianga) in January-February 2014; 4. Borkou (Faya-Largeau, West Palm Groves, Yarda-Kouroudi and Misky - Tibesti south) in January-February 2015; 5. Tibesti (Zoumri, Yebbigué, Zoaurké and Misky) in May-June 2015; 6. Ennedi in November-December 2016 (see Annex 3). 38 water points were inspected twice in two different years. Differences of water table depths between years are within 5 m.

SRTM version 4.1 (Jarvis et al., 2008) was used to compare the GPS data collected in the field. Differences were within 4 m ± 3. One point, located in a narrow valley, or gueltas, showed a maximum difference of 39 m.

4.3.2. Data used in the chapter

For the Tibesti Mountains, the water table elevation measured in the field are completed by data from four studies conducted during the 1990's (O.N.H.P.V., 1991; O.N.H.P.V., 1992; Direction de l'Hydraulique et de l'Assainissement, 1993; BURGEAP, 1999).

SRTM was also used to define the topography of the hydrogeological cross-sections. The basement elevation model used in these cross-sections is from Mahamoud (1986).

The geological data are from the SIRE database (2016). At the time of writing, available geological information from the SIRE database were restricted to the region north of 22°N and west of 18°E in the Tibesti Mountains, and 16°N for the rest of the region. Hydrogeological data concerning the oases of Gouro, Ounianga, Fada, Faya-Largeau and the West Palm Groves are mostly from BRGM (1991). The location of paleohydrological deposits are from the SIRE database and from Pachur and Altmann (2007).

4.4. Results

4.4.1. The Tibesti Mountains

All the permanent water points in the Tibesti Mountains are found south of 22°N (Figure 4.3). Wells (improved or traditional) and boreholes are generally constructed in the alluvial system of temporary river systems, named enneris in the Tibesti region. These enneris are known to be active every 1 – 3 years if they are located within the southern slopes (1 year) or the eastern and northern slopes (3 years). The hydrologically active part of the enneri can be easily distinguished from the inactive, by the color of the sediment. The active parts have a grey color (more silty and enriched with clays) striped by white deposits (efflorescences) and a narrow zone of vegetation (from a thin line to an oasis). Water table depths of wells and boreholes range between 1 and 12 m bgl (below ground level) within the alluvial systems located on the northern slopes (Zoumri and Yebbigué) and between 1 and 45 m bgl within the alluvial systems located on the southern slopes (Misky and Zouarké). One borehole in the Zouarké basin has a water table at - 141 m bgl.

In addition to the wells and boreholes located along the enneris systems, springs (or the intersection of the phreatic aquifer with the topography) supply extended palm groves in Aouzou, Omou, Yebbibou, Kilenge, and along the enneri Zoumri (Zoumri, Osouni, Zoui, Bardaï). The springs of Yebbibou, Kilenge and Zoumri (estimated outflow of 120 to 480 m^3d^{-1}, MEH, 2016) are located within or at the base of the volcanic plateaus. These plateaus are composed of basaltic lavas, pyroclastic deposits, slags and volcanic alluvial sediments, ranging in altitudes from 1,500 to 2,200 masl. The springs of Aouzou, and the palm groves of Omou, Osouni, Zoui and Bardaï are located within the “Grès de Bardaï” formation (Paleozoic sandstone), close to the contact with the Precambrian basement. A thin line of vegetation can be observed for 90 km to the NNE of Aouzou (enneri Yebbigué) and for 120 km to the NNW of Bardaï (enneri Zoumri).

Hydraulic heads vary: (1) from 1,308 masl to 914 masl in the Zoumri system (direction NW); (2) from 1,520 masl to 909 masl in the Yebbigué system (direction N); (3) from 1,264 masl to 678 masl in the Misky system (direction S); and (4) from 820 masl to 665 masl in the Zouarké system (direction WSW). Mean hydraulic gradients vary between 4‰ and 6‰.

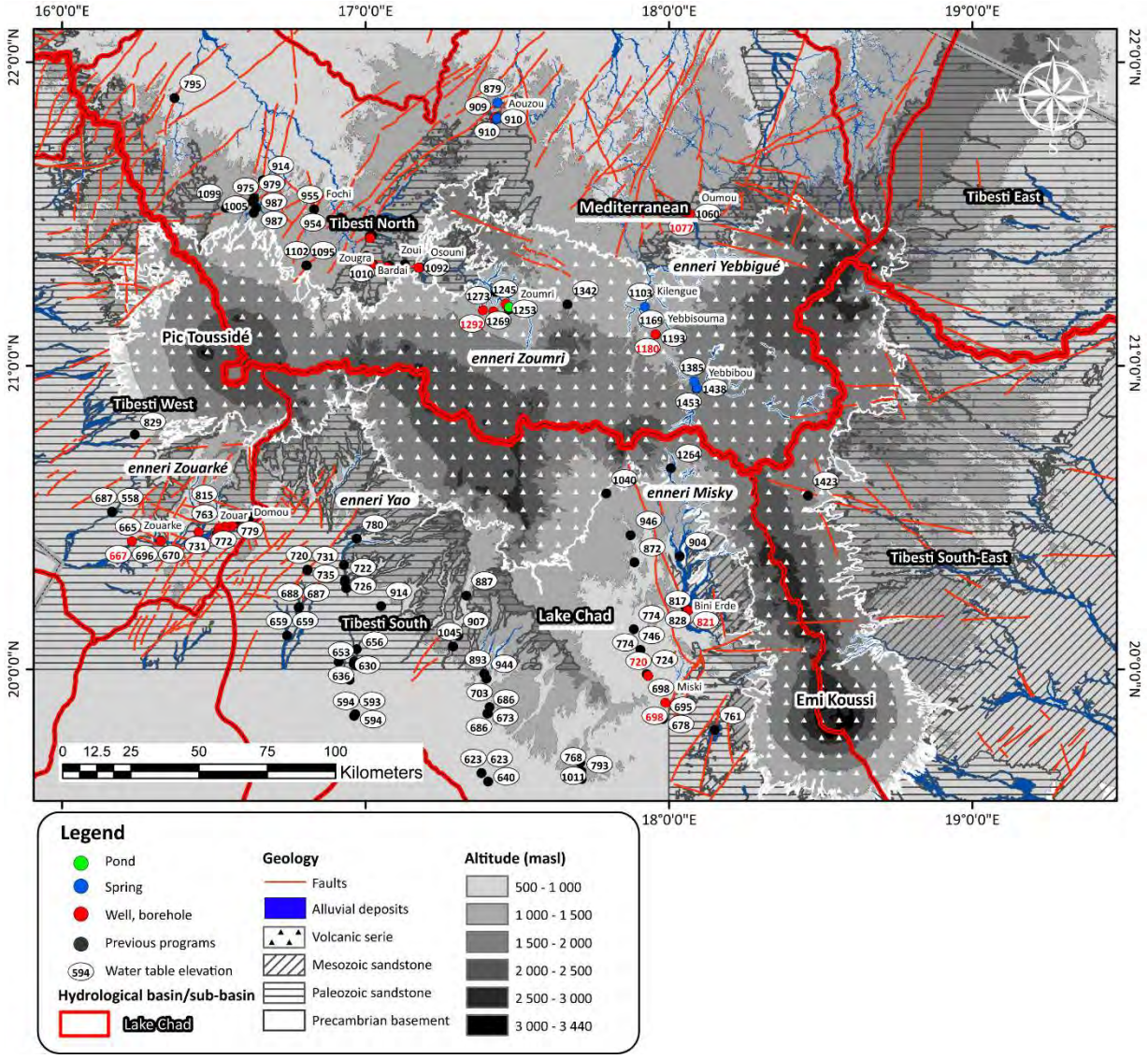

Figure 4.3: Geological and topographical map of the Tibesti Mountains. Inspected water points are shown grouped as pond, spring or well/borehole. The measured water table elevation is shown in blue when corresponding to surface water or groundwater discharge, in red when corresponding to measurements from a well or a borehole. The black points correspond to water table elevation measurements from previous investigations. The major geological units are also shown (Precambrian basement, Paleozoic and Mesozoic sandstone, volcanic series, alluvial sediments), as well as the hydrological basins and sub-basins.

4.4.2. The Ennedi Mountains

4.4.2.1. General observations

Within the Ennedi Mountains, groundwater is found in the proximity of wadis. Wadis are known in the Ennedi Mountains to be active every year, and several times per year in particularly favorable years and locations (see Chapter 5). In the downstream of wadis, numerous temporary ponds are found in low-lying flat areas. Within the major alluvial systems, the water table of traditional and improved wells is between < 1 and 7 m bgl. Maximum depths were found in Kondor (improved well, 37 m bgl).

Springs might be associated to the wadi system, supplying a continuous inflow to the alluvial aquifer. Springs are always associated with major fractures, often seen to extend up to the highest altitudes of the mountain chain. Springs are also often associated with the development of spectacular gueltas or of perennial ponds (Onoua, wadi Widei). The most important are the gueltas of Archeï and Bachiquele. Both are the result of several upstream springs (up to 30 for Bachiquele), discharging from the Paleozoic sandstone along major faults (directions 120 – 130°N in Bachiquele), collecting into ponds in the wadi's alluvial system, which widens downstream. Estimated flows are 600 m^3d^{-1} and 1,000 m^3d^{-1} for Archeï and Bachiquele systems, respectively (MEH, 2015).

Wells, boreholes and springs are mostly located within the southern slopes of the Ennedi Mountains (Figure 4.4). Water points are rarer towards the north-west (wadi Wei, wadi Widei, Onoua, Bir Koraa) and towards the north (wadi Tebi, Tangalia, Eheri, Mourdi Djouna).

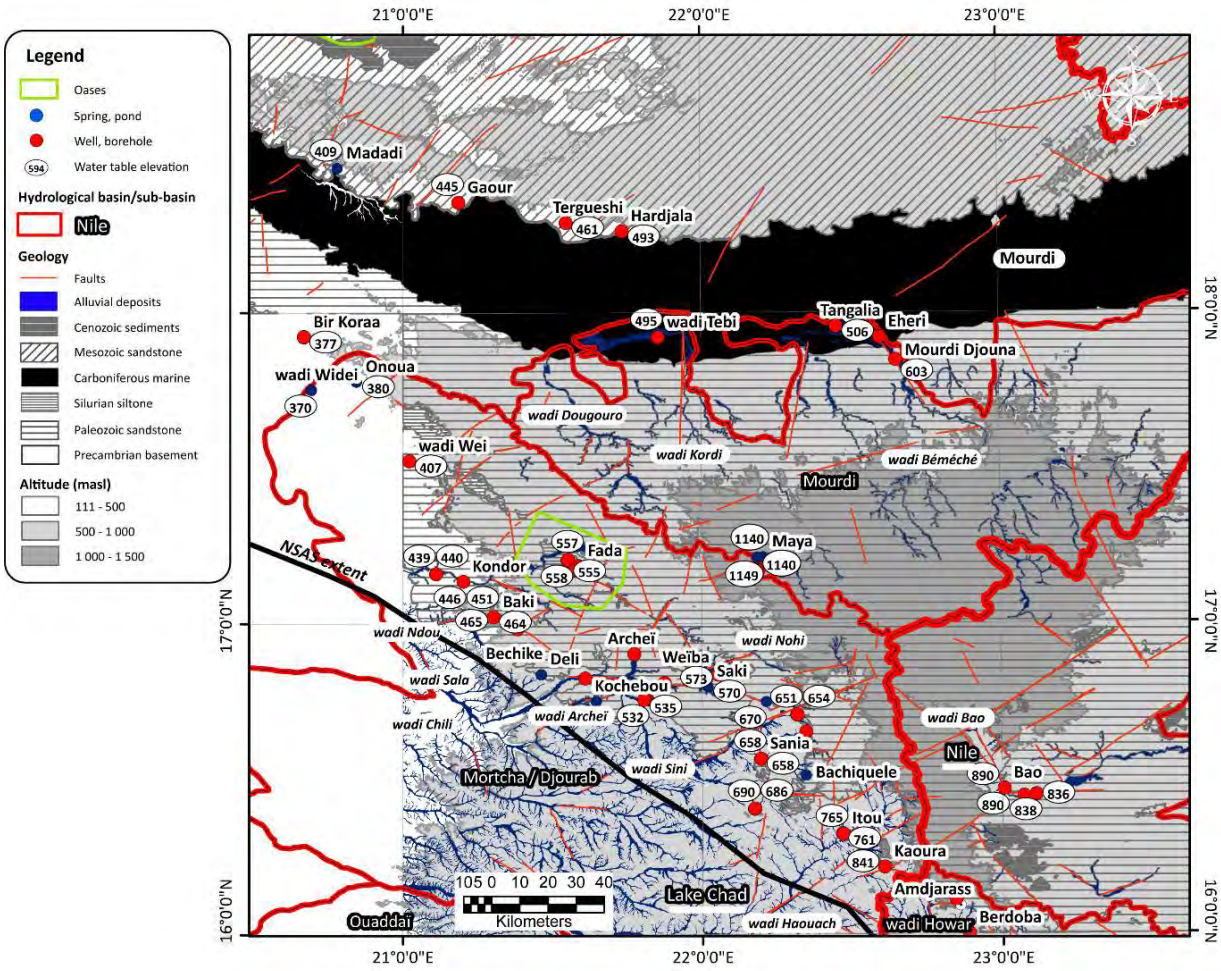

Figure 4.4: Geological and topographical map of the Ennedi Mountains. Inspected water points are shown grouped as pond/spring or well/borehole. The measured water table elevation is shown, as well as the hydrological basins and sub-basins and the major geological units (SIRE database).

4.4.2.2. Litho-hydrostratistratigraphic units

In the Ennedi Mountains, groundwater occurrences are mostly associated with the Cambro-Ordovician sandstone and the Lower Devonian sandstone (Figure 4.5). Fewer examples of groundwater are associated to the Upper Devonian formation.

In the southern slopes of the Ennedi Mountains, springs (Bachiquele, Alliba, Archeï, Deli) are mostly located at the base of the Cambro-Ordovician sandstone, close to the boundary with the Precambrian basement. The Cambro-Ordovician sandstone shows intense fracturing, at a meso and macro scale.

The Cambro-Ordovician sandstone is overlain by the low-permeable glacially-related deposits of the end of the Ordovician and by the low-conductive Silurian siltstone. These formations potentially act as confining layers. However, the horizontal discontinuity of the Silurian formation indicates that this effect might be restricted to specific areas where the Silurian formation is thicker (see Chapters 2 and 3).

The oases of Fada develops on an alluvial plain corresponding to the Silurian formation, close to the limit with the Lower Devonian sandstone. The water table intersects the surface in the center of the oases. From Fada towards the north-west (to Faya-Largeau and the West Palm Groves), several water points are associated to the Lower Devonian formation. The Lower Devonian sandstone has similar mineralogical, sedimentological and structural characteristics as the Cambro-Ordovician sandstone.

The higher elevations of the Ennedi Mountains are characterized by plains surrounded by cliffs of the Upper Devonian sandstone. The Mid and Upper Devonian formations are characterized by lower intergranular porosities. Nevertheless, in our study we identified these high plateaus as playing an important role (see also Chapters 5 and 6) as they: (1) collect and store rainwater in natural ponds for several months after the end of the rainy season (e.g. Maya); (2) convey rainwater towards the Mourdi depression through the wadis systems.

West of Kondor, the mountainous topography changes into a lowland (see Chapters 2 and 3). The water occurrences become rarer and associated with the Upper Devonian formation (e.g. Bir Koraa, wadi Widei).

Within the northern slopes of the mountain chain, water points concentrate in correspondence with the Lower Carboniferous sandstone sequence and the downstream zone of the major alluvial systems originating within the high plains of the Ennedi Mountains (Tebi, Mourdi Djouna).

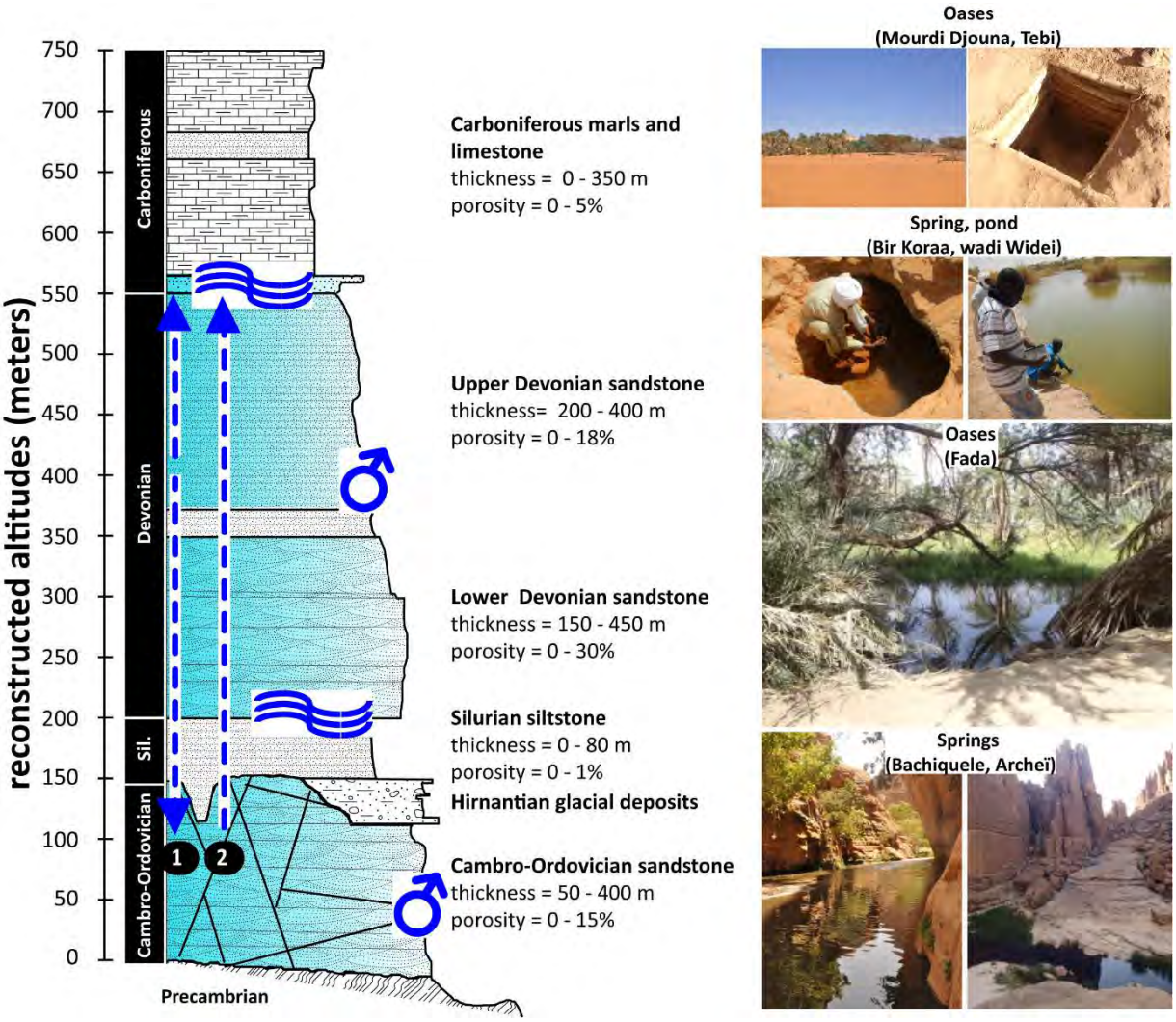

Figure 4.5: Synthetic litho-hydrostratigraphic log indicating the ranges of thicknesses and intergranular porosities of the different geological formations. The observation of groundwater occurrences (springs of Archeï and Bachiquele, oases of Fada, spring of Bir Koraa, pond of wadi Wideï, oases of Mourdi Djouna and Tebi) are documented with photos and their approximate locations are indicated on the log (circle with arrow: spring, waves: oases, shallow water table). Arrow 1 and 2 indicate the possible connections between aquifer's layers.

4.4.2.3. Groundwater flow patterns

Hereafter, WNW-ESE and SSW-NNE geological cross-sections are shown (Figures 4.6 and 4.7) to illustrate the groundwater flow directions inferred from the hydraulic heads. In the eastern Ennedi Mountains (Bao, Amdjarass, Bedoba, Nile hydrological basin), hydraulic heads vary from 912 masl (Amdjarass) to 778 masl (Berdoba). From the ridges, marking the limit between the Nile and Lake Chad hydrological basin, the hydraulic heads show a progressive decrease towards the WNW (Figure 4.7, cross-section A). The gradient follows the topography and as shown in Chapter 2, the topography parallels the basement structure (uplifted zone along the Ennedi-Oweinat direction and subsided zone along the Borkou-Kufra Trough). A major wadi system (wadi Sala) also follows the same directions as the groundwater gradient. The decrease of the hydraulic heads was measured at several points: (1)

841 masl in Kaoura, (2) 658 masl in Bachiquele, (3) 573-583 masl in Archeï and Weïba, (4) 557 masl in Fada, (5) 407 masl in wadi Wei, and (6) 370 masl in wadi Wideï. At the highest altitudes of the Ennedi Mountains (Maya) hydraulic heads were measured at 1,149 masl.

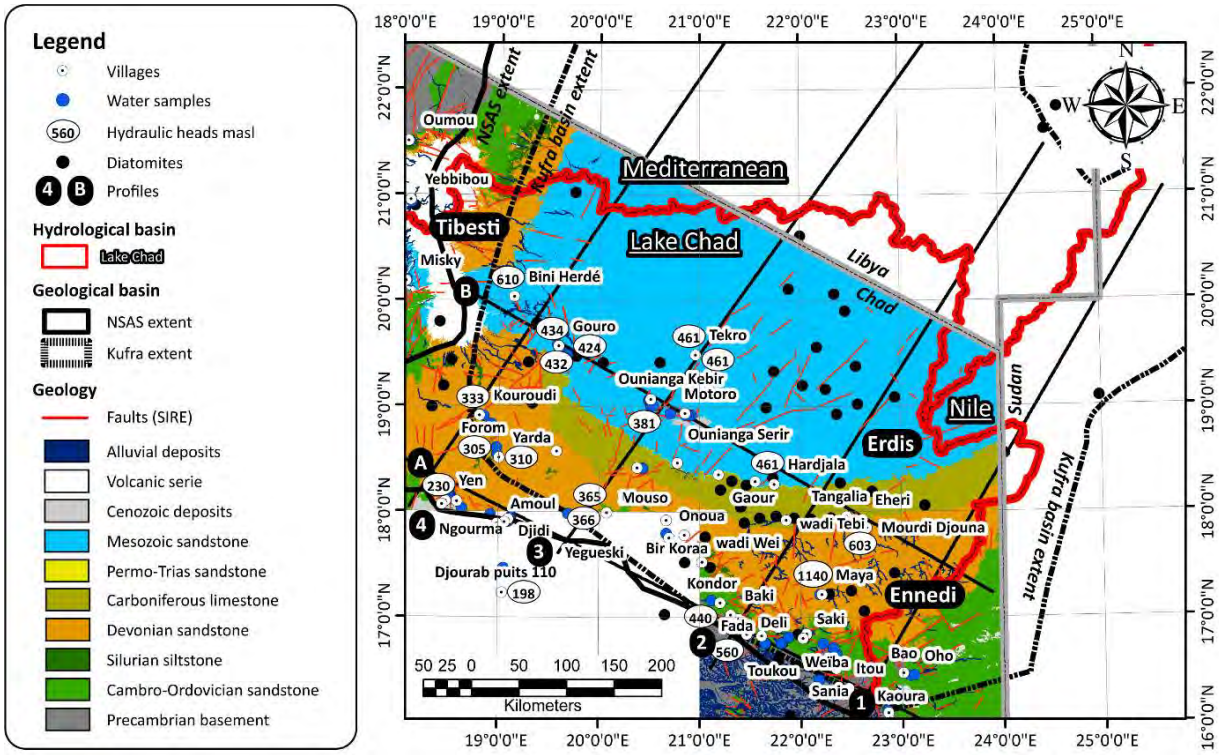

Figure 4.6: Geological map (faults and geological formations are from the SIRE database) showing the location of water samples and hydraulic heads (masl) measured in the field (only a selection of values is shown), the location of diatomites (from Pachur and Altmann, 2006) and of the geological profiles shown and described in the text. The hydrological (from SIRE database) and geological basins (NSAS extent is from Voss and Soliman, 2014, Kufra basin extent is from Heron et al., 2009, see Chapter 2) are also shown.

The flow converges from the Ennedi Mountains (and from the Tibesti Mountains) to the depressional region of Faya-Largeau (217 masl). Mean hydraulic gradients vary between 3 and 4‰ within the Mountains of the Ennedi and between 1 and 2‰ in the more depressional areas surrounding the mountainous relief.

SSW-NNE cross-sections 1 and 2 (Figure 4.7) show a groundwater flow towards the southern slopes of the Ennedi Mountain (cross-section 1 Bao 890 masl, Kaoura 841 masl, cross-section 2 Fada 557 masl, Bechike 465 masl), with a mean hydraulic gradient of 1-2‰, and a groundwater flow directed towards the Mourdi depression (cross-section 2 wadi Tebi 495 masl), with a mean hydraulic gradient of 1‰. A question mark is indicated on cross-sections 1 and 2 because the water table level was not directly measured but results from the interpolation of proximal observational points.

In cross-section 2, the position of diatomites in an extended depressional zone located at higher elevations than the current discharge zones indicates a past discharge zone with and inflow from the NNE, originating from the Erdis plateaus.

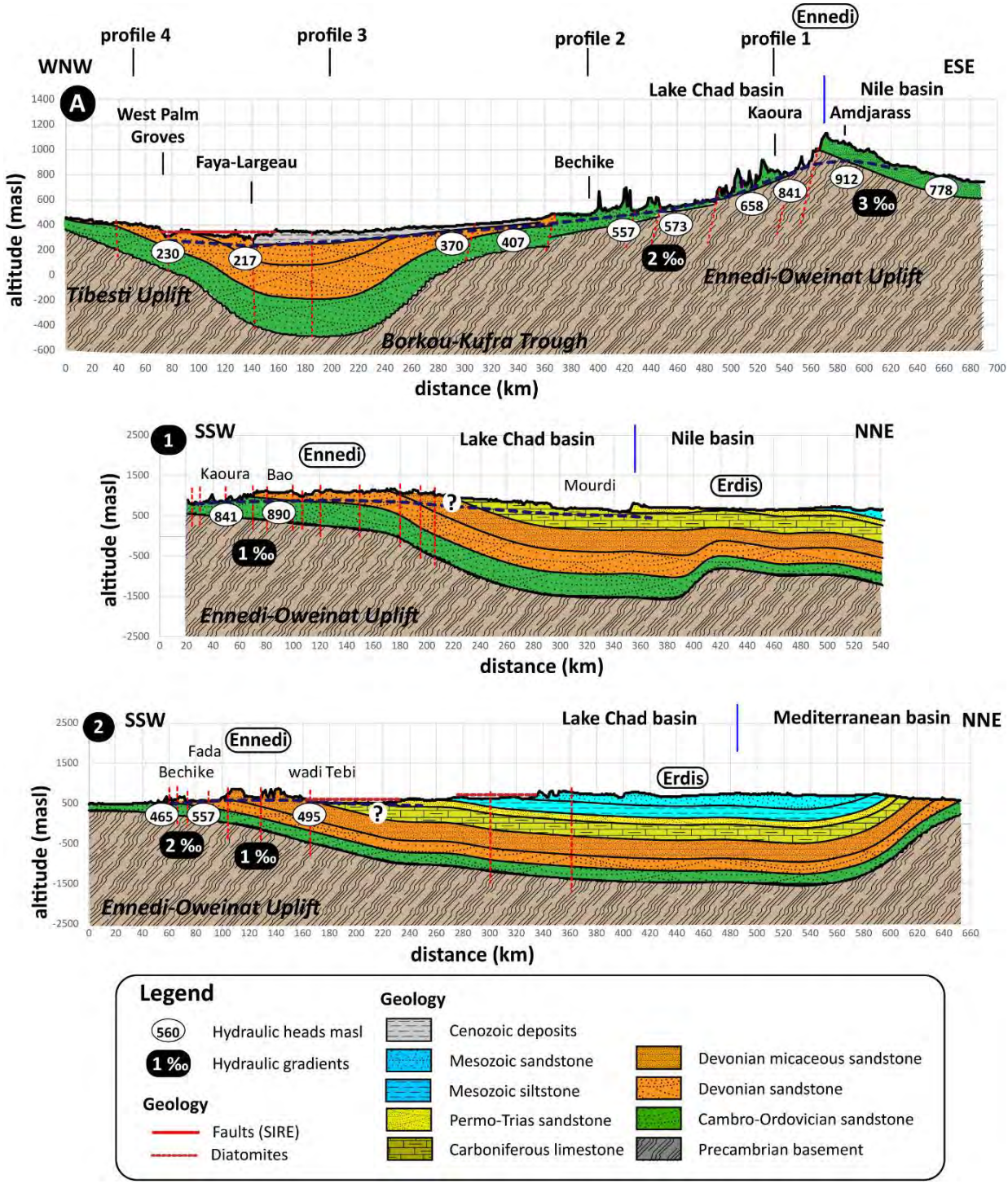

Figure 4.7: Geological cross-sections WNW-ESE (profile A) and SSW-NNE (profiles 1 and 2, the position of the cross-section is shown in Figure 4.6). Hydraulic heads and gradients are derived from our measurements in the field. Geological information are based on the SIRE database (faults, geological formations, diatomites). Faults are assumed to traverse all the geological formations up to the basement elevation. Geological data in Libya and Sudan and location of diatomite deposits are from Pachur and Altmann (2006). Topography was extracted from SRTM and the basement elevation is from Mahamoud (1986).

Figure 4.5 shows two blue arrows (path 1 and 2) representing the possible connections between aquifers determined by the hydraulic heads distribution. Arrow 1 shows the groundwater flowing from the Upper Devonian formation, forming the high plains of the Ennedi Mountains, towards the south, discharging at the base of the Cambro-Ordovician sandstone. Groundwater is also flowing towards the north, where the water table is found close to the surface in correspondence to the Lower Carboniferous sandstone and the major alluvial systems (wadis Kordi and Béméché) originating in the Ennedi Mountains. Arrow 2 shows the potential groundwater flow directed towards the north, as suggested by the questions marks in Figure 4.7 (cross-sections 1 and 2).

4.4.3. The central lowlands

4.4.3.1. General observations

Numerous alluvial systems are seen to originate in the Tibesti Mountains, reaching the foothill of the Mountain chain in the region of Gouro or south of Emi Koussi (Tibesti South sub-basin, Figure 4.8). The enneris associated to these alluvial systems are active once every 3-4 years (see Chapter 5). Bini Herdé is an improved well, constructed in the alluvial system of a wadi showing a low frequency hydrological activity.

The central zone of lowlands is characterized by discharge points and zones such as lakes (Lakes of Ounianga), springs (Lakes of Ounianga, Gouro, Madadi), a shallow water table (wadi Doum, Gouro, Kouroudi) and artesian springs (Faya-Largeau, West Palm Groves). This region holds also several examples of paleohydrological deposits (lacustrine and palustrine sediments), testifying to the previous extent of lakes (e.g. Mega-Lake Chad) during the more humid periods of the late Pleistocene to mid-Holocene.

The lakes of Ounianga are composed of two major groups: Ounianga Kebir to the west and Ounianga Serir to the east, and a small group of lakes (Motoro) located in between these two groups. Calculated surfaces of lake water (Chapter 6) are 5 x10^6 m^2 in Ounianga Kebir, 0.06 x 10^6 m^2 for the small group of lakes in Motoro and 12 x 10^6 m^2 in Ounianga Serir. Interesting, the group of “big” lakes (Kebir meaning big in Arabic, Serir meaning small) is actually smaller than the group of “small” lakes.

Ounianga Kebir is composed of 4 lakes: lakes Yoa, Oma, Béver, Mioji-Forodone. Ounianga Serir is composed of 14 lakes: the main ones are Edem, Teli, Agouta, Hogou, Djara, Bedrim and Boukou. The biggest lakes are lake Yoa in Ounianga Kebir, with a surface of 3.6 km^2 and a depth of 27 m, and lake Teli in Ounianga Serir, with a surface of 6 km^2 and a depth of 10 m. These lakes have an elongated SSW-NNE shape. Intense wind deflation characterize this region. Each lake is separated from the neighboring one by outcrops of the underlying sandstone (Lakes Formation) and/or by diatomite deposits more or less covered by aeolian sediments.

Groundwater discharges through numerous springs, which emerge from all sides of the shorelines (Schneider, 1989). According to BRGM (1991), springs discharge at a rate of 120 to 240 m^3d^{-1} in Ounianga Kebir.

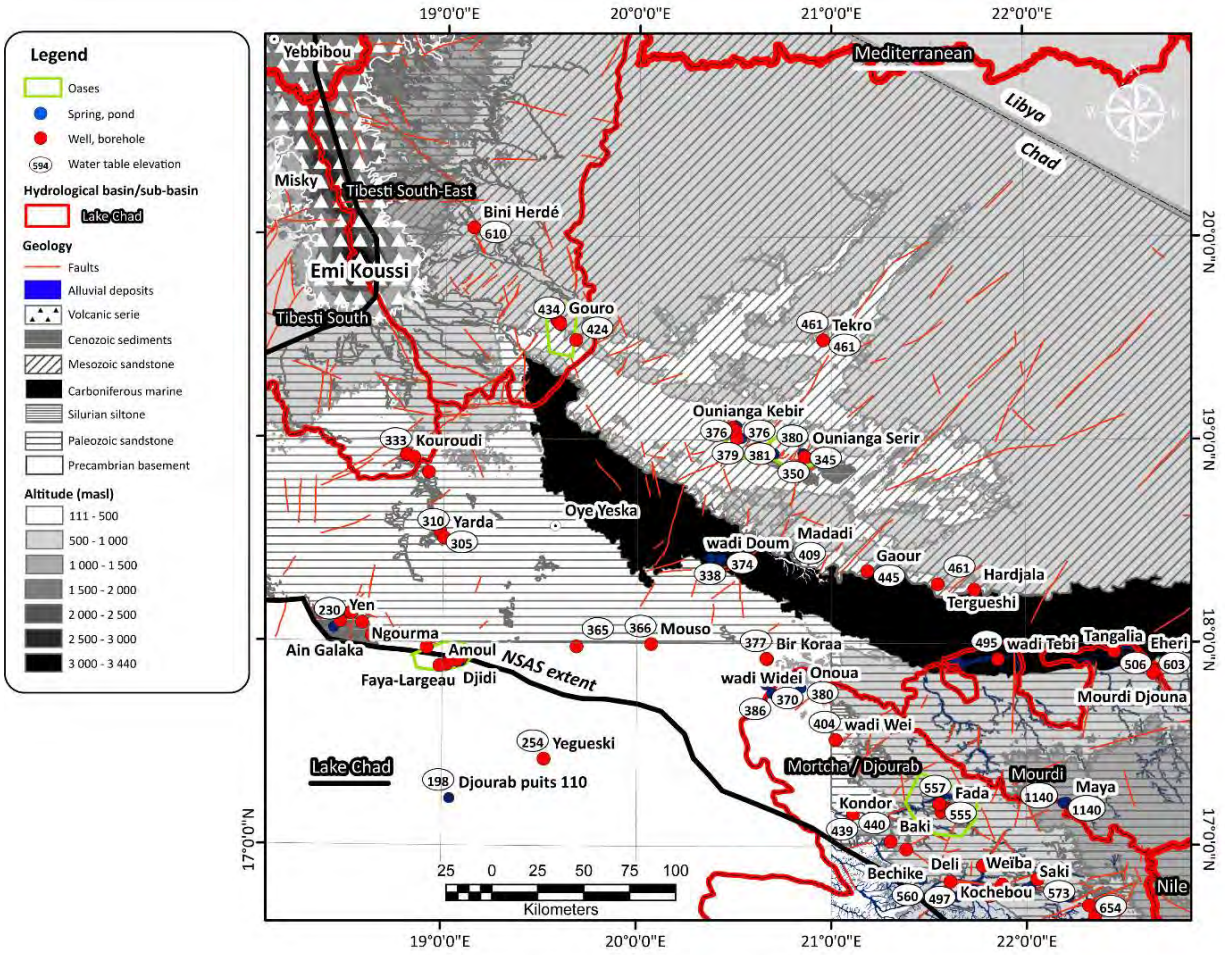

Figure 4.8: Geological and topographical map of the Central lowlands. Inspected water points are shown grouped as pond/spring or well/borehole. The measured water table elevation is shown, as well as the hydrological basins and sub-basins, and the major geological units.

The region surrounding Faya-Largeau and the West Palm Groves (i.e. Aïn Galaka, Elleboye) is characterized by numerous oases and agriculture plants supplied by artesian springs (Kirdimi, Aïn Galaka) and artesian boreholes (Faya-Largeau). According to BRGM (1991), in Faya-Largeau the Paleozoic sandstone is found at depths of 20 to 70 m bgl, underlying the Cenozoic sediments. These sediments are composed of silty material of low conductive character. They are identified as a layer confining the aquifer seated in the Paleozoic sandstone (BRGM, 1991). BRGM (1991) also note that directions N40-50° are seen to be favorable for the circulation of groundwater from the deep aquifer. The springs of Kirdimi discharge along these same directions. Natural ponds are resulting from the natural discharge of springs (Aïn Galaka, Bedo), or from the inability to control the flow from artesian boreholes. North of Faya-Largeau, the oases of Bedo formed around a sebkha where Trona

($NaHCO_3.Na_2CO_3.2H_2O$) and Gaylussite ($Na_2Ca(CO_3)_2.5H_2O$) are found in significant quantities and are currently being exploited.

4.4.3.2. Litho-hydrostratigraphic units

Groundwater occurrences found in relationship to the Upper Cretaceous (Chieun and Tekro) formations are few and represent the most northern points observed in the field (Figure 4.9). Lower and Upper Cretaceous (Ounianga, Chieun and Tekro formations) are composed of a fine to coarse sandstone, showing quartzitic re-cristallisation, and intercalation of more silty layers.

Several important discharge points (Gouro, Ounianga Kebir, Motoro and Ounianga Serir) are found within the Jurassic-Lower Cretaceous formation, forming a platform. Let us also note the salt pans of Demi and Tiguidei, East of Ounianga Serir (not inspected). In Gouro, springs and a water table close to the surface are observed. In Ounianga Kebir and Serir, the water table intersects the topography.

The Soeka red argillite and Lakes formations white fine quartzwacke form a relatively low conductive strata between the Ounianga formation, overlying, and the Permo-Trias formation, underlying. Springs and a shallow groundwater are found at the foothill of the Permo-Trias escarpment, between Madadi and Hardjalla. In Tergeshi, the water table is close to the surface. In Madadi, the spring discharges at ground level.

Wadi Doum is the only example of groundwater occurrence located in the mid-section of the Carboniferous sequence (intercalations of fine sandstone, marls and micritic limestone of low hydraulic conductivity). In this location, the water table is close to the surface. Wadi Doum lies in a topographical low of comparable elevations as Ounianga Serir. Also, west of wadi Doum, important structural discontinuities are observed (see also Chapters 2 and 3).

Examples of water points associated to the Upper Devonian formation are Oye Yeska and more southeasterly Mouso, Bir Koraa, Onoua and wadi Widei. Onoua and wadi Widei are natural ponds, the latter being highly saline. This region corresponds to the western Ennedi, where the mountainous topography changes into a lowland.

Within the South Tibesti sub-basin (Yarda-Kouroudi, Bedo, West Palm Groves and Faya-Largeau), groundwater occurrences are associated to the Lower Devonian sandstone.

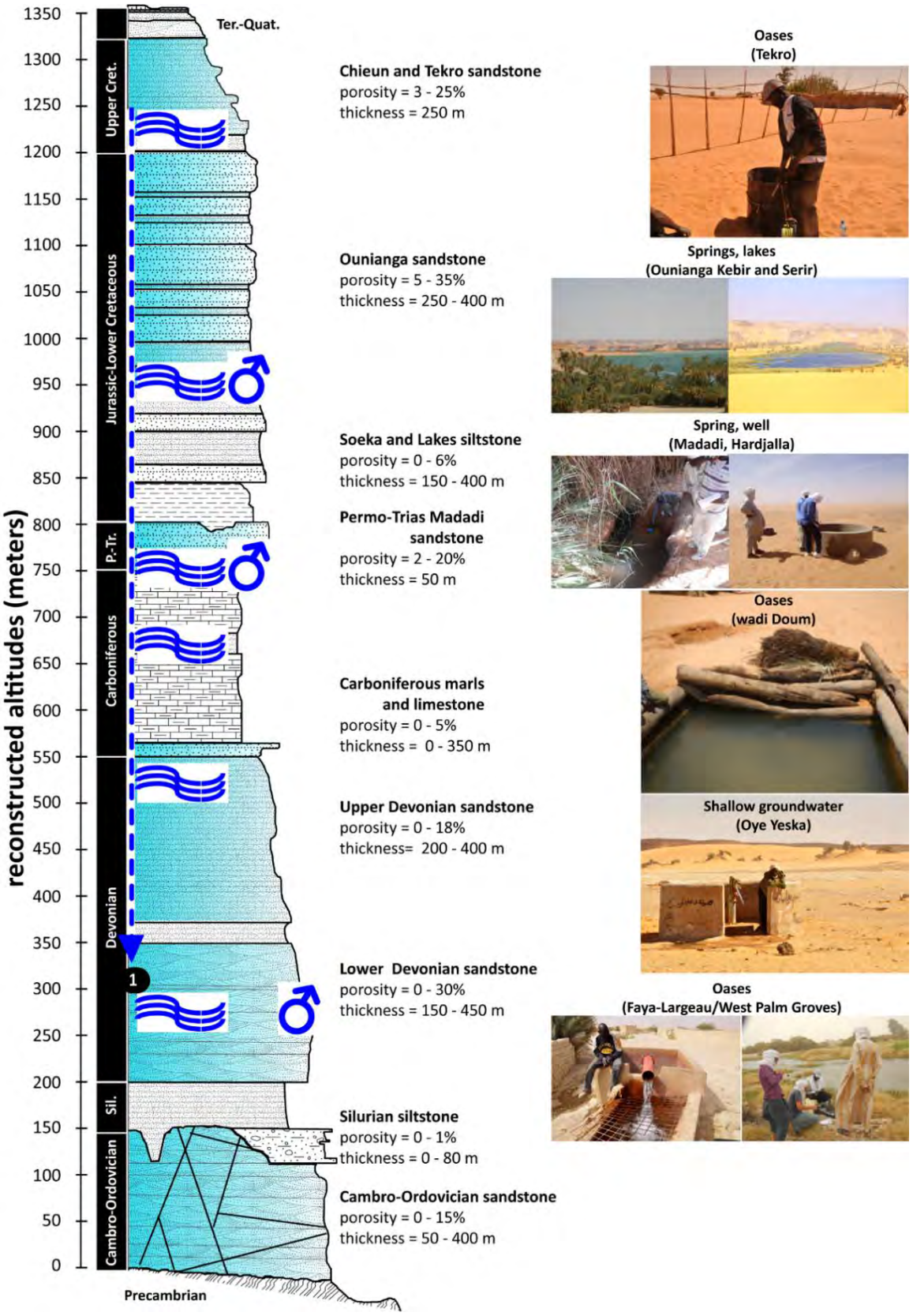

Figure 4.9: Synthetic litho-stratigraphic log indicating the ranges of thicknesses and intergranular porosities of the different geological formations. The observation of groundwater occurrences (oases of Faya-Largeau and West Palm Groves, shallow groundwater in Oye Yeska, oases of wadi Doum, spring and well in Madadi and Hardjalla, springs and lakes in Ounianga Kebir and Serir, oases of Tekro) are documented with photos and their approximate locations are indicated on the litho-stratigraphic log (circle with arrow: spring, waves: oases, shallow water table). Arrow 1 indicates the possible connection between aquifer's layers.

4.4.3.3. Groundwater flow patterns

The hydraulic heads in cross-section B (Figure 4.10) show that the flow originates in the Tibesti and Ennedi Mountains and converges at the emplacement of the Ounianga lakes, located in a topographic low. From the Tibesti Mountains, hydraulic heads decrease from 610 masl in Bini Herdé to 434 masl in Gouro. From the Ennedi Mountains, hydraulic heads decrease from: (1) 603 masl in Mourdi Djouna, (2) 495 masl in wadi Tebi, (3) 461 masl in Tergueshi, (4) 445 masl in Gaour, and (5) 409 masl in Madadi. In Ounianga Kebir, hydraulic heads are 400 masl and 345 masl in Ounianga Serir. Mean hydraulic gradients are 1‰. The position of the diatomite deposits shows that discharge was occurring via intermediate collecting zones, generally located at the foothill of the mountain chains (WNW of Gouro, Mourdi depression).

Cross-sections 3 and 4 show a general groundwater flow directed towards the SSW, with a mean hydraulic gradient of 0.5-1‰. The deposits of diatomites at higher elevations than the current discharge zones (cross-section 4), is indicating the past important inflow of surface and groundwater from the Tibesti Mountains.

In the central depressional zone marked by the Borkou-Kufra Trough (cross-section 3), hydraulic heads decrease in a SW direction from (1) 461 masl in Tekro, (2) 345 to 400 masl in Ounianga, (3) 374 masl in wadi Doum, (4) to 365 masl in Mouso. Closer to the Tibesti Mountains (cross-section 4), hydraulic heads decrease in a SSE direction from (1) 434 masl in Gouro, (2) 333 in Kouroudi, (3) 230 masl in the West Palm Groves. Hydraulic heads in Faya-Largeau are 217 masl. A small number of samples have also been collected in the Lake Chad geological basin (Kouba Olanga, Erg Djourab). Water table elevations vary from 254 masl in Yegeski and 198 masl at Djourab puits 110, to 241 masl in Kouba Olanga.

The blue arrow in Figure 4.9 is indicating the groundwater flowing towards the SW from Tekro (Chieun and Tekro formations) to Faya-Largeau (Lower Devonian).

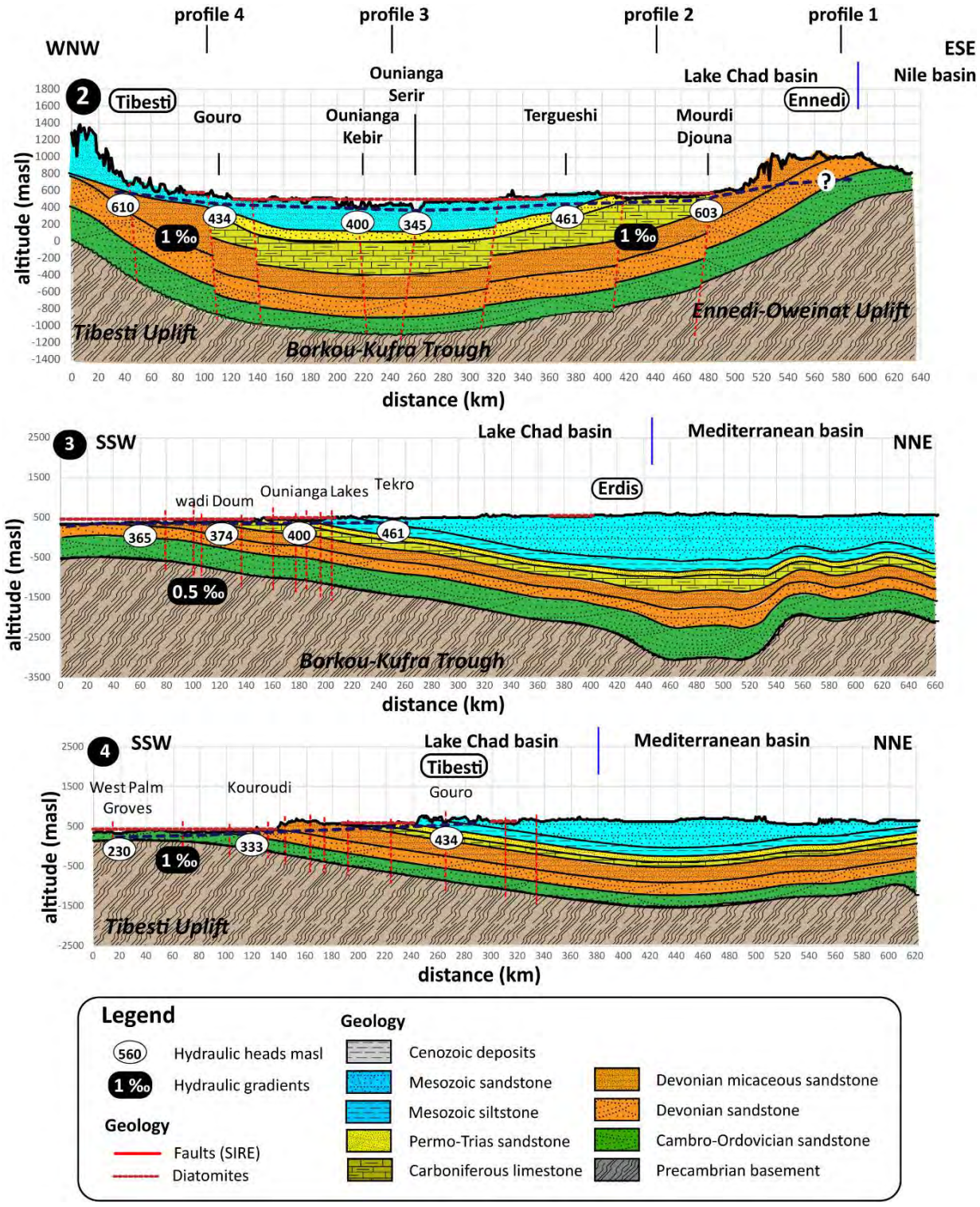

Figure 4.10: Geological cross-sections WNW-ESE (profile B) and SSW-NNE (profiles 3 and 4, the position of the cross-section is shown in Figure 4.6). Hydraulic heads and gradients are derived based on our measurements. Geological information are from the SIRE database (faults, geological formations, diatomite). Faults are assumed to traverse all the geological formations up to the basement elevation Geological data in Libya and Sudan and location of diatomite deposits are from Pachur and Altmann (2006). Topography was extracted from SRTM and the basement elevation is from Mahamoud (1986).

4.5. Discussion

4.5.1. Hydraulic heads distribution: modern and paleorecharge

The observed hydraulic heads and gradients are in general agreement with the conceptual flow model of Ball (1927) and Sandford (1935). All the previous hydrogeological models (e.g. Heinl and Brinkmann, 1989; Gossel et al., 2004; Voss and Soliman, 2014) were based on these measurements. The current study confirms the groundwater flow patterns as described by previous authors, and provides a denser coverage of up-to-date data.

Higher hydraulic heads and gradients (3-4‰ in the Ennedi and 4-6‰ in the Tibesti), indicate a zone of recharge within the Mountains of the Ennedi and Tibesti. Groundwater flows in a WNW direction from the Ennedi Mountains and in a SE and SSE direction from the Tibesti Mountains, towards the main discharge zones in Northern Chad (oases of Ounianga Kebir, Ounianga Serir and Faya-Largeau). The discharge zones are located along a SSW-NNE central depressional zone, identified as the Borkou-Kufra Trough (Williams, 1966, or the Pelusium mega shear zone, Mohamed et al. 2017). Mohamed et al. (2017) identifies this zone as characterized by increased fracturing and therefore higher hydraulic conductivities (and connectivity between aquifers). This seems to be confirmed by our field measurements, indicating lower hydraulic gradients (0.5 ‰) between Tekro and Faya-Largeau.

The hydraulic heads measured by Ball (1927) and Sandford (1935) in the SSW-NNE depressional zone between Faya-Largeau (Chad) and Kufra (Libya), indicate a groundwater flow towards the SW in Chad and towards the NW in Libya, paralleling the topography (see Figure 1.1). Within the investigated water points, the lowest hydraulic heads are found in Faya-Largeau (217 masl) and more southerly in the Djourab puits 110 (198 masl).

The exact location of the groundwater divide is unknown. The zone is broadly defined as following the ridges which separate the Lake Chad and Mediterranean hydrological basins. This region do not currently experience modern recharge (see remote sensing analysis in Chapter 5), but has potentially experienced large amounts of recharge in the past pluvial Pleistocene and Holocene, as attested by the presence of lacustrine deposits.

Therefore, the groundwater flow observed by previous authors and confirmed by our fieldwork is potentially indicating the zones of recharge during the previous pluvial periods. The aquifer's properties and the large vertical and horizontal extension insure a transient time of several thousand years (Vasseur et al., 2015), maintaining higher hydraulic heads despite the absence of current recharge over most of the region.

4.5.2. Influence of modern recharge

The influence of recharge occurring in the Ennedi and Tibesti Mountains is likely to be important for the Northern Chad extent of the NSAS. However, it is more challenging to assess whether this recharge plays a role for the entire aquifer system, as suggested by Vasseur et al. (2015).

In Northern Chad, the aquifer system is characterized by several productive (Cambro-Ordovician, Devonian, Permo-Trias and Cretaceous) and less productive layers (Silurian, Carboniferous and Jurassic-Lower Cretaceous). Discharge points are generally located: (1) at a topographic break, (2) in correspondence to sandstone layers showing high intergranular porosities but in proximity of an underlying, less permeable layer and (3) associated to structural discontinuities, faults and fractures, which increases the hydraulic conductivity and connectivity between aquifers. The groundwater flow patterns, although based on relatively few points of observation (2 water points every 1,000 km^2), are showing that the hydraulic heads parallel the topography. The measured hydraulic heads are showing a groundwater flow restricted to the Chad sector of the NSAS, flowing towards the SW.

However, Vasseur et al. (2015) affirmed that modern recharge occurring in the unconfined sector of the NSAS (defined by these authors as the zone south of the Post-Nubian limit, 25°N) plays a major role in maintaining higher hydraulic heads and gradients. They indicate that without the unconfined and recharged sector, oases would already have disappeared. Similar conclusions were also presented by Ahmad (1983) and more recently by Mohamed et al. (2017). Mohamed et al. (2017) concluded that the unconfined and more elevated regions of the southern Kufra basin is supplying the northern Kufra basin. As such, these authors describe the groundwater flow patterns in a similar manner as hypothesized by the early researchers (the *allochtonous theory*, Chapter 1, Sandford, 1935; Hellström, 1940), according to which the southern borders of the NSAS, recharged and more elevated, are supplying the lower-lying areas of Libya and Egypt, where most of the oases are found.

For recharge occurring in the Ennedi Mountains to reach the northern Kufra basin to the NE, part of the groundwater should be confined under the Carboniferous marls and limestone (see Figure 4.7 cross-sections 1 and 2). Pallas (1980) recognizes that the low conductive Carboniferous formation (see Chapter 3) could act as a confining layer and effectively separate the aquifer seated in the Paleozoic formations (recharged in the Ennedi Mountains), from the unconfined aquifer seated in the Mesozoic formations (resulting from past recharge).

The confinement of the aquifer under the Carboniferous formation (north of the Mourdi depression, north of 18°N) could eventually explain how recharge occurring in the Ennedi Mountains can influence the entire groundwater system of the NSAS. At the same time, a groundwater flow towards the north through the confined aquifer could eventually also contribute to the supply of the Lakes of Ounianga.

However, all previous researchers (e.g. Sandford, 1935; Hellström, 1940; Vasseur et al. 2015) have described the NSAS as an unconfined aquifer south of 25°N (Figure 1.1).

4.6. Concluding remarks

This chapter concludes the first part of this thesis, which aim was to describe the geological and sedimentological character of the Kufra basin in Northern Chad and the relationship between geology, topography and groundwater. This chapter enabled to present the hydrological and hydrogeological systems of the Tibesti Mountains and of the Nubian Sandstone Aquifer System of Northern Chad, which will be referred to in the following chapters.

The regional groundwater flow patterns determined from our measurements in the field are in agreement with the hydraulic heads measured by previous authors. As indicated by the conceptual model presented by Ball (1927) and Sandford (1935), groundwater flows towards the SW in Chad and towards the NE in Libya. The groundwater divide is hypothetically located in a zone where no modern recharge is currently occurring (see Chapter 5 and 6). As presented by Vasseur et al. (2015), the NSAS is in a transient state since the installment of the arid and hyper-arid climate, and as such the observed hydraulic heads and gradients are the result of previous recharge. Protracted humid periods occurred in the Sahara from 14,000 to 8,000 yrs. BP and from 7,000 to 4,000 yrs. BP. The region has since then experienced increased arid conditions, with significant climatic fluctuations at a decadal scale (Edmunds et al., 1999).

The study of the hydraulic heads distribution in the NSAS enabled additionally to discuss the role of the Carboniferous formation on the groundwater flow system. If the Carboniferous formation confines the aquifer more southerly than what indicated by previous authors (e.g. Vasseur et al., 2015), modern recharge occurring in the Ennedi Mountains (Paleozoic formations) could eventually be seen as an important component of the groundwater system for the entire Kufra basin. The regional groundwater flow could also be contributing to the supply of the lakes of Ounianga. Otherwise, the lakes of Ounianga are supplied by the unconfined aquifer seated in the Mesozoic formations.

Chapter 5 investigates the geographical and temporal patterns of precipitation and the resulting hydrological response (runoff and accumulation) with RFE2.0. Chapter 6 investigates the groundwater dynamics in the main discharge zones and in temporarily flooded areas with spatially distributed evapotranspiration maps extracted from LandSat8OLI images.

Chapter 5

Rainfall and surface water dynamics

5.1. Introduction and outline of the chapter

5.1.1. Introduction and aim

For a sustainable water resources management, it is fundamental to characterize the spatial and temporal dynamics of recharge, particularly in arid environments. The Chad Water Authority recognized the need to better characterize the mechanisms, dynamics and rates of modern recharge occurring in the Ennedi Mountains as to be one of the main concerns. In the framework of the JASAD activity, pilot projects have been formulated, but so far, never implemented.

Only very few meteorological and hydrological data for the remote region of Northern Chad are available. Hydrological investigations were lastly conducted in the Tibesti Mountains between 1960's and 1980' by the *"Geographisches Institutes der Freien Universität Berlin"* and in the Ennedi Mountains between 1957 and 1959 by the *"Office de la Recherche Scientifique et Technique d'Outre-Mer"*.

To understand the dynamics of precipitation and runoff in arid climates, an approach capable of adequately quantifying the distribution of precipitation over large areas and to analyze its variability over several years, has to be elaborated. A precondition for such an endeavor is to achieve high spatial and temporal resolution. This is a challenging task, given the little ground-truth of meteorological data available.

This chapter investigates the basis for "potential recharge" occurring within the two mountainous areas of Northern Chad, the Ennedi and Tibesti Mountains, focusing on the temporal and spatial distribution of rainfall and the resulting hydrological response (= flooded surface). The analysis is performed by using the African Rainfall Estimation Algorithm Version 2 (RFE 2.0) and LandSat8OLI images.

The specific questions investigated in this chapter are: (1) what are spatial and temporal dynamics of precipitation?, (2) what are the spatial and temporal dynamics of "potential recharge"? and (3) what are the main processes of surface water redistribution in the Ennedi Mountains?

5.1.2. Content of the chapter

The chapter is structured as follows. Section 5.2 presents a brief synthesis of the meteorological dynamics and the available meteorological and hydrological data for Northern Chad. The methodology describing the remote sensing data used in this study and the processing procedures is described in section 5.3.

The results are presented in two parts. The first part (section 5.4.1) analyzes the patterns of precipitation at a monthly basis (mean monthly rainfall rates, years 2013-2016). Precipitation dynamics are based on the RFE 2.0 product, extracted for the locations of permanent water points inspected in the field (see Chapter 4). The proximal locations and/or the locations situated in the same catchment and representing similar climatic characteristics are grouped. The rainfall patterns are presented by regions: (1) the mountainous Tibesti, (2) the Ennedi Mountains, (3) the central lowlands. As stated in Chapter 4, the Tibesti Mountains were only marginally investigated. The hydrochemical and stable isotopic signatures of groundwater in this mountainous region (see Chapter 7) are however interesting as they provide clues for the interpretation of the groundwater signatures in the NSAS. Precipitation rates and distribution in the Tibesti Mountains are therefore analyzed in this chapter as they will be used for the analysis of hydrochemical and stable isotopic signature distribution in Chapter 7.

In the second part (section 5.4.2), precipitation (RFE 2.0) and surface water index (MNDWI36 based on LandSat8OLI data) are compared on a monthly basis from January 2013 to December 2016. The objective of this comparison is to establish the different hydrological responses as a function of yearly precipitation. To perform this comparison, RFE 2.0 rasters were resampled to the resolution and extent of the LandSat8OLI scenes and calculations (mean and maximum rainfall rates) are undertaken on the entire image. The results are therefore presented by LandSat8 scene (the spatial coverage of LandSat8OLI scenes are shown in Figure 5.4). Only the extent of the NSAS (not the mountainous Tibesti) is covered by this analysis. The dynamics are presented first on a regional and annual scale, followed by a section describing in more detail the zones interested by surface water accumulation following rainfall.

The chapter concludes with a synthesis of the geographical and temporal distribution of the zones experiencing such dynamics (section 5.5).

5.2. Climatic and hydrological context

5.2.1. Characteristics of the studied area

In Northern Chad, precipitation is highly variable, both in time and space. Annual rainfall varies significantly from year to year and most of the annual precipitation occurs during a very short period of the year (2-3 months).

The most prominent meteoric dynamics, in terms of amounts and geographical coverage, are the West African "monsoons". The monsoons follow the seasonal latitudinal migration of the Intertropical Convergence Zone (ITCZ). In summer (July/August), monsoon winds, originating in the region of the Guinean Gulf, are driven inland along an atmospheric pressure gradient resulting from the differential land-ocean heating (Gasse, 2000). Annual rainfall is proportional to the number of months during which an area receives the moist monsoon flow, so that land becomes progressively drier northward towards the Sahara (Gasse, 2000). In addition to the rainy season in the summer, the Sudano-Saharian depressions interest the region during the month of May (Mainguet, 1968), and the Mediterranean depressions, originating north of the Sahara, during the winter months (January) when the ITCZ is displaced equatorward (Nicholson and Flohn, 1980).

5.2.2. Historical meteorological data

For the region of Northern Chad, the available historical data are from 8 meteorological stations (Table 5.1). Bardaï, Zouar and Trou au Natron are located in the mountainous Tibesti, Fada in the southern slopes of the Ennedi Mountains, and Koro Toro, Faya-Largeau, Ounianga Kebir and Kufra (Libya), in the central lowlands. Climatic data are compiled from ORSTOM (1973), Heckendorff (1978), Geomorphological Laboratorium (FU Berlin) included in Pachur and Altmann (2007), Mahamoud (1986), Beauvilain (1995), MEH (2014). They represent monthly data, mostly of rainfall rates. In some instances, monthly temperatures (Tibesti Mountains and Faya-Largeau), humidity, wind speed and evapotranspiration rates are also reported (Faya-Largeau, 13 years of observation, BRGM, 1991).

Table 5.1: Meteorological stations of Northern Chad: geographical coordinates and altitude, type, timeframe of complete years of measurement recordings, average rainfall rates, minimum and maximum rates and years of occurrence (5, 7 and 17 times meaning minimum rainfall rates of 0 mm were recorded for 7, 5 and 17 years).

Meteorological station	Longitude	Latitude	Altitude	Type	Start -End measurement	Complete year of record	Average rainfall (mm)	Minimum rainfall		Maximum rainfall	
								rate (mm)	year	rate (mm)	year
Bardaï	16.921	21.506	1018	Pluviometer	1957 - 1972	13	8 - 10	0	1972	61	1966
Zouar	16.205	20.506	775	Pluviometer	1944 - 1969	14	44 - 49	0	1969	136	1958
Trou au Natron	16.600	20.967	2450	Pluviometer	1965 - 1969	5	93	9	1967	190	1966
Fada	21.556	17.171	540	Synoptic station	1934 - 1965	28	98	12	1941	192	1954
Koro Toro	18.288	16.038	270	Pluviometer	1945/1952 - 1965	12	46	0	1953	118	1957
Faya-Largeau	19.122	17.922	233	Synoptic station	1933 - 1994	49	15	0	7 times	103	1936
Ounianga Kebir	21.506	19.005	401	Pluviometer	1953 - 1965	12	3	0	5 times	21	1953
Kufra	23.333	24.200	389	Pluviometer	1933 - 1974	34	2	0	17 times	13	1952

Rainfall rates decrease from South (16°N, Koro Toro) to North (24°N, Kufra), spanning from 40-50 mmy^{-1} in Koro Toro, 10-20 mmy^{-1} in Faya-Largeau, < 5 mmy^{-1} in Ounianga Kebir and about 2 mmy^{-1} in Kufra (Table 5.1). The Tibesti and Ennedi Mountains receive increased precipitations, with a mean annual rainfall of 90 mmy^{-1} in Trou au Natron (2,450 masl, Tibesti Mountains) and 100 mmy^{-1} in Fada. In these mountainous regions, precipitation rates are also markedly higher within the southern slopes

than within the northern slopes (Roche, 1958). For example, Bardaï, located in the northern slopes of the Tibesti Mountains receive 10 mmy^{-1} compared to 40-50 mmy^{-1} received in Zouar (southern slopes).

5.2.3. Conditions for recharge and wadi flow

In Northern Chad, most of the annual precipitation occurs between mid July and mid September, during 3 (Faya-Largeau) to 10 (Fada) high-intensity storms (Schneider, 1989). Precipitation rates might therefore exceed evaporation rates during a short period of the year and recharge could occur. Low-intensity rainfall occurring in an arid and hyper-arid climate, will most likely be entirely lost by evaporation. Therefore, recharge is mostly resulting from the high-intensity rainfall events. In the Ennedi Mountains, intensities of individual storms were estimated by Roche in 1958 to be between 9 and 54 mmh^{-1} for precipitation events of more than 20 mm (4 events).

During these events, precipitation rates can exceed the infiltration capacity of the soil, provoking runoff and flash-floods. Large volumes of surface water might be transported and concentrated as far as several hundred kilometers from the zone of origin, and it is expected that concentrated recharge will occur along the inundated branches. Rodier and Roche (1978) observed over a nine year period in the Tibesti Mountains, the occurrence of seven floods along the enneri Zoumri-Bardangué (mean annual precipitation 15-20 mmy^{-1}). In 1954, discharge reached 425 m^3s^{-1}. In 1963, three flood events occurred subsequently, with flood flows between 4 and 32 m^3s^{-1}. Roche (1958) observed 17 floods in the Ennedi Mountains during the 1958 rainy season, with flows varying between 19 and 325 m^3s^{-1}. He estimated the specific flow for a ten-year frequency flood event at 8 to 10 $m^3\ s^{-1}km^{-2}$ for hydrological basins of 10 to 25 km^2 surface.

5.3. Data processing and analysis

5.3.1. Precipitation data

A range of satellite products of rainfall estimates are available for the African continent (TRMM 3B42, CMORPH, TAMSAT, RFE 2.0, PERSIANN, ARC 2.0, CHIRPS, TARCAT). We selected the African Rainfall Estimation Algorithm Version 2 (RFE 2.0) because it covers the entire region in one raster map and does not have any data gaps. RFE 2.0 has been operational since 2001, replacing the previous algorithm (RFE 1.0). Improved accuracy, increased speed and convenient portability makes RFE 2.0 a better method than RFE 1.0 to estimate daily precipitation over Africa (NOAA, 2001). RFE 2.0 uses four types of input data, including three satellite sources, to create the final rainfall estimates.

In arid climates, a certain number of effects might lower the accuracy of satellite rainfall estimates. For example, Dinku et al. (2011) analyzed the reliability of rainfall estimates from different satellite products, and concluded that, in dry regions, underestimations of rainfall rates might occur over mountainous areas (orographic effect) and overestimations of rates might occur over flat desert lands.

Higher accuracy of estimations are expected for medium and high-intensity rainfalls than for low-intensity precipitations, but Hermance and Sulieman (2014) observed, for several high-intensity storms, an underestimation of a factor of two in the sahelian Sudan. Additionally, the reliability of rainfall estimates from satellite products are seen to increase for longer time steps (Dembélé and Zwart, 2016), daily estimates being often less accurate. Given these constraints, the analysis of rainfall estimates from RFE 2.0 was performed using monthly data.

RFE 2.0 were acquired by downloading spatially distributed rainfall data from the FAO's FEWS-NET portal (https://www.fews.net). The raster data (10 km resolution) represent monthly rainfall estimates from January 2013 to December 2016. Image processing was performed in RStudio v. 1.1.463 (Team, 2015) and cartographic manipulations were performed in ArcGIS (ArcMap 10.5).

The coordinate system of the rasters were first projected to the local coordinate system (UTM 34N) and monthly mean and annual precipitation estimates were prepared. Rates were extracted for all the localities inspected in the field (see Chapter 4). The graphs (section 5.4.1) are presented with different colors for the different regions: (1) Tibesti Mountains (in blue); (2) Ennedi Mountains (in orange); (3) central lowlands (in green if included within the extent of the NSAS, in yellow if included outside the extent of the NSAS). The analysis by locality was performed because the precipitation data are later used to interpret the stable isotopic and hydrochemical signatures of water samples collected at these same localities (Chapter 7).

To compare the precipitation rates and the subsequent hydrological response, rasters were resampled to the resolution of LandSat8 images (12 scenes for a total of 576 resampled precipitation images). Mean, maximum, standard deviation and sum were calculated for the entire image. This analysis is presented in the second part of the results section.

Absolute rates and patterns were compared to historical data (see section 5.2.2). For example, a mean annual rainfall of 98 mm (28 years of observation) for Fada, 21 mm for Faya-Largeau (28 years) and 3 mm for Ounianga Kebir (12 years) have been reported (ORSTOM, 1973). In the Tibesti, a mean annual rainfall of 42-45 mm in Zouar, 93 mm in Trou au Natron and 7-10 mm in Bardaï, are estimated from historical observations (ORSTOM, 1973; Heckendorff, 1978; Pachur and Altmann, 2007). Mean annual rainfall amounts extracted from RFE 2.0 are 89 mm in Fada, 18 mm in Faya-Largeau and 106 mm in Trou au Natron, which compared to historical data correspond to a difference of 9-14%. The rates of Ounianga Kebir, Zouar and Bardaï are significantly different (18 mmy^{-1}, 63 – 72 mmy^{-1} and 38 mmy^{-1}, respectively). Note, however, that historical data corresponds to observations carried out between 1940 and 1970. The climatic setting could have therefore evolved since this monitoring period.

5.3.2. Surface water dynamics

5.3.2.1. Choice of LandSat8OLI: time and area covered by the analysis

In desert regions such as Northern Chad, surface water features (wadis, ponds, lakes) are generally restricted to narrow areas (< 1,000 m). Therefore, satellites with higher spatial resolutions are required to monitor surface water occurrences and dynamics. LandSat8OLI mission (30 m resolution for the OLI bands, OLI = Operational Land Imager) was launched in 2013 and is currently still acquiring images, consequently, the evaluation focused on the years 2013-2016. Images of a selected scene are acquired every 16 days. The surface covered by a scene is approximately 185 km x 180 km. A total of 448 images from 12 scenes were downloaded from the website https://glovis.usgs.gov/, to cover the entire region and timeframe of the investigation. The images were selected in order to cover all months during which more than 5 mm of precipitation have occurred (evaluated from RFE 2.0 data).

5.3.2.2. Processing of LandSat8 images for surface water determination

Processing of LandSat8 images was performed in RStudio v. 1.1.463 (Team, 2015). Some specific steps (extracting surface slope angle and solar zenith angle for preprocessing) were performed in ArcGIS (ArcMap 10.5).

The 448 images were first preprocessed in order to mask any cloud occurrence, to suppress the influence of topography and to convert OLI digital numbers to at-sensor radiance and reflectance values. Cloud masking was performed by using the quality assessment file indicating the probability of clouds (BQA file, Scaramuzza et al., 2012) provided with the LandSat8 images. A topographic correction was performed by calculating the solar illumination angle and applying a threshold of the lower 1% quantile. Conversion from digital numbers to at-sensor radiance and reflectance values was performed following the procedure described in USGS (2015). Uncertainties are estimated at 3% reflectance and 5% radiance (Czapla-Myers et al., 2013; Markham et al., 2013) for the OLI bands.

Finally, the Modified Normalized Water Index 3-6 (MNDWI36) of (Xu, 2006) was calculated for the whole set of images. In the second part of the results (section 5.4.2), the hydrological dynamics detected from the MNDWI36 index are presented qualitatively and quantitatively. A positive MNDWI36 (> 0) is taken as corresponding to one unit of 30 m x 30 m surface water (pixel resolution of LandSat8). As LandSat8 images are provided every 16 days, but a considerable number of images had to be discarded because not fulfilling the quality requirements, the MNDWI36 corresponding for the given month is the calculated surface water for one image, or the mean between 2 images.

5.3.2.2.1. Topographic normalization or correction

The effect of sun incidence over a terrain relief can significantly affect the radiometric properties of remotely sensed data, leading to an over-estimation of surface water occurrence.

A certain number of topographic normalization or correction procedures were tested (cosine correction, Minnaert and C corrections, SCS correction, C + SCS correction and PSSR correction (Smith et al., 1980; Justice et al., 1981; Teillet et al., 1982; Gu and Gillespie, 1998; Soenen et al., 2005; Flood et al., 2013). A straightforward suppression of the "shadowed-pixels" was finally chosen because of its simple implementation.

First the solar illumination surface, defined as the cosine of the incident angle *i*, *cos(i)*, is calculated:

$$\cos(i) = cos\theta_0 cos\theta_n + sin\theta_0 sin\theta_n \cos(\varphi_0 - \varphi_n) \quad (5.1)$$

where θ_0, θ_n, φ_0, φ_n denote the surface slope angle, the solar zenith angle, the solar azimuth angle and the surface aspect angle, respectively.

The annual distribution of the illumination surrface shows a shift towards higher values during the summer months and towards lower values during the winter season. The threshold of the illumination surface to be applied in order to correctly distinguish shadowed from non-shadowed surfaces, is seen to vary between 0.60 in March, 0.73 from June to August and 0.70 in October, corresponding to the lower 1% quantile of the illumination surface. It was therefore applied as seen to satisfactorily discriminate between shadowed and non-shadowed surfaces.

However, for two scenes covering the eastern and north-eastern Tibesti Mountains (path/row 183045 and 183046), a distorted radiometric signature was detected even after applying the correction above-mentioned. These two scenes were therefore discarded from further analysis.

5.3.2.2.2. Normalized Difference Water Index

The classical NDWI (McFeeters, 1996) and the two modified versions (MNDWI36 and MNDWI37, Xu, 2006) were compared and visually verified for their coherence with the "ground-truth" extent of surface water (comparison of index results and true-color images of inspected locations). For the investigated region, the modified MNDWI36 with a threshold of > 0, was found to be the most sensitive and yet conservative index.

$$MNDWI36 = \frac{r_6 - r_3}{r_6 + r_3} \quad (5.2)$$

Where r_n (n = 3, 6) are the reflectance values of bands 3 and 6.

5.4. Results

5.4.1. Annual rainfall patterns and geographical distribution

5.4.1.1. The Mountainous Tibesti

The precipitation distribution in the Tibesti Mountains is presented for four hydrological sub-basins (see Chapter 4): (1) Tibesti West includes water points located in the alluvial system of enneri Zoaurké, in proximity to the village of Zouar; (2) Tibesti South includes water points located in the alluvial system of the Misky enneri; (3) Zoumri including water points located along the enneri Zoumri (Zoui, Bardaï, Zougoura) and (4) Yebbigué, including water points located along the enneri Yebbigué (Yebbibou, Kilengue, Omou, Aouzou). Tibesti West and South are located on the southern slopes and are part of the Lake Chad hydrological basin, Zoumri and Yebbigué are located on the northern slopes and are part of the Mediterranean hydrological basin (see Chapter 4).

In terms of mean annual rainfall (Figure 5.1), the inspected region receives between 45 (northern slopes) and 60 mmy^{-1} (southern slopes). The southern and northern slopes feature distinct patterns. The southern slopes are characterized by a rainy season spanning from July to September, the month of August being the most humid (30 mm $month^{-1}$). Light precipitation may occur also in March (6 mm $month^{-1}$). The northern slopes are characterized by the marked increase in precipitations during the months of August (22 mm $month^{-1}$). Low amounts of precipitation might also occur from March to May (6 mm $month^{-1}$).

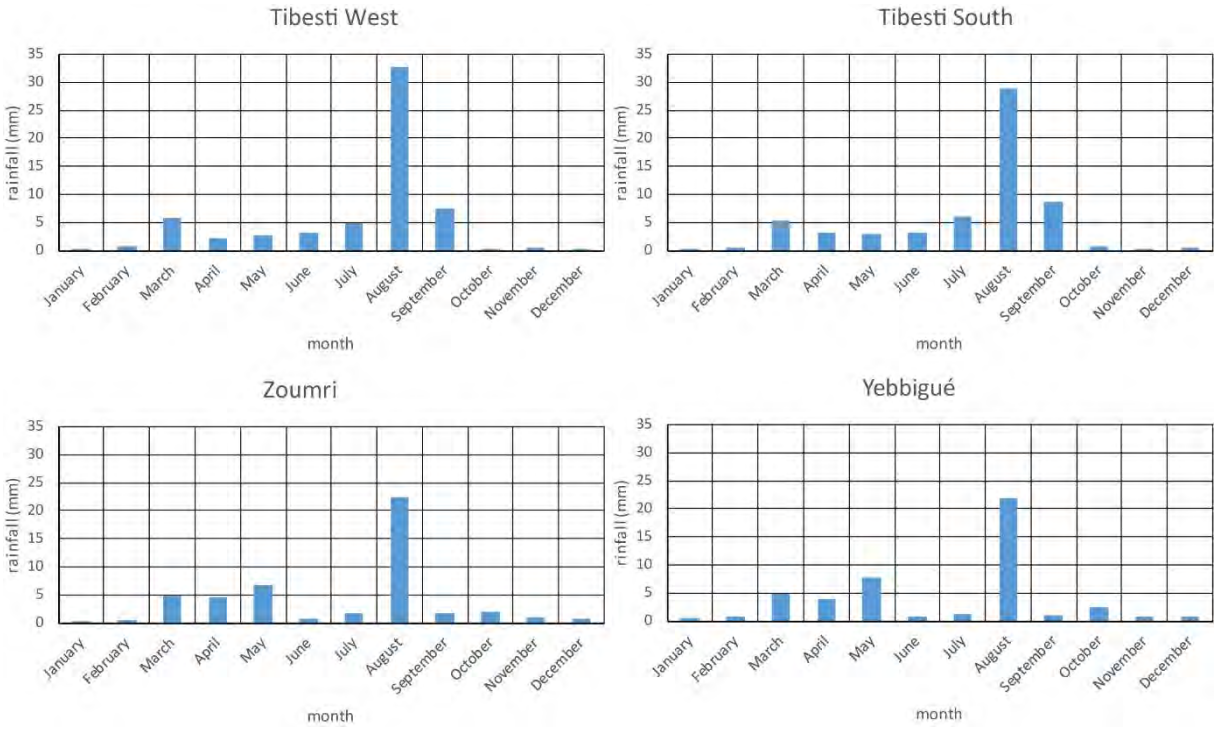

Figure 5.1: Monthly distribution of rainfall (mm, years 2013-2016) in the Tibesti Mountains. The rates are average values determined from RFE 2.0 data, extracted for the localities inspected in the field. They are grouped as to represent the precipitation dynamics of four hydrological sub-basins (Tibesti West, South, Zoumri and Yebbigué).

The distribution shows the predominance of the summer rains for all the localities. Rates are higher for the southern slopes than for the northern slopes. The northern slopes show additionally an increased influence of the winter rains.

5.4.1.2. The Ennedi Mountains

The precipitation distribution in the Ennedi Mountains are presented for six hydrological sub-basins (see Chapter 4): (1) the eastern sector, being part of the Nile hydrological basin (Bao, Oho, Berdoba, Amdjarass); (2) the northern sector, being part of the Mourdi sub-basin (including Eheri, Tangalia, wadi Tebi, Hardjalla, Gaour, Madadi and wadi Doum), (3) the highest altitudes (Maya), and the southern sector, the latter being part of the Mortcha/Djourab sub-basin, additionally subdivided into a (4) a south-eastern zone (Sala upstream, including Itou, Sania, Bachiquele, Weïba, Saki, Archeï, Deli), (5) a south-central zone (Sala midstream including Baki, Bechike, Fada, Kondor and wadi Wei) and (6) a south-western zone (Sala downstream including wadi Widei, Onoua, Mouso).

In terms of mean annual rainfall (Figure 5.2), the southern slopes located centrally (Sala midstream and upstream) and easterly (Nile hydrological basin), including the higher altitudes, receive between 100 and 150 mmy^{-1}, showing a predominance of the summer rains. The rainy season lasts from July to September, the month of August being the wettest (60 – 110 mm $month^{-1}$). The most favorable region is located between Itou and Saki (Sala upstream). The southwestern and northern sectors (Sala downstream and Mourdi sub-basin), have annual mean rainfall between 30 and 40 mmy^{-1}. The rainy season is concentrated during the month of August only (20 – 30 mm $month^{-1}$).

Similarly to the Tibesti Mountains, the southern slopes and the highest altitudes receive enhanced rainfall, compared to the northern slopes. Additionally, the most favorable region is located centrally (Sala upstream), diminishing in amounts towards the east (Nile hydrological basin) and towards the west (Sala midstream and downstream). This region corresponds to the intersection of the NW-SE ridges, separating the Mourdi and the Mortcha/Djourab sub-basins, and the NNE-SSW ridges, separating the Nile and the Lake Chad hydrological basins (see Chapter 4). The region formed by the intersection of these two directions corresponds to the highest altitudes of the Ennedi Mountains. Towards the west (Sala downstream), the mountainous topography gradually changes into a lowland. At the same time, rainfall amounts decrease substantially.

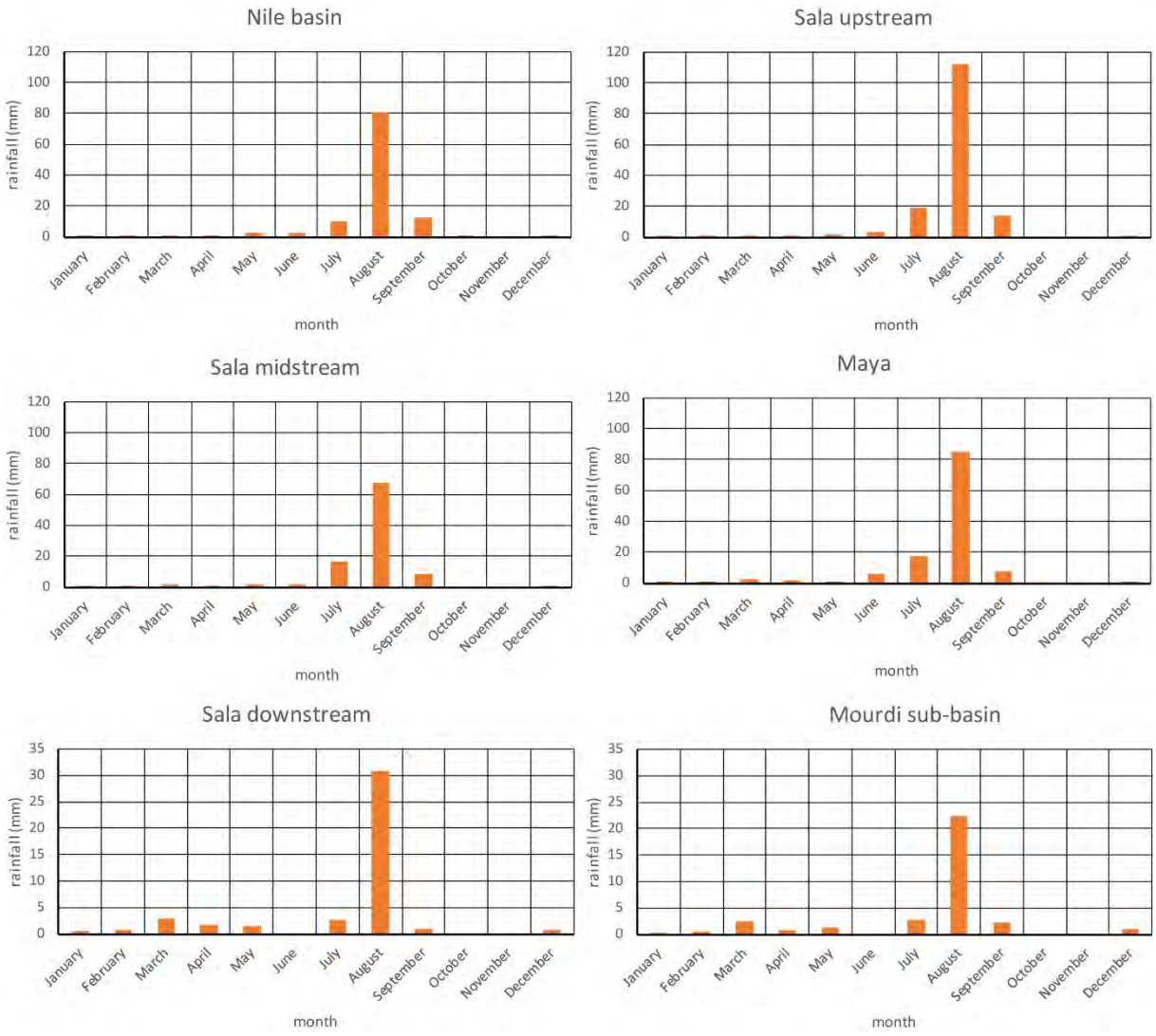

Figure 5.2: Monthly distribution of rainfall (mm, years 2013-2016) in the Ennedi Mountains. The rates are average values determined from RFE 2.0 data, extracted for the localities inspected in the field. They are grouped as to represent the precipitation dynamics of six hydrological basins or sub-basins (Nile basin, Sala upstream, Sala midstream, Mourdi sub-basin). Note the different scales of rainfall rates used for the 4 upper histograms and the 2 lower histograms (Sala downstream and Mourdi sub-basin).

5.4.1.3. The central lowlands

We define the central lowlands as being the region between the eastern foothills of the Tibesti mountains (Bini Herdé, Gouro, Kouroudi, Forom, Yarda), Tekro, the Lakes of Ounianga (Kebir, Serir, Motoro) and Faya-Largeau (Kirdimi, Yen, Ngourma, Djidi, Amoul, Oye Yeska). This region extends southerly into the Lake Chad geological basin (Djourab puits 110, Yegeski, Kouba Olanga). The meteoric dynamics in the central lowlands are presented by groups of localities (see Chapter 4), representing proximal points with similar precipitation rates and yearly distribution: (1) Tibesti South-East (Gouro), (2) Ounianga Kebir (including Ounianga Kebir and Tekro), (3) Ounianga Serir, (4) Tibesti South downstream, including the region comprised between Yarda-Kouroudi (Kouroudi, Forom, Yarda), the West Palm Groves (Kirdimi, Yen, Ngourma) and Faya-Largeau (Djidi, Amoul), (5) Djourab (Djourab puits

110 and Yegeski), corresponding to the region in the Lake Chad basin, adjacent to the limit with the NSAS, and (6) Kouba (Kouba Olanga), located more southerly. The localities inspected in Ounianga Kebir and Serir should theoretically be associated to one group, because of their proximity. Differences in the meteoric patterns were, however, observed and therefore the monthly precipitation distributions are presented as two separate groups.

In terms of mean annual rainfall (Figure 5.3), the Gouro oases receives only 7 mmy^{-1}. This corresponds to the lowest rate observed over the entire region. Rates are generally sensibly higher in the lowlands comprised within the NSAS: 15 mmy^{-1} in Ounianga Kebir and in the southern Tibesti, 35 mmy^{-1} in Ounianga Serir. In the Lake Chad basin, rainfall rates increase from 30 mmy^{-1} (Djourab) to 90 mmy^{-1} (Kouba) in a southerly direction.

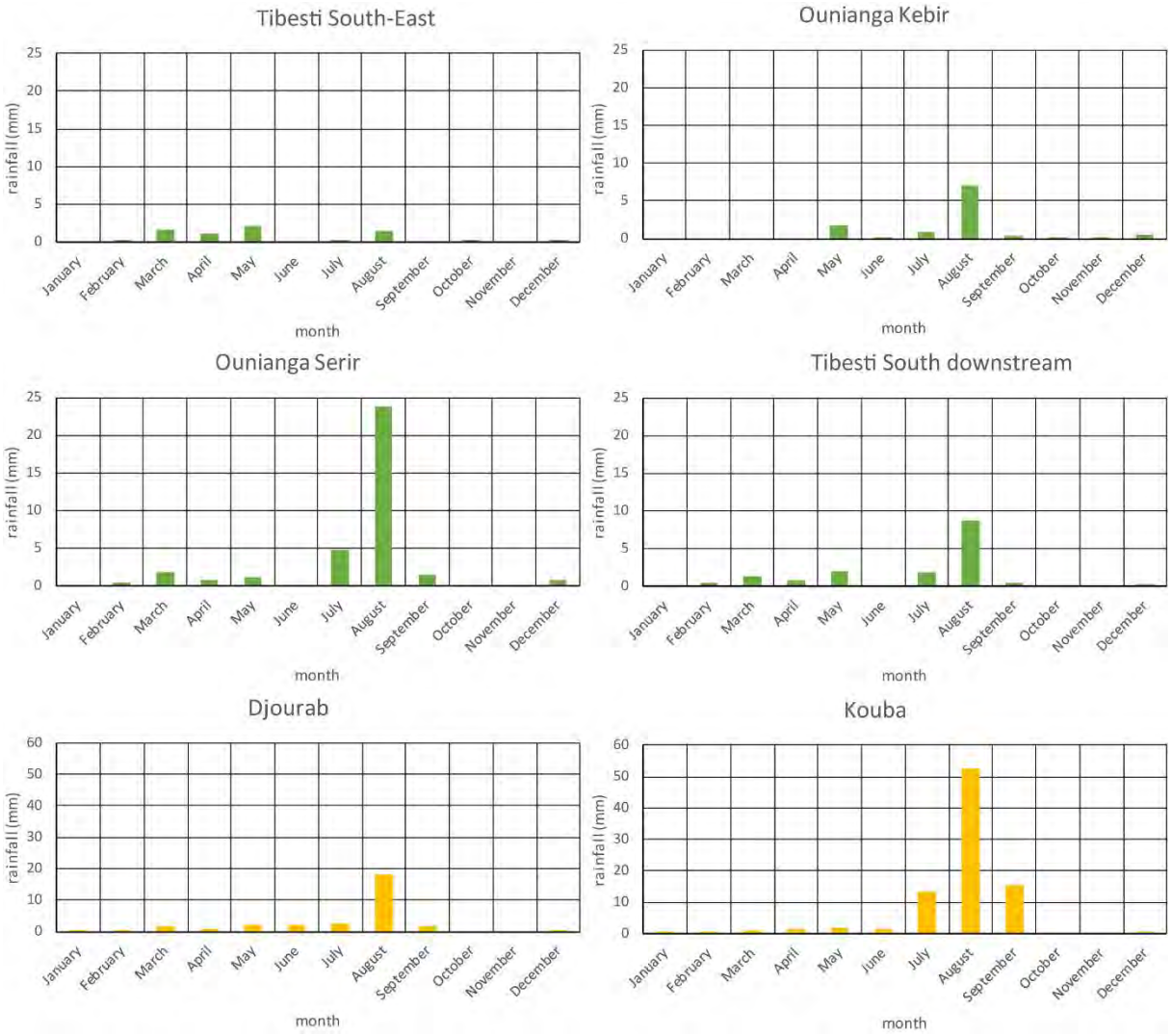

Figure 5.3: Monthly distribution of rainfall (mm, years 2013-2016) in the central lowlands. The rates are average values determined from RFE 2.0 data, extracted for the localities inspected in the field. They are grouped as to represent the precipitation dynamics of six regions (Tibesti South-East, Ounianga Kebir, Ounianga Serir, Tibesti South downstream, Djourab and Kouba). Note the different scales of rainfall rates used for the 4 upper histograms and the 2 lower histograms (Djourab and Kouba).

The month of August is again the wettest, and for most of the region, the only month during which precipitations might be of a slight entity. Rates vary from 8 mm month^{-1} in Ounianga Kebir and in the southern Tibesti region, to 25 mm month^{-1} in Ounianga Serir. In the Lake Chad basin, the increase of rates towards the south is also seen by the longer rainy season (from July to September in Kouba). Rates and distributions of rainfall in Kouba are comparable to those of the Ennedi Mountains.

5.4.1.4. Synthesis of annual rainfall distribution

Table 5.2 synthetizes the cumulated annual rainfall rates for the above-described zones. Mean and standard deviation are calculated for the years 2013 to 2016.

Table 5.2: Cumulated annual rainfall rates (mmy^{-1}). Mean annual and standard deviation are calculated for the years 2013 to 2016 from RFE 2.0 data extracted for the localities described in the text.

Locality	mean	std dev
Tibesti West	60	26
Tibesti South	60	26
Zoumri	47	31
Yebbigué	46	31
Nile basin	111	34
Sala upstream	152	66
Sala midstream	99	38
Sala downstream	42	19
Maya	119	35
Mourdi sub-basin	33	14
Tibesti South-East	7	4
Ounianga Kebir	16	9
Ounianga Serir	35	25
Tibesti South downstream	16	8
Djourab	31	11
Kouba	89	16

Figure 5.4 shows the mean monthly precipitation rates (years 2013-2016) for the months of most significant precipitation (scale in mm month^{-1}).

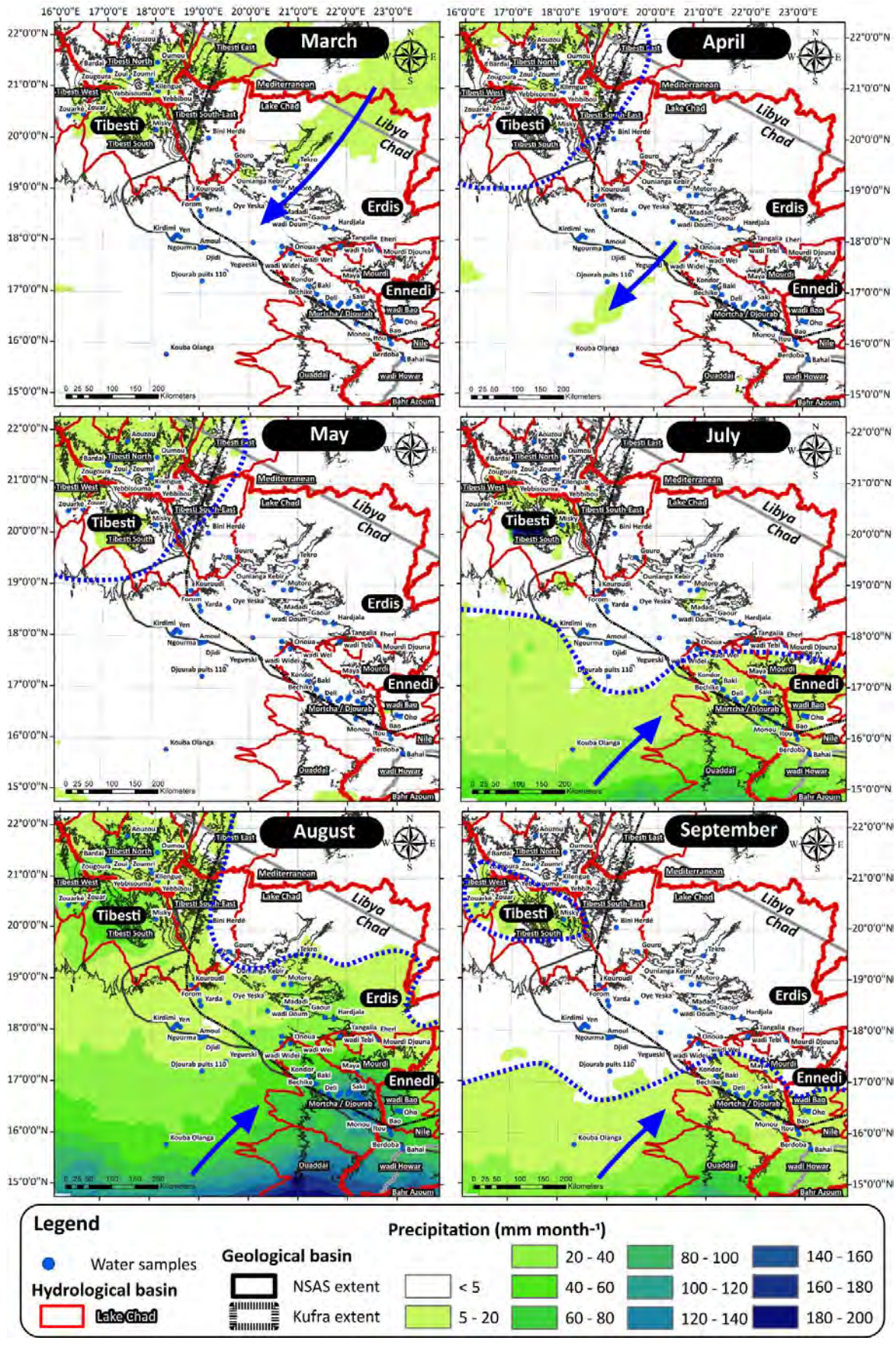

Figure 5.4: Monthly mean precipitation rates (mm month^{-1}) for the months of March, April, May, July, August and September (years 2013-2016). Blue arrows and dashed lines indicate the directions and locations of the precipitation dynamics over the region. Topographic contours (equidistance 500 m) are shown as background.

In March and April, precipitation is originating from the NE, and persists in the Tibesti Mountains during the month of May. From July to September, precipitations are originating from the South-West (monsoons), corresponding to the most important meteoric dynamics in terms of amounts and geographic coverage. The pattern of the monsoonal rains shows that the highest intensities are experienced during the month of August. However, some regions in the lowlands experience only very small amounts of rainfall, as shown by the depression of the meteoric front in the central zone located in between the Ennedi and Tibesti Mountains.

5.4.2. Hydrological dynamics in response to rainfall

5.4.2.1. Identification of surface water areas

The use of the MNDWI36 index allowed detecting surface water occurrences and their extent. This evaluation was based on: 1) previous knowledge on surface water occurrences; 2) inspection of the index results compared to true-color images; 3) verification in the field (2016) of a few localities previously identified from MNDWI36. The field verification identified one large surface water occurrence (Onoua), not reported on previous maps. In other cases, humidity in the ground could still be felt physically while visiting the sites (the image date corresponded to 1 month before the actual field work). The verification of water occurrences detected by remote sensing triggered the discovery of diatomite deposits in some localities at the southern front of the Ennedi Mountains.

Within the selected scenes, 4 scenes have perennial surface water (path/row 180049, long 21.21 – 23.34°E, lat 14.84 – 16.95°N: Lake Kariari; pat/row 181047, long 20.31 – 22.48°E, lat 17.73 – 19.83°N: Ounianga Serir's lakes; path row 182047, long 18.78 – 20.94°E, lat 17.72 – 19.84°N: Ounianga Kebir's lakes; path/row 183047, long 17.24 – 19.34°E, lat 17.70 – 19.86°N: Bedo's oases). The remaining scenes show occurrences of surface water as a result of rainfall events. A total of 174 images from the initial set was finally selected for the analysis presented in the next section. Figure 5.5 presents the number of images per LandSat8 scene (path/row of the scenes are indicated).

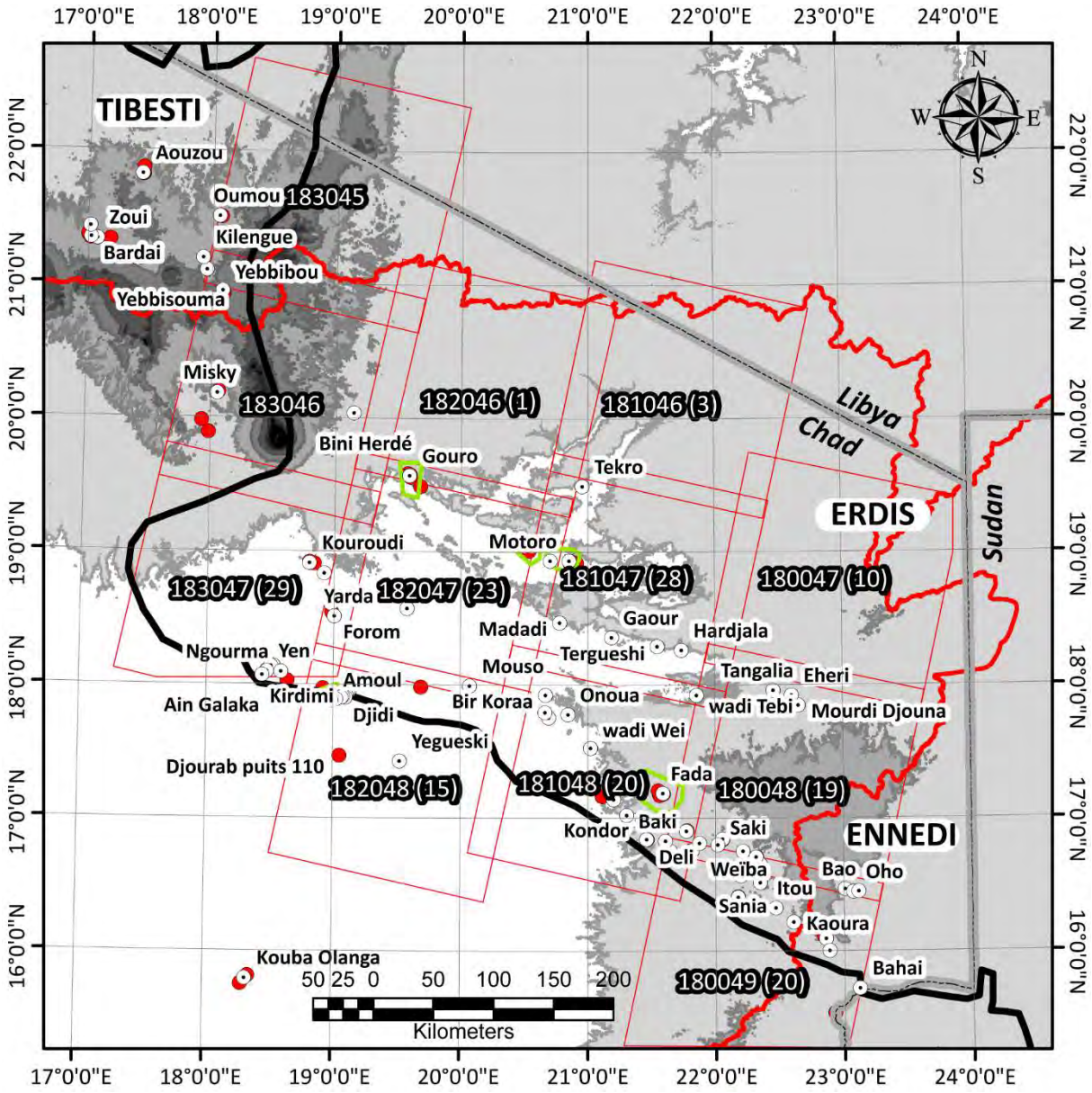

Figure 5.5: LandSat8 scenes with the associated identifier (path/row) and the corresponding number of images used in the following analysis. Topography (equidistance 500 m) is shown as background.

5.4.2.2. Regional variability and yearly amplitude

Table 5.3 synthetizes the mean and maximum rainfall rates and their associated hydrological response (MNDWI36), presented per LandSat8 scene and per year (2013 to 2016). In a general way, we use the term hydrological response to describe the flooded surfaces. The data in the table are ordered to represent their geographical position (north to south is shown from top to bottom, east to west is shown from left to right).

Table 5.3: Mean and maximum precipitation rates and their associated hydrological response in terms of flooded areas (10^6 m^2) per year (2013 – 2016) and per LandSat8 scene (see Figure 5.5 for the corresponding spatial coverage of the LandSat8 scene). The data in the table are ordered to represent their geographical position (north to south is shown from top to bottom, east to west is shown from left to right).

West | **Center - West**

North

	183045 lat 20.59 - 22.74° long 17.89 - 20.09°				182046 lat 19.16 - 21.28° long 19.06 - 21.27°			
	rainfall (mmy-¹)		surface water (10^6m^2)		rainfall (mmy-¹)		surface water (10^6m^2)	
Year	Mean	Max	Min	Max	Mean	Max	Min	Max
Tot 2013	19	122	0	0	6	56	0	0.1
Tot 2014	33	434	0	0	13	85	0	0.2
Tot 2015	47	309	0	0	8	98	0	0.4
Tot 2016	19	146	0	1.6	16	71	0	0
Tot 2013-16	**30**	**253**	**0**	**1.6**	**11**	**78**	**0**	**0.4**
	183046 lat 19.15 - 21.30° long 17.56 - 19.74°				182047 lat 17.72 - 19.84° long 18.78 - 20.94°			
	rainfall (mmy-¹)		surface water (10^6m^2)		rainfall (mmy-¹)		surface water (10^6m^2)	
Year	Mean	Max	Min	Max	Mean	Max	Min	Max
Tot 2013	20	156	0	7.0	7	47	1.8	4.1
Tot 2014	30	1103	0	18.4	34	143	2.6	4.6
Tot 2015	58	260	0	14.4	9	57	1.5	3.2
Tot 2016	24	329	0	17.0	25	144	2.7	4.0
Tot 2013-16	**33**	**462**	**0**	**18.4**	**19**	**98**	**1.5**	**4.6**

South

	183047 lat 17.70 - 19.86° long 17.24 - 19.34°				182048 lat 16.27 - 18.40° long 18.47 - 20.61°			
	rainfall (mmy-¹)		surface water (10^6m^2)		rainfall (mmy-¹)		surface water (10^6m^2)	
Year	Mean	Max	Min	Max	Mean	Max	Min	Max
Tot 2013	8	65	0	0.1	47	224	0	0.1
Tot 2014	32	114	0	3.2	68	238	0	0.5
Tot 2015	24	165	0	0	30	225	0	0
Tot 2016	20	130	0.5	14.3	43	248	0.1	0.2
Tot 2013-16	**21**	**118**	**0**	**14.3**	**47**	**234**	**0**	**0.5**

Center East | **East**

North

	181046 lat 19.17 - 21.27° long 20.66 - 22.85°				180047 lat 17.72 - 19.84° long 21.87 - 24.04°			
	rainfall (mmy-¹)		surface water (10^6m^2)		rainfall (mmy-¹)		surface water (10^6m^2)	
Year	Mean	Max	Min	Max	Mean	Max	Min	Max
Tot 2013	4	37	0	0	7	37	0	0
Tot 2014	21	108	0	0	32	119	0	1.6
Tot 2015	5	45	0	0	18	81	0	0.8
Tot 2016	27	92	0	0	18	94	0	0
Tot 2013-16	**14**	**70**	**0**	**0**	**19**	**83**	**0**	**1.6**
	181047 lat 17.73 - 19.83° long 20.31 - 22.48°				180048 lat 16.28 - 18.39° long 21.53 - 23.68°			
	rainfall (mmy-¹)		surface water (10^6m^2)		rainfall (mmy-¹)		surface water (10^6m^2)	
Year	Mean	Max	Min	Max	Mean	Max	Min	Max
Tot 2013	10	55	3.8	6.7	56	200	0	20.6
Tot 2014	50	160	3.6	36.6	100	414	0	41.0
Tot 2015	24	95	4.3	4.9	93	318	0	18.2
Tot 2016	28	142	4.2	5.9	36	169	0.2	4.9
Tot 2013-16	**28**	**113**	**3.6**	**36.6**	**72**	**275**	**0**	**41.0**

South

	181048 lat 16.29 - 18.39° long 19.99 - 22.14°				180049 lat 14.84 - 16.95° long 21.21 - 23.34°			
	rainfall (mmy-¹)		surface water (10^6m^2)		rainfall (mmy-¹)		surface water (10^6m^2)	
Year	Mean	Max	Min	Max	Mean	Max	Min	Max
Tot 2013	62	162	0	17.8	125	307	0.5	69.4
Tot 2014	120	362	0	42.4	200	524	1.7	85.8
Tot 2015	61	296	0.1	2.5	180	375	0	40.6
Tot 2016	63	201	0	8.8	81	315	19.1	41.8
Tot 2013-16	**76**	**255**	**0**	**42.4**	**146**	**380**	**0**	**85.8**

The regional trends shown by the distribution of precipitation rates and their associated hydrological response are summarized as follows: (1) there is a general increase in precipitation rates and their hydrological response from north (scenes 182046, 181046 and 180047, 10 – 20 mmy^{-1}) to south (scenes 182048, 181048 and 180049, 50 - 150 mmy^{-1}); (2) higher rainfall rates are observed in the eastern and north-eastern Tibesti Mountains (scenes 183045 and 183046, 30 mmy^{-1}) but the hydrological response remains low, while the region south of the Tibesti Mountains (scene 183047) receives 20 mmy^{-1} but shows a more intense response; (3) in the central lowlands (scenes 182047, 182048, 181047) precipitation rates are between 20 and 50 mmy^{-1}, increasing towards the west when approaching the Ennedi Mountains (scenes 181048, 180048 and 180049, 70-150 mmy^{-1}). The hydrological response follows this same trend, becoming increasingly dynamic from the region of Faya-Largeau to the Ennedi Mountains; (4) within the Erdis plateaus (scene 180047) a slight increase in rainfall rates (20 mmy^{-1}) and hydrological response is shown, compared to the adjacent more western images (scenes 181046 and 181047).

Scene 182047 covers the region of the lakes of Ounianga Kebir and scene 181047 covers the region of the lakes of Ounianga Serir. For these two scenes, surface water occurrence was detected in the whole set of analyzed images. A minimum surface water extent was determined at 1.7 km^2 and 3.7 km^2 for scene 182047 and 181047, respectively. Surfaces of the group of lakes of Ounianga Kebir and Serir were verified in ArcMap, indicating areas of 5 km^2 and 12 km^2, respectively. As will be shown in Chapter 6, the lakes are often shallow and covered by vegetation at their borders. The discrepancy between the MNDWI36 and the real surface extent is likely the result of a false classification due to the presence of vegetation.

Figure 5.6 shows the regional spatial distribution of the total precipitation rates for the years 2013 to 2016 and the observed positive MNDWI36 (red dots), indicating the location of surface water extent (= hydrological response).

The temporal and geographical distribution of the hydrological response determined with the MNDWI36 correlates well to the geographical coverage and total annual precipitation rates. With the increase of precipitation and hydrological dynamics, higher correlation coefficients (R^2 0.6 - 0.8) are determined between monthly precipitation rates (mean and maximum) and surface water detected with the MNDWI36 index.

As shown in Figure 5.6, the geographical distribution of the meteoric pattern is similar between years but marked by some differences: some years experience increased precipitation rates over the Ennedi and Tibesti Mountains (2014 and 2015) and during some years, regions located in the central lowlands receive less than 5 mmy^{-1} of rainfall (2013 and 2015). The flooded areas indicate this same trend.

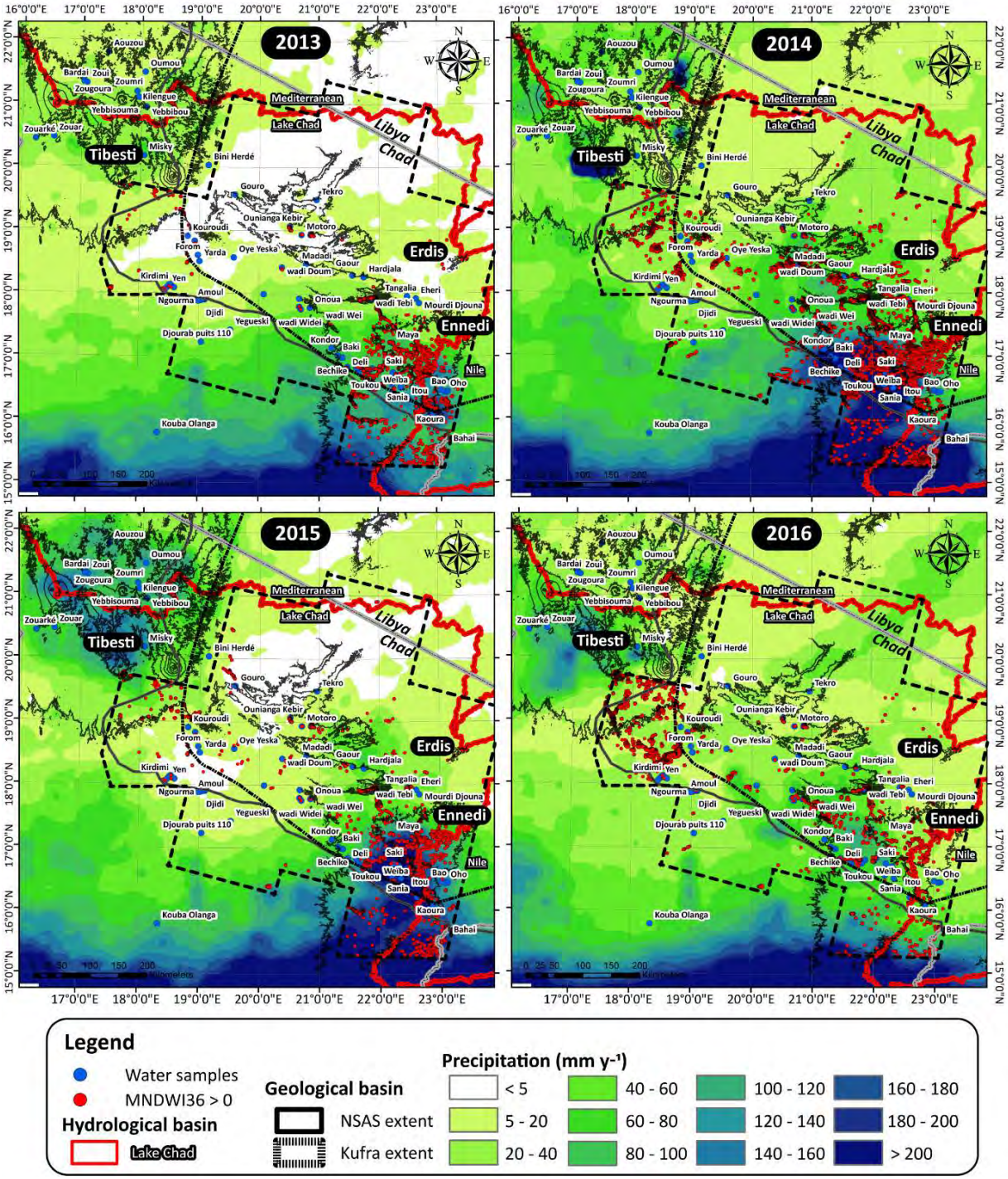

Figure 5.6: Total precipitation rates for the years 2013 to 2016 and MNDWI36 > 0, indicating the location of surface water detected from LandSat8. The coverage of LandSat8 images is indicated by the dashed line. Topographic contours (equidistance 500 m) are shown as background.

Compared to 2013, the more favorable 2014 rainy season shows increased surface water extent in the central lowlands. The hydrological response between years 2015 and 2016 is somehow distinct. In 2015, a high response is detected over the Ennedi Mountains and a low response in the region south of the Tibesti Mountains (Kouroudi, Yarda, Yen, Ngourma, Aïn Galaka). Note however the detection of surface water along wadis originating in the Tibesti Mountains (NW of Gouro and NW of Kouroudi). In

2016, many examples of surface water accumulation (ponds) were detected in the region south of the Tibesti, which do not show a clear relationship with the precipitation rates and distribution. The lower hydrological response in the Ennedi Mountains is resulting from the absence of images fulfilling the quality requirements during the month of August.

5.4.2.3. Local hydrological responses and dynamics

The geographical distribution of rainfall rates and the observed hydrological response indicate two distinct zones: a large area from the foothill of the Tibesti Mountains to the western foothill of the Ennedi Mountains (21°E) and covering the Erdis plateaus (north of 18°) characterized by diminished dynamics, and the region of the Ennedi Mountains (south of 18°N and east of 21°E) characterized by increased dynamics.

North of 18°N and west of 21°E, the region has mean annual rainfall rates below 50 mmy^{-1} (Figure 5.7). Examples of surface water occurrences are detected with a frequency between 1 and 2 times over a period of 4 years (2014 and 2016). The most favorable years in terms of rainfall rates (2014 and 2016) provoke increased extent of surface water occurrences. Although with a relatively small amplitude, the scenes covering the region surrounding the two lakes of Ounianga show some variability (scenes 182047, Ounianga Kebir, scene 181047, Ounianga Serir). The highest variability for the scene 181047 is seen to be related to surface water accumulation in the downstream of wadi Kordi (lower right corner in Figure 5.9B and C, indicated as a black arrow on Figure 5.7). To note the important contribution of surface water conveyed by the wadi, compared to the “stable” perennial surface water of the lakes.

Examples of surface water occurrences are provided by Figures 5.8 and 5.9: (1) for the region south of the Tibesti (West Palm Groves, Yarda-Kouroudi, Figures 5.8A and B), (2) for the zone between Faya-Largeau and Mouso, extending into the Djourab (Lake Chad basin, Figures 5.8C and D), (3) for the zone between the oases of Gouro, the lakes of Ounianga Kebir, and more southernly, wadi Doum and Yarda-Kouroudi (Figures 5.8E and F), (4) for the region between Gouro and the lakes of Ounianga (Figure 5.9A), (5) for the region south-east of the Ounianga lakes (Permo-Trias escarpment, Figures 5.9B and C) and (6) for the region south of the Erdis plateaus (Figures 5.9 D and E).

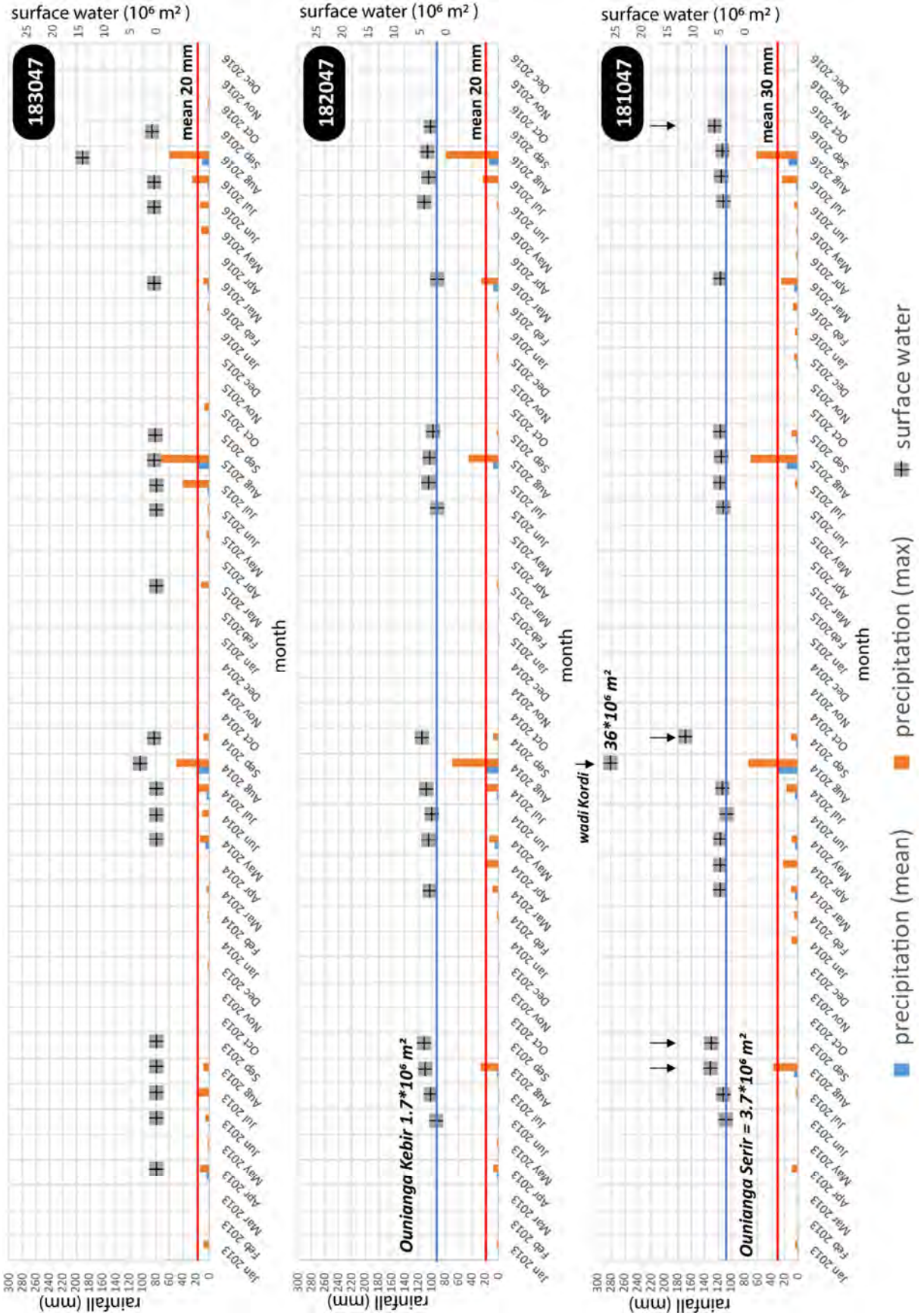

Figure 5.7: Timeline of precipitations (mean, max) and hydrological response for scenes 183047, 182047 and 181047. The red line indicates the annual mean precipitation (sum of the monthly mean rates).

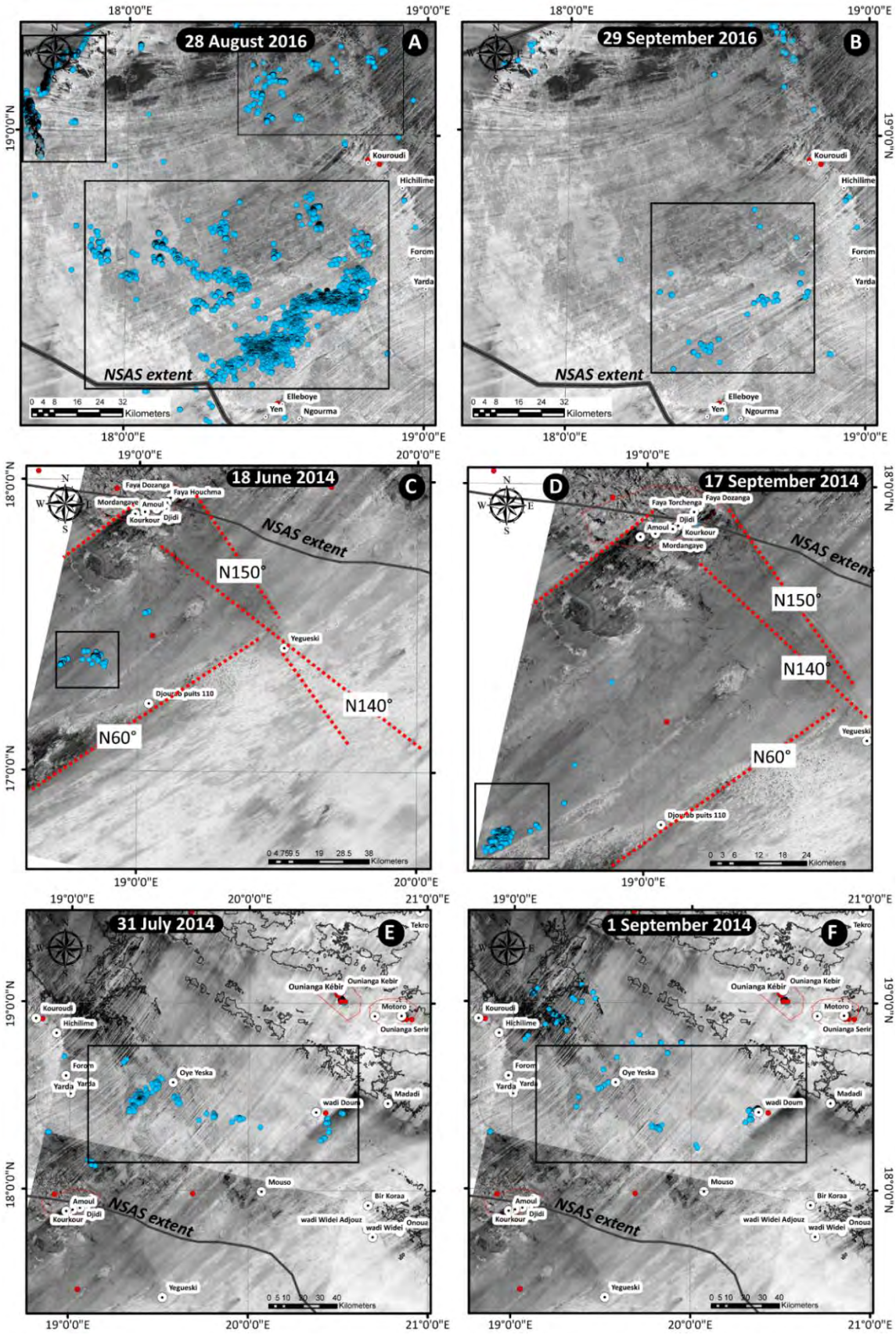

Figure 5.8: Hydrological response in the region south-west of Yarda-Kouroudi and north-west of the West Palm Groves (A and B), south-west of Faya-Largeau, in the Djourab (Lake Chad basin, C and D), and south-west of the Ounianga Lakes (E and F), showed for its extent and amplitude. Background is band 7 of LandSat8 image. Red dots are the inspected localities in the field, blue dots are MNDWI36 > 0.

In response to rainfall, surface water accumulates in a region located between Yarda-Kouroudi and the West Palm Groves (Figure 5.8A and B). In the Djourab area, surface water accumulates within a region marked by faults of direction N60° and lineaments of direction N140° and N150°, the latter marking the escarpment north of Faya-Largeau (Figure 5.8C and D, see also Chapter 2). In the region South of Ounianga Kebir, surface water accumulates in a region between Oye Yeska and wadi Doum (Figures 5.8E and F). In 2016, the hydrological response concentrates in the region of Mouso, more southerly than in 2014 (Oye Yeska, wadi Doum). Persistence of surface water is detected for approximately a month after the last precipitation.

The region of Gouro corresponds to the zone of lowest mean annual rainfall. In addition, during the years 2013 to 2016, we observed only one event resulting in runoff in the enneri north of the oases (Figure 5.9A). Several perennial discharge points are however observed in Ounianga. For the region between the Ounianga Lakes, the Erdis plateaus and the Permo-Trias escarpment, north of the Mourdi depression (Hardjalla, Tergeshi, Gaour, Madadi, wadi Doum, Figures 5.9 B-C-D-E), 2014 has been the only rainy season which has provoked some amounts of detectable surface water. The persistence of surface water is observable for approximately one month after the rainfall event.

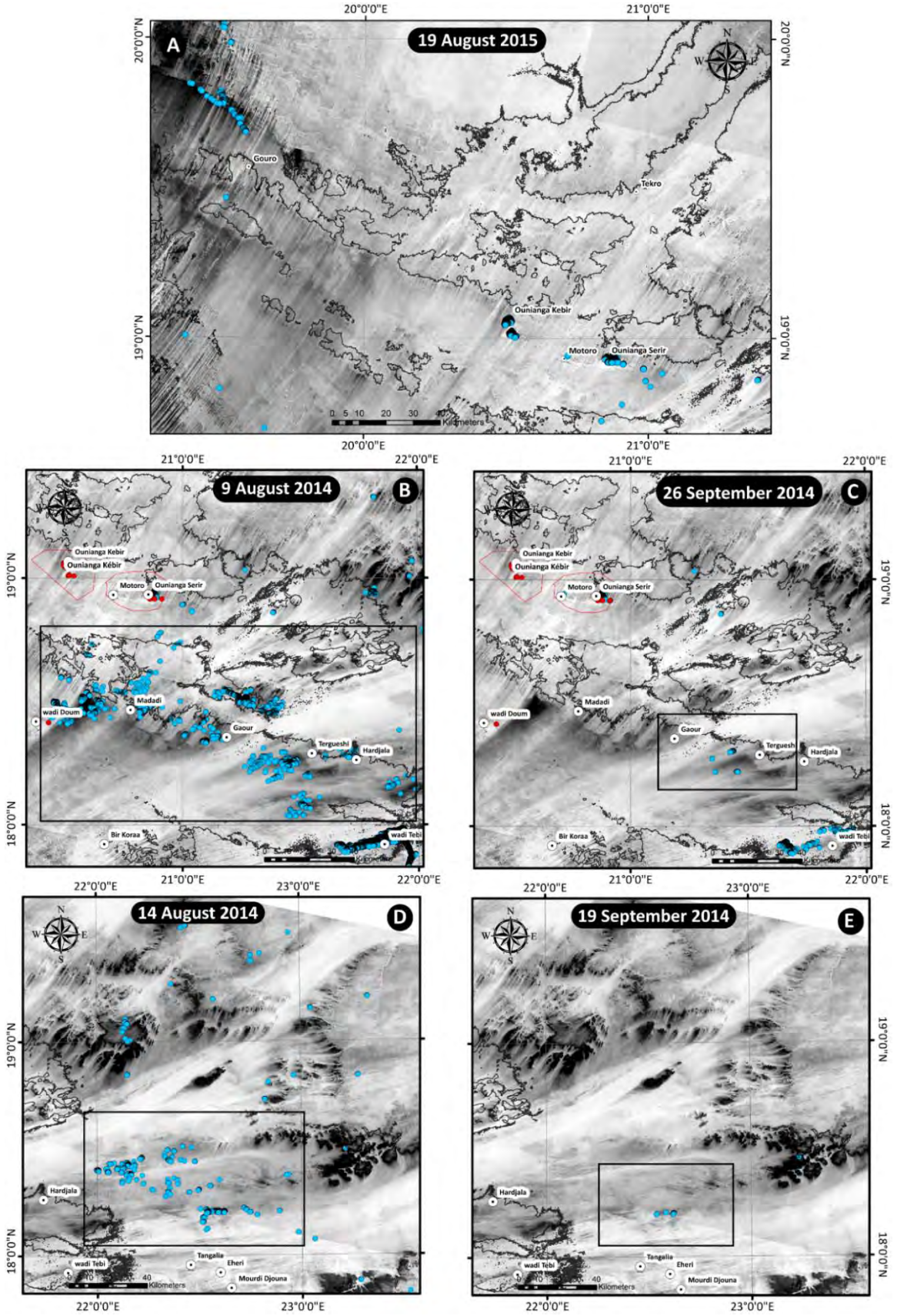

Figure 5.9: Hydrological response in the region between Gouro and the Ounianga lakes (A), in the region south-east of the Ounianga Lakes (B and C), in the Erdis plateaus (D and E) showed for its extent and amplitude. Background is band 7 of LandSat8 image. Red dots are the inspected localities in the field, blue dots are MNDWI36 > 0.

Mean annual precipitation increases substantially over the Ennedi Mountains (south of 18°N and east of 21°E, 70-150 mmy^{-1}), as well as the amplitude and frequency of the hydrological response (Figure 5.10). Every year, during and after the rainy season, the region of the Ennedi Mountains shows increased extent of surface water occurrences within the high plains and along the major wadis flowing towards the south and towards the north (Figure 5.11) of the mountain chain. The amplitude of the phenomena is correlated to the intensities and geographic distribution of the rains, the south-east and south-central zones experiencing increased rainfall compared to the north and north-western zones. Figure 5.11 provides several examples of flooded areas occurring between years 2013 to 2016.

The hydrological dynamics in the Ennedi Mountains indicates that wadi Kordi is flooded every year (Figures 5.11A-B-C-D), while an important flood occurs only once in four years for wadi Béméché (Figure 5.11E). However, positive MNDWI36 are also visible in 2015 and 2016 in the downstream of wadi Béméché. The high plains of the Ennedi Mountains also show a yearly hydrological dynamics (Figures 5.1F-G-H). The southern flowing wadis are also flooded every year (Figures 5.11M-N-O-P-Q). During the most favorable years (e.g. 2014), extended areas along the wadis are covered with surface water. Persistence of surface water after the rainy season is seen to concentrate in the downstream of wadi Kordi, in the high plains (Figure 5.11I-J-K-L) and within the southern flowing wadis. Surface water accumulates in the downstream of the wadis where it can be detected for several months after the end of the rainy season (Figure 5.11R, observed up to December).

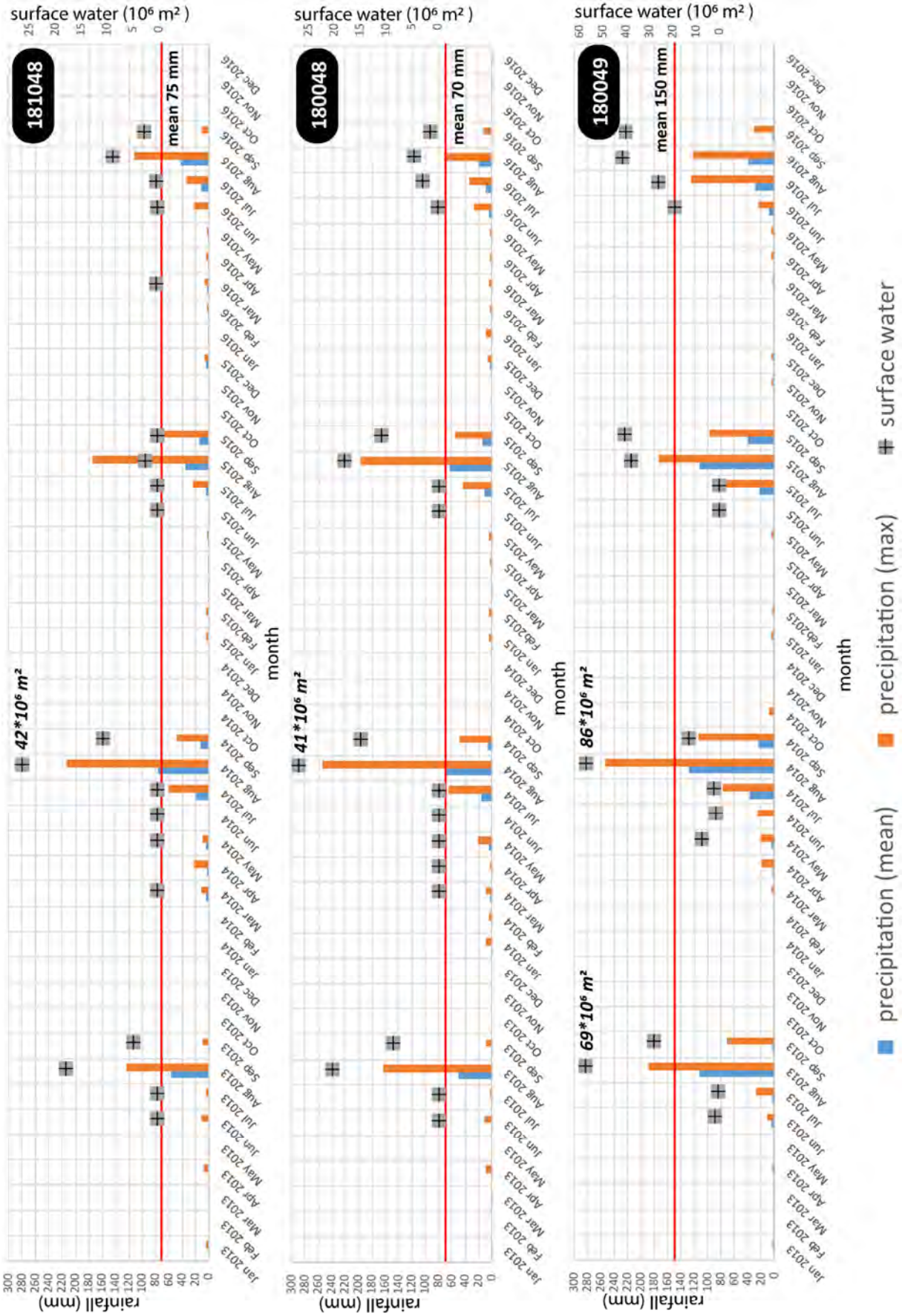

Figure 5.10: Timeline of precipitations (mean, max) and hydrological response for scenes 181048, 180048 and 180049. The red line indicates the annual mean precipitation (sum of the monthly mean rates).

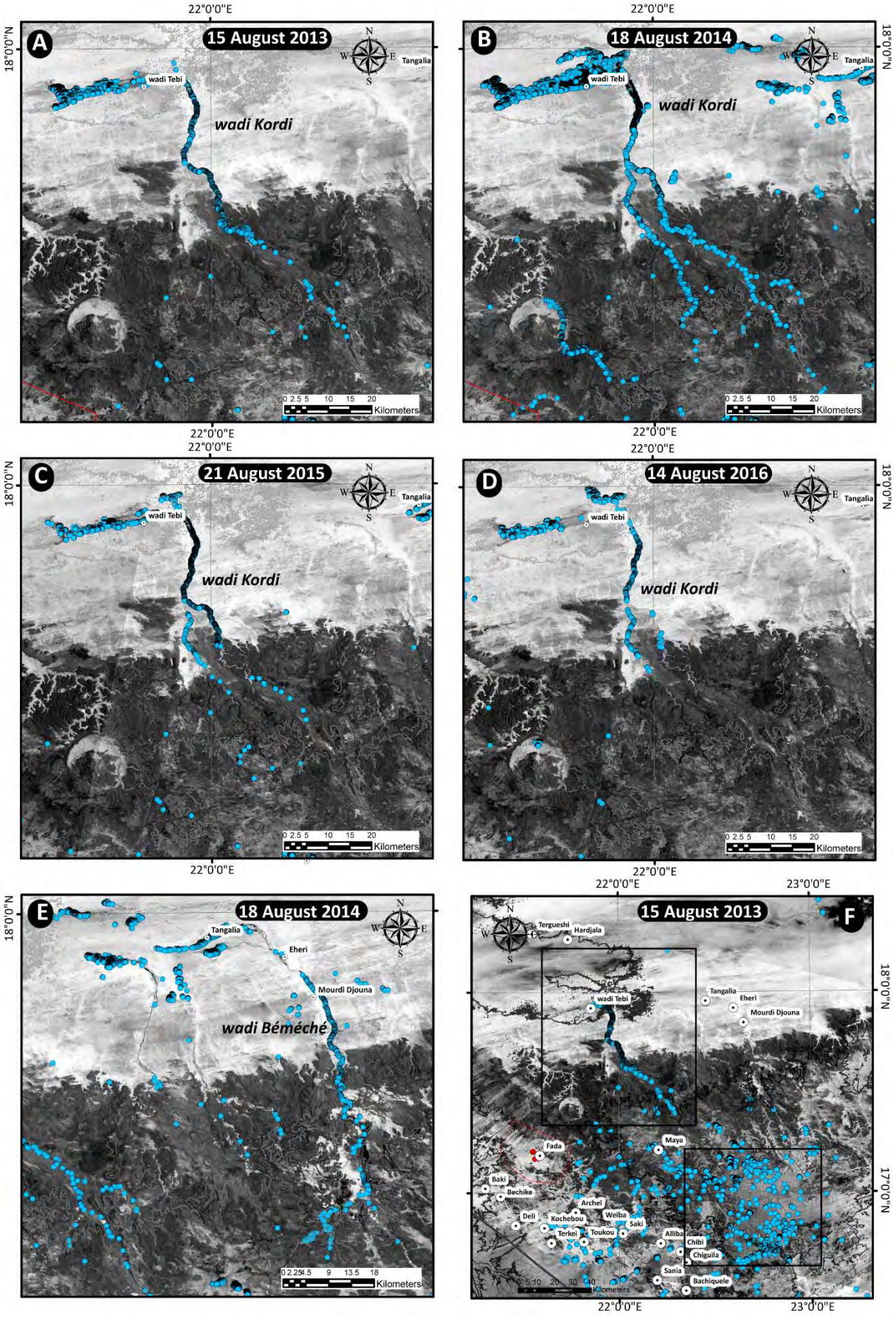
A
15 August 2013
wadi Tebi
wadi Kordi
Tangalia
B
18 August 2014
wadi Tebi
wadi Kordi
Tangalia
C
21 August 2015
wadi Tebi
wadi Kordi
Tangalia
D
14 August 2016
wadi Tebi
wadi Kordi
Tangalia
E
18 August 2014
Tangalia
Eheri
Mourdi Djouna
wadi Bémèché
F
15 August 2013
Tergueshi
Hardjala
wadi Tebi
Tangalia
Eheri
Mourdi Djouna
Maya
Fada
Baki
Bechike
Archei
Deli
Kochebou
Weiba
Saki
Terkei
Toukou
Alliba
Chibi
Chiguila
Sania
Bachiquele
Kilometers
22°0'0"E
23°0'0"E
18°0'0"N
17°0'0"N

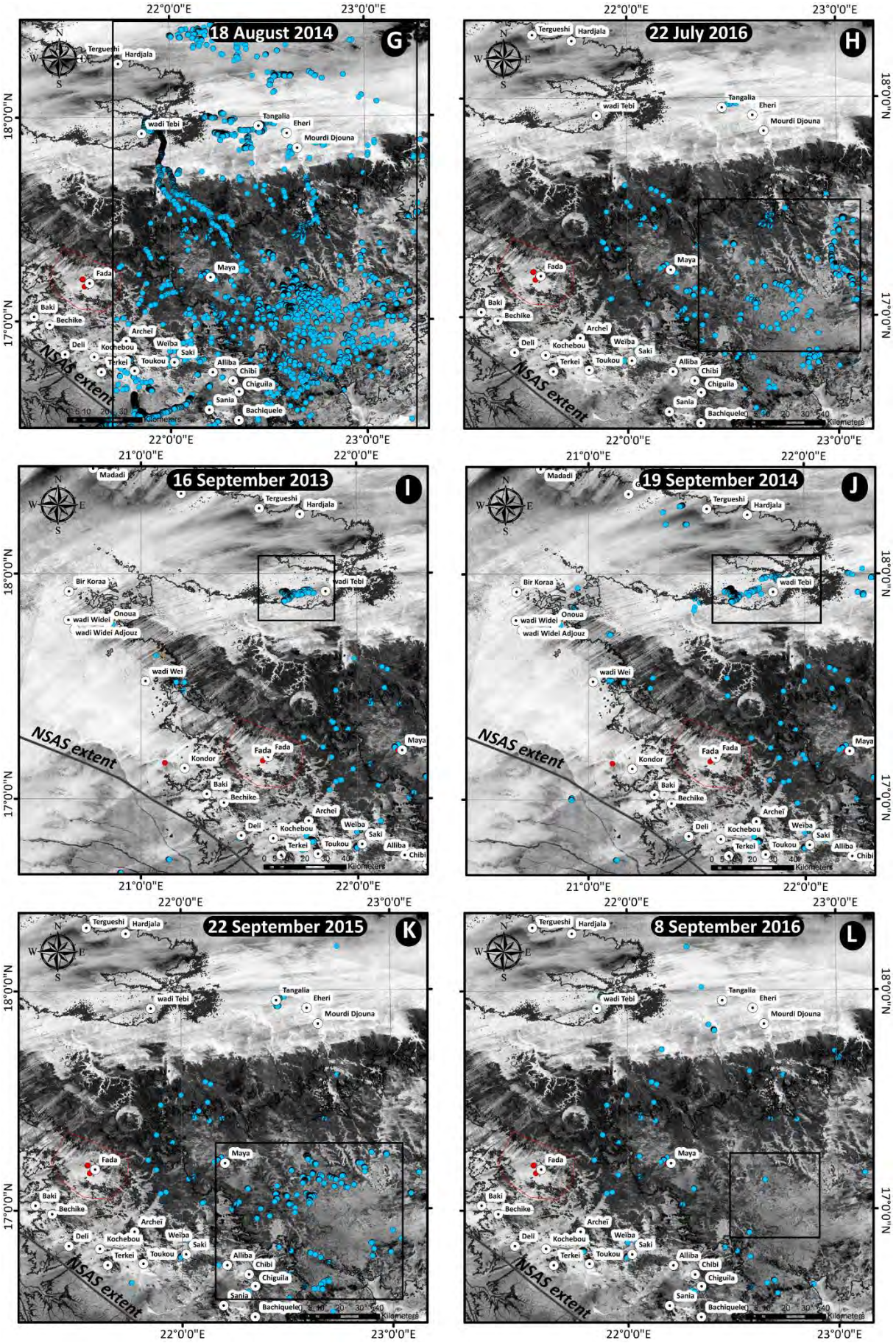
18 August 2014
G
22 July 2016
H
16 September 2013
I
19 September 2014
J
22 September 2015
K
8 September 2016
L
22°0'0"E
23°0'0"E
21°0'0"E
18°0'0"N
17°0'0"N
NSAS extent
Terguechi
Hardjala
wadi Tebi
Tangalia
Eheri
Mourdi Djouna
Maya
Fada
Baki
Bechike
Archei
Deli
Kochebou
Weiba
Saki
Terkei
Toukou
Alliba
Chibi
Chiguila
Sania
Bachiqueleq
Madadi
Bir Koraa
Onoua
wadi Widei
wadi Widei Adjouz
wadi Wei
Kondor
Kilometers

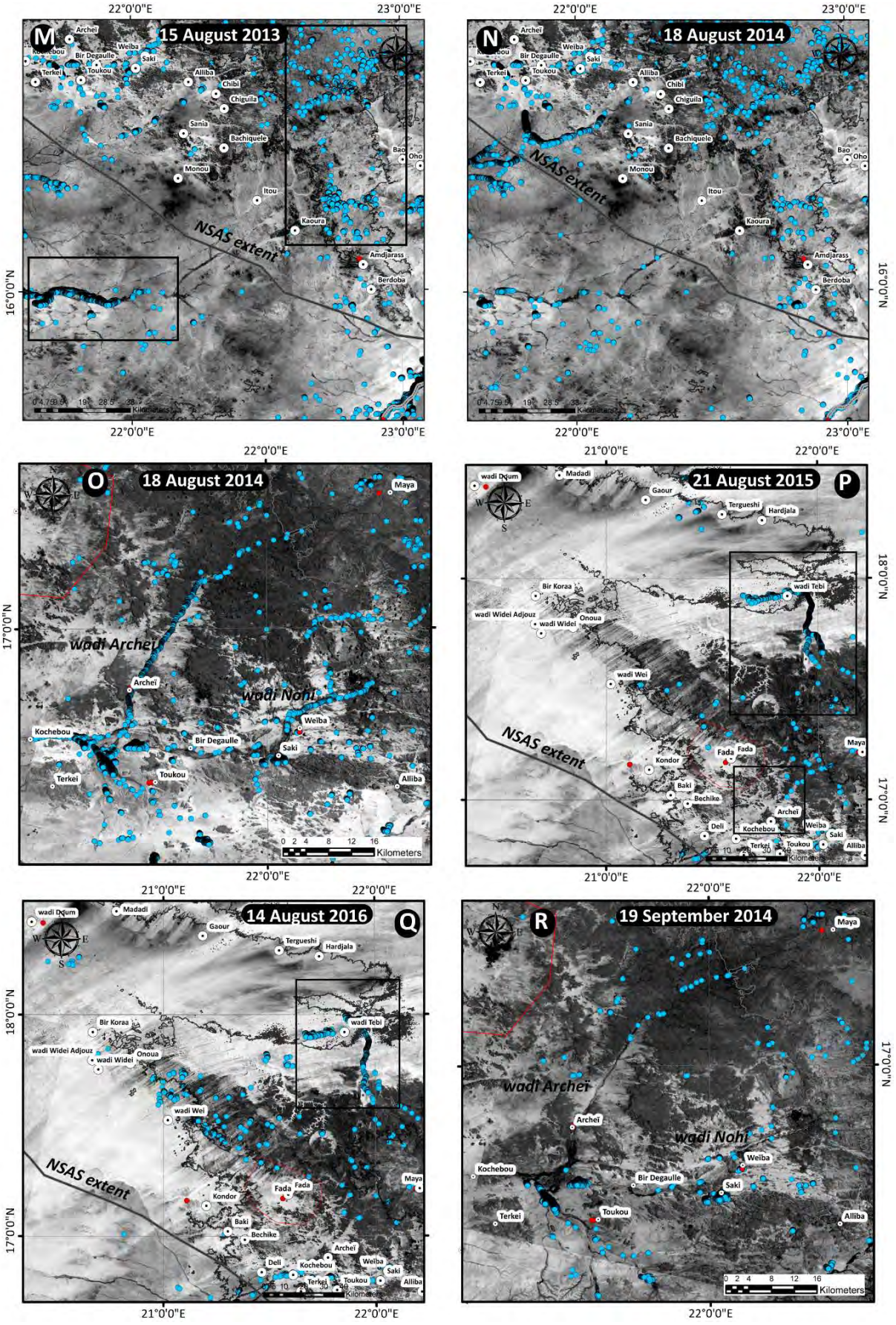

Figure 5.11: Hydrological response in the Ennedi Mountains. Red dots are the inspected localities in the field, blue dots are MNDWI36 > 0.

5.5. Synthesis of observations

The analysis of the spatial and temporal dynamics of precipitation shows that the summer monsoons are the most important meteoric dynamics for the investigated region. Most of the annual precipitation occurs during the month of August. Some regions also receive low amounts of winter rains (mountainous Tibesti, central lowlands).

The overall pattern of the meteoric dynamics shows the importance of topography in provoking increased precipitation. Increased precipitation occurs in the Tibesti and Ennedi Mountains but considerable less amounts interest the depressional region extending in between the two mountains. The SW-NE pattern of the summer monsoons provokes a significant difference of rainfall rates between the southern slopes and higher altitudes of these two mountain chains, and the northern slopes. In the Ennedi Mountains, the highest rainfall rates are experienced by the region corresponding to the intersection of the NW-SE ridges, separating the Mourdi and the Mortcha/Djourab sub-basins, and the NNE-SSW ridges, separating the Nile and the Lake Chad hydrological basins (see Chapter 2 and 4). The region formed by the intersection of these two directions corresponds to the highest altitudes of the Ennedi Mountains.

The Ennedi Mountains show increased hydrological dynamics compared to the other regions investigated herein. The amplitude of the hydrological response is correlated to the geographic distribution of the rainfall rates and occurs yearly. High-intensity precipitation events provoke runoff along the wadis flowing towards the north (wadi Kordi and wadi Bembéché) and the wadis flowing towards the south (wadi Haouach, Sini-Chili, Sala). The intensity of the response is higher in the south-east of the Ennedi Mountains (Archeï, Bachiquele, Kaoura) than in the south-west (Fada, wadi Wei), but is higher in the north-west (wadi Kordi) than in the north-east, mirroring the intensities of precipitation. Persistence of surface water after the rainy season concentrates in the downstream of the alluvial systems.

In the high plains of the Ennedi Mountains, several examples of localized ponds develop during the rainy season and slowly dry out during the dry season. In the southern slopes, important springs such as Archeï and Bachiquele, discharge at the base of the Cambro-Ordovician basement, but fractures are seen to connect the system to the high plains. The accumulation of rainfall in these localized ponds and potential infiltration could therefore be an important mechanism of recharge, providing storage to the downstream system during the dry season (see also Chapter 4).

In the western Ennedi (Sala downstream), the mountainous topography gradually changes into a lowland. At the same time, rainfall amounts decrease substantially. However, where the mountain chain changes into a lowland, the meteoric perturbation travels further and reaches the Erdis plateau.

South of the Erdis plateaus, a slight increase of rainfall rates (20 mmy^{-1}) and a higher hydrological response was detected, compared to the adjacent Mourdi depression. The zone located along the Mourdi depression (wadi Doum, Madadi, Gaour, Tergueshi, Hardjalla) shows some hydrological response only during the most favorable years (year 2014 for our time of observation).

Rainfall rates also increase towards the Tibesti Mountains. On the eastern slopes, however, the hydrological response remains low (wadis north of the Gouro oases and north-west of Kouroudi, originating in the Tibesti Mountains). The region south of the Tibesti Mountains (Yarda-Kouroudi, West Palm Groves, Faya-Largeau), is characterized by slightly higher rainfall rates and a stronger hydrological dynamics (2 events in 4 years) than the eastern Tibesti slopes and the central lowlands.

5.6. Concluding remarks

The combined used of precipitation estimates (RFE 2.0) and MNDWI36 index (LandSat8) enabled to understand the spatial and temporal distribution of precipitation and the resulting hydrological response. It provided the means to identify regions where recharge is potentially occurring and to investigate the main processes of surface water redistribution in the Ennedi Mountains. MNDWI36 index allowed detecting surface water occurrences, their extent and their temporal variability. Also, the amplitude and the frequency of the hydrological response (MNDWI36) correlate well with the precipitation patterns (RFE 2.0). Combining these two products allowed therefore investigating the dynamics of the precipitation-runoff-accumulation process at a regional scale.

Higher hydraulic heads and divergent flows, presented in Chapter 4, identify the Ennedi Mountains as a zone of recharge. Higher precipitation rates interest this mountainous region, where there is potential for diffuse recharge. From year to year, we observe some differences in the temporal distribution of monthly rates, but yearly, flooded surfaces are detected along the main wadis and within the high plains. Within these zones, episodic concentrated recharge might occur. The analysis performed by remote sensing shows that wadis play a critical role in redistributing precipitation. For example, wadi Kordi, shows important floods every year (approximately 100 km of flooded length). These floods correspond to the only mechanism of conveying surface water to the northern slopes, characterized by low rainfall rates.

In order to analyze the relative importance of concentrated recharge rates as opposed to diffuse recharge, evapotranspiration dynamics needs to be further investigated. Next chapter (Chapter 6) uses these same LandSat8 images to extract actual evapotranspiration distribution within the flooded areas. In addition, this procedure is useful to detect the variabilities of permanent surface water, which in regions of low precipitation rates, are the result of groundwater discharge dynamics.

Chapter 6

Potential and actual evapotranspiration

6.1. Introduction and outline of the chapter

6.1.1. Introduction and aim

Evapotranspiration is a fundamental process of the water cycle. Worldwide, 70% of precipitation is lost to evapotranspiration and in arid regions, this rate can increase above 90% (Baumgartner and Reichel, 1975). The intensity of the single precipitation is important, as short, high-intensity rainfall events rapidly concentrate volumes of water potentially exceeding the maximum infiltration rates of the soil, and surface runoff occurs. The partitioning of precipitation into surface-runoff, infiltration and evapotranspiration is dependent on the catchment characteristics such as soil type, geology and topography. In addition to the physical catchment characteristics, antecedent moisture conditions and the depth to the water table strongly influence evapotranspiration rates. For example, if the water table is close to the surface, phreatic evaporation can be sustained through capillary rise.

Analyzing the spatial and temporal dynamics of evapotranspiration can provide important indications on the above-mentioned characteristics and the relevant processes in a catchment. For example, in response to precipitation, surface water flow emerges along wadis and rapidly disappears (see Chapter 5). Tracing the evapotranspiration rates in the vicinity of wadis can provide information on the rise of the water table (i.e. a proxy of recharge) during the flood event. Moreover, the discharge zones of the system, featuring a small depth to groundwater, can be identified because phreatic evaporation will occur even in the absence of precipitation.

Remote sensing technology (for example based on LandSat images) can be employed to calculate evapotranspiration of large spatial scales. The overarching goal of this chapter is to investigate the dynamics of evapotranspiration of the Nubian Sandstone Aquifer System of Northern Chad in order to improve the understanding of the relevant hydrological processes near the surface. To a certain extent, these processes provide information on the deeper, hydrogeological system as well. In order to reach this goal the following steps are taken: (1) Establish a time series of evapotranspiration maps. This is challenging as only a few snap-shots in time are available and no continuous time series can be directly established; (2) Based on these time series, evapotranspiration dynamics are studied near wadis

(Ennedi Mountains), where concentrated recharge might occur after high-intensity rainfall events and in the main discharge zones (oases, lakes).

Questions guiding this study are: (1) what are the spatial and temporal dynamics of climatic forcing (precipitation and evapotranspiration)? (2) what is the relative importance between diffuse and concentrated recharge? (3) can we establish a temporal dynamics of groundwater fluctuations and phreatic evaporation in the discharge zones (e.g oases of Ounianga Kebir, Ounianga Serir, Gouro, Bedo, West Palm Groves, Faya-Largeau)? (4) are these fluctuations directly influenced by climatic forcing or rather the result of long-term dynamics of the aquifer system? (5) how much is lost through evapotranspiration?

6.1.2. Content of the chapter

The chapter is structured as follows. The next section (section 6.2) presents some background information on the fundamentals of evapotranspiration (ET) and briefly introduces to some methods used to estimate potential and actual ET. The methodology section (section 6.3) describes the equations for estimating potential and actual evapotranspiration, the meteorological data used and the processing of LandSat8 images.

The results are presented in two parts. The first part (section 6.4.1) discusses estimates of the annual changes of available energy and potential evapotranspiration, the latter by using the Turc, Hargreaves and Penman methods. These estimates are useful because they show the annual dynamics as a continuous time series and set a maximum evaporative rate for the region under investigation. As LandSat8 images represent only a few snap-shots in time, the possibility of using the potential evapotranspiration's continuous series to interpolate the actual evapotranspiration maps, is further explored (see below).

The second part (section 6.4.2) presents a series of spatially distributed actual evapotranspiration maps. The method used is based on the S-SEBI approach applied to LandSat8 images. The use of LandSat8 images and the applied method enables to analyze spatial and temporal differences of actual evapotranspiration on a regional scale. First, we present a comparison of potential and actual evapotranspiration calculations, in order to assess whether daily estimates of potential evapotranspiration can be used to interpolate the actual evapotranspiration rates, for the dates without an image (section 6.4.2.1). Secondly, we present a standard deviation map of actual evapotranspiration, highlighting the zones of interest (section 6.4.2.2). Section 6.4.2.3 describes the western region, comprising the southern Erdis plateaus and the Ennedi Mountains, where the temporal dynamics of evapotranspiration results from precipitation, runoff and accumulation of surface water during the rainy season. Evapotranspiration rates are then investigated in the main oases

(Ounianga Lakes, Gouro, Bedo, West Palm Groves, Faya-Largeau, section 6.4.2.4). The main discharge zones in the NSAS of Northern Chad are located in a zone of low precipitation rates. A synthesis of the total losses of evapotranspiration from the NSAS is presented in section 6.4.3.

The chapter concludes by discussing the different rates of evaporation found in the literature and by comparing them to potential evapotranspiration rates calculated in this study (section 6.5.1). A synthesis of the main observations and a critical review on the remote sensing approach employed in this study are presented in sections 6.5.2 and 6.5.3.

6.2. Fundamentals of evaporation

Evaporation is defined as the process of transformation of liquid water into water vapor. It includes evaporation of water from oceans, lakes, rivers and reservoirs, from soil surfaces and from water intercepted by vegetative surfaces. Transpiration is the evaporation from leaf stomata, and the term evapotranspiration defines the sum of transpiration from plants and evaporation from soil moisture and any surface water. The rate of evaporation is determined by climatic factors such as air temperature, vapor pressure and wind speed, the net available heat and the wetness of the evaporating surface (McMahon et al., 2013).

Evaporation is a key parameter of the energy balance, defined by the following relationship:

$$R_n = H + \lambda ET_{act} + G \quad (6.1)$$

Net radiation (R_n, in MJd^{-1} or in $Wm^{-2}s^{-1}$) corresponds to the amount of radiation absorbed by the land surface (G = soil heat flux) and the available energy for exchange processes (H = sensible heat flux, λET_{act} = latent heat flux of actual evaporation). The sensible heat flux is the energy necessary to transfer heat from the surface to the air and reversely. The latent heat flux of actual evaporation is the energy needed to vaporize water. The energy absorbed to the ground, G, can be assumed to be negligible (Allen et al., 1998) over the course of 24h.

The net radiation also corresponds to the difference of the net shortwave radiation (S_n) and of the net longwave emission (L_n):

$$R_n = S_n - L_n = (1 - \alpha_{surf}) * S - L_{out} + L_{in} \quad (6.2)$$

The shortwave net radiation (S_n) corresponds to the difference between the incident to reflected incoming shortwave radiation (Figure 6.1). The atmospheric conditions determine the amount of incoming radiation directly reflected from the atmosphere. The proportion of the incident radiation that is reflected by the atmosphere is the atmospheric albedo, α_{atm}. Likewise, the proportion of the incident radiation that is reflected by the land surface is the surface albedo, α_{surf}. On average, about

30% of solar radiation is reflected by the earth-atmosphere system (atmospheric albedo and surface albedo). The rates might increase to 40% for non-vegetated areas such as the Sahara desert. As shown by Charney et al. (1977), an increase of albedo in semi-arid regions as a consequence of desertification, causes a net decrease in net radiation flux into the ground and therefore a net decrease in convective clouds and precipitation.

The incoming solar radiation (S) is dependent on the latitude and the day of the year, which determines the maximum amount of solar radiation (termed extraterrestrial solar irradiance, S_{exo}), and the atmospheric conditions.

The longwave net radiation corresponds to the difference between the surface emitted longwave radiation (L_{out}), a function of surface temperature and emissivity, and the incoming longwave radiation reflected by clouds (L_{in}, Figure 6.1), a function of atmospheric temperature and emissivity.

Many methods have been developed to estimate evapotranspiration, or more specifically (McMahon et al., 2013): (1) potential evapotranspiration, (2) reference crop evapotranspiration, (3) pan evaporation or open-surface water evaporation, and (4) actual evapotranspiration from the landscape.

The Penman (Penman, 1948), Penman-Monteith (Allen et al., 1998) and Priestley and Taylor (Priestley and Taylor, 1972) are three key methods used to estimate potential evapotranspiration. If only air temperature is available, the Turc (Turc, 1961) and Hargreaves (Hargreaves, 1975) are viable methods to estimate potential ET. Adopting the characteristics of a hypothetical reference crop, the Penman-Monteith equation becomes the FAO-56 reference crop or standardized reference evapotranspiration equation (Allen et al., 1998). Class-A evaporation pans provide useful data if pan coefficients are known for a given region. However, as presented by Sellers (1964), pan evaporation might overestimate evaporation rates by a factor of 1.6 compared to the Penman method.

Promising methods capable of capturing the surface heterogeneities on a large spatial scale are based on the use of remote sensing techniques. Remote sensing products such as LandSat, represent the longest continuous set of images of land surface changes (acquired since 1972), and its resolution (30 m) allows to spatially represent ET fluxes.

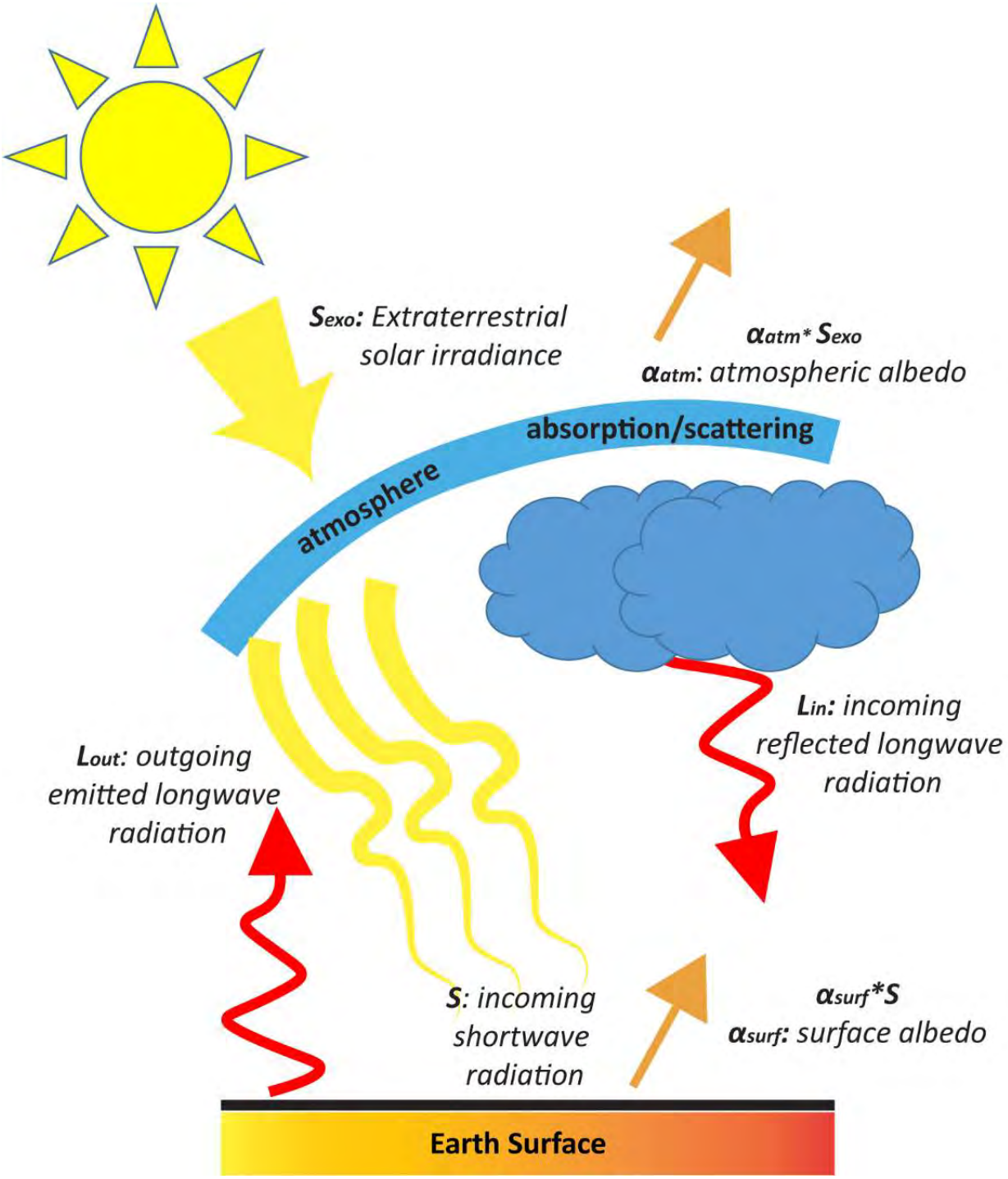

Figure 6.1: Schematic representation of solar radiation and its components: S_{exo} is the extraterrestrial solar irradiance at the top of the atmosphere, S is the incoming shortwave radiation reaching the ground, $\alpha_{atm}*S_{exo}$ and $\alpha_{surf}*S$ represent the part of radiation lost to reflection (atmospheric and surface albedo), L_{out} is the part of radiation lost by surface emission in the form of longwave radiation and L_{in} is the incoming longwave radiation resulting from the backscattered reflection of the longwave emission from clouds.

6.3. Methods

6.3.1. Climatic data

In order to compute all the following steps (daily net radiation, potential evapotranspiration, actual evapotranspiration), some minimum ground-based meteorological data are needed. These data are: actual duration of sunshine *(n),* minimum, maximum and mean daily air temperature (T_{min}, T_{max}, T_{mean}), minimum, maximum and mean daily relative humidity (RH_{min}, RH_{max}, RH_{mean}) and wind speed.

Table 6.1 presents the set of data used in the calculations. The actual duration of sunshine (*n*) is taken from the WMO database (mean monthly and mean annual values), relative humidity (*RH*) are from BRGM (1991) for Faya-Largeau (monthly values) and wind speed were taken from Infoclimat.org website (mean monthly values) also for Faya-Largeau.

Table 6.1: Climatic monthly data used in the following calculations. Air temperature data represent a monthly mean value calculated from daily estimates at selected localities (see below).

Month	n (hours)	Air Temperature (°C)			Humidity (%)			Wind speed (m s^{-1})
		min	max	mean	min	max	mean	
January	9.9	11.6	30.9	21.3	15	34	25	3.9
February	10.4	12.8	32.6	22.7	12	29	21	3.7
March	9.9	16.5	36.8	26.6	10	27	19	3.6
April	10.3	19.3	39.6	29.5	9	27	18	3.3
May	11.1	21.1	41.3	31.2	10	27	19	2.9
June	11.1	22.0	41.9	32.0	11	31	21	2.8
July	10.8	21.0	40.8	30.9	14	45	30	2.3
August	10.3	20.7	39.8	30.3	18	56	37	2.2
September	10.4	19.9	39.6	29.7	12	35	24	2.9
October	10.3	18.7	37.8	28.2	13	30	22	3.3
November	10.3	15.7	34.5	25.1	13	33	24	3.8
December	9.9	12.7	31.3	22.0	16	37	27	3.8
Mean annual	10.4							

Air temperature values (T_{min}, T_{max}, T_{mean}) were taken from Global TempSIM (version 1.0, http://www.ars.usda.gov/services/software) which predicts the daily maximum and minimum air temperatures for a yearly cycle at any location on the globe based on the compilation and interpolation of 30 years (1961-1990) temperature records (Legates and Willmott, 1990a; Legates and Willmott, 1990b; Willmott and Matsuura, 1995). Mean absolute errors are estimated between 1.9 and 5°C. Data were extracted for representative localities distributed over the entire area investigated in this study: Amdjarass (long 22.854 lat 16.099, alt. 925 masl), Fada (long 21.557 lat 17.193, alt. 575 masl), Nohi (long 21.775 lat 16.906, alt. 585 masl), Mourdi Djouna (long 22.653 lat 17.847, alt. 610 masl), Ounianga Kebir (long 20.491 lat 19.055, alt. 385 masl), Ounianga Serir (long 20.860 lat 18.916, alt. 350 masl),

Gouro (long 19.590 lat 19.576, alt. 435 masl), Tekro (long 20.956 lat 19.492, alt. 460 masl), Kirdimi (long 18.507 lat 18.136, alt. 255 masl) and Faya-Largeau (long 19.087 lat 17.918, alt. 235 masl).

6.3.2. Determination of daily net radiation

The determination of daily net radiation (R_n) is performed by the calculation of: (1) the extraterrestrial solar irradiance, (2) the incoming solar radiation, (3) the net longwave radiation, and (4) by applying two extreme values of albedo (Brutsaert, 1984): 0.08 for deep water and 0.4 for white sand (see equation 6.1). The equations here presented follow the procedure described in Parodi (2002).

6.3.2.1. Extraterrestrial solar irradiance

The extraterrestrial solar irradiance (S_{exo}, in $MJm^{-2}d^{-1}$) is determined with the expression:

$$S_{exo} = \frac{24}{\pi} * SC * \ 0.0036 * \ E_0 * \sin(\theta) * sin(\delta) * \left(w_s - tan(w_s)\right) \tag{6.3}$$

Where *SC* denotes the solar constant (1367 Wm^{-2}) and Θ is the latitude (in radians). For the investigated region, latitude varies between 14.84°N and 22.74°N.

The eccentricity correction factor (E_0) is determined as:

$$E_0 = 1.00011 + 0.34221 * cos(d_a) + 0.00128 * sin(d_a) + 0.000719 * cos(2 * d_a) + 0.000077 * sin(2 * d_a) \tag{6.4}$$

Where the day angle (d_a) is determined by:

$$d_a = \frac{2 * \pi * (d_n - 1)}{365} \tag{6.5}$$

And d_n is the Julian day.

The solar declination of the day (δ) of acquisition is given by:

$$\delta = 0.006918 - 0.399912 * cos(d_a) + 0.070257 * sin(d_a) - 0.006758 * cos(2 * d_a) + 0.000907 * sin(2 * d_a) - 0.002697 * cos(3 * d_a) + 0.00148 * sin(3 * d_a) \tag{6.6}$$

The sunshine hour angle (w_s) is determined by:

$$w_s = arccos[-tan(\theta) * tan(\delta)] \tag{6.7}$$

6.3.2.2. Incoming shortwave solar radiation

A general approximation assumes that during a day of clear sky, 75% of the extraterrestrial solar irradiance traverses the atmospheric layer, while the proportion is reduced to 25% during fully overcast days. The ratio between extraterrestrial and incoming solar radiation sets approximately between 69 and 72% for the region under investigation.

For the determination of the incoming solar radiation, two approaches are tested. The first uses the ratio between the actual duration of sunshine and the total duration of sunshine (in the absence of clouds or shadows). The second approach uses the difference between daily maximum and minimum air temperatures.

The first method to estimate the incoming shortwave solar radiation (*S,* in $MJm^{-2}d^{-1}$) uses the following equation:

$$S = \left(0.25 + 0.5 * \frac{n}{N}\right) * S_{exo} \quad (6.8)$$

Total duration of sunshine (*N)* is calculated:

$$N = \frac{24}{\pi} * w_s \quad (6.9)$$

The second method to estimate shortwave incoming solar radiation (*S,* in $MJm^{-2}d^{-1}$) uses the following expression:

$$S = 0.16 * \sqrt{T_{max} - T_{min}} * S_{exo} \quad (6.10)$$

Where T_{max} and T_{min} are the maximum and minimum daily air temperature.

6.3.2.3. Net longwave radiation

Net daily longwave emission (L_n, in $MJm^{-2}d^{-1}$) was determined by using the expression:

$$L_n = \frac{1}{11.5741} * -f * \varepsilon' * \sigma * (T_{mean} + 273)^4 \quad (6.11)$$

Where σ is the Stefan Bolzmann constant ($5.6697*10^{-8}$ $Wm^{-2}K^{-4}$) and T_{mean} is the mean air temperature of the day (in °C). The cloudiness factor is determined by using the sunshine fraction (*n/N*) and coefficient values for arid environments:

$$f = 1.35 * \left(\frac{0.5}{0.5 + 0.25}\right) * \frac{n}{N} + \left(-0.35 + \frac{0.25}{0.5 + 0.25} * 1.35\right) \quad (6.12)$$

Net emissivity (ε') is given by:

$$\varepsilon' = -0.02 + 0.261 * e^{(-0.000777 * T_{mean}{}^2)} \quad (6.13)$$

6.3.3. Potential evapotranspiration (Turc, Hargreaves, Penman)

Potential evapotranspiration was estimated with the expression from Turc (Turc, 1961), Hargreaves (Hargreaves, 1975) and Penman (Penman, 1948).

The Turc potential ET (in mmd^{-1}) was determined with the adjustment provided by Alexandris et al. (2008) for non-humid climates (RH < 50%):

$$ETP_{Turc} = 0.013 * \left(\frac{T_{mean}}{T_{mean} + 15}\right) * (23.88 * S + 50) * \left(1 + \frac{50 - RH_{mean}}{70}\right) \quad (6.14)$$

Where T_{mean} is the mean air temperature for the day, S is the incoming shortwave solar radiation (in $MJm^{-2}d^{-1}$, section 6.3.2.2.) and RH_{mean} is the relative mean humidity (in %).

The Hargreaves potential ET was determined with (in mmd^{-1}):

$$ETP_{Hargreaves} = \frac{0.0023}{\lambda} * S_{exo} * (T_{mean} + 17.8) * \sqrt{T_{max} - T_{min}} \quad (6.15)$$

Where T_{max} *and* T_{min} are the maximum and minimum daily temperatures, λ is the latent heat of vaporization (2.45 $MJkg^{-1}$ at 20°C) and S_{exo} is the extraterrestrial solar irradiance (in $MJm^{-2}d^{-1}$, section 6.3.1.1).

In order to compare daily available net radiation and potential evapotranspiration estimates, the former are converted to $mm.d^{-1}$ (0.408 * R_n in $MJm^{-2}d^{-1}$).

The Penman potential evapotranspiration is calculated with the expression (in mmd^{-1}):

$$ETP_{Penman} = \frac{\Delta}{\Delta + \gamma} * \frac{R_n}{\lambda} + \frac{\gamma}{\Delta + \gamma} * E_a \quad (6.16)$$

Where R_n is the net radiation at the water surface (equation 6.1).

Δ is the slope of the saturation vapor pressure curve (in kPa $°C^{-1}$), determined as follows:

$$\Delta = \frac{4098 * \left[0.6108 * e^{\left(\frac{17.27 * T_{mean}}{T_{mean} + 237.3}\right)}\right]}{(T_{mean} + 237.3)^2} \quad (6.17)$$

γ is the psychrometric constant (in kPa $°C^{-1}$), determined as follows:

$$\gamma = 0.00163 * \frac{P}{\lambda} \quad (6.18)$$

And P is the atmospheric pressure (in kPa):

$$P = 101.3 * \left(\frac{293 - 0.0065 * Elev}{293}\right)^{5.26} \quad (6.19)$$

Where *Elev* is the elevation above sea level. We performed the calculation for a minimum elevation corresponding to 235 masl in Faya-Largeau and a maximum elevation corresponding to 925 masl in Amdjarass.

E_a (in mmd^{-1}) is a function of wind speed, saturation vapor pressure and average vapor pressure:

$$E_a = f(u) * ({v_a}^* - v_a) \quad (6.20)$$

f(u) is the wind function, as expressed in Penman (1956):

$$f(u) = 1.313 + 1.381 * u_2 \quad (6.21)$$

Where u_2 is the wind speed (in ms^{-1}).

$(v_a^* - v_a)$ is the vapor pressure deficit (in kPa). v_a^* is the daily saturation vapor pressure, determined with the expression:

$$v_a{}^* = \frac{v_T{}^*(T_{max}) + v_T{}^*(T_{min})}{2} \quad (6.22)$$

And v_T^* is determined for the minimum and the maximum temperature of the day:

$$v_T{}^* = 0.6108 * e^{\left[\frac{17.27*T}{T+237.3}\right]} \quad (6.23)$$

v_a is the mean actual vapor pressure, determined:

$$v_a = \frac{v_a{}^*(T_{max}) * \frac{RH_{max}}{100} + v_a{}^*(T_{min}) * \frac{RH_{min}}{100}}{2} \quad (6.24)$$

Where RH_{max} and RH_{min} are the maximum and minimum relative humidity (in %).

6.3.4. Estimation of actual evapotranspiration from LandSat8

6.3.4.1. General considerations

Several remote sensing products could have been used to estimate actual evapotranspiration. LandSat8 images were chosen because of their high spatial resolution (30 m). In addition to the Operational Land Imager (OLI) Sensors, providing multispectral images within the visible to near infrared wavelength, the LandSat8 satellite is also composed of the Thermal Infrared Sensors (TIRS), providing images (band 10 and 11) in the thermal wavelength at a resolution of 100 m. The two thermal bands, allow to apply techniques such as the split-window algorithm to estimate surface temperature.

In chapter 5, we already introduced the pre-processing steps (cloud mask, topographic correction, conversion from digital number to physical values). These steps are the same when calculating actual evapotranspiration or when extracting MNDWI36 values. Additionally, the TIRS digital numbers are converted to at-sensor radiance and brightness temperature, using the procedure described in USGS (2015). Uncertainties are estimated at 2% (band 10) and 4% (band 11) radiance for the TIRS bands (Roy et al., 2014). The thermal bands were resampled to the 30 m resolution of the visible and near infrared bands.

The procedure applied to calculate actual ET (see below) is based on the determination of an evaporative fraction expressing the “wetness” of a pixel, it is therefore not applicable if no “wet” pixels are present in the image. The MNDWI36 (see Chapter 5) was therefore used to undertake a first selection before processing the images for actual evapotranspiration estimation. From an initial set of 448 images, 165 were found to have some index of water and were processed to extract estimations

of actual evapotranspiration (see Figure 5.4 in Chapter 5). Within this set of images, 95 images were then selected as fulfilling the quality requirements (e.g. minimum cloud cover). All pre-processing and processing steps were performed in RStudio v. 1.1.463 (Team, 2015).

6.3.4.2. Principles of the method

The estimation of actual evapotranspiration from LandSat8 images is based on the energy balance equation. As already introduced, the net daily radiation (R_n) determines the amount of energy to heat the surface (the term *G* or soil heat flux), to exchange the heat from the surface to the air or reversely (the *H* term or sensible heat flux) and to change the state of water (the λET term or latent heat flux).

Given the limited amount of ground-truth for meteorological data, we used the simplified S-SEBI procedure from Roerink et al. (2000). This procedure determines an instantaneous evaporative fraction from the relationship between the albedo and the surface temperature, for a given pixel of the processed image. The evaporative fraction is defined as the ratio between the latent heat flux and the sum of sensible and latent heat flux. It, therefore, assumes that the content of water in the system largely rules the partition of the energy available for the different processes.

$$\Lambda = \frac{\lambda ET}{\lambda ET + H} = \frac{\lambda ET}{R_n - G} \tag{6.25}$$

In the original formulation from Roerink et al. (2000), *G* is estimated as a function of net radiation, surface temperature, albedo and Normalized Difference Vegetation Index (NDVI). The procedure described in Parodi (2002), indicates that *G* can be considered negligible on a daily basis.

The instantaneous evaporative fraction (Λ) is assumed to be constant on a 24h-basis (Parodi, 2002), as the relative partition of energy fluxes among its main components remains unchanged:

$$\Lambda_{24h} = \Lambda_{inst} \tag{6.26}$$

This assumption is surprisingly robust (Parodi, 2002), but significant variability might be caused by variably cloudy weather and by the proximity to surface discontinuities or fronts.

Daily actual evapotranspiration (ET_{day} in mmd^{-1}) is calculated:

$$ET_{day} = \frac{8.64 * 10^7 * \Lambda * R_n}{\lambda * \rho_w} = \frac{\Lambda * R_n}{28.588} \tag{6.27}$$

Where $\lambda = 2.47*10^6$ Jkg^{-1}, $\rho_w = 1000$ kgm^{-3} and R_n is the daily net radiation (in Wm^{-2}).

6.3.4.3. Determination of surface albedo

Broadband at-sensor albedo (α_{toa}) was determined by applying a classical procedure of linear conversion of the narrow bands through a weighting factor (Silva et al., 2016):

$$\alpha_{toa} = \sum_{b=2}^{7} p_b * r_b \quad (6.28)$$

Where p_b denotes the weighting factor and r_b the reflectance of bands 2 to 7 (b) of the LandSat8 multispectral image. The weighting factor is determined by the estimation of the solar constant (k_b, Chander and Markham, 2003):

$$k_b = \frac{\pi * L_b}{r_b * cos(Z * d_r)} \quad (6.29)$$

Where L_b is the radiance of bands 2 to 7 (b), Z is the sun zenith angle (extracted by the metadata file, 90°-sun elevation angle) and d_r corresponds to the correction of the eccentricity of the terrestrial orbit, given by:

$$d_r = \left(\frac{1}{d_{ES}}\right)^2 \quad (6.30)$$

Where d_{ES} is the Earth to Sun distance (extracted by the metadata file).

The values of the weighting factor (p_b) for each band is obtained by the ratio between k_b of band b (b = 2, 3, 4, 5, 6, 7) and the sum of all k_b value.

The conversion of the broadband at-sensor albedo (α_{toa}) to the surface albedo (α_{surf}) was performed using the following equation (Zhong and Yinhai, 1988; Bastiaanssen et al., 1998):

$$\alpha_{surf} = \frac{(\alpha_{toa} - \alpha_{atm})}{\tau_{oc}} \quad (6.31)$$

A mean value of 0.03 was applied for the atmospheric albedo (α_{atm}, Allen et al., 2002) and a constant value of 0.5 was applied for the two-way atmospheric transmittance (τ_{oc}, Parodi, 2002). Tests of more complex procedures for the determination of the two-way transmittance values (Allen et al., 2002) resulted in estimations of albedo which were seen to be too high, compared to typical albedo values for similar morphological contexts. Although simple, the use of constant values was therefore preferred.

6.3.4.4. Determination of surface temperature

Land surface temperature (T_{surf}) is determined using the practical split-window algorithm presented by Du et al. (2015):

$$T_{surf} = b_0 + \left(b_1 + b_2 * \frac{1-\varepsilon}{\varepsilon} + b_3 * \frac{\Delta\varepsilon}{\varepsilon^2}\right) * \frac{T_{10}+T_{11}}{2} + \left(b_4 + b_5 * \frac{1-\varepsilon}{\varepsilon} + b_6 * \frac{\Delta\varepsilon}{\varepsilon^2}\right) * \frac{T_{10}+T_{11}}{2} + b_7 * (T_{10} - T_{11})^2 \quad (6.32)$$

Where T_{10} and T_{11} are the brightness temperatures (in Kelvin) of the two thermal bands (band 10 and 11, USGS, 2015), resampled to the spatial resolution corresponding to the visible and near-IR bands (30 m resolution). b_n (n = 0,1, …, 7) are the coefficient corresponding to atmospheric water vapor of 0 to 2.5 gcm^{-2}, respectively: b_0 = -2.78009; b_1 = 1.01408; b_2 = 0.15833; b_3 = -0.34991; b_4 = 4.04487; b_5 = 3.55414; b_6 = -8.88394; b_7 = 0.09152. Root-mean-square error of temperature estimates associated to these coefficients are ± 0.34 K. The sensitivity of surface temperature to the abovementioned coefficients was tested by varying the values corresponding to different atmospheric water vapor conditions, but results showed a low variability (maximum 3% of variability). A value of 0.001 was set for the difference of band emissivity ($\Delta\varepsilon$). The mean land emissivity (ε) was determined by using the empirical equation from Valor and Caselles (1996):

$$\varepsilon = \varepsilon_v * P_v + \varepsilon_g * (1 - P_v) + 4 * d\varepsilon * P_v * (1 - P_v) \quad (6.33)$$

Where the emissivity of full vegetation cover (ε_v) was set at 0.99, the emissivity of bare soil (ε_g) at 0.91 and the vegetation structure parameter ($d\varepsilon$) at 0.02 (Valor and Caselles, 1996). The fractional vegetation cover (P_v) is determined by the equation:

$$P_v = \frac{NDVI - NDVI_g}{NDVI_v - NDVI_g} \quad (6.34)$$

NDVI was determined from the LandSat8 images with the common band rationing (modified for LandSat8 band widths):

$$NDVI = \frac{r_5 - r_4}{r_5 + r_4} \quad (6.35)$$

Where r_n (n = 4, 5) are the reflectance values of bands 4 and 5. Values of NDVI < 0.2 ($NDVI_g$) were considered as representing bare soils (P_v = 0) and values of NDVI > 0.5 ($NDVI_v$) were considered as representing full vegetation (P_v = 1).

6.3.4.5. Evaporative fraction

The evaporative fraction (Λ) for each pixel of the satellite image is determined by plotting all pixels in a coordinate system of surface temperature (in °C) versus surface albedo (Figure 6.2). Pixels close to a line of slope 0 and intercepting at the minimum value of surface temperature (T_{min}) represent "wet" pixels, mostly controlled by evaporative processes (sensible heat flux is null). Pixels close to a line of equation $y = a*x + b$, with slope (a) and intercept (b) being determined by the maximum values of T_{surf} and α_{surf}, represent "dry" pixels, mostly controlled by radiative processes (latent heat flux is null). The evaporative fraction is then determined (Roerink et al., 2000):

$$\Lambda = \frac{b + a * \alpha_{surf} - T_{surf}}{b - T_{min} + a * \alpha_{surf}} \quad (6.36)$$

Assuming a constant atmospheric condition over the image and the presence of sufficient "wet" pixels.

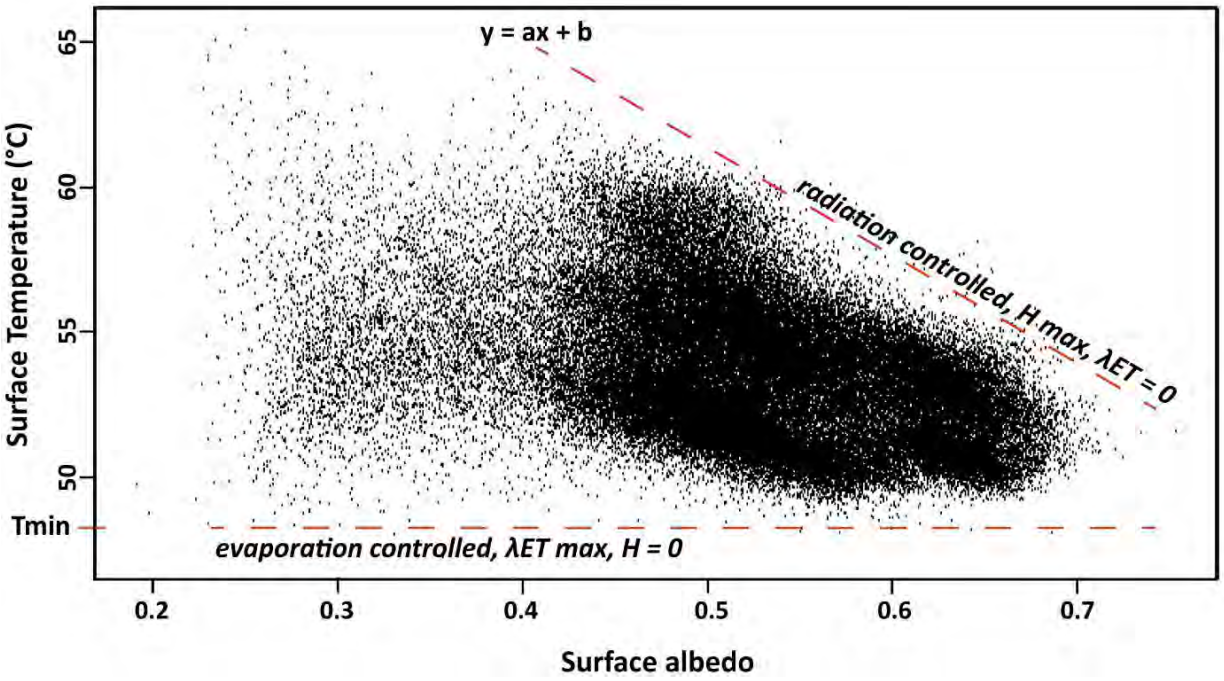

Figure 6.2: Plot of surface temperature versus surface albedo for the determination of the evaporative fraction (LandSat8 scene 180047 of 15 August 2013).

6.4. Results

6.4.1. Net radiation and potential evapotranspiration

Figure 6.3A presents the annual variation of the energy components (in $MJm^{-2}d^{-1}$), applied to the region of Northern Chad: extraterrestrial solar irradiance, incoming solar radiation, net longwave radiation and daily net radiation. The upper and lower limit of daily net radiation were calculated using two extreme values of albedo: 0.08 for deep water and 0.4 for white sand. The temporal pattern is well expressed by the curve showing lower total available radiation during the winter months and higher total radiation rates during the summer months.

Figure 6.3B compares the energy components (extraterrestrial solar irradiance, incoming solar radiation and net radiation, in mmd^{-1}) with the potential evapotranspiration (ETP) calculated by using the Turc, Hargreaves and Penman methods. The daily rates of ETP calculated with the Turc and Hargreaves methods are averaged.

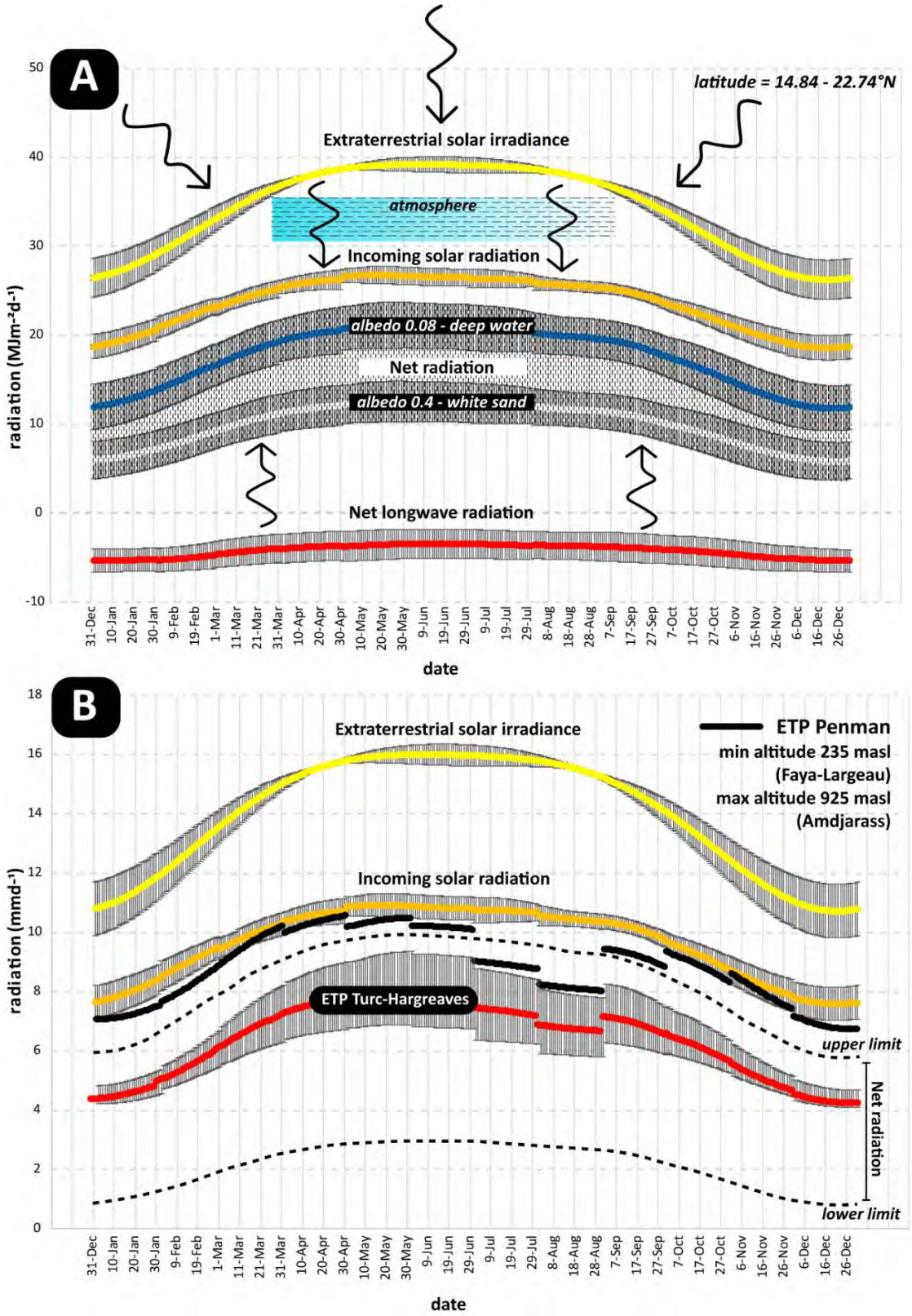

Figure 6.3: A) Annual dynamics of the radiation components (in $MJm^{-2}d^{-1}$): extraterrestrial solar irradiance, incoming solar radiation, net outgoing longwave emission and daily net radiation. Daily net radiation was calculated by using two extreme values of albedo, 0.08 for deep water and 0.4 for white sand. B) Extraterrestrial solar irradiance, incoming solar radiation and daily net radiation (upper limit corresponds to deep water as reflecting surface, lower limit corresponds to white sand as reflecting surface) are converted to mmd^{-1} and compared to the yearly changes of potential evapotranspiration calculated with the Turc, Hargreaves and Penman expressions. The daily rates are calculated using long-term averaged values (see Table 6.1).

Daily net radiation varies between 6 and 9 mmd^{-1} for the upper limit (in the case of deep water being the reflecting surface) and between 1 and 3 mmd^{-1} for the lower limit (in the case of white sand being the reflecting surface). Minimum and maximum values represent the values in winter and summer, respectively. Annual rates amount at 786 mm (lower limit) to 3,030 mm (upper limit). Potential evapotranspiration determined with the Turc and Hargreaves methods are estimated between 4 and 8 mmd^{-1}, for an annual ETP rate varying between 2,300 and 2,470 mm. Potential evapotranspiration calculated with the Penman expression varies between 7 and 11 mmd^{-1}, for an annual rate of ETP of 3,235 mm.

The annual estimates of the Turc, Hargreaves and Penman ETP reveal a decreasing rate of potential evapotranspiration during the months of July and August, resulting from the increased humidity experienced by the region with the arrival of the summer monsoons. To be noted that the Hargreaves expression uses only the extraterrestrial solar irradiance and air temperature data (min, max, mean), and not the humidity data. In our example, however, the Turc and Hargreaves are presented as averaged.

The Penman ETP estimates are systematically higher than the Turc-Hargreaves estimates, which is the result of the aerodynamic term included in the Penman equation. Winds are blowing with decreased intensities from February to August (2 to 3 ms^{-1} in Faya-Largeau and Fada) and increased intensities from August to November (4 ms^{-1}). The highest intensities are reached along the axis between Tekro and Faya-Largeau.

6.4.2. Actual evapotranspiration

6.4.2.1. Potential and actual evapotranspiration

Figure 6.4 shows the comparison between potential (Turc-Hargreaves and Penman) and actual evapotranspiration values (mean of the whole image, mean of the “wet” pixels only, “wet” pixels meaning with a positive MNDWI36 index), for the same dates. Estimations of actual evapotranspiration show no correlation with the estimations of potential evapotranspiration. This is particularly true when comparing the mean ET value of the whole image (R^2 = 1-2%, Figure 6.4 left). R^2 is slightly higher when the mean values of the “wet” pixels are used (R^2 = 11-18%, Figure 6.4 right).

Potential evapotranspiration determined with the Turc and Hargreaves methods are estimated between 6 and 8 mmd^{-1}, and between 8 and 11 mmd^{-1} with the Penman method. Mean actual evapotranspiration estimates, calculated for the whole set of the 95 processed images, vary between 0.2 and 2 mmd^{-1} (for the entire image) and between 0.5 and 7 mmd^{-1} (for the “wet” pixels only).

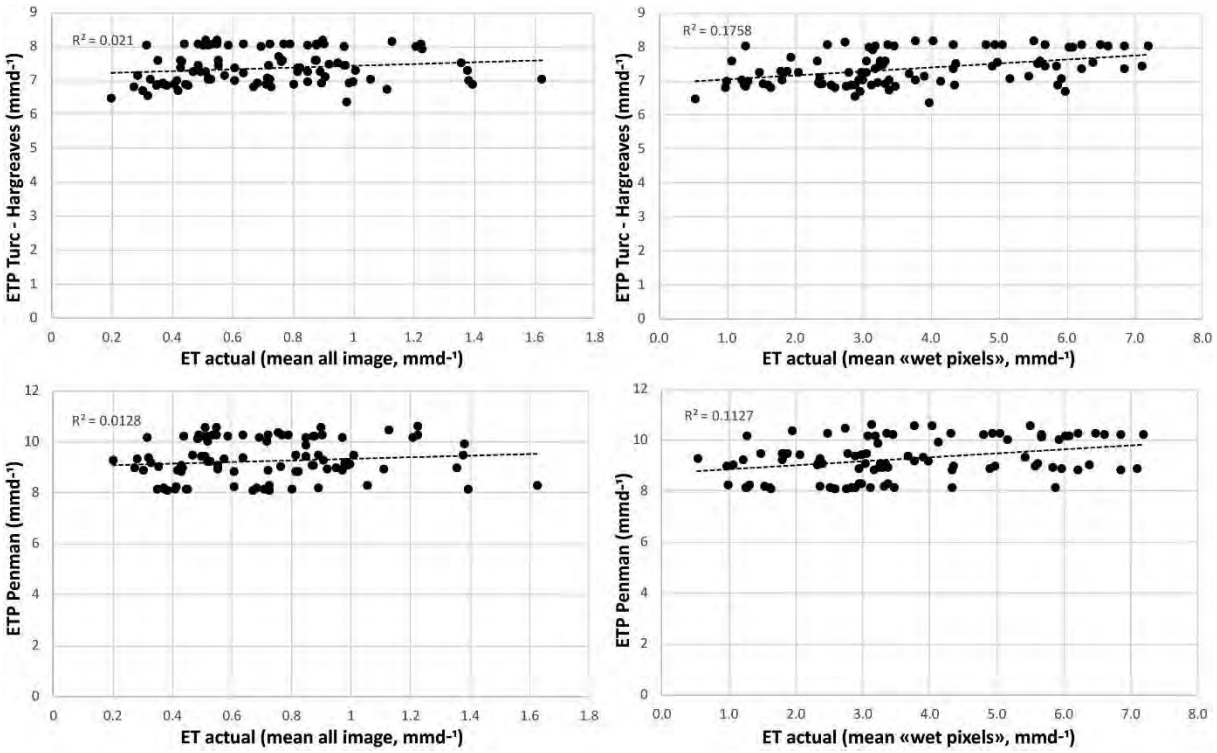

Figure 6.4: Comparison of potential evapotranspiration (Turc-Hargreaves and Penman) and actual evapotranspiration extracted from LandSat8 images. Each point represents an image date. On the left, potential evapotranspiration is compared to the mean ET value for the whole image. On the right, it is compared with the mean ET value for the "wet pixels" of the image. Correlation coefficients (R^2) are shown.

When considering the whole image, mean actual ET is low compared to the mean actual ET of the "wet pixels" and to the estimates of daily potential evapotranspiration. This is to be expected as the region is generally arid with only a limited amount of surface water occurrences. When only the "wet" pixels are taken into consideration, the rates are more close to the ETP estimates. Rates of actual ET of the "wet" pixels show however a higher variability (Δ = 6.5 mmd^{-1}). This is also to be expected as the satellite captures all kinds of "surface water occurrence", such as free surface water (lakes) or different degrees of soil wetness during and after a flood event. In addition, a 30 m pixel might contain humid and not humid areas, the value given being the mean of ET for the pixel under consideration. Figure 6.5 presents an example of the differences between mean actual ET calculated for the whole image or only for the "wet" pixels (scene 180048 for the 15thof August 2013). On the right, the MNDWI36 is superposed to the actual evapotranspiration map.

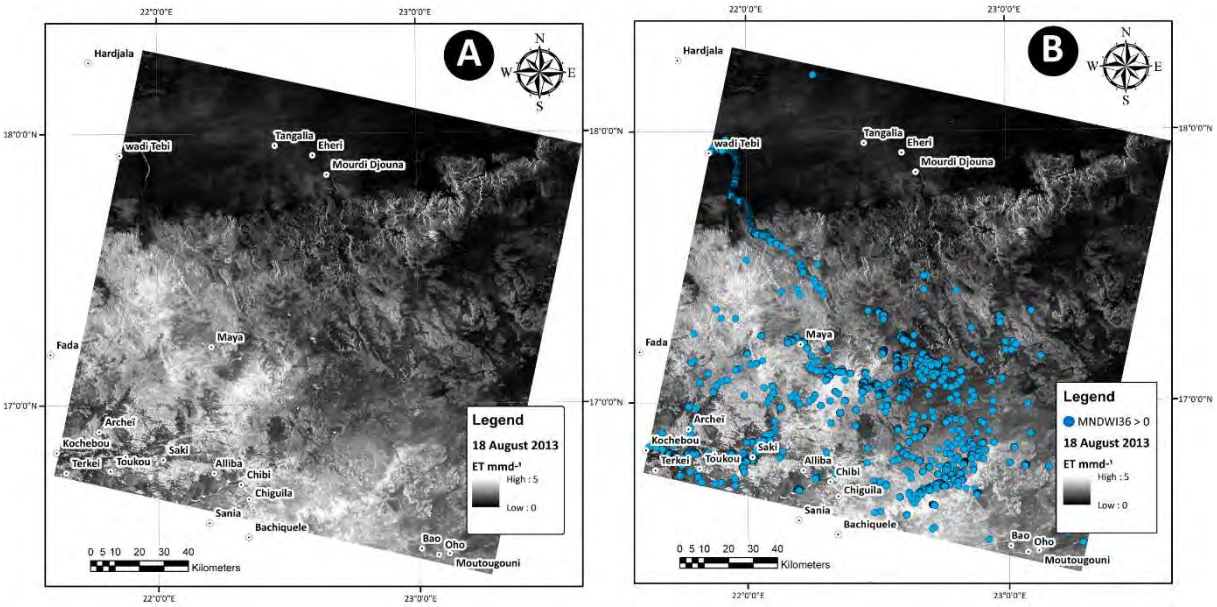

Figure 6.5: Actual ET map of 15 August 2013 (scene 180048 over the Ennedi Mountains). On the right, the MNDWI36 is superposed to the map. The comparison expresses the differences of correlation degree between actual and potential evapotranspiration, if the whole image (A) or only pixels corresponding to a positive MNDWI36 index (B) are used.

The weak correlation between actual ET and ETP estimates shows that, in this region, it is not possible to use the ETP continuous series to interpolate the actual evapotranspiration maps for the dates without an image. The slightly higher correlation shown when using only the pixels with a positive MNDWI36, tends to indicate that higher correlation coefficients could be expected in more humid environments.

The few ground-truth meteorological data available for the region of Northern Chad are not sufficient to calibrate nor to perform an uncertainty analysis on our actual ET estimates. Absolute values of actual ET will have considerable uncertainties. However, despite limited accuracy concerning absolute values, the relative changes from image to image are highly useful to observe evapotranspiration processes occurring in the alluvial systems of wadis, especially when combined with the MNDWI36 index (see Chapter 5).

6.4.2.2. Regional distribution of actual ET

The total range of actual evapotranspiration rates (minimum and maximum values), is between 0 and 7 mmd^{-1} for the 95 processed images. Figure 6.6 shows the standard deviation, indicating the different degree of changes between scenes of different dates.

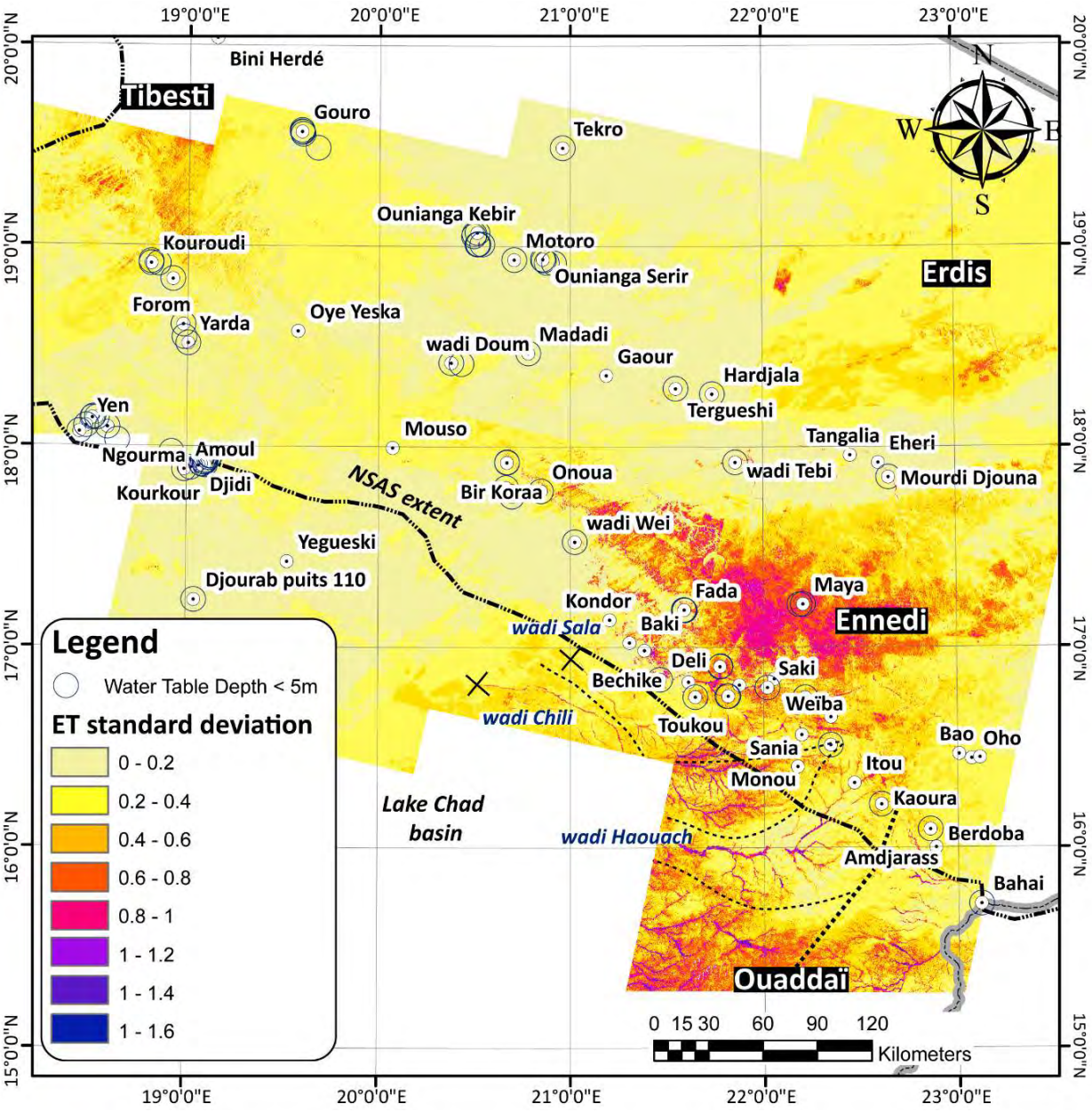

Figure 6.6: Standard deviation of actual evapotranspiration. Blue circles means inspected localities with a water table depth < 5 m bgl.

A low standard deviation means no significant changes of ET during the year. This can be either associated with no ET at all (dry areas), or with permanently flooded areas (e.g. lakes, perennial ponds). A large standard deviation means that areas experience episodic precipitation and runoff, with subsequent increase of ET (for example along wadis).

The lakes of Ounianga Kebir and Serir are located in a region of low actual ET standard deviation. This zone extends south-easterly into the Mourdi depression (Gaour, Hardjalla, wadi Tebi, Tangalia, Eheri, Mourdi Djouna), and south-westerly towards the West Palm Groves (Oye Yeska, Forom, Yarda, Yen,

Ngourma). Another zone of low amplitude of actual ET changes extends from the south-west of the Ennedi Mountains (wadi Wei, Bir Koraa) towards the Djourab (Yegeski, puits Djourab 110).

WNW of the lakes of Ounianga, the oases of Gouro are located at the foothill of the Tibesti Mountains. A slightly higher standard deviation is detected in proximity of the Tibesti Mountains from Gouro to Kouroudi. Similar amplitudes of changes are also observed in the central lowlands between Bir Koraa, Mouso, wadi Doum, Oye Yeska, the West Palm Groves (Yen, Ngourma) and Faya-Largeau (Amoul, Djidi, Kourkour), and south of the Erdis plateaus.

ET standard deviation is higher within the region of the Ennedi Mountains and more southerly (Ouaddaï). The networks of the wadis are well distinguishable, indicating an increased hydrological activity provoking large variations of the ET rates. In the Ouaddaï basement and south of the Ennedi Mountains, the inundated branches of wadis Haouach, Chili (named Sini in its upstream zone) and Sala show their catchment extent (dashed lines) and mark the NE-SW and NNE-SSW ridges, which separate the Nile from the Lake Chad hydrological basins (Chapter 4). Along wadis Chili and Sala, the changes of actual ET are no more detectable north-west of 20°30’ – 21°E (location is indicated by a cross).

6.4.2.3. Distribution of ET in the eastern zone resulting from precipitation

As shown by Figure 6.6, the highest changes of ET are concentrated in the eastern regions (Ouaddaï, Ennedi). Moderate ET changes are also detected south of the Erdis plateau, in a low-lying zone at the foothill of the topographic break. As seen by the analysis of precipitation in Chapter 5, rates are slightly increased south of the Erdis plateaus because of the absence of the Ennedi topographic relief, otherwise blocking the SW-originating monsoonal pattern.

The analysis of the monthly distribution of precipitation rates for different years (2013 to 2016) shows a comparable temporal distribution but variable rates between years (Chapter 5). The actual ET rates and the amplitude of the changes are correlated to the rates of precipitation. Figure 6.7 shows a comparison between the years 2013 and 2014. The figure shows an increased actual evapotranspiration rate in 2014 compared to 2013, in response to the more elevated precipitations occurring in 2014.

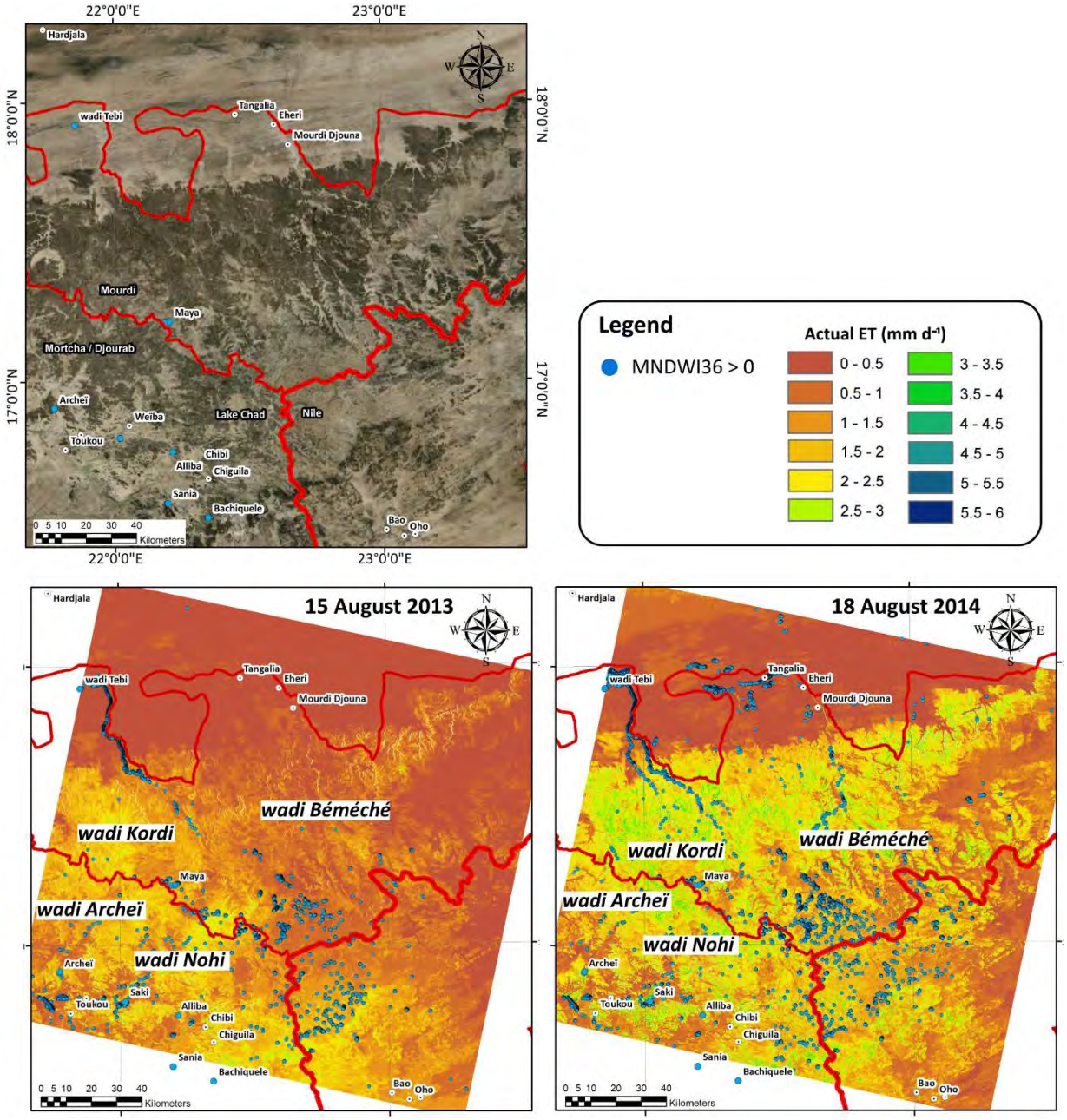

Figure 6.7: Actual evapotranspiration rates in the Ennedi Mountains (in mmd^{-1}). Are compared years 2013 and 2014 (scene 180048).The MNDWI36 positive index is also shown.

The temporal dynamics of runoff and accumulation of surface water in response to rainfall within the Ennedi Mountains is shown in the following selection of images. Year 2014 is taken as an example for most of the zones here described, because of the higher rates of precipitation, therefore allowing to establish a maximum amplitude of the response within the years of observation (2013-2016, see Chapter 5).

In 2014, a mean rate of 5 mm and 10 mm of rain have occurred south of the Erdis plateaus during the months of July and August, respectively. Mean precipitations rates of 20 mm during the month of July, 70 mm during the month of August and 10 mm during the month of September have occurred over

the Ennedi Mountains. The MNDWI36 index shows increased surface water on 18th of August 2014 south of the Erdis plateaus, qualitatively matching the pattern of precipitations. In the Ennedi Mountains, more extended areas of surface water (MNDWI36 > 0) are visible on 2nd of August 2014, decreasing on the subsequent image (18th August 2014). And finally, both the regions (south of the Erdis plateaus and Ennedi Mountains) show higher rates of actual ET on 2nd of August 2014, decreasing on the subsequent image (18th August 2014).

The increased surface water extent (positive MNDWI36 index) and highest rates of actual ET occurring beginning of August, is explained as the result of humid evaporating surfaces after rainfall and a time of acquisition of the satellite image shortly after the precipitation event. Images might be acquired soon after a rainfall event or several days after. An increased time between the rainfall event and the acquisition of the image mid of August, might explain why ET rates are higher beginning of August and not during the period of highest rainfall rates (mid-August).

Figures 6.8 to 6.12 show the 2014 temporal pattern of wadis Archeï, Nohi, the high plains, wadi Kordi and wadis Haouach and Sini-Chili, from soon after the first precipitations (2 August), during the time of supposedly maximum precipitation rates (18 August) and at the end of the rainy season (3 September). As seen in Chapter 5, wadis Kordi, Archeï, Nohi and the high plains of the mountain chain, experience a yearly dynamics of precipitation-runoff-accumulation. Wadi Béméché shows an increased response only during the years of higher precipitation rates (e.g. 2014).

The overall distribution of the response in the Ennedi Mountains indicates that in the high plains and along wadis connected through fractures to the high plains and flowing towards the south and towards the north, surface water accumulates rapidly after precipitation (wadis Archeï, Nohi, Kordi and the high plains, Figures 6.8 to 6.11). The more southern wadis (Haouach, Sini-Chili) show a maximum extent of surface water and highest evapotranspiration rates at the same time as the downstream areas of the wadis connected to the high plains (Figure 6.12). Also to be noted that, the hydrological response within the northern slopes (Mourdi sub-basin) is visible only along narrow areas of the wadi systems and no response is observed within the Mourdi depression, apart from the concentrated flow of wadis Kordi (Figure 6.11) and Béméché. Surface water accumulates in the downstream area of the northerly and southerly flowing wadis, where it progressively disappears after the rainy season as a result of evapotranspiration and potentially infiltration.

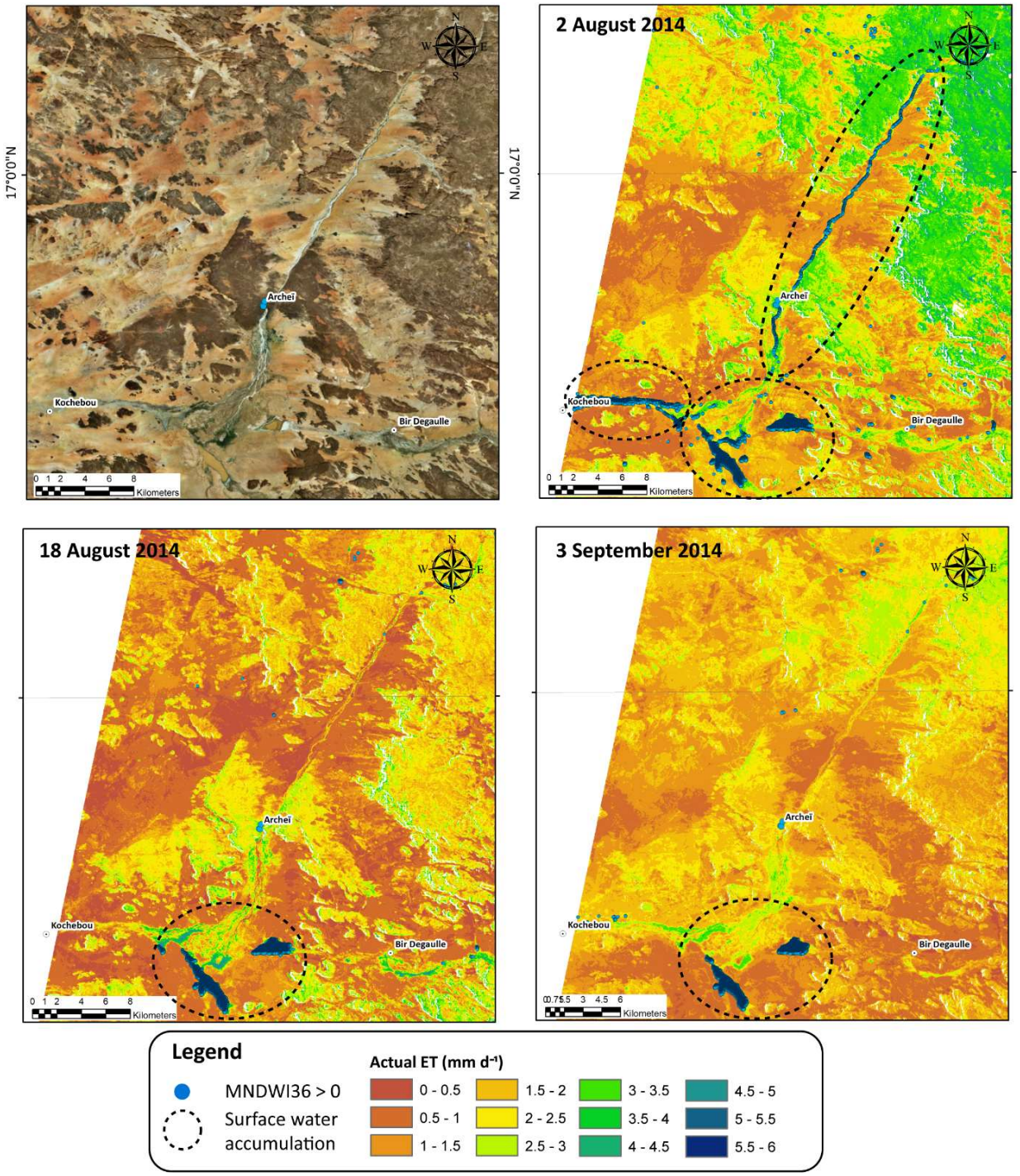

Figure 6.8: Evapotranspiration maps (in mmd^{-1}) showing the dynamics of runoff and accumulation in wadi Archeï during the 2014 rainy season. Localities of water accumulation (MNDWI36) are indicated.

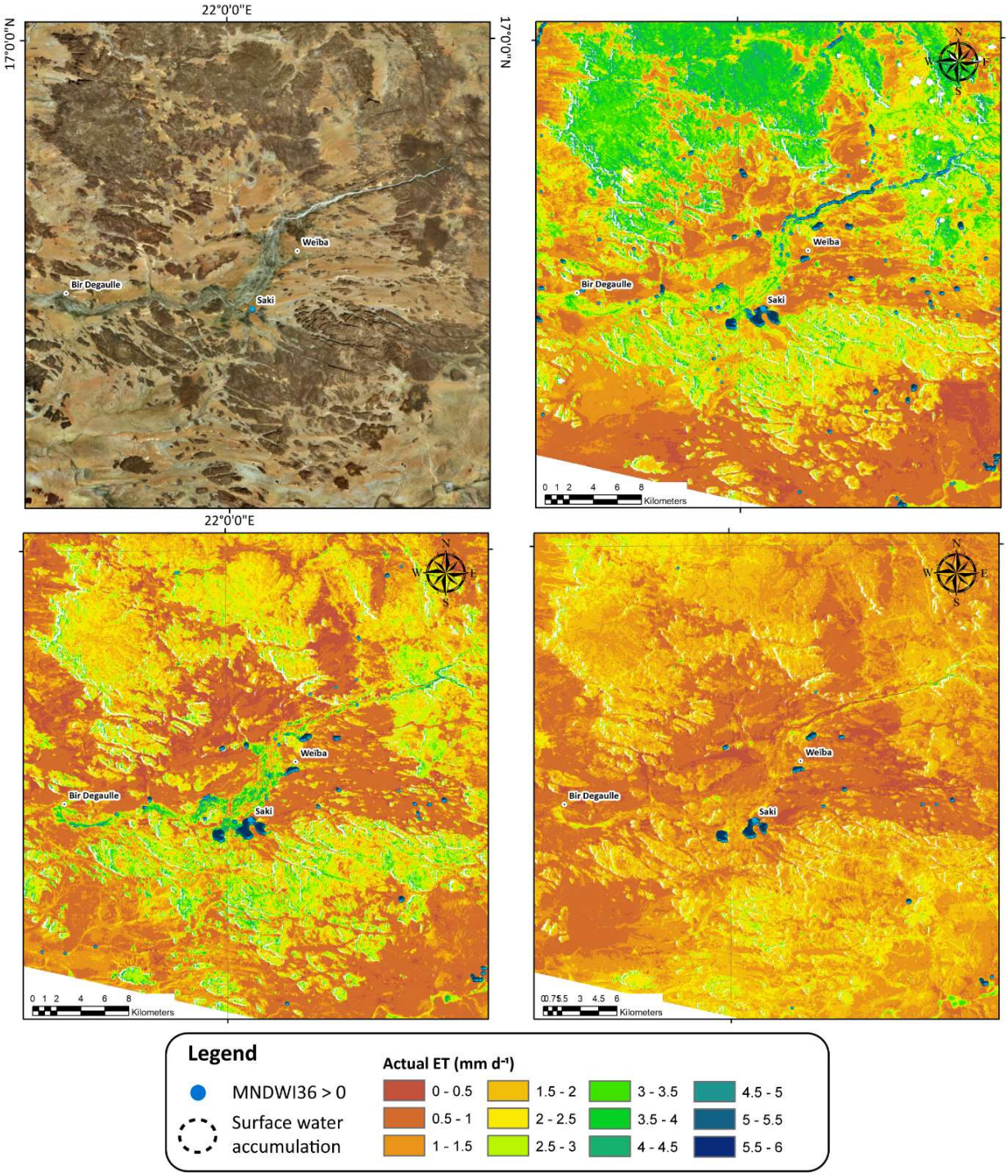

Figure 6.9: Evapotranspiration maps (in mmd^{-1}) showing the dynamics of runoff and accumulation in wadi Nohi during the 2014 rainy season. Localities of water accumulation (MNDWI36) are indicated.

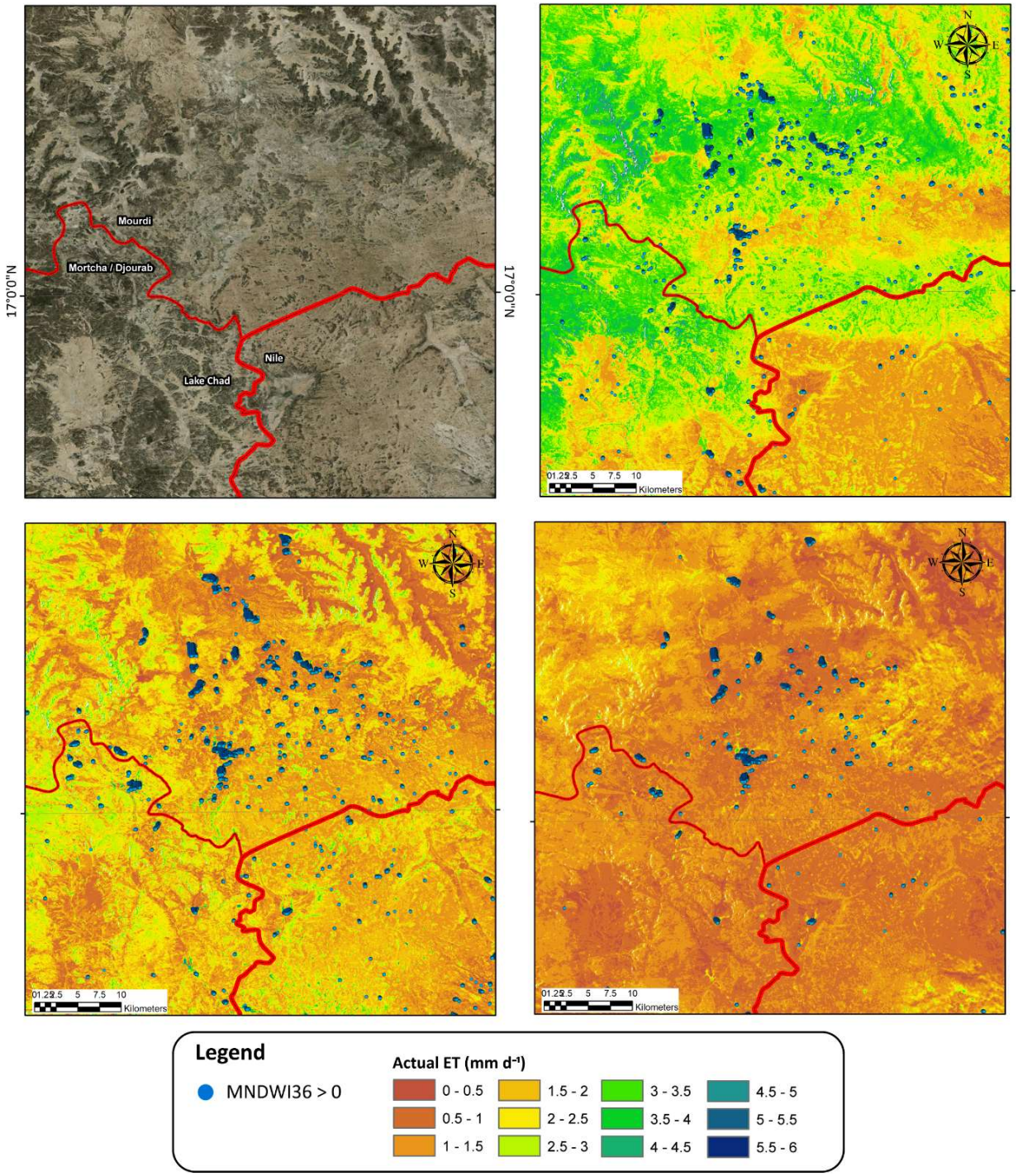

Figure 6.10: Evapotranspiration maps (in mmd^{-1}) showing the dynamics of surface water accumulation in the high plains of the Ennedi Mountains during the 2014 rainy season. Localities of water accumulation (MNDWI36) are indicated.

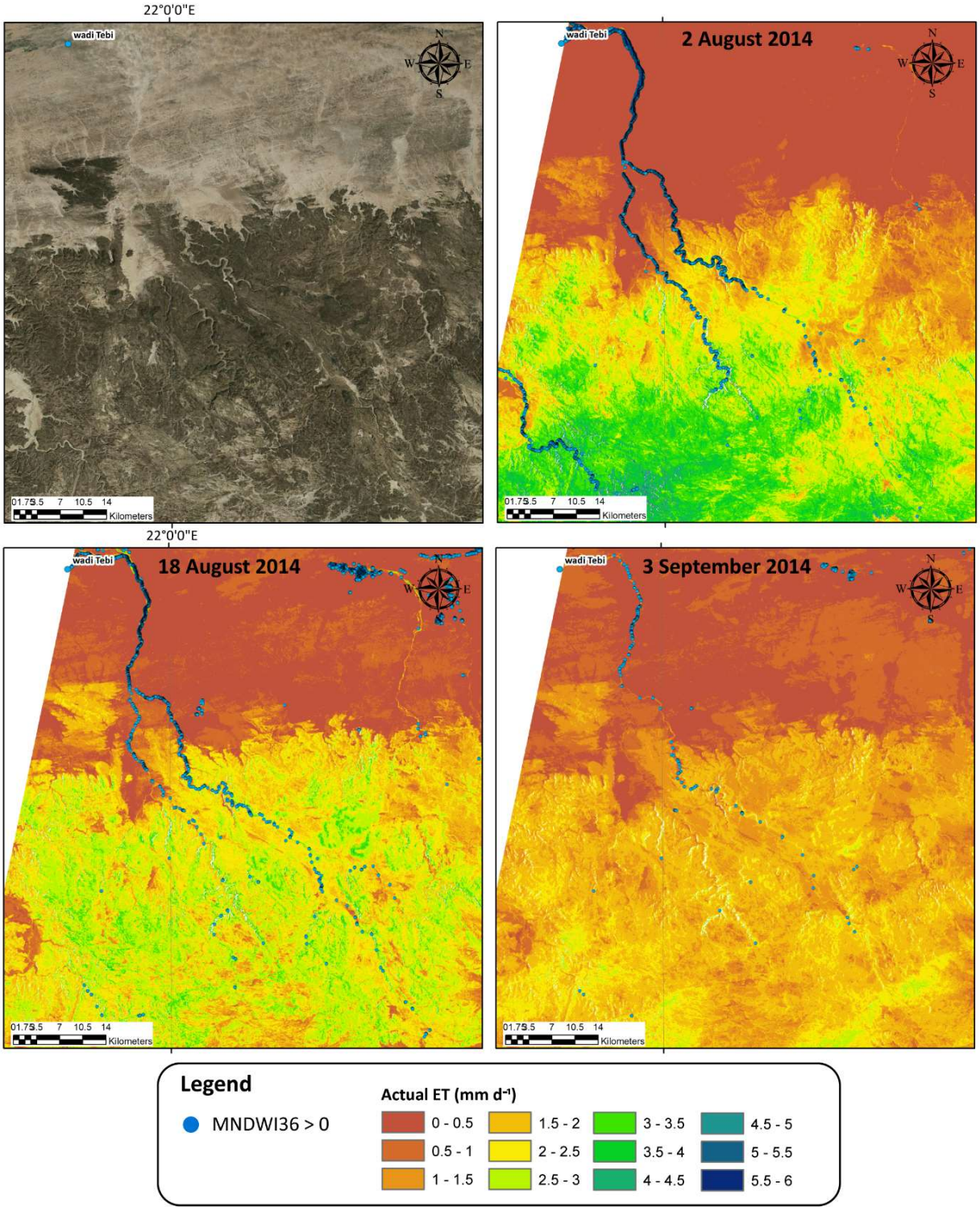

Figure 6.11: Evapotranspiration maps (in mmd^{-1}) showing the dynamics of runoff and accumulation in wadi Kordi during the 2014 rainy season. Localities of water accumulation (MNDWI36) are indicated.

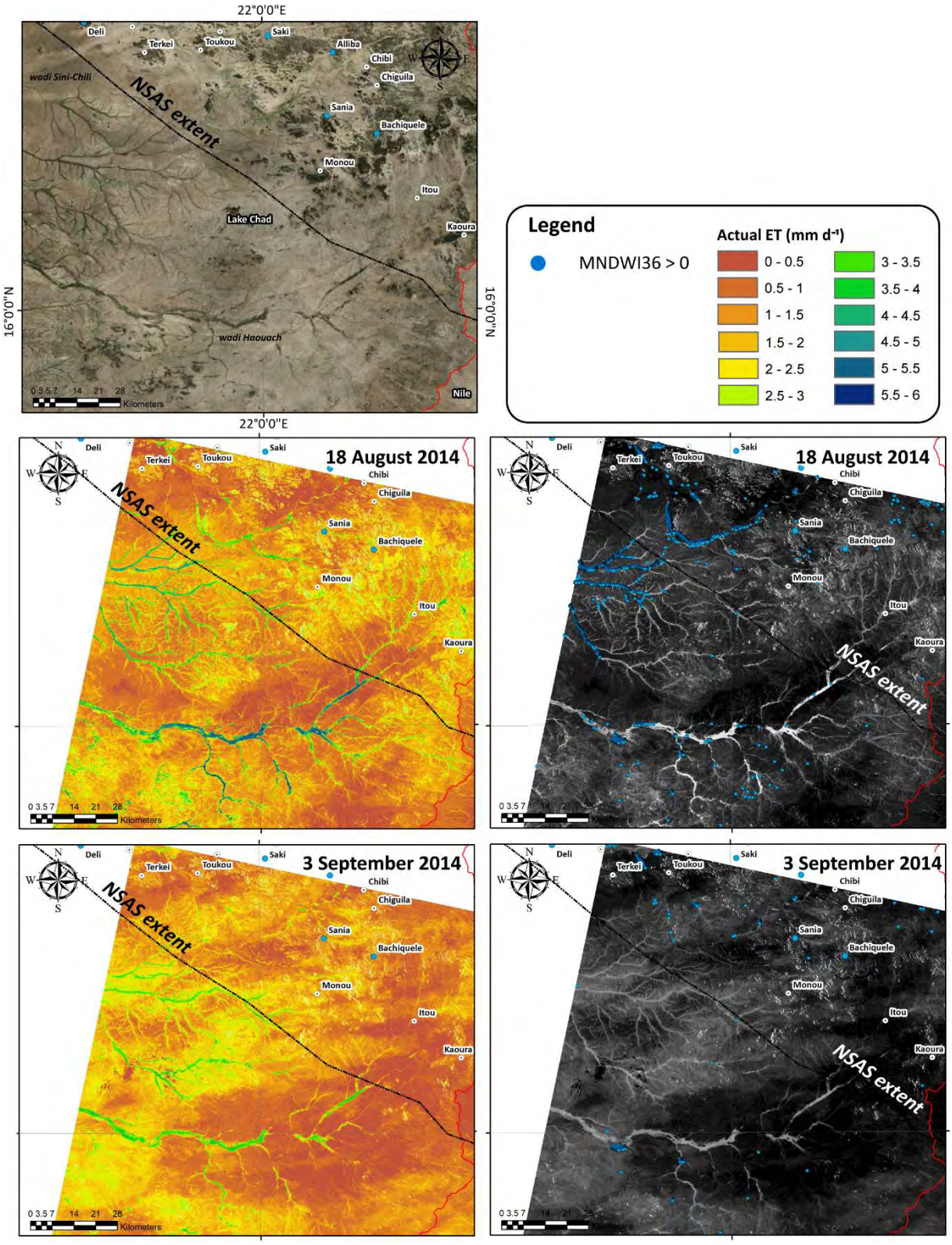

Figure 6.12: Evapotranspiration maps (in mmd^{-1}) showing the dynamics of runoff and accumulation in wadi Haouach and wadi Sini-Chili during the 2014 rainy season. The evapotranspiration map is shown with colors on the left and with a scale of greys on the right. On the right image, localities of water accumulation (MNDWI36) are indicated.

Mid of August, the zones of water accumulation in the downstream of wadis Archeï and Nohi, along the main branches of wadi Kordi and in the high plains, show a relatively constant extent compared to the image of 2nd August 2014 (Figures 6.8 to 6.11). Higher evapotranspiration rates and increased surface water extent is also seen to occur for wadis Haouach and Sini-Chili on 18th of August (Figure 6.12).

The images of September show only few remaining zones of surface water accumulation (ponds). In wadi Archeï (Figure 6.8), two ponds collect surface water downstream. The evapotranspiration map shows, however, higher rates in correspondence to the alluvial system with sparse or dense vegetation persisting during the month of September. Wadi Nohi (Figure 6.9) also shows the accumulation of water in restricted areas. Low rates of evapotranspiration are detected in the alluvial system of wadi Nohi during the month of September. The high plains (Figure 6.10) show the accumulation of runoff in localized zones, in the form of natural ponds. These zones are representing local low-lying flat areas of 1 km maximum width, located in correspondence to fractures or discontinuities in the sandstone layers. These natural ponds persist during the month of September. Persistence of surface water at the beginning of September occurs in the downstream zone and along the main channel of Wadi Kordi (Figure 6.11). Slightly higher actual evapotranspiration rates were also detected during the month of August in a wadi east of wadi Kordi, where surface water accumulation (MNDWI36 > 0) was only detectable in the downstream area. Wadis Haouach and Sini-Chili also show decreased extent of surface water and lower evapotranspiration rates at the beginning of September (Figure 6.12).

Towards the West, the Ennedi region is increasingly dry. Figure 6.13 uses the two most representative images (7 September 2013 and 25 August 2014) to show the extent of the “inundated” wadi network (wadi Chili and Sala). As shown by the true-color image, the wadi is also marked by a line of vegetation. The higher evapotranspiration rates (2 to 3 mmd^{-1}) along the branches of the wadis are the result of vegetation and soil moisture, and not surface water, as indicated by the relatively few zones of water accumulation (MNDWI36 > 0). The higher ET rates disappear north-west of 20°30’E.

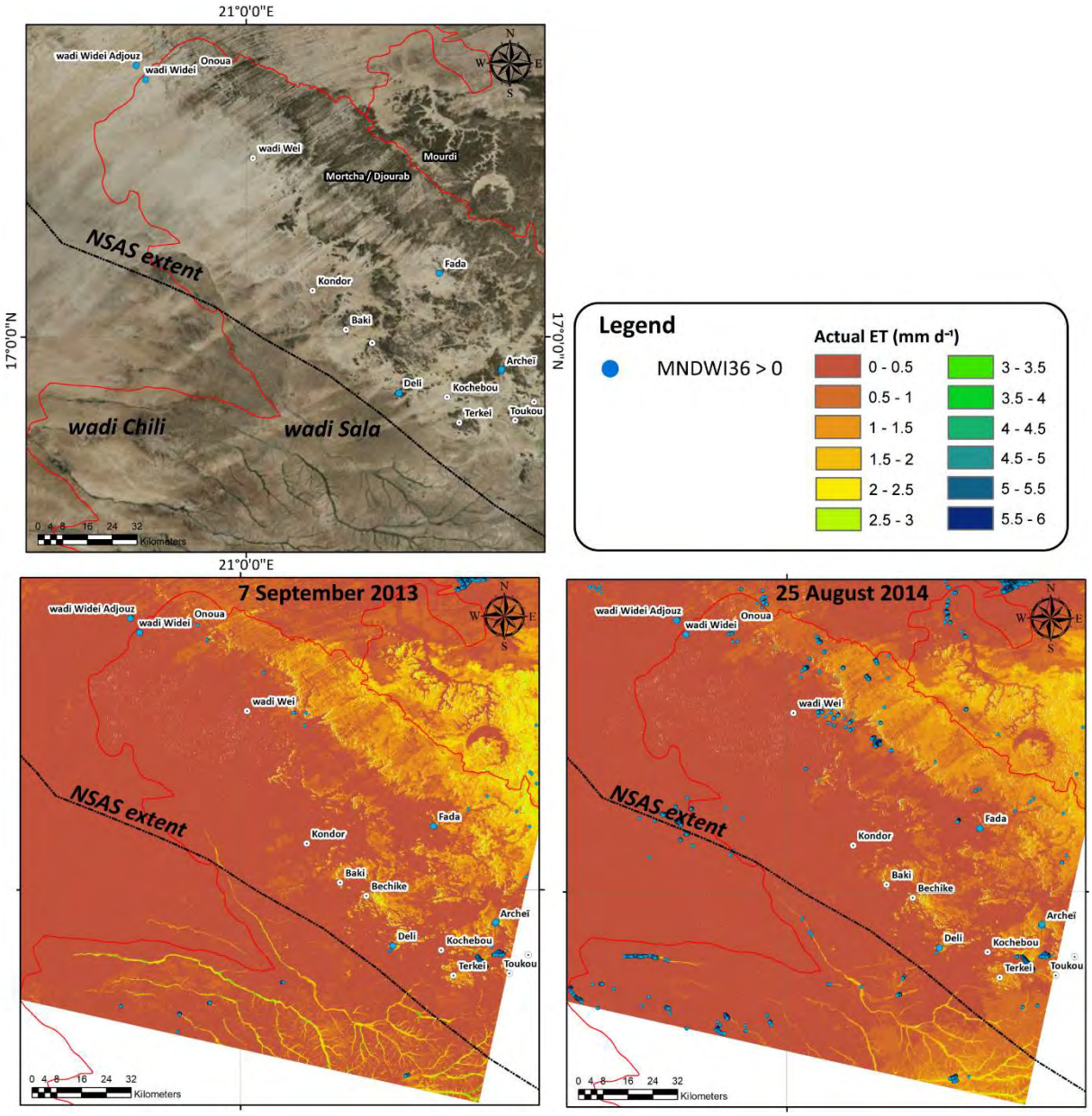

Figure 6.13: Evapotranspiration maps (in mmd^{-1}) of the western Ennedi (7 September 2013 and 25 August 2014). Localities of water accumulation (MNDWI36) are indicated.

6.4.2.4. Distribution of ET in the main discharge zones of the NSAS of Northern Chad

The southern slopes of the Tibesti Mountains (West Palm Groves, Faya-Largeau, Yarda-Kouroudi) feature very low rates of precipitation. Variabilities of actual evapotranspiration rates (absolute rates or extent of surfaces of increased ET rates) are also low, generally more marked during the rainy seasons (winter and summer rains). Figure 6.14 shows the oases of the West Palm Groves and of Faya-Largeau, with a true-color image as a background (on the top) and a selected number of actual evapotranspiration maps of different dates. An increased evapotranspiration rate is observed after the winter rains (West Palm Groves, 21 March 2016) and after the summer monsoons (West Palm Groves,

24 September 2014). The intensity of the response remains nevertheless low. In Faya-Largeau, an increase of evapotranspiration is seen to occur beginning of July 2016 (a mean of 5 mm of rain occurred during the month of July over the region, Chapter 5). The absence of images fulfilling the quality requirements for the month of August, do not, however, permit to confirm this trend.

Evapotranspiration annual volumes from the vegetated areas of the oases of Faya-Largeau and the West Palm Groves are estimated at 10 x 10^6 m^3y^{-1} and 4 x 10^6 m^3y^{-1}, respectively (see section 6.4.3). Evapotranspiration losses from the oases of Faya-Largeau are comparable to losses from the lakes of Ounianga Kebir (see below). However, the total extent of the Faya-Largeau oases and its vegetated and agricultural areas are 3 times the extent of the lakes in Ounianga Kebir. Irrigation in Faya-Largeau is performed by flooding the palm groves, which might be the reason for the highest losses in Faya-Largeau (mean actual ET value 1.2 mmd^{-1}) compared to the West Palm Groves (mean actual ET value 1 mmd^{-1}).

South-west of Kouroudi, the Bedo salt pans have a limited extent of perennial surface water (MNDWI36, Figure 6.15), but actual evapotranspiration maps show higher evapotranspiration rates in correspondence to vegetated areas and zones of phreatic evaporation.

The differences of evapotranspiration rates, the extent of vegetated areas and of zones of phreatic evaporation are small from date to date, but show a pattern repeated annually (Figure 6.15). For the images inspected in this study, maxima occur during the months of March to May. A decrease of the extent of humid vegetated areas is observed for the months of June, July and September. The pattern therefore doesn't linearly correlate to the rainfall rates.

Evapotranspiration annual volumes from the vegetated areas of the oases of Bedo are estimated at 3 x 10^6 m^3y^{-1} (see section 6.4.3), corresponding to 3-4 times the losses from the Gouro oases, but 13-30% of the losses from the Ounianga lakes (see below).

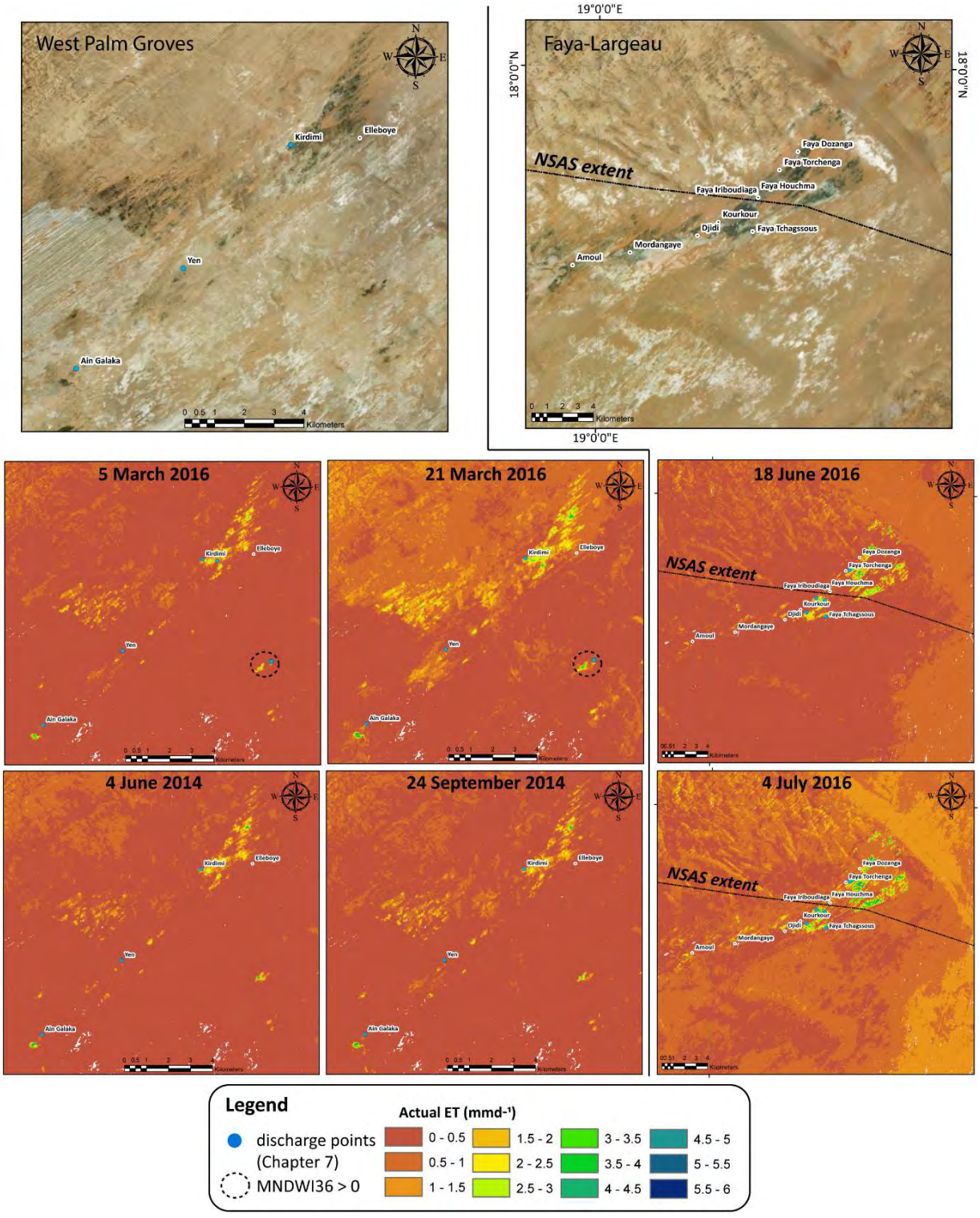

Figure 6.14: West Palm Groves and oases of Faya-Largeau. On the top, the oases are shown with a true-color image as a background. Below, are shown the evapotranspiration maps for different dates (in mmd^{-1}). Localities of groundwater discharge are indicated when sampled (see Chapter 7, blue dots).

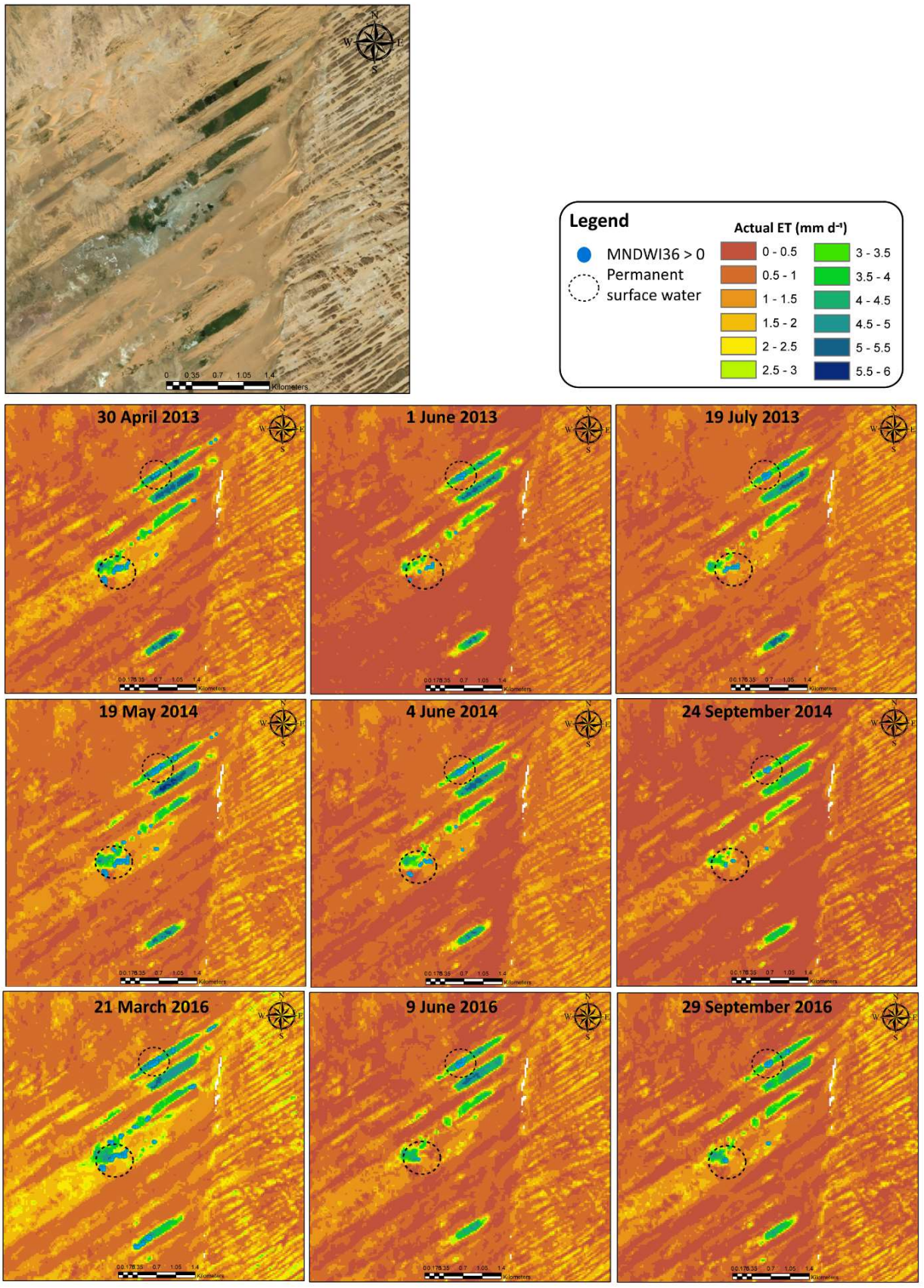

Figure 6.15: Oases of Bedo. On the top, the oasis is shown with a true-color image as a background. Below, are shown the evapotranspiration maps for different dates (mmd^{-1}). The differences in extent of vegetated areas and zones of phreatic evaporation are small within date, but show an annual pattern. The zones of permanent surface water are indicated.

The region extending between the south-eastern slopes of the Tibesti Mountains (oasis of Gouro) and the Ounianga Lakes, is interested by very low annual precipitation rates. Surface water accumulates only during a short period of time during the most favorable years (e.g. 2014). Small changes of actual ET (Figure 6.6) were detected in this region. Figure 6.16 shows the distribution of actual evapotranspiration rates (mean value of all the processed images covering the oases) within the oases of Gouro.

In Gouro, groundwater is generally close to but not reaching the surface, apart from two localities (Guelta voyageur and spring of Houkoudoubou). Densely vegetated areas have comparable actual evapotranspiration rates (Figure 6.16, 3 to 5 mmd^{-1}) as zones identified as shallow water covered by vegetation in Ounianga Kebir and Serir (see below). Rates of 0.5 to 2 mmd^{-1} are observed over sparsely vegetated areas, potentially with some contribution of phreatic evaporation. Higher rates of evapotranspiration are observed within the vegetated areas located to the NE, close to the outcrop of rock formations (note the red color of the Ounianga formation), indicating a groundwater flow direction from the NE to SW.

Evapotranspiration annual volumes from the vegetated areas of the oases of Gouro are estimated at 0.8×10^6 m^3y^{-1} (see section 6.4.3). Losses in Gouro correspond to 3 – 8% compared to the losses of evapotranspiration from the oases of Ounianga Kebir and Serir (see below).

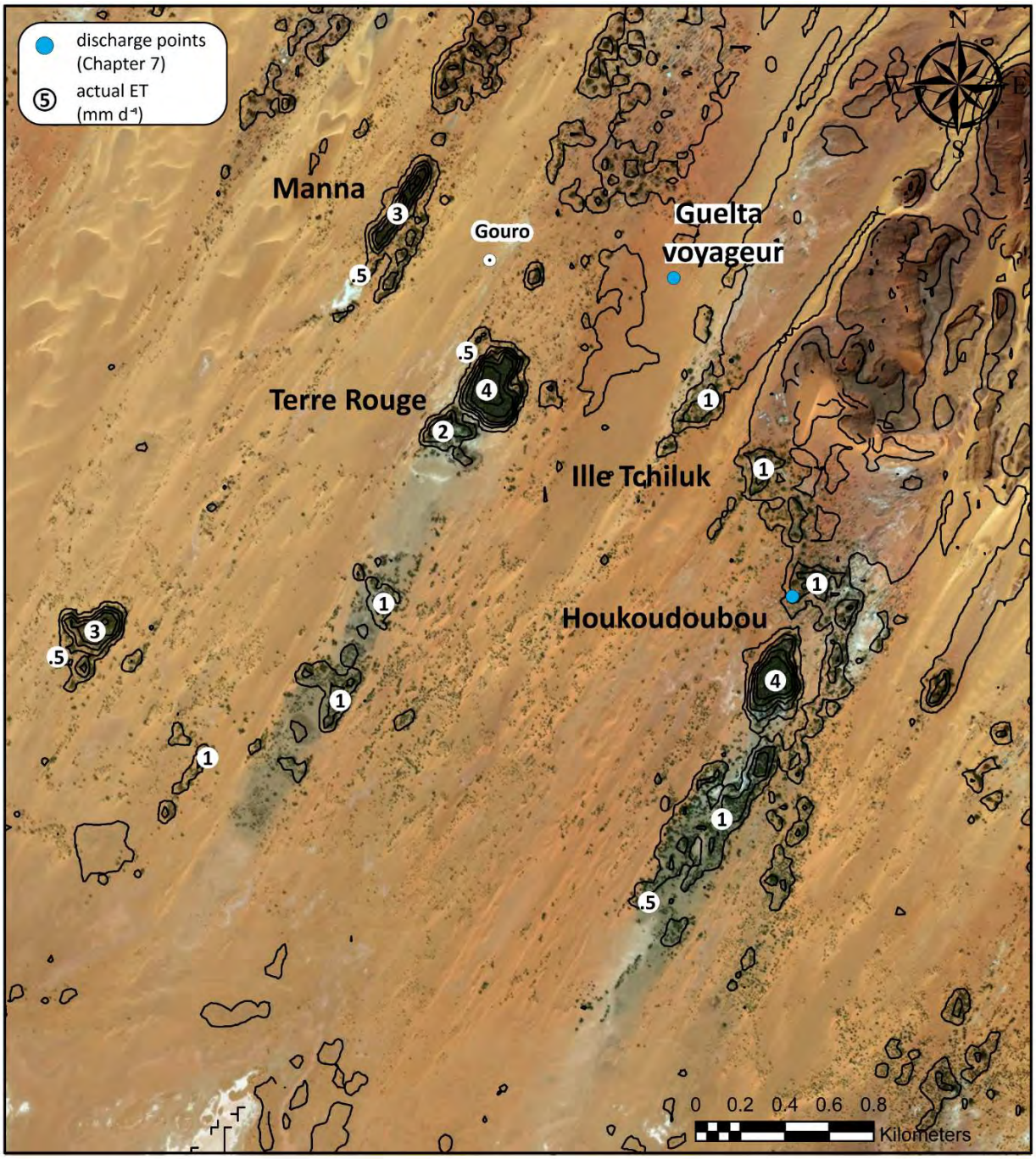

Figure 6.16: Oases of Gouro. Actual evapotranspiration rates are shown as contours (contours path 0.5 mmd^{-1}). They are calculated based on all the processed images fulfilling the quality requirements. The background is a true-color image. Localities of groundwater discharge (springs) are indicated when sampled (see Chapter 7, blue dots).

Actual evapotranspiration rates (mean values of all the images covering the lakes, contours every 0.5 mmd^{-1}) of the group of lakes of Ounianga Kebir (Yoa, Oma, Bever, Mijoi, Forodone) and of Ounianga Serir (lakes Edem, Teli, Agouta, Hogou, Djara, Bedrim and Boukou) are shown in Figures 6.17 and 6.18. A true-color image is shown as background.

In Ounianga Kebir (Figure 6.17), the contours show a sharp increase in actual evapotranspiration rates close to the borders of the lakes (1 to 5 mmd^{-1} for lakes Yoa and Oma, 1 to 4 mmd^{-1} for lakes Bever and Mijoi) and maximum actual ET rates in the deepest parts of the lakes (5-6 mmd^{-1} and 4-5 mmd^{-1}, respectively). Lake Forodone has actual ET rates of 3 mmd^{-1} in its center. Around the lakes, in a zone varying in wideness but approximately within 100 m from the borders of the lakes, low actual ET rates (0.5 mmd^{-1}) are observed, indicating phreatic evaporation. Actual ET rates between 1 and 2 mmd^{-1} are detected for the vegetated zones, particularly extended in the southern borders of the lakes.

Cross-sections (A-B and C-D) show the topography and distribution of actual ET. These cross-sections were done in order to verify the depth to groundwater and related actual ET rates. Additionally, these observations are used in Chapter 7 when describing the chemical composition of the lakes of Ounianga Kebir. Lakes Oma and Bever are located in a topographical depression, also corresponding to a zone of diatomite accumulation. Groundwater flow directions are inferred from the position and altitude of the lakes (hydraulic gradient 1-1.5‰).

In Ounianga Serir (Figure 6.18), mean rates are slightly higher (lakes Edem and Teli, 6 mmd^{-1}) than for the group of lakes of Ounianga Kebir. Deeper waters have higher rates than the shallower zones, partly covered by vegetation (1 to 5 mmd^{-1}). A zone of low actual ET rate (0.5 mmd^{-1}) marks the contour of the northern borders of the lakes. In the southern margins, low actual ET rates are restricted to zones of sparse vegetation.

While the group of lakes of Ounianga Kebir do not show a clear difference of the extent of surface water between different dates, the group of lakes of Ounianga Serir have visible variabilities. Figure 6.8 indicates the zones of higher variability of surface water extent (blue squares). The images with the most extended cover of surface water (3 April, 6 June and 24 June 2014) occur before the main precipitations, generally concentrated during the month of August in the region of the lakes. Similar pattern were observed at the oasis of Bedo.

When applying the annual potential evapotranspiration calculated with the Turc, Hargreaves and Penman methods, ETP annual volumes are estimated at 12 to 17 x 10^6 m^3y^{-1} for the group of lakes of Ounianga Kebir, and at 28 to 39 x 10^6 m^3y^{-1} for the group of lakes of Ounianga Serir. These values correspond to maximum amounts lost annually. Figures 6.17 and 6.18 show however that depending on the depth of the lakes, evapotranspiration rates vary significantly. When applying the mean actual evapotranspiration rate extracted from the processed LandSat8 images, evapotranspiration annual volumes amount at 10 x 10^6 m^3y^{-1} for the group of lakes of Ounianga Kebir and at 23 x 10^6 m^3y^{-1} for the group of lakes of Ounianga Serir (see section 6.4.3). These estimates also include the phreatic zone contouring the lakes (ET > 0.5 mmd^{-1}).

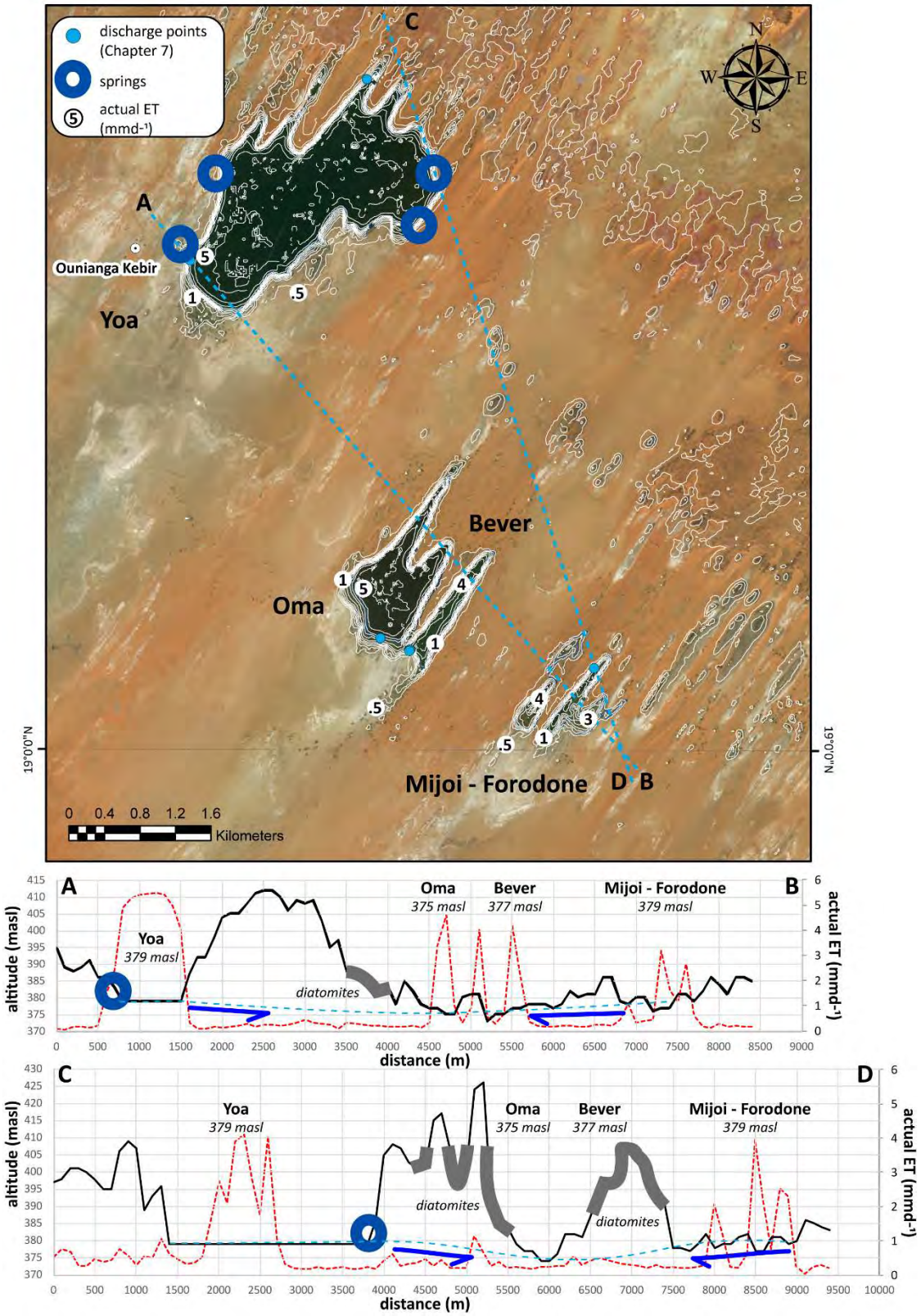

Figure 6.17: Lakes of Ounianga Kebir. Mean actual evapotranspiration rates are shown as contours (contour path 0.5 mmd^{-1}). They are calculated based on all the processed images fulfilling the quality requirements. The background is a true-color image. Springs location are from Schneider (1994). Localities of groundwater discharge (springs) are indicated when sampled (see Chapter 7, blue dots). Cross-sections A-B and C-D show the topography (black line) and actual ET rates (red dashed line). Lakes Oma and Bever are located in a central low-lying zone where diatomites are more densely represented. Groundwater flow directions are inferred from the elevation of the lakes.

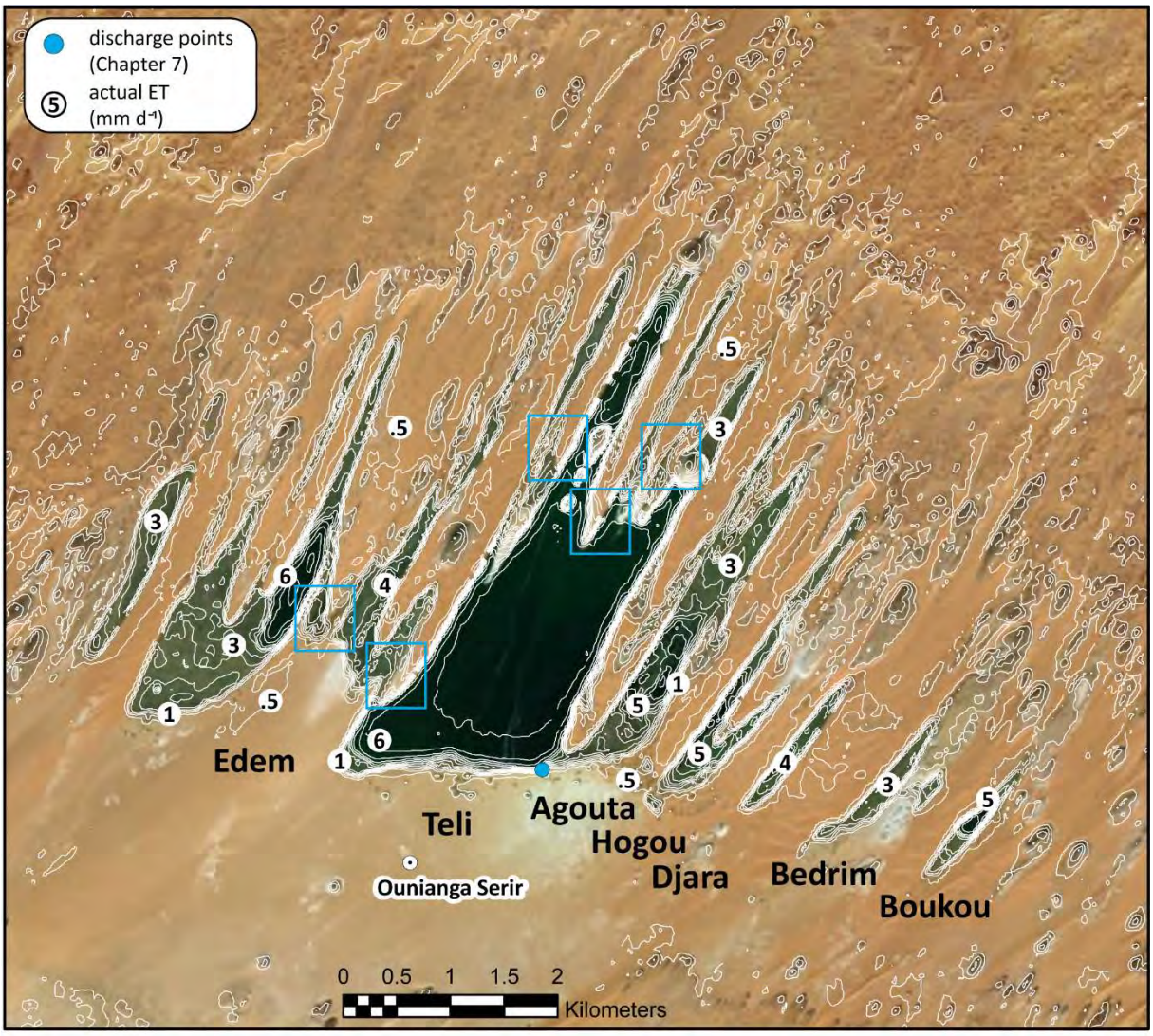

Figure 6.18: Lakes of Ounianga Serir. Mean actual evapotranspiration rates are shown as contours (contours path 0.5 mmd^{-1}). They are calculated based on all the processed images fulfilling the quality requirements. The background is a true-color image. Blue squares indicate the zones of highest changes of actual ET (standard deviation). Localities of groundwater discharge (springs) are indicated when sampled (see Chapter 7, blue dots).

6.4.3. Synthesis of losses through evapotranspiration

Table 6.2 synthetizes the estimated annual evapotranspiration losses from the main zones of discharge previously described: the lakes of Ounianga Kebir, Serir, the oases of Gouro, Bedo, Faya-Largeau and the West Palm Groves. These surface water occurrences constitute the most important discharge locations of the NSAS of Northern Chad. Other zones of discharge are associated with zones of vegetation and some surface water occurrences (natural ponds, lakes) of small extent: in the NW region of the Ennedi Mountains, wadi Wei, wadi Wideï, Fada, in the south of the Tibesti Mountains, Yarda-Kouroudi, and in the central lowlands, wadi Doum and the lakes of Motoro. These discharge zones are not included in this analysis.

The extracted surfaces of Table 6.2 include all the zones of phreatic evapotranspiration or sparse vegetation surrounding the lakes and the major oases. The actual ET rates are based on the mean of all 95 processed images. They mostly correspond to rates calculated for the months of June to September. Few images represent also the months of March (7 images), April (3 images) and May (4 images).

Table 6.2: Actual evapotranspiration losses from the main discharge zones of the NSAS of Northern Chad. ETa mean corresponds to the mean daily actual evapotranspiration rates (mmd^{-1}), calculated from all the processed images. ETa year (in $10^6 m^3$) corresponds to the estimate of annual losses through evapotranspiration. It corresponds to the product of the surface (defined by the zone of increased ET rates because of the presence of surface water, vegetation and phreatic evaporation) and the mean ET daily rates.

	Surface ($10^6 m^2$)	ETa mean (mmd^{-1})	ETa year ($10^6 m^3$)
Ounianga Kebir	8.0	3.5	10.2
Ounianga Serir	24.1	2.6	22.9
Gouro	2.4	0.9	0.8
Bedo	6.6	1.2	2.9
Faya-Largeau	24.0	1.2	10.5
West Palm Groves	10.8	1	3.9
Total	**75.8**		**51.1**

Estimated losses of evapotranspiration from the main discharge zones amounts to 51.1 x 10^6 m^3y^{-1}. As previously stated, this estimate do not include rates of phreatic evapotranspiration, which might occur in other zones of discharge. When applying rates of potential evapotranspiration (Turc, Hargreaves and Penman) to the free surface water extent of the lakes of Ounianga (surfaces of Ounianga Kebir 5.2 x 10^6 m^2 and of Ounianga Serir 12.1 x 10^6 m^2), estimation of ET losses for these two lakes vary from 11.9 to 16.7 x 10^6 m^3y^{-1} for Ounianga Kebir and from 27.9 to 39.2 x 10^6 m^3y^{-1} for Ounianga Serir. These rates represent maximum annual rates of losses through evapotranspiration from the lake's water. Using these volumes, total annual losses reach 57.8 to 74.0 x 10^6 m^3y^{-1}.

In addition to these main discharge zones, alluvial systems of wadis (Ennedi Mountains) and enneris (Tibesti Mountains) are important features of preferential fluxes, as observed by the previous analysis. Moreover, most of the perennial water points are located along theses alluvial systems (see Chapter 4). It is expected that a certain amount of phreatic evapotranspiration will occur from the alluvial systems during the whole year.

The total surface of alluvial sediments within wadis (or enneris) systems of the NSAS of Northern Chad is 2415.4 x 10^6 m^2 (based on the information from the SIRE database). Mean actual ET rate (95 processed images) extracted from the zones comprised within these alluvial sediments is 0.8 mmd^{-1}, corresponding to a total annual loss through evapotranspiration of 705.3 x 10^6 m^3y^{-1}. This value

corresponds to the amount of phreatic evaporation, assuming that the water table depth do not vary significantly over the year. The small differences of water table depths observed from measurements undertaken at three years of interval and in different epochs of the year (see Annex 3), is indicating that in the least for the southern slopes of the Ennedi Mountains, the water table is relatively stable. However, this stability might not be representative of all the alluvial systems. Additionally, given that evapotranspiration in these areas is limited by the availability of water and not energy, the estimated values constitute an upper boundary for evapotranspiration, as they correspond to daily rates mostly calculated during the rainy season.

Compared to the estimated volume of losses from the main discharge zones, losses of evapotranspiration within the alluvial systems of wadis and enneris are one order of magnitude higher than the cumulated losses from the discharge points.

By grouping these estimates (discharge points and alluvial systems), total losses through evapotranspiration from the NSAS in Northern Chad are between 756 x 10^6 m^3 (if only actual evapotranspiration rates are used, as described above) to 779 x 10^6 m^3 (if potential evapotranspiration rates are used for the surface water of the lakes of Ounianga). In Chapter 8, these estimates will be compared to the volumes of precipitation in a preliminary surface water balance.

6.5. Discussion

6.5.1. Evapotranspiration rates from literature

Estimated potential evapotranspiration rates from the literature are found to be very variable. Rates between 2,150 and 3,450 mmy^{-1} were measured in N'Djaména (Piche and Colorado pan) and between 3,180 and 3,800 mmy^{-1} (Colorado and Class A pan) in Bol (Gischler, 1967). Roche (1958) indicated an approximate value of 10 mmd^{-1} of evapotranspiration in the Ennedi region. Potential evapotranspiration from Trabucco and Zomer (2009), calculated with the equation of Hargreaves et al. (1985) and data from the WorldClim database (Hijmans et al., 2004), indicate values of 1,300 – 1,800 mmy^{-1} for the mountainous Tibesti and between 1,900 – 2,200 mmy^{-1} for the rest of the lowlands and the Ennedi Mountains. All of these values vary between the range of values estimated in this study (daily net radiation: 786 to 3,030 mmy^{-1}; ETP Turc and Hargreaves methods: 2,300 to 2,470 mmy^{-1}; ETP Penman: 3,235 mmy^{-1}).

Very different rates are measured with a Piche pan in Faya-Largeau and reported in BRGM (1991). Evaporation rates are indicated to be between 6,060 and 9,165 mmy^{-1}. A mean annual value of 7,390 mm was calculated for a period of 9 years of observations (1953-962). Comparable annual rates were given by Kröpelin et al. (2008) for the lakes of Ounianga. However, for a number of reasons, these

values seem to be too high. If extraterrestrial solar irradiance was entirely available, daily rates of evapotranspiration would range between 10 and 16 mmd^{-1}, depending on the day of the year. Estimates from BRGM (1991) and Kröpelin et al. (2008) indicate daily rates of 17 to 25 mmd^{-1}. As indicated by Sellers (1964), pan evaporation might overestimate evaporation rates by a factor of 1.6 compared to the Penman method. Additionally, high intensities winds, an important parameter providing energy to a system, are blowing for the whole year. This parameter is however difficult to take into account without ground-based measurements.

6.5.2. Main findings

The use of actual evapotranspiration and inundation maps based on the MNDWI36 index enabled to observe the dynamics of runoff-accumulation-evapotranspiration in a region poorly investigated and with only few ground-based meteorological data. Floods are traced along the wadi networks, thus allowing a better delineation of the catchments. Actual evapotranspiration and inundation maps provide information on the zones of surface water accumulation, thus indicating the locations where recharge could occur. They also allow identifying where phreatic evaporation occurs in the absence of precipitation or infiltration through wadis, which is only possible if the water table is close to the surface. Examples are shown for wadis Archeï and Nohi, the high plains, wadi Kordi and wadis Haouach and Sini-Chili, where higher evapotranspiration rates resulting from phreatic evaporation and transpiration from vegetation are seen to persist after the end of the rainy season.

The evapotranspiration maps based on LadSat8 images enabled additionally to distinguish different ET rates for (1) deep waters, (2) shallow waters, (3) dense vegetation, (4) sparse vegetation, (5) phreatic evaporation. Shallow waters and dense vegetation have generally similar evapotranspiration rates, as well as sparse vegetation and phreatic evaporation. However, the use of actual evapotranspiration maps and true-color images provides some information to distinguish between these different zones.

The overall distribution of the evapotranspiration rates and changes from date to date (Figure 6.6) correlate well with the distribution of precipitation described in Chapter 5. Low ET rates and variabilities (e.g. Mourdi depression, Ounianga Lakes, Gouro and Bedo oases) correspond to zones of very low precipitation rates. Regions experiencing low rates of precipitation (south of the Erdis plateaus, oases of West Palm Groves and of Faya-Largeau) show a slight increase in evapotranspiration rates following the rainfall events. The amplitude of changes remains low but it is observable. South of the Tibesti, the images investigated showed a response also after the winter rains. Zones of higher annual changes of actual ET rates, correspond to zones of higher precipitation rates (Ennedi Mountains, Ouaddaï). In these zones, the rates of actual evapotranspiration are higher during the years of increased precipitation than during the years of lower precipitation.

Finally, even without a complete time series, groundwater, meteoric and hydrological dynamics can be investigated, if several years of observation are undertaken. For example, observing a generally stable (Ounianga Kebir) or slightly variable extent of surface water (Ounianga Serir, Bedo) within zones experiencing low rates of precipitation, provides indications on the groundwater dynamics. Capot-Rey (1961) indicated a cyclic oscillation of the water table in Ounianga (lake level) and in the oases south of the Tibesti Mountains (groundwater level), with the highest levels being measured during the winter months and the lowest levels during the summer months. BRGM (1991) interpreted these patterns as the result of the lower evapotranspiration rates experienced during the winter months, enabling the water table to rise, compared to the higher actual evapotranspiration rates during the summer months. The observation provided by remote sensing over the lakes of Ounianga Serir and the oasis of Bedo, indicate a similar pattern as measured and presented by Capot-Rey (1961): increased inundated surfaces are observed during April and June in Ounianga Serir and during April to May in Bedo, previously to the summer monsoons (August and September).

6.5.3. Critical review and further improvements

In general, the uncertainties of the ET estimates are considerable and hard to quantify. The three main difficulties in the approach described in this chapter are: (1) the lack of field-based meteorological observation covering the period of analysis of the satellite images, hindering the calibration of the actual ET rates; (2) the absence of an obvious relation between potential and actual evapotranspiration, even on permanently inundated areas such as lakes and (3) the limited number of subsequent images usable for actual ET estimates. For example, the S-SEBI method can only be applied if a sufficient number of “wet” pixels are detected. In the arid region of Northern Chad this is one major limiting factor. During the months of precipitation, clouds may cover large regions. Additionally, if atmospheric disturbances (clouds, aerosols) are present, even clear-sky images could eventually show a less contrasted response and lower rates of evapotranspiration.

The use of LandSat8 images, although providing the appropriate spatial resolution, has a relatively small aerial coverage per image. The LandSat8 satellite has to overpass the region for four consecutive days to cover the longitudinal extent of the investigated region (satellite path is NNE to SSW). The dates of the images within neighboring regions have therefore 1 day of difference. Some examples of hydrological features (e.g. wadi Archeï, wadi Kordi) are located at the intersection of images of different dates, complicating the full representation and the study of the processes. To reduce the computational steps and obtain a homogenized signal when investigating a large region such as the Nubian Sandstone Aquifer System, a product with a larger acquisition surface would be therefore advisable. For example, a combination of LandSat and Sentinel images could be tested.

Moreover, to obtain more accurate ET estimates it r would be advisable to: (1) install meteoric station equipped with radiation measurement devices; (2) include the use of other remote sensing products to account for atmospheric properties (aerosol, ozone, water vapor concentrations). Finally, a more extended period of observation would be advisable (i.e. LandSat images are acquired since 1972).

The analysis of the precipitation rates based on a monthly step do not allow observing the single event. Therefore, the intensities, frequencies and time between subsequent events are not considered explicitly. In arid climates, single high-intensity precipitation events will more likely provoke increased runoff than medium to low-intensity events. The response of the hydrological system will also depend on whether the precipitation events have occurred as one single high intensity or smaller multiple events, but repeated in a short period of time. In this case, antecedent moisture conditions will potentially increase the infiltration rate and, therefore, the rate of recharge. An analysis of precipitation dynamics at a smaller time step would therefore better support the interpretation of the processes observed with LandSat8 images. Additionally, in order to better constrain precipitation rates and their associated uncertainties, more than one product should be used (a list of remote sensing rainfall estimates for the African continent was presented in Chapter 5).

6.6. Concluding remarks

This chapter concludes the second part of this thesis, which focused on the study of the meteorological and hydrological processes of the Nubian Sandstone Aquifer System of Northern Chad, by the use of remote sensing (Chapters 5 and 6). The combined use of different remote sensing products allowed gathering information on the meteorological and hydrological dynamics and some information on the groundwater dynamics, otherwise difficult to acquire.

The actual evapotranspiration maps provided information on the phreatic evaporation and groundwater fluctuations in the discharge zones, allowing to establish a temporal dynamics and to discuss the reasons of such fluctuations. Zones of surface water accumulation and increased ET rates were identified in the downstream zone of wadis and within the high plains of the Ennedi Mountains. Estimates of total natural discharge from the NSAS through evapotranspiration indicate that the losses from these alluvial systems are potentially one order of magnitude higher than the cumulated losses from the main discharge zones.

Additional information on the zones of recharge and on the organization of the groundwater flow system of the NSAS is provided by the hydrochemical and stable isotopic signature of groundwater, presented and discussed in the next chapter (Chapter 7). In Chapter 8, estimations of actual evapotranspiration will also be further used to present a preliminary surface water balance.

Chapter 7

Hydrochemistry and stable isotopes

7.1. Introduction and outline of the chapter

The hydrochemical and stable isotopic signature of groundwater provide valuable information on the origin of groundwater and relevant hydrogeological processes. For example, several authors working in the arid climate of Northern Africa have used the stable isotopic signature of groundwater to identify the zones experiencing modern recharge (see section 7.2 of this chapter). For the region of the Kufra basin of Northern Chad, however, only a few examples of groundwater chemical and stable isotopic analysis, are found within the reports of the Chadian Authorities or of international consultants, achieved in the framework of drilling programs. The aim of this chapter is to present a conceptual model of the regional groundwater flow system of the Nubian Sandstone Aquifer System (NSAS) of Northern Chad, based on the distribution of the chemical and stable isotopic composition of groundwater and data presented in the previous chapters (hydraulic heads, precipitation and evapotranspiration distribution).

This chapter presents first a review of previous studies investigating the origin of groundwater in the NSAS and in Northern Africa by the use of stable isotopes, dating and geochemistry (section 7.2). Section 7.3 presents the sampling, the analytical procedures and the data used in this chapter.

The distribution of the hydrochemical and stable isotopic signature of groundwater from the mountainous Tibesti is then presented (section 7.4.1). The sampled water points (Zoumri, Yebbigué, Zouarké, Misky) are not directly related to the NSAS of Northern Chad (see Figure 7.2). The higher altitudes of the Tibesti Mountains, however, provide the opportunity to identify the stable isotopic fractionation processes resulting from the current meteorological and hydrological processes and to compare it to the fractionation resulting from paleoclimatic changes. The distribution of the chemical and isotopic composition of groundwater of the NSAS of Northern Chad is presented in the second part of the result's section (section 7.4.2).

A discussion on the main findings conclude the chapter (section 7.5). The spatial representation of the hydrochemical and stable isotopic signature, supported by data from the field (hydraulic heads, Chapter 4) and from remote sensing data analysis (precipitation and evapotranspiration maps, Chapters 5 and 6) are used to investigate the following questions: (1) what is the regional groundwater

flow organization (recharge and discharge zones)? (2) what is the origin of groundwater discharging in the main oases (e.g. Ounianga Lakes, oases of Faya-Largeau)? and (3) how well does the hydrochemical composition of groundwater in the discharge zones correlate to the signature of groundwater in other parts of the NSAS?

7.2. Review of the use of stable isotopes, dating and geochemistry

7.2.1. Isotopic signature of Northern African groundwater and global/continental processes

The first environmental isotopic investigations are form Degens (1963) and Münnich and Vogel (1963). Groundwater from the main Egyptian oases were dated by ^{14}C at 20,000 to 40,000 yrs. BP. Compared to groundwater recharged from current rainfall, generally featuring enriched stable isotopic ratios ($\delta^{18}O$ -6 to +6‰ and $\delta^{2}H$ -40 to +20‰), these authors evidenced distinct depleted ratios for the Holocene - late Pleistocene paleo water ($\delta^{18}O$ -9 to -12‰ and $\delta^{2}H$ -70 to -90‰).

This same clear distinction was subsequently observed by Castany et al. (1974) in Senegal, Libya and Eastern Morocco, Gonfiantini et al. (1974) in Tunisia and Algeria, Dray et al. (1983) in the Southern Sahara, Muller and Haynes (1984) and Sultan et al. (1997) in the Western Desert of Egypt, El Bakri et al. (1991) in the Nile Valley of Egypt, Grönig et al. (1993), Vrbka and Thorweihe (1993) and Suckow et al. (1993) in North-Western Sudan, and Sturchio et al. (1996) in the Gulf of Suez of Egypt.

Sonntag et al. (1978) dated groundwater from various regions of the northern Sahara (Murzuk, Kufra, Western Desert) and concluded that the isotopic depleted values of the Saharan paleo water were due to the lower moisture deficit in the air over the oceans during the last ice age. Cooler temperatures have characterized the climate up to the Pleistocene-Holocene boundary (see Chapter 4). An enhanced Atlantic source across the Sahara region, displacing the southwestern monsoon regime south of 16°N, would also have contributed in the particularly depleted isotopic ratios of groundwater recharged during this period. As shown by Sonntag et al. (1976, 1978), Sultan et al. (1997), Edmunds (2005), Edmunds (2009) and Abouelmagd et al. (2012), stable isotopic signatures of paleo water in central and northern Sahara are progressively depleted from west to east, compared to the east to west depletion of modern rainfall (Joseph et al., 2012).

7.2.2. Groundwater age and origin in the Kufra basin

According to Edmunds and Wright (1979), groundwater ages in the Kufra (and Sirte) basin indicate a recharge epoch during the main pluvial phase of the Weichselian (Wurm) glaciation (between 38,000 and 14,000 yrs. BP). In the Kufra oases, Swailem et al. (1983) identified a shallow aquifer at 80 m depth

($\delta^2H = 5.6\delta^{18}O - 25$) and a deep aquifer at 290 m depth ($\delta^2H = 7.5\delta^{18}O - 5$), dated at 25,600 and 37,500 yrs. BP. Faitouri and Sanford (2015) dated two samples of groundwater from the Kufrah wellfield at 12,000 yrs. BP for the shallow aquifer and 20,500 yrs. BP for the deep aquifer. These samples showed depleted stable isotopic signatures ($\delta^{18}O$ -11.4‰ and δ^2H -84.1‰).

Within a generalized signature indicating recharge during the cooler pluvial periods of the Pleistocene (12,000 to 38,000 yrs. BP), localized "less old" groundwater lenses (5,000 – 8,000 yrs. BP, Edmunds and Wright, 1979) were found in the Kufra (and Sirte) basin. These signatures are generally located in the surrounding of paleo watercourses and provide evidence of a significant recharge period during the Holocene.

In other parts of the NSAS, evidence of infiltration of current precipitation and modern recharge has also been observed. Muller and Haynes (1984) concluded that infrequent precipitation events in the zone of "no rain" in the Western Desert of Egypt have contributed to the local recharge of groundwater within the past 20 years. Sultan et al. (2011) observed a linear correlation between more enriched isotopic signatures and rainfall distribution rates in the Sinai Peninsula (Egypt). Vrbka and Thorweihe (1993) identified indices of groundwater recharged by modern precipitation in perched aquifers and along wadis courses in Northern Sudan (Wadi El Milk – Wadi Muqaddam area).

7.2.3. Chemical signature of the NSAS's groundwater

Most of the studies previously cited have used stable isotopic ratios and ^{14}C to develop insights on the origin of groundwater. However, only a few number of researches have also combined the analysis of chemical parameters (Degens, 1963; Sturchio et al., 1996; Sultan et al., 2000). Degens (1963) analyzed groundwater from the Egyptian and Libyan oases, showing that groundwater has a general Na-HCO_3-SO_4-Cl content associated to $\delta^{18}O$ of < -6‰.

Hesse et al. (1987) observed an hydrochemical zoning for groundwater of the Dongola area of Egypt: groundwater highly mixed with the Nile water were dominated by Ca-Mg-HCO_3 evolving towards an increased content of Na, SO_4 and Cl at the expenses of Ca, Mg and HCO_3 for deep and shallow wells away from the Nile river. Wright et al. (1982) observed an increase of Na+K and SO_4 contents over Ca+Mg and HCO_3 along the flow lines for groundwater from the Kufra sub-basin. Pachur and Altmann (2007) observed a general enrichment in sodium, chloride and sulfates in groundwater (23-26 m depth) and surface water from the East and West Lakes of the Kufra oases.

7.3. Methods

7.3.1. Sampling campaigns

Several field campaigns were necessary to cover such a vast and inaccessible region (Table 7.1, see also Chapter 1). Altogether, these field campaigns have provided to this research, 223 water samples from 185 different water points, the difference being the resampled locations, covering a total surface of approximately 100,000 km^2. To the best of our knowledge, this represents the most comprehensive sampling campaign that has been carried out in the Kufra Basin.

Table 7.1: Field campaigns and sampling.

Campaign	Date	Nb. Samples	Resampling
Ennedi	February 2013	34	
Ennedi-Ounianga	July-August 2013	15	
Faya-Largeau to Ounianga	January-February 2014	44	2 water points from July-August 2013
Borkou (Faya-Largeau, West Palm Groves, Yarda-Kouroudi and Misky - Tibesti south)	January-February 2015	27	1 water point from January-February 2014
Tibesti (Zoumri, Yebbigué, Zoaurké and Misky)	May-June 2015	47	3 water points from January-February 2015
Ennedi	November-December 2016	37	22 water points from February 2013 8 water points from July-August 2013 2 water points from January-February 2014
additional samples			
Lakes of Ounianga	October 2011	16	
Maya Guelta	October 2015	3	
Total		**223**	

The most important perennial water points (lakes and springs) were systematically included in the sampling. Sampling locations were also chosen in order to ensure a regular geographical coverage. A denser sampling distribution was generally performed within the major oases or villages. Additionally, multitemporal sampling was performed for a certain number of locations in order to assess the dynamics of the system.

Water sampling was performed mostly at water points crowded with people, camels and donkeys. It was therefore not possible to perform any additional manipulation, as for example emptying the well previously to sampling. However, the intensive use of these wells might be considered similar to the effect of draining the well. Only few examples of open wells (e.g. Hardjalla) were unused at the time of sampling. As a consequence, these examples often show some effect of stable isotopic fractionation. The water samples were mostly retrieved from open wells with the help of the local community and by using the bucket dedicated for the water abstraction.

A range of *in-situ* parameters were measured (pH, T, EC) and water samples were filtered (anions, stable isotopes) and acidified with nitric acid (cations), then stored in HDPE and glass bottles in a portable refrigerator. The samples were then transferred to Switzerland to be analyzed for major ions and stable isotopic contents at the University of Neuchâtel.

7.3.2. Laboratory analysis and data treatment

7.3.2.1. Major Ions

Major ions were measured by ion chromatography (Dionex DX-120). Quality assessment was performed by ionic balance calculation. Samples with an ionic balance > 10% were discarded and are not shown herein (Annex 4).

For the determination of the water types, all concentrations are converted to % meqL^{-1} and all parameters below a threshold of 12.5% are removed. The remaining ions are considered major ions and are ordered according to their percentage: the cations are ordered first, followed by the anions.

Samples presenting a specific contamination are indicated. As a reference, the norms for drinking water set by the Chad Water Authority (Ministère de l'eau, 2010) were used. Upper limits of 2,500 µS/cm electrical conductivity, 0.5 mgL^{-1} NH_4, 0 mgL^{-1} NO_2^-, 50 mgL^{-1} NO_3^-, 0.7 mgL^{-1} F^-, 250 mgL^{-1} SO_4^{2-} and 250 mgL^{-1} Cl^- were applied.

7.3.2.2. Stable Isotopes

Stable isotopes ($\delta^{18}O$ and δ^2H, Annex 5) were measured by cavity ring-down spectroscopy (Picarro L2140). Hydrogen and oxygen isotopes data are reported in terms of conventional delta (δ) notation and in units of permil deviation relative to a standard reference:

$$\delta\ (‰) = \left[\frac{R_{sample}}{R_{standard}} - 1\right] * 10^3 \qquad (7.1)$$

Where R = $^2H/^1H$ and $^{18}O/^{16}O$. The standard used is the Vienna Standard Mean Ocean Water. Deviation from the mean value for repeated injections are smaller than ± 2‰ and ± 0.3‰ for δD and $\delta^{18}O$ values, respectively.

38 water points were sampled and analyzed twice at different dates. Differences of values between the first and the second sampling campaign were considered to be significant if higher than the analytical precision values ($\delta^{18}O$ 0.3‰ and δ^2H 2‰).

Stable isotopic ratios were compared to the Global Meteoric Water Line (GMWL, Craig, 1961). The N'Djaména Meteoric Water Line (NMWL) is based on the isotopic content of rain collected in N'Djaména (750 km south-west of Faya-Largeau, 1964-2015, https://nucleus.iaea.org). The Sahelo-Sudanese Meteoric Water Line (SSML) was defined by Joseph et al. (2012) as $\delta^2H = 7.6*\delta^{18}O - 7.1$. Edmunds (2005) and Joseph et al. (2012) indicate considerable recycling of continental water through evaporation/evapotranspiration in the current climate.

The rainfall isotopic content measured in Faya-Largeau (1971 and 1977, IAEA-GNIP database) was used for comparison. The enriched values (-3.3 to 0.5‰ $\delta^{18}O$ and -15 to 1‰ δ^2H, 3 measures August 1968,

July 1973 and August 1977) of Faya-Largeau's rainfall are compatible with the general isotopic content of current rains measured in Central and Northern Africa (Joseph et al., 2012; Sonntag et al., 1976; Sonntag et al., 1978).

7.3.3. Additional data used in the chapter

7.3.3.1. Applicable to the whole region

Shuttle Radar Topography Mission (SRTM) version 4.1 (Jarvis et al., 2008) was used to verify the GPS data collected in the field. Differences are estimated at 4 m ± 3 mean standard deviation, with a maximum difference of 39 m in correspondence to a water point located in a narrow valley (gueltas).

The geological data used in this work is from the SIRE database (2016). At the time of writing, available geological information from the SIRE database are restricted to the region north of 22°N and west of 18°E in the Tibesti Mountains, and 16°N for the rest of the region.

7.3.3.2. Specific to the Tibesti Mountains

Hydraulic heads contours in the Tibesti Mountains are derived from our fieldwork measurements completed by data from four studies conducted during the 1990's (O.N.H.P.V., 1991; O.N.H.P.V., 1992; Direction de l'Hydraulique et de l'Assainissment, 1993; BURGEAP, 1999), for a total of 154 hydraulic heads data.

7.3.3.3. Specific to the Nubian Sandstone Aquifer System

To support the interpretation of the hydrochemical (major ions) composition, we refer to the results from the geochemical analysis of rock samples, presented in Chapter 3. To support the interpretation of the stable isotopic signature, we refer to the analysis of remote sensing data (precipitation and MNDWI36, Chapter 5, evapotranspiration, Chapter 6). We also refer to the measured hydraulic heads presented in Chapter 4.

The conceptual groundwater flow model (equipotentials, flow directions) was constructed based on the hydraulic heads measured in the field. Note that for such a large area, the number of observations is small. The positions of paleohydrological deposits (diatomites) were used to define the potential groundwater flow directions in zones where no water points are found (Erdis plateaus, northeastern Tibesti). This implies that groundwater flow directions were maintained during the last arid phase (see Chapter 4), as diatomite or other paleohydrological deposits indicate the location of past discharge zones corresponding to the more humid periods of the Pleistocene and Holocene.

Fractures play a critical role in the groundwater flow patterns. Flow directions, therefore, were drawn considering these features. In the uplifted zones (Ennedi, Tibesti Mountains), where increased precipitation occurs, fractures (open fractures, sinks or wadis) constitute preferential paths for

recharge and substantially increase the overall hydraulic conductivity of the rock formation (Chapter 3). In the central lowlands, a zone of preferential flow corresponds to the NNW Hercynian Borkou-Kufra Trough (or Pelusium mega shear zone, Chapter 4).

7.4. Results

7.4.1. Groundwater of the Tibesti Mountains

7.4.1.1. Stable isotopic signature

Hydraulic heads of the sampled groundwater in the Tibesti Mountains vary between 665 and 1,520 masl (see Chapter 4). Stable isotopic ratios vary between -11.7 and -3.4‰ $\delta^{18}O$ and between -86 and -21‰ $\delta^{2}H$ (Figure 7.1). The samples plot along, but slightly below, the Global Meteoric Water Line (GMWL). For comparison, the N'Djaména Meteoric Water Line (NMWL) and the Sahelo-Sudanese Meteoric Water Line (SSMWL) are also plotted. All the samples show more depleted ratios than what expected from current rains occurring at lower latitudes and elevations (N'Djaména 12°N and 299 masl, Faya-Largeau 17°N and 242 masl).

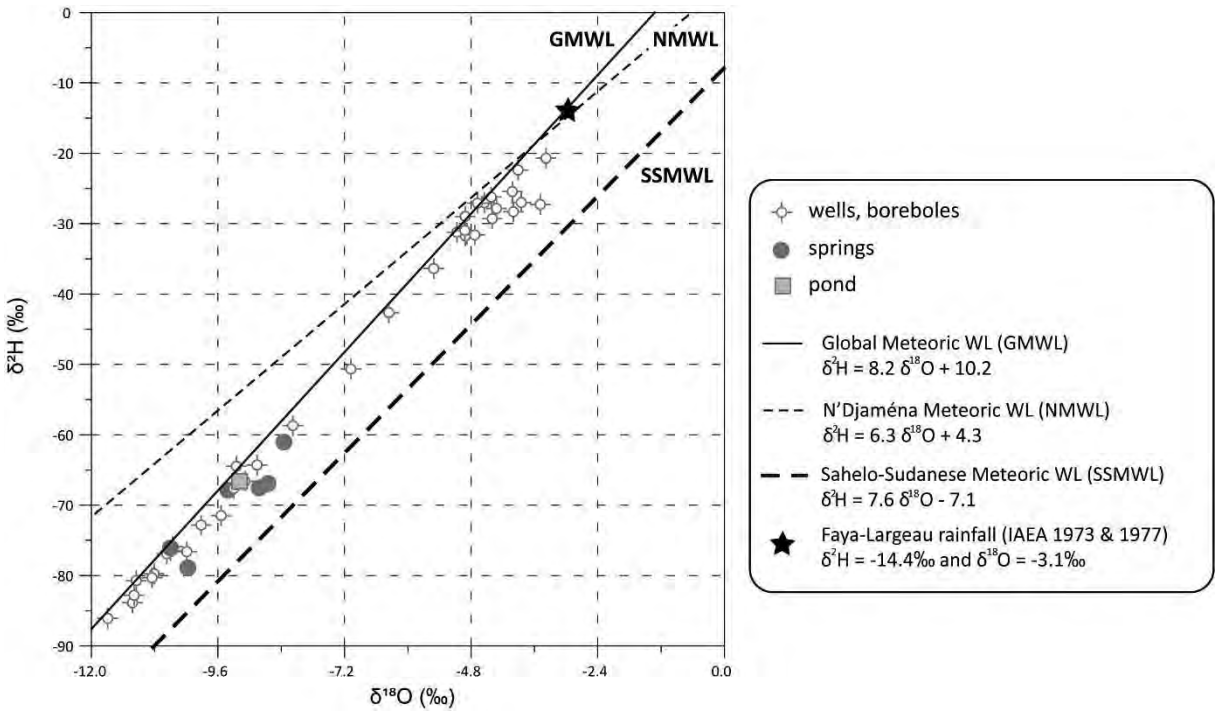

Figure 7.1: $\delta^{2}H$ versus $\delta^{18}O$ ratios shown by their water point characteristic (borehole, well, spring, pond – surface water).

The samples show two distinct groups: one group shows enriched ratios (-5.1 to -3.4‰ $\delta^{18}O$ and -32 to -21‰ $\delta^{2}H$) and one group shows depleted ratios (-8.2 to -11.7‰ $\delta^{18}O$ and -59 to -86‰ $\delta^{2}H$). Few samples show isotopic ratios between -5.5 to -7.1‰ $\delta^{18}O$ and -51 to -36‰ $\delta^{2}H$. Within the enriched group, few samples lie in a typical position generally interpreted as having been affected by

evaporative processes. All the springs (and the pond) sampled in the Tibesti Mountains have depleted ratios.

In terms of mean annual rainfall (Figure 5.1, Chapter 5), the sampled locations receive between 45 (northern slopes) and 60 mmy^{-1} (southern slopes). Figure 7.2 shows the distribution of the stable isotopic signatures and the distribution of rainfall as a background. The distribution of precipitation shows that higher rates are concentrated within the southern slopes and along the higher altitudes. The more enriched isotopic ratios ($\delta^2H \geq -40‰$) concentrate within the sampled water points located in the southern slopes. In the northern slopes, intermediate values ($-70‰ \leq \delta^2H < -40‰$) are found within the sampled water points located in the upper parts of the alluvial systems (enneris Yebbigué and Zoumri), and more depleted ratios ($\delta^2H < -70‰$) are found in the lower zones.

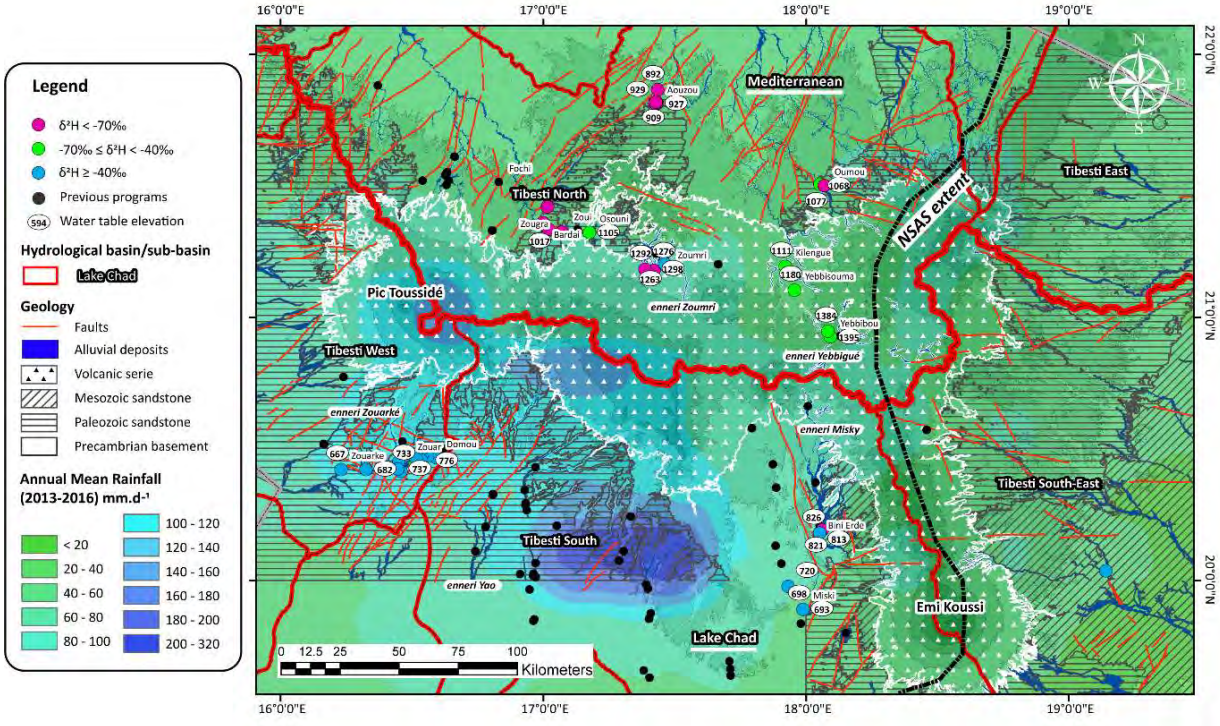

Figure 7.2: Classified deuterium ratios compared to mean annual rainfall in the Tibesti Mountains.

Groundwater from the Zouarké and Misky enneris systems (southern slopes) have stable isotopic signatures ranging from -6.4 to -3.4‰ $\delta^{18}O$ and -43 to -21‰ δ^2H and from -4.9 to -3.9‰ $\delta^{18}O$ and -32 to -27‰ δ^2H, respectively. One sample from a borehole (at 821 masl) in Misky have a depleted ratio (-9.5‰ $\delta^{18}O$ and -71‰ δ^2H), although located in proximity to another water point with enriched isotopic ratios.

Groundwater from the Zoumri and Yebbigué systems have isotopic signatures ranging from -11.7 to -8.2‰ $\delta^{18}O$ and -86 to -59‰ δ^2H and from -11.2 to -8.4‰ $\delta^{18}O$ and -81 to -61‰ δ^2H, respectively.

More enriched ratios are found in three sites located in the upper part of the enneri systems (Zoumri -4.8‰ $\delta^{18}O$ and -28‰ $\delta^{2}H$ and Yebbisouma -7.1‰ $\delta^{18}O$ and -51‰ $\delta^{2}H$). Hydraulic heads in these three locations are 1,265 masl for Zoumri and 1,180 masl for Yebbisouma. These water points are proximal to other water points characterized by a depleted signature.

7.4.1.2. Chemical species distribution

Groundwater in the Tibesti Mountains is generally low to medium mineralized (163 to 2,110 μScm^{-1}, Annex 4). pH varies from 6.1 to 8.3. 78% of the whole set of samples can be classified into four major water types: Ca-Na-HCO_3, Na-Ca-HCO_3, Na-HCO_3 and Na-HCO_3-Cl. The latter two groups are often accompanied by some enrichments in K.

Sodium and bicarbonates are the most abundant and dominant ions. Concentrations vary between 13-318 mgL^{-1} Na and 65-765 mgL^{-1} HCO_3. High concentrations of fluorine are found in the Zouarké catchment (up to 4 mgL^{-1}) and in samples located in the upstream of the enneri Zoumri (up to 2 mgL^{-1}). All samples from the Misky catchment show high concentrations of sulfates (342-591 mgL^{-1}). Figures 7.3 and 7.4 show the distribution of chemical species, and their associated isotopic ratios, within the reconstructed groundwater flow patterns of the Zouarké, Misky, Yebbigué and Zoumri systems.

An observed sequential reaction occurring along the flow lines is the change from chemical compositions of Ca-Na-HCO_3 or Na-Ca-HCO_3 to chemical compositions of Na-HCO_3 and Na-HCO_3-Cl (Zouarké, Misky, Yebbigué, Figures 7.3 and 7.4).

Groundwater from the upper parts of enneri Zoumri (Figure 7.4, Zoumri), seated in the Tibesti volcanic series, is mainly characterized by a chemical composition of Na-HCO_3. Along the flowlines, the chemical composition evolves to Na-HCO_3-Cl. In the lower parts, within the Paleozoic sandstone, groundwater shows increased concentrations of Ca (Bardaï, Zougra, Aouzou).

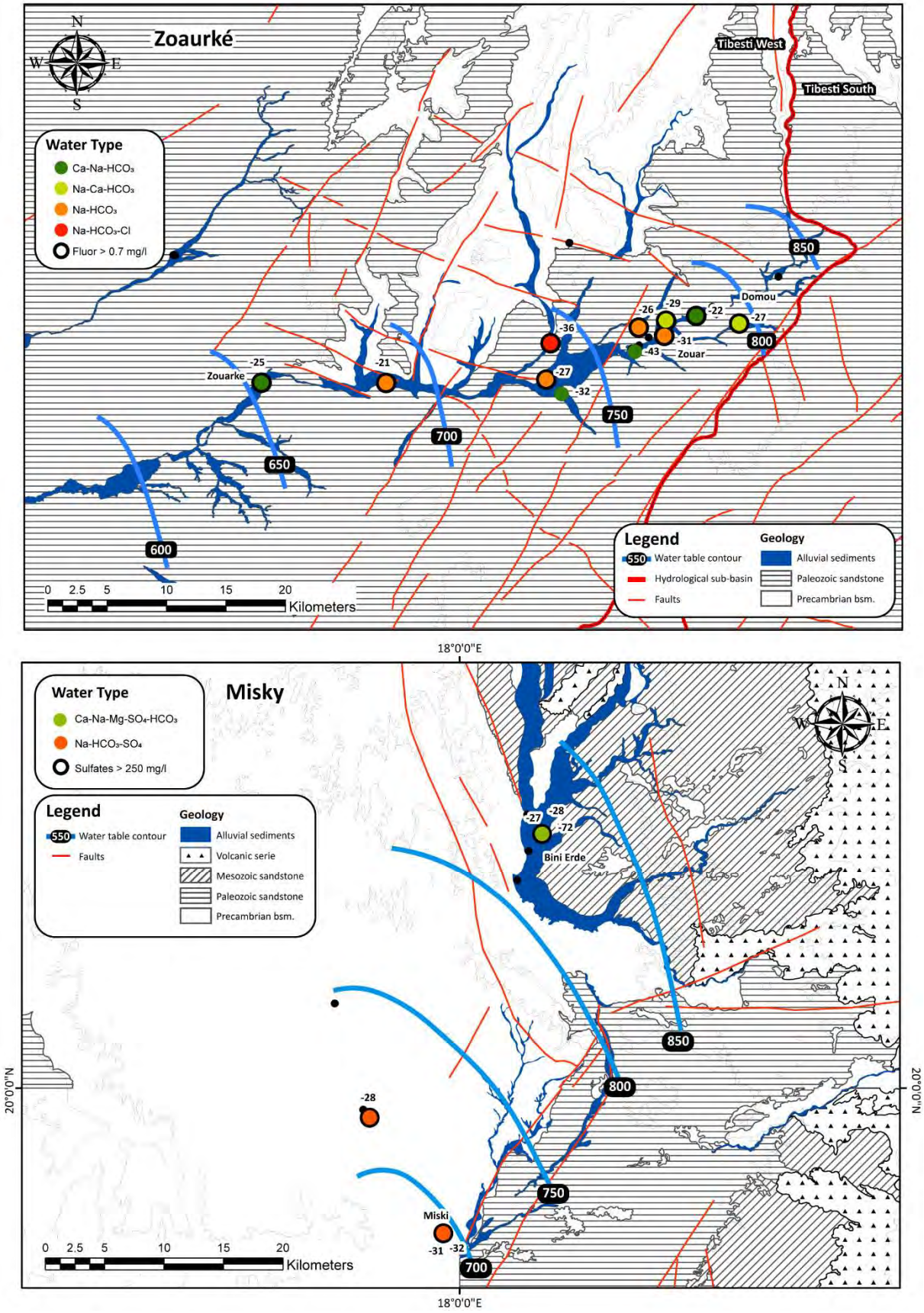

Figure 7.3: Chemical species distribution and deuterium ratios in the Zouarké and Misky basins (southern slopes, Tibesti Mountains). Concentrations higher than the recommended limit, are indicated as a black circle. Hydraulic heads contours and the main geological units are also indicated.

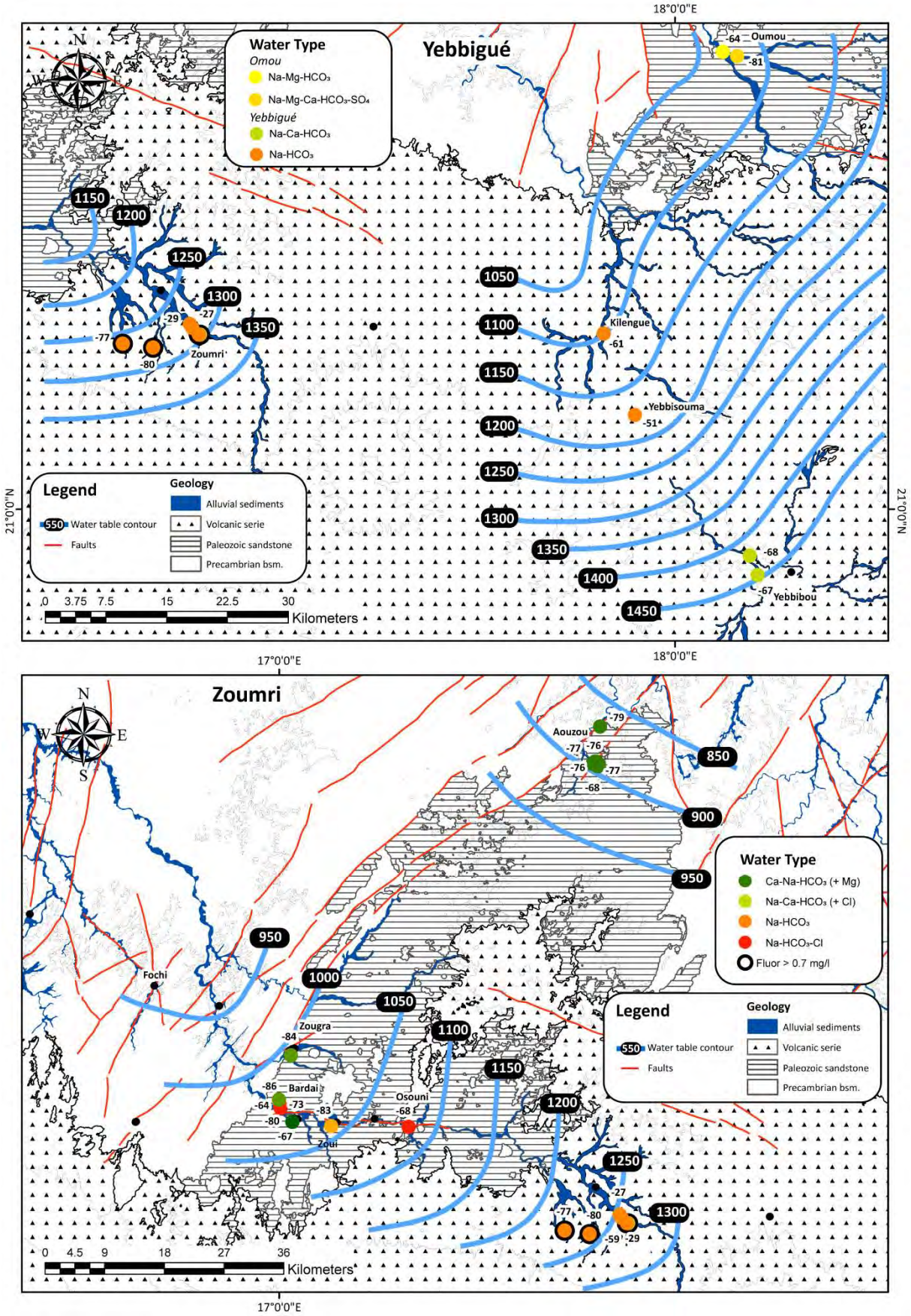

Figure 7.4: Chemical species distribution and deuterium ratios in the Yebbigué and Zoumri basins (northern slopes, Tibesti Mountains). Concentrations higher than the recommended limit are indicated as a black circle.

7.4.2. Groundwater of the Nubian Sandstone Aquifer System

7.4.2.1. Stable isotopic signature

Water samples collected within the NSAS of Northern Chad and the neighboring Lake Chad geological basin have contents of 18-oxygen and deuterium varying from -11.7 to +20.1‰ $\delta^{18}O$ and from -84 to +91‰ $\delta^{2}H$. Non-evaporated samples plot along the Global Meteoric Water Line (GMWL) or parallel but slightly below, close to Sahelo-Sudanese Meteoric Water Line (SSMWL, Figure 7.5). Apart from a small number of samples (Itou, Toukou, Maya, Bini Herdé) with stable isotopic ratios similar to the isotopic content of rains measured in Faya-Largeau (-3.3 to 0.5‰ $\delta^{18}O$ and -15 to 1‰ $\delta^{2}H$), all the non-evaporated samples show more depleted ratios than contemporary precipitation within the region.

Figure 7.5 shows the deuterium versus 18-oxygen plots of the samples from the NSAS of Northern Chad and neighboring Lake Chad geological basin. The plots are presented by zones: the south and the north of the Ennedi Mountains, Gouro, Ounianga, the south of the Tibesti Mountains and the Lake Chad basin. These zones are chosen as they represent similar precipitation rates (e.g. southern Ennedi against northern Ennedi).

In the southern Ennedi, contents of 18-oxygen and deuterium vary from -8.9 to +20.1‰ $\delta^{18}O$ and from -67 to +91‰ $\delta^{2}H$. Samples showing fractionation from evaporation correspond to samples of natural ponds (Saki, Terkei, Fada, Onoua, wadi Wideï), open wells not in use by the local population at the time of sampling (Weïba) and an example of a spring of low discharge rates (Deli), percolating from a zone of accumulation (pond). Evaporated samples plot along a line expressed by the equation $\delta^{2}H = 4.6* \delta^{18}O – 10.5$.

Non-evaporated samples can be classified into two groups. Most of the samples are comprised between -7.3 to -2.0‰ $\delta^{18}O$ and between -51 to -9‰ $\delta^{2}H$, plotting along the GMWL. Few samples (wadi Wideï, Bir Koraa, Mouso), plot along a line of lower slope, with values generally more depleted (-8.9 to -6.4‰ $\delta^{18}O$ and -67 to -54‰ $\delta^{2}H$).

In the Ennedi North, contents of 18-oxygen and deuterium vary from -10.5 to +5.9‰ $\delta^{18}O$ and from -76 to +29‰ $\delta^{2}H$. Evaporated samples correspond to samples of surface water from a natural pond (Maya) and a well not in use at the time of sampling (Hardjalla). With a similar pattern as for samples form the southern slopes, stable isotopic ratios show two groups: a group of water points with more enriched ratios (Maya, Mourdi Djouna, Eheri, Tangalia, wadi Tebi, -4.8 to -2.0‰ $\delta^{18}O$ and -31 to -11‰ $\delta^{2}H$) and a group with more depleted ratios (Tergueshi, Gaour, Madadi, wadi Doum, -10.5 to -8.9‰ $\delta^{18}O$ and from -76 to -68‰ $\delta^{2}H$).

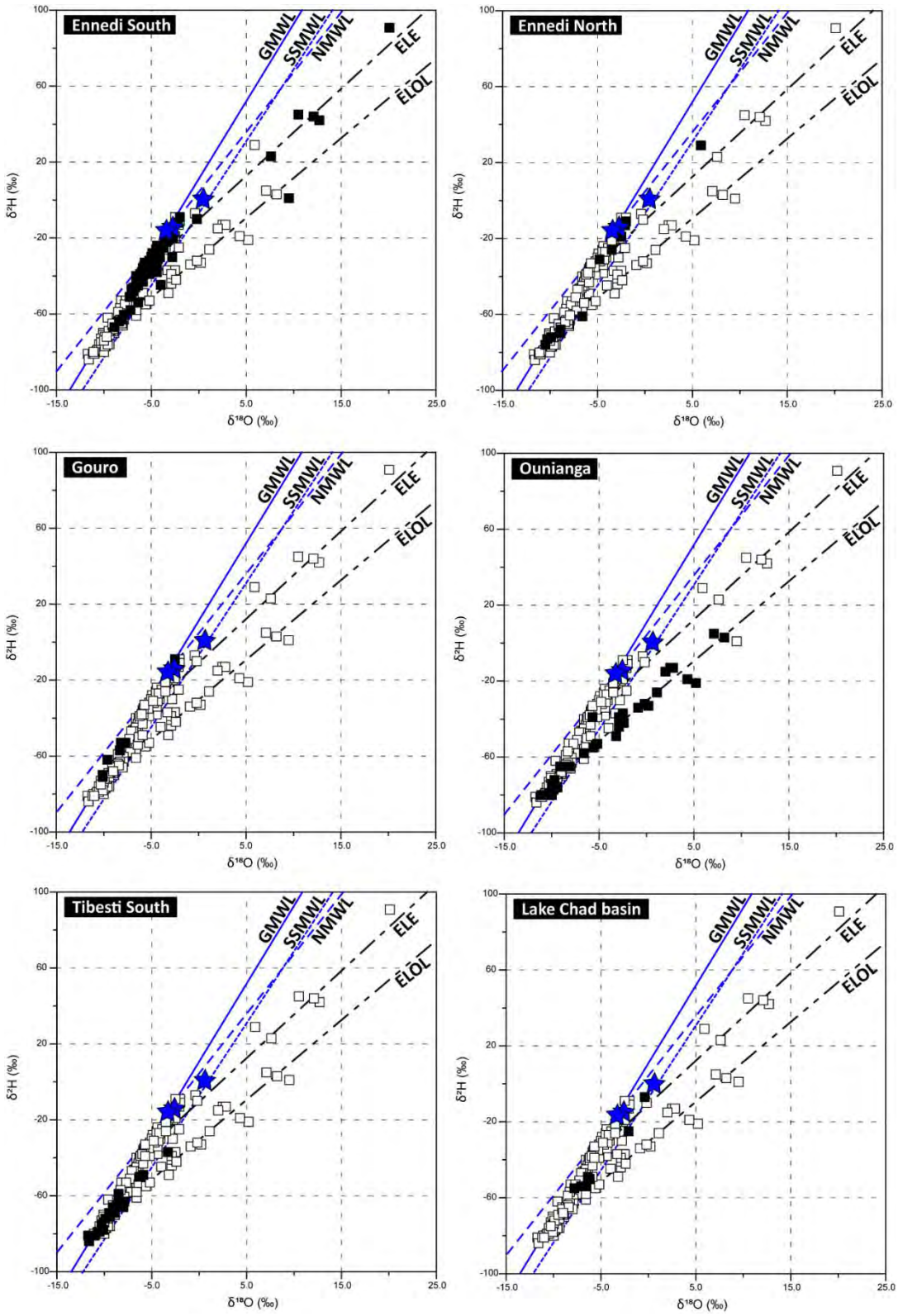

Figure 7.5: δ^2H versus $\delta^{18}O$ ratios showed by zones (white squares: all samples, black squares: samples from the specific zone): South Ennedi, North Ennedi, Gouro, Ounianga, South Tibesti, Lake Chad geological basin. The lines correspond to the Global Meteoric Water Line (GMWL $\delta^2H = 8.2\delta^{18}O +10.2$), the N'Djaména Meteoric Water Line (NMWL $\delta^2H = 6.3\delta^{18}O +4.3$), the Sahelo-Sudanese Meteoric Water Line (SSMWL $\delta^2H = 7.6\delta^{18}O -7.1$) and the calculated evaporation line for samples from the Ennedi (ELE $\delta^2H = 4.6\delta^{18}O -10.5$) and from the Ounianga Lakes (ELOL $\delta^2H = 4.2\delta^{18}O -30.4$). The isotopic ratios of rainfall in Faya-Largeau from the IAEA database (3 measures August 1968, July 1973 and August 1977) are plotted as blue stars.

On the eastern slopes of the Tibesti Mountains, water samples from the oases of Gouro also show one example with enriched stable isotopic ratios (Bini Herdé, -2.5‰ $\delta^{18}O$ and -9‰ $\delta^{2}H$) and a group of samples with more depleted ratios in Gouro (-10.1 to -7.7‰ $\delta^{18}O$ and from -71 to -53‰ $\delta^{2}H$).

The lakes and shallow groundwater of Ounianga Kebir, Serir and Motoro, have contents of 18-oxygen and deuterium varying from -11.4 to +8.2‰ $\delta^{18}O$ and from -85 to +5‰ $\delta^{2}H$. The isotopic ratios are generally depleted (-11.4 to +6.6‰ $\delta^{18}O$ and -85 to -58‰ $\delta^{2}H$) or plotting along a line expressed by the equation $\delta^{2}H = 4.2* \delta^{18}O - 30.4$ indicating fractionation from evaporation. The evaporation line intersects the GMWL in the zone of the group of depleted samples. One sample in Ounianga Serir (surface water of lake Edem, see Chapter 6), has more enriched values (-5.7‰ $\delta^{18}O$ and -39‰ $\delta^{2}H$).

In the Southern Tibesti, contents of 18-oxygen and deuterium vary from -11.7 to -3.3‰ $\delta^{18}O$ and from -84 to -37‰ $\delta^{2}H$. One evaporated sample correspond to surface water of a natural pond (Aïn Galaka) created by the discharge of an artesian spring. The samples are generally depleted (-11.7 to -7.9‰ $\delta^{18}O$ and -84 to -59‰ $\delta^{2}H$). Two samples show slightly more enriched stable isotopic ratios (Elleboye, -6.3 to 5.9‰ $\delta^{18}O$ and -50 to -49‰ $\delta^{2}H$).

In the Lake Chad geological basin, contents of 18-oxygen and deuterium vary from -7.8 to -6.2‰ $\delta^{18}O$ and from -55 to -49‰ $\delta^{2}H$. Two evaporated samples have isotopic ratios of -2.1 to -0.4‰ $\delta^{18}O$ and -25 to -7‰ $\delta^{2}H$.

7.4.2.2. Multisampling and variability of the isotopic signature

For 26 water points re-sampled at different dates, isotopic differences were found to be below the analytical precision, indicating a constancy of the signature within years (most of the samples were repeated after 3 years). Also, differences in water level depths from year to year were below 5 m (Annex 3).

In twelve cases, the isotopic signature shifted significantly (11 in the Ennedi Mountains, 1 at Ounianga Kebir). For four of these cases (Wadi Widei, Kondor 1 and 2), there are doubts about the exact repetition of the sampling point at different dates.

For six of the remaining samples, all located in the Ennedi Mountains, the shift occurred towards a more enriched signature (Bao-Oho, Berdoba, Itou, Fada, Archeï). Signatures in 2013 varied between -4.7 to -6.4‰ $\delta^{18}O$ and between -30 to -45‰ $\delta^{2}H$, shifting in 2016 to values varying between -2.0 to -5.2‰ $\delta^{18}O$ and between -9 to -39‰ $\delta^{2}H$. In two more examples (Fada, Deli), the shift occurred from a signature in 2013 fractionated by evaporation (-0.2 to -2.8‰ $\delta^{18}O$ and -10 to -30‰ $\delta^{2}H$), shifting towards a non-evaporated and more depleted signature in 2016 (-2.7 to -4.4‰ $\delta^{18}O$ and -20 to -34‰

δ^2H). All of these water points are located within an active wadi system and are characterized by precipitation rates above 60 mmy^{-1}.

7.4.2.3. Stable isotopic signature and relationship to water heads and rainfall rates

Hydraulic heads of the sampled water points vary from 198 to 1,149 masl (see Chapter 4). In terms of mean annual rainfall (Figure 5.2, Chapter 5), the southern slopes of the Ennedi Mountains receive between 100 and 150 mmy^{-1}, while the southwestern and northern regions have annual mean rainfall rates between 30 and 40 mmy^{-1}. In the central lowlands, the lowest rates of precipitation were observed within the eastern slopes of the Tibesti Mountains (Gouro, Figure 5.3, Chapter 5), with only 7 mmy^{-1}. The rest of the region receives between 15 mmy^{-1} in Ounianga Kebir and in the southern Tibesti and 35 mmy^{-1} in Ounianga Serir. In the Lake Chad geological basin, rainfall rates increase from 30 mmy^{-1} (Djourab) to 90 mmy^{-1} (Kouba) in a southerly direction.

Figure 7.6 shows the relationship between the hydraulic heads (on the left, see Chapter 4) and the yearly rainfall rates (on the right, see Chapter 5), with the stable isotopic signatures ($\delta^{18}O$). The two figures show a distinct clustering of the isotopic ratios.

When the hydraulic heads are compared with the 18-oxygen ratio, the relationship shows a progressive change from a group of samples with lower hydraulic heads (below 450 masl) and a more depleted isotopic content ($\delta^{18}O < -6.0‰$), towards a group of samples with higher hydraulic heads (above 450 masl) and more enriched isotopic contents ($\delta^{18}O > -6.0‰$). Some samples show an increased enrichment ($\delta^{18}O > -6.0‰$) and hydraulic heads above 400 masl.

When precipitation rates (extracted by localities, see Chapter 5) are compared with the stable isotopic contents, the enriched group of samples are seen to be related to higher precipitation rates (above 60 mmy^{-1}) but also to lower precipitation rates (below 40 mmy^{-1}), while the most depleted samples are always associated to low precipitation rates.

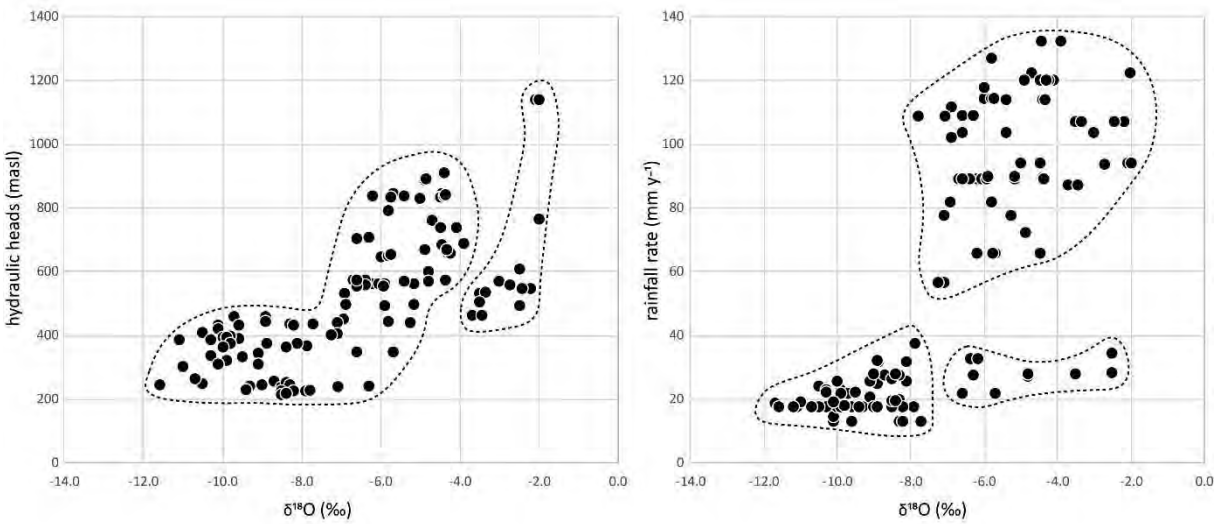

Figure 7.6: Hydraulic heads (masl) and rainfall rates (mmy^{-1}) against $\delta^{18}O$ (‰). Only non-evaporated samples are shown.

Figure 7.7 shows the spatial relationship between δ^2H, the distribution of rainfall (mean 2013-2016) and the measured hydraulic heads. The isotopic ratios have been classified (δ^2H < -70‰, -70‰ ≤ δ^2H < -40‰, δ^2H ≥ -40‰) to improve the visibility of the distribution. The dashed line indicates when a marked difference of stable isotopic ratios was observed between samples located in proximity and characterized by similar rainfall rates (NW of Gouro, NW of the Ennedi Mountains, Ounianga Serir, Elleboye).

More enriched isotopic ratios are located in the Ennedi Mountains (east of the dashed line of Figure 7.7) and in Bini Herdé (eastern slopes of the Tibesti Mountains). More depleted ratios are located in the central depressional zone, characterized by lower hydraulic heads and precipitation rates.

The southern slopes of the Ennedi Mountains are characterized by increased rainfall rates (> 60 mmy^{-1}) and hydraulic heads decreasing from 912 masl in Amdjarass to 404 masl in wadi Wei in a SE-NW direction. The isotopic ratios progressively decrease from -4.4‰ $\delta^{18}O$ and -24‰ δ^2H in Amdjarass to -7.3‰ $\delta^{18}O$ and -51‰ δ^2H in wadi Wei (hydraulic heads 404 masl).

The higher elevations (e.g. Maya, hydraulic heads 1,140 masl) are also characterized by increased precipitation rates. Stable isotopic ratios are within the most enriched found in the whole region of the NSAS of Northern Chad (-2.1 ‰ $\delta^{18}O$ and -12‰ δ^2H).

Otherwise, the northern slopes of the Ennedi Mountains are characterized by lower precipitation rates. However, the few examples of water points in the northern slopes, restricted to the downstream area of the major alluvial systems (wadi Kordi and Béméché, see Chapter 5), have stable isotopic ratios similar to the content measured in groundwater from other zones characterized by higher rates of

precipitation (higher altitudes, southern slopes). They represent the group of samples characterized by enriched ratios but lower rates of precipitation of Figure 7.6. Hydraulic heads decrease from 603 masl in Mourdi Djouna to 495 masl in wadi Tebi. The sample from wadi Tebi (downstream of wadi Kordi) shows however more enriched ratios (-2.5‰ $\delta^{18}O$ and -19‰ $\delta^{2}H$) than the samples collected in the downstream of wadi Béméché (Mourdi Djouna, Eheri, Tangalia -4.8 to -3.5‰ $\delta^{18}O$ and -31 to -26‰ $\delta^{2}H$). The analysis LandSat8 images (Chapter 5) has shown that wadi Kordi experiences an important flooding in the least once every year, compared to wadi Béméché which experiences one important flooding every three years.

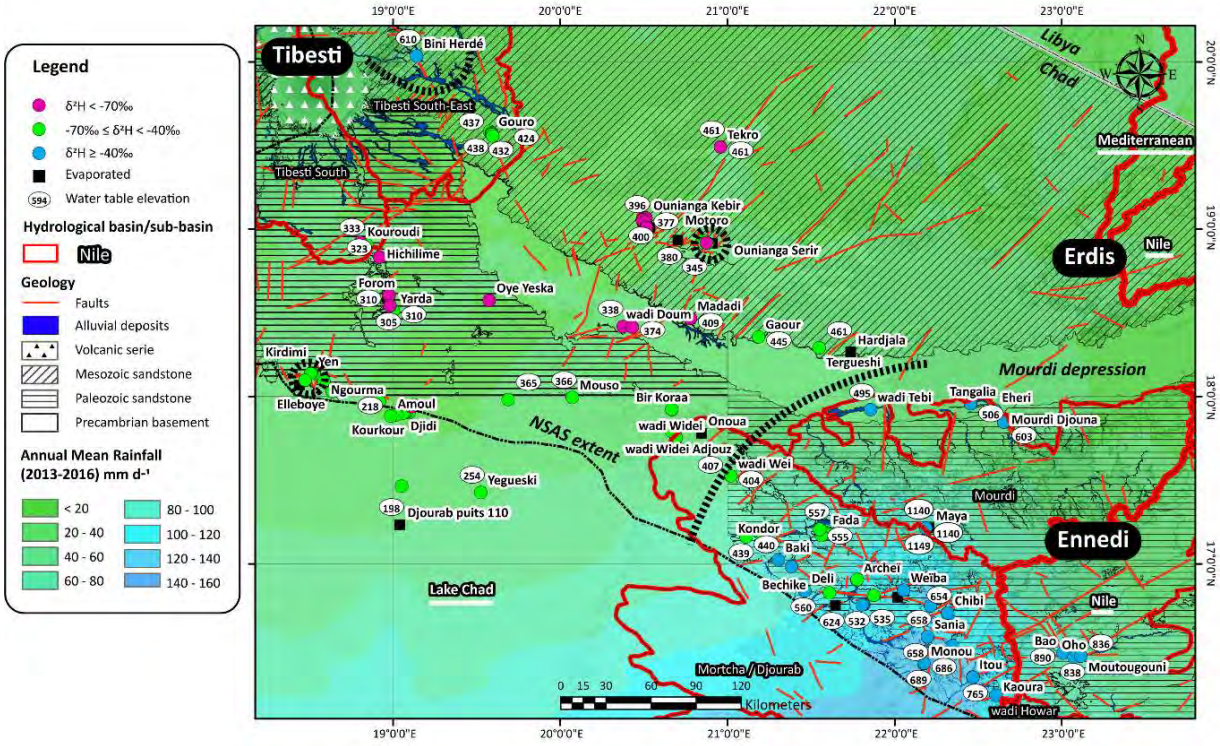

Figure 7.7: Spatial distribution of isotopic ratios (classified, $\delta^{2}H < -70‰$, $-70‰ \geq \delta^{2}H > -40‰$, $\delta^{2}H \geq -40‰$), annual mean precipitation rates (2013-2016) and hydraulic heads (topographic contours are in background of the precipitation raster map). Samples showing fractionation by evaporation are also shown. Dashed lines (Elleboye, Bini Herdé,Ounianga Serir, Ennedi Mountains) indicate when a marked differences of isotopic ratios was observed (see Figure 7.5).

Similar frequencies as wadi Béméché were observed in the wadi north of the oasis of Gouro (Chapter 5). The sample from Bini Herdé (hydraulic heads 610 masl) shows enriched ratios (-2.5‰ $\delta^{18}O$ and -9‰ $\delta^{2}H$) comparable to those measured within the alluvial systems of the Ennedi Mountains. Within the oases of Gouro, hydraulic heads decrease in a NNW to SSE direction, from 438 masl in Gouro Manna to 424 masl in Gouro Kosh. Stable isotopic ratios become slightly more depleted, from -7.7‰ $\delta^{18}O$ and -53‰ $\delta^{2}H$ in Gouro Manna to -10.1‰ $\delta^{18}O$ and -71‰ $\delta^{2}H$ in Gouro Kosh (Figure 7.8A).

From the Ennedi Mountains towards the central lowlands, precipitation rates decrease to < 40 mmy^{-1}. Hydraulic heads decrease from 386 masl in wadi Widei to 365 masl in Mouso and, north of the Mourdi

depression, from 395 masl in Hardjalla to 374 masl in wadi Doum. Figure 7.5 has shown a marked difference of isotopic ratios for these samples, compared to the range of values found in the Ennedi Mountains. Isotopic ratios vary from -7.9‰ $\delta^{18}O$ and -61‰ $\delta^{2}H$ in wadi Widei to -7.2‰ $\delta^{18}O$ and -58‰ $\delta^{2}H$ in Mouso and from -8.9‰ $\delta^{18}O$ and -68‰ $\delta^{2}H$ in Tergueshi (hydraulic heads 461 masl) to -10.6‰ $\delta^{18}O$ and -76‰ $\delta^{2}H$ in Madadi (hydraulic heads 409 masl).

In the central lowlands, hydraulic heads decrease from Tekro (460 masl) to Ounianga Kebir (375 – 400 masl) to Ounianga Serir (345 – 360 masl). Stable isotopic ratios of non-evaporated samples from Tekro and from Ounianga Serir are slightly less depleted (Tekro -9.7‰ $\delta^{18}O$ and -72 ‰ $\delta^{2}H$, Ounianga Serir -10.0 to -8.1‰ $\delta^{18}O$ and -74 to -65 ‰ $\delta^{2}H$) than in Ounianga Kebir (-11.4 to -9.6‰ $\delta^{18}O$ and -85 to -76 ‰ $\delta^{2}H$). The surface water of lake Edem (see Chapter 6), has more enriched stable isotopic ratios (-5.7‰ $\delta^{18}O$ and -39‰ $\delta^{2}H$).

In Yarda-Kouroudi hydraulic heads decrease from 337 masl in Kouroudi to 310 masl in Yarda. Stable isotopic ratios are also generally depleted, varying between -11.0 to -8.0 ‰ $\delta^{18}O$ and -81 to -66‰ $\delta^{2}H$, with no apparent correlation to the flow directions. In the oases of Faya-Largeau (Amoul, Djidi, Kourkour), the isotopic signature varies between -11.2 to -8.2‰ $\delta^{18}O$ and -59 to -84‰ $\delta^{2}H$. The stable isotopic ratios are seen to have a general trend from more depleted isotopic ratios where hydraulic heads are higher (Faya Torchenga, 250 masl, Figure 7.8B), becoming slightly more enriched where hydraulic heads are lower (Amoul, 218 masl). A slope of 6.4 was calculated for the linear regression of these isotopic ratios, indicating potential evaporative processes along the flow direction. Within the West Palm Groves (Kirdimi, Yen, Ngourma, Elleboye), isotopic ratios are slightly more enriched (-9 to -5.9‰ $\delta^{18}O$ and -68 to -49‰ $\delta^{2}H$), showing no apparent relationship with the hydraulic gradient (hydraulic heads from 256 masl in Kirdimi to 230 masl in Aïn Galaka). No relationship has either been observed in the oases of Faya-Largeau and West Palm Groves between samples from water points clearly associated to an artesian flow (artesian boreholes or springs) and samples from open wells (traditional and improved) or boreholes, capturing the shallow aquifer.

Slightly enriched isotopic ratios are also found in the Lake Chad geological basin (hydraulic heads from 255 masl in Yegeski to 198 masl in Djourab – puits 110), varying between -6.4 and -6.2‰ $\delta^{18}O$ and between -54 and -49‰ $\delta^{2}H$.

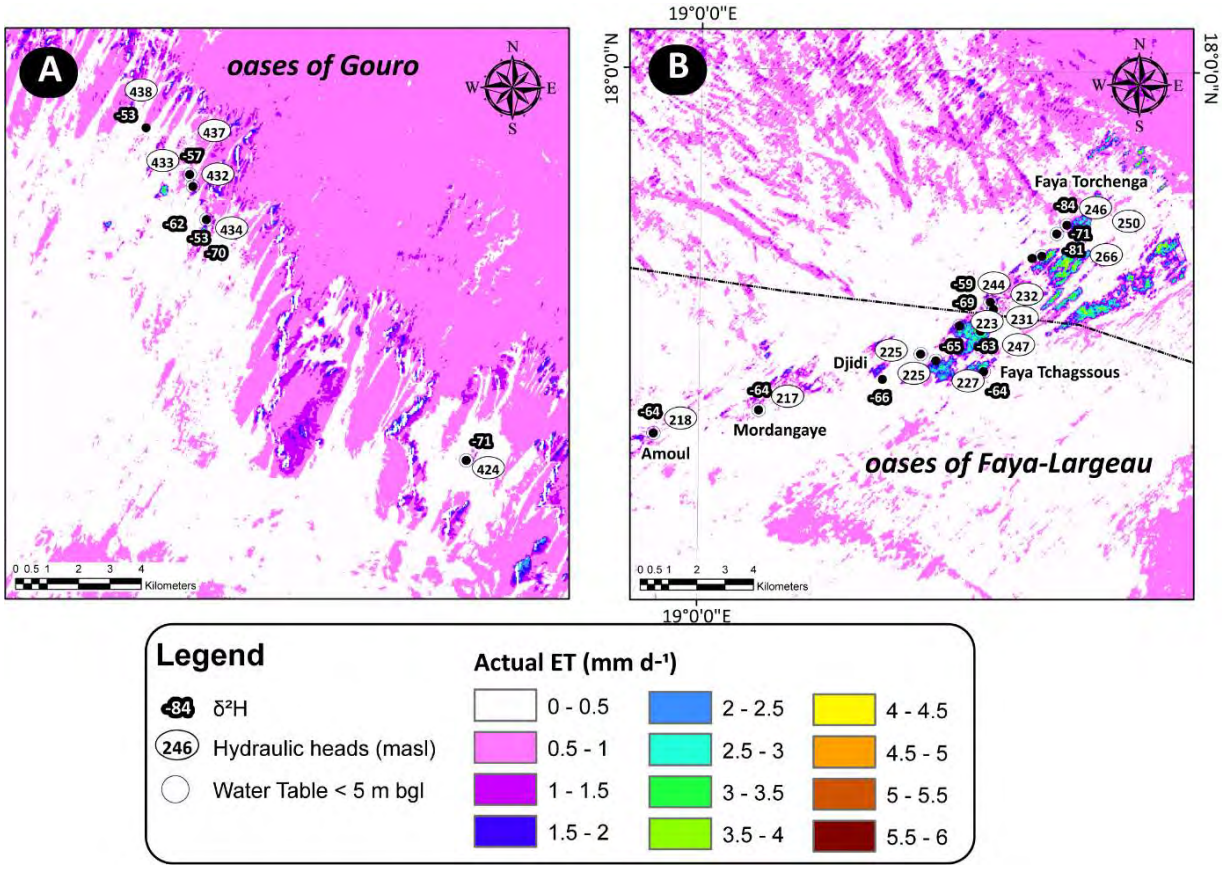

Figure 7.8: Stable isotopic and hydraulic heads A) of the oases of Faya-Largeau and B) of the oases of Gouro. The actual evapotranspiration map is shown as background.

7.4.2.4. Physical parameters, hydrochemical signatures and relationship to the stable isotopic ratios

Within the collected set of water samples, 69% have a low to medium level of mineralization, with electrical conductivity values spanning from 18 to 665 μScm^{-1}, and 86% have a pH comprised between 6 and 9 (Annex 4). 12% of the samples show electrical conductivities > 2,500 μScm^{-1}. Surface water from the lakes of Ounianga have the highest mineralization within the collected samples (up to 196 $mScm^{-1}$) and alkaline pH (pH 9.0-11.2).

77% of the whole set of samples are represented by the following five hydrochemical families: Ca-(Mg)-HCO_3, Ca-(Mg)-Na-HCO_3, Na-Ca-HCO_3, Na-HCO_3 and Na-Mg-HCO_3. Hydrochemical signatures showing a specific enrichment in SO_4 (9% of samples), Cl (8% of samples) or K (6% of samples) were also found and are indicated accordingly (Annex 4).

The general distribution of cations shows a linear relationship between an end-group with higher contents of Ca (+Mg) and an end-group with higher contents of Na (+K). A correlation 0.75 (R^2) is observed between Na and K, dominated by a strong relationship between these elements for the group of samples from the Ounianga lakes, also showing the highest ionic concentration. Ca and Mg also

show a linear relationship. The distribution of anions shows the general dominance of HCO_3, variable contents of SO_4 and Cl, and high correlations (R^2 = 0.99, SO_4+Cl versus HCO_3, R^2 = 0.99, Ca+Na versus HCO_3+SO_4+Cl).

Figure 7.9 shows the relationship between the cation and anion contents (Ca+Mg vs. Na+K and Cl+SO_4 vs. HCO_3, in meq%) and the stable isotopic ratios of the analyzed samples. The chemical and stable isotopic distribution shows that the more enriched ($\delta^2H \geq -40‰$) and intermediate ($-40‰ > \delta^2H \geq -70‰$) isotopic ratios are generally associated to samples with similar chemical contents, characterized by a Ca-Mg-(Na)-HCO_3 water type. The most depleted ($\delta^2H < -70‰$) have higher contents of Na, Cl and SO_4.

The relationship between the chemical composition of the samples and their stable isotopic signature is expressed by the cation's facies change from Ca-Mg-dominant (enriched), through Ca-Na, Na-Ca to Na-dominant (depleted, Figure 7.9A) and by the anion's facies change from HCO_3-dominant with low concentrations of Cl – SO_4 (enriched and intermediate) to HCO_3-dominant showing higher concentrations of Cl and SO_4 (depleted, Figure 7.9B).

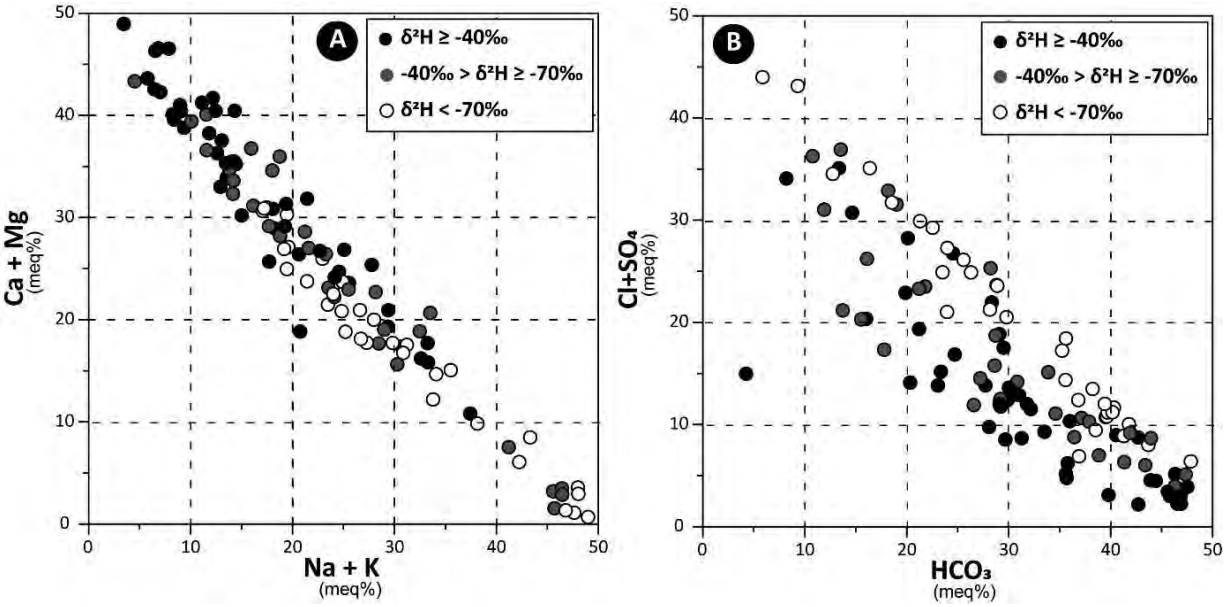

Figure 7.9: A) Ca+Mg (meq%) vs. Na+K (meq%) showing the progressive cation's facies change from Ca+Mg-dominant species (enriched and intermediate stable isotopic ratios) to Na+K-dominant species (depleted stable isotopic ratios); B) Cl+SO_4 (meq%) vs. HCO_3 (meq%) showing a difference in anionic species, enriched and intermediate samples being HCO_3-dominant with low concentrations of Cl+SO_4, while depleted samples show a higher amount of Cl-SO_4.

7.4.2.5. Groundwater conceptual flow model: spatial distribution of chemical and stable isotopic signature

Figure 7.10 shows the distribution of the chemical and stable isotopic signatures of groundwater in the Ennedi Mountains.

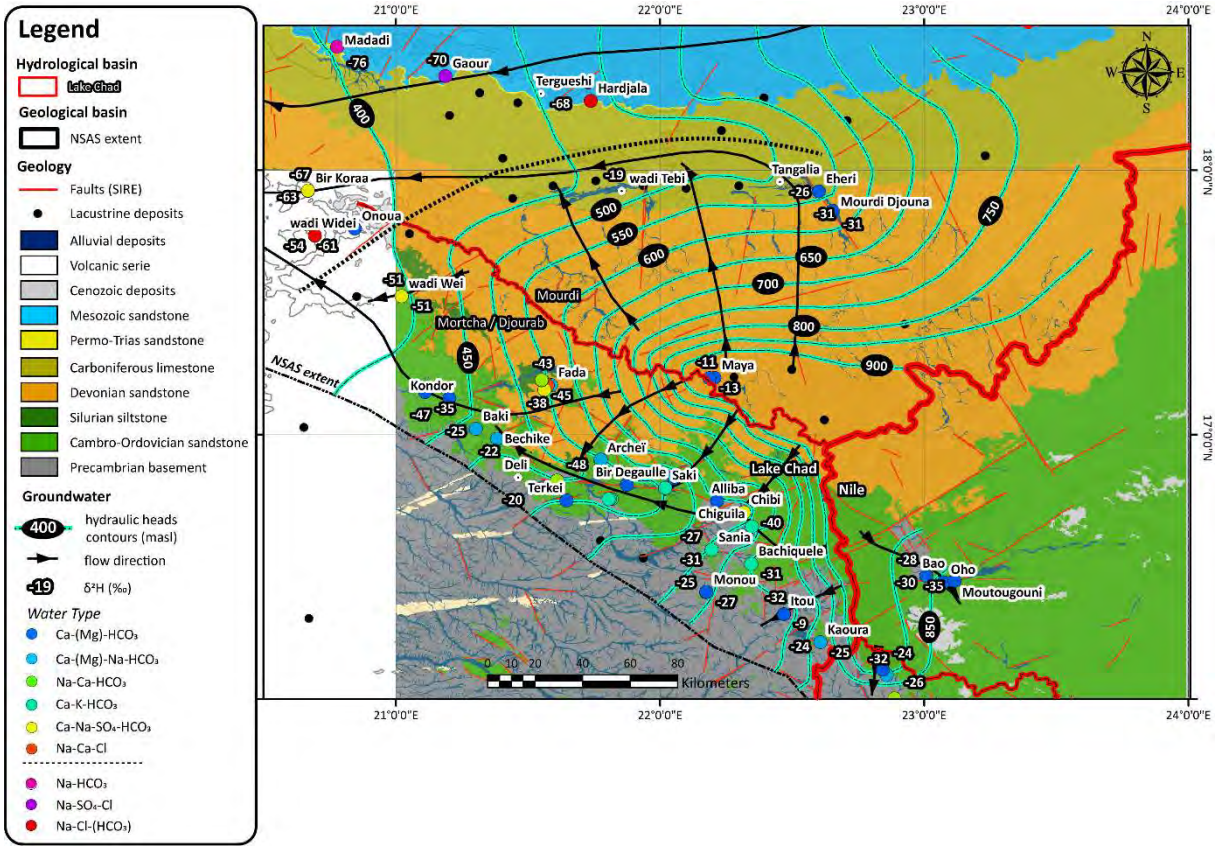

Figure 7.10: Chemical species and deuterium distribution in the Ennedi Mountains. Hydraulic heads contours and groundwater flow directions are derived from the hydraulic heads measurements. The dashed line indicates a marked difference of isotopic ratios between groundwater located within the Ennedi Mountains, characterized by increased rainfall, and the north-western zone characterized by lower rainfall rates. Geology is shown as background.

The southern Ennedi shows a relatively large variability of chemical species. However, higher contents of Ca (and Mg) are characteristic of this zone. Water type are mostly varying between Ca-(Mg)-HCO_3, Ca-(Mg)-Na-HCO_3 and Na-Ca-HCO_3. pH varies from 6.2 -7.9 and conductivities vary from 92 to 844 μScm^{-1}. A group of samples shows higher contents of K, geographically located between Toukou and Bachiquele. In some other localities, higher contents of SO_4 were detected (e.g. Chibi, Fada, Wadi Wei, Bir Koraa).

Groundwater from the highest elevations and sampled in the downstream of the main wadis flowing towards the Mourdi depression (Carboniferous limestone and marls) have similar chemical contents as samples from the Ennedi South region (Figures 7.10). Similar stable isotopic compositions were also

observed for samples from the southern slopes, the highest altitudes and groundwater from the few points located in the northern slopes in correspondence to wadis Kordi and Béméché.

A consistent difference of stable isotopic ratios was determined NW of the Ennedi Mountains (NW of the dashed line in Figure 7.10). No clear chemical difference is observed for the group of samples located between wadi Weï and Mouso from the samples located in the Ennedi Mountains. A more net distinction is seen for the group of samples located north of the Carboniferous limestone (Hardjalla, Gaour, Madadi). The chemical composition is dominated by Na-HCO_3 with high contents of SO_4 and Cl (water types Na-HCO_3, Na-SO_4-Cl and Na-Cl-(HCO_3)). Wadi Doum (NW of Madadi) distinguishes from the previous localities, by a Na-Mg-HCO_3 signature and very low Cl and SO_4 content. Conductivities vary between 235 in Madadi (spring) to 2,122 µScm^{-1} in Hardjalla (evaporated groundwater in a well not in use at the time of sampling). pH vary between 6.8 in wadi Doum and 9 in Tergueshi.

Figure 7.11 shows the distribution of the chemical and stable isotopic signature of groundwater in the central lowlands of the NSAS.

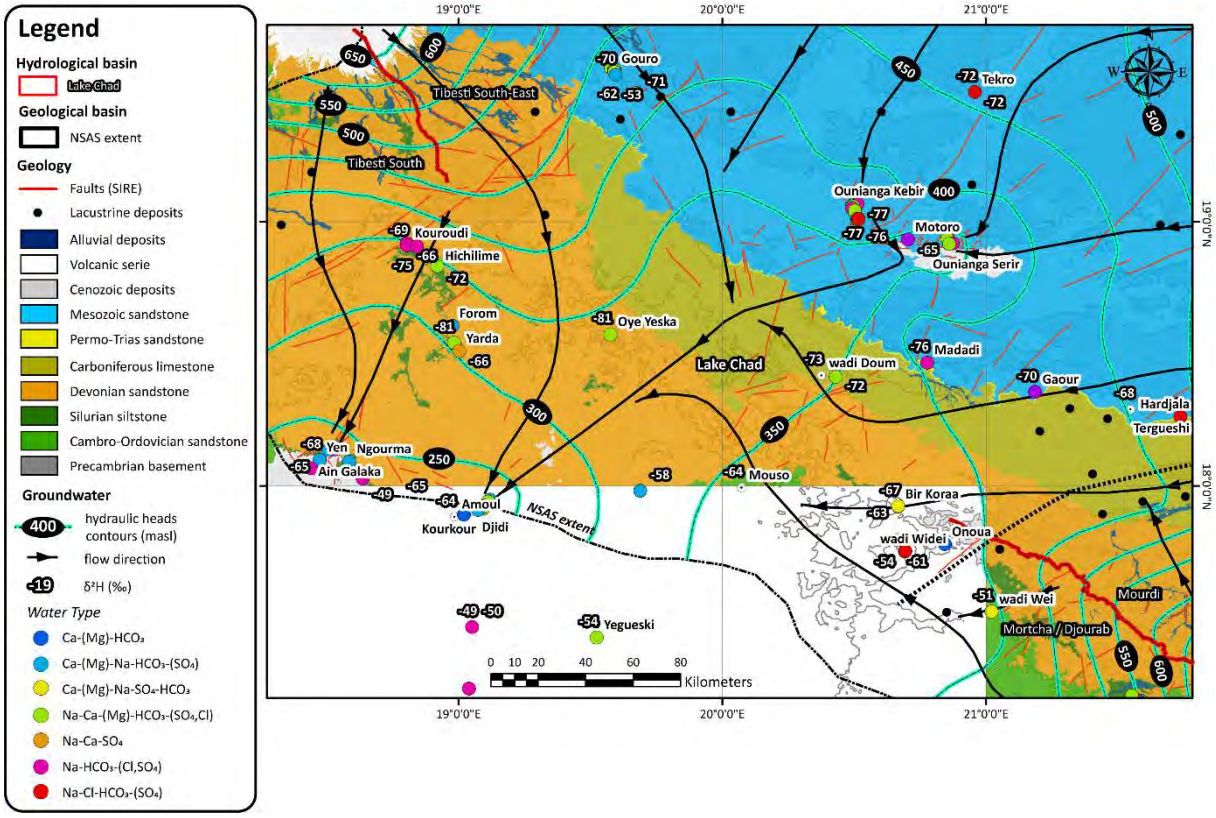

Figure 7.11: Chemical species and deuterium distribution in the central lowlands. Hydraulic heads contours and groundwater flow directions are derived from the hydraulic heads measurements. The dashed line indicates the marked difference of isotopic ratios between groundwater located within the Ennedi Mountains, characterized by increased rainfall, and the central lowlands characterized by lower rainfall rates. Geology is shown as background.

On the southeastern slopes of the Tibesti Mountains, the water sample from Bini Herdé has a chemical composition Ca-(Mg)-HCO_3. In Gouro, water samples have chemical compositions varying between Ca-Na-HCO_3 and Na-Ca-HCO_3 (Figure 7.12A). A similar compositional difference was also observed in the stable isotopic signature, more enriched for the sample of Bini Herdé, compared to samples from the Gouro oasis. Within the oasis, the water points located centrally show an enrichment in SO_4. Electrical conductivities are low (143 – 481 µS/cm) and pH neutral (6.9-7.6).

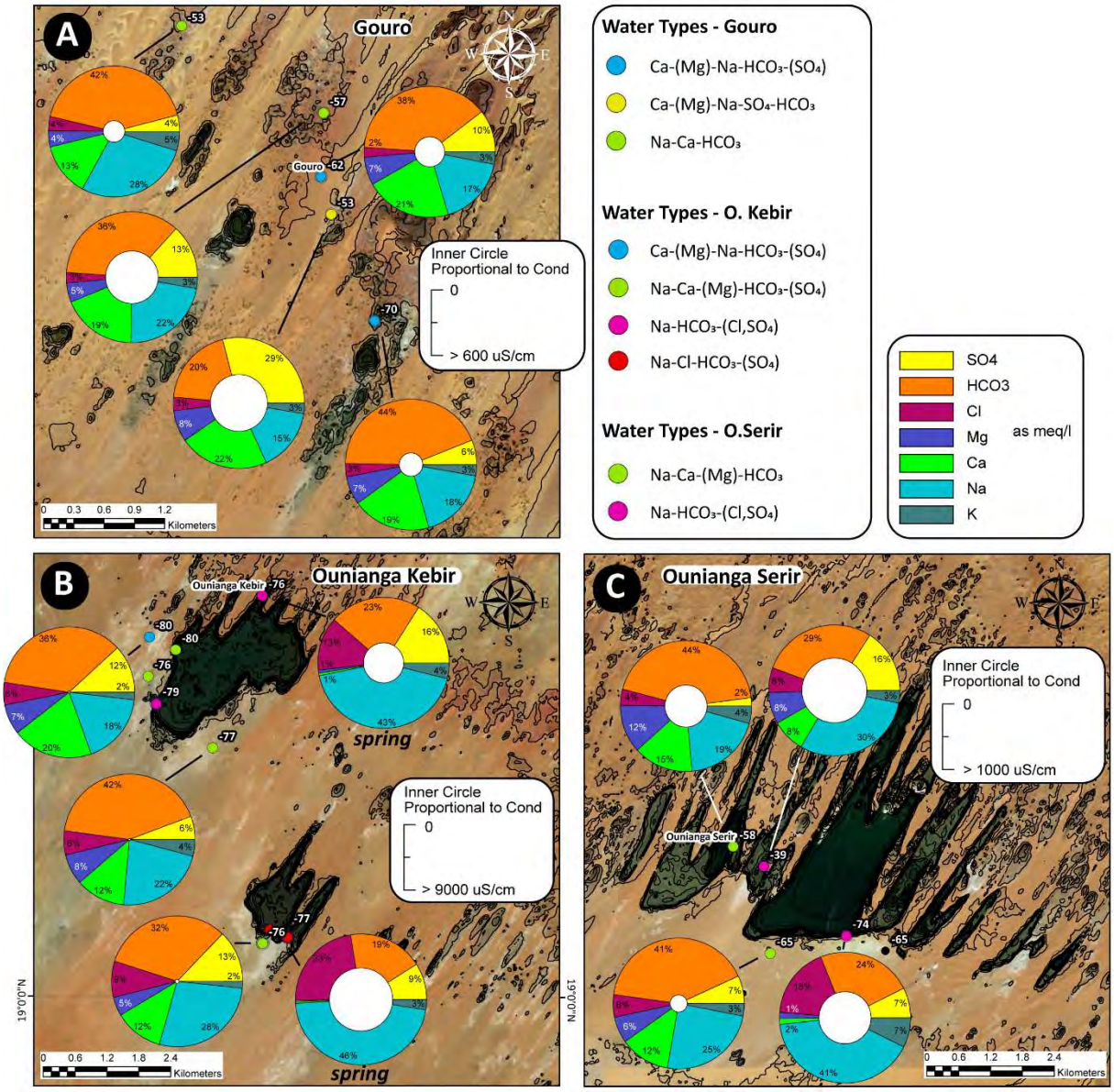

Figure 7.12: Water types and isotopic signature (are indicated the deuterium ratios) for the oases of A) Gouro, B) Ounianga Kebir and C) Ounianga Serir.

The lakes and shallow groundwater from Ounianga Kebir, Ounianga Serir, Motoro and Tekro are characterized by a dominance of Na and HCO_3 (water types Na-Ca-HCO_3 and Na-HCO_3) and variable contents of Cl and SO_4 (Figure 7.12B and C). The sample from Tekro and the springs discharging into

the lakes of Ounianga show higher contents of Cl (water types Na-HCO_3-(Cl, SO_4) and Na-Cl-(HCO_3)). Springs and surface waters have pH values between 8.2 and 10.5. Evaporated samples have a pH between 8.7 and 11.2. Groundwater from traditional and improved wells, located in proximity to the lakes, have pH values of 6.4-7.4, lower electrical conductivities (280-660 μScm^{-1}), increased contents of Ca and Mg, and lower contents of Cl than the springs and lake waters.

Slightly more enriched isotopic ratios were measured for surface water and shallow groundwater from Ounianga Serir than for samples from Ounianga Kebir. In terms of hydrochemistry, what mostly distinguishes the group of lakes of Ounianga Kebir and Ounianga Serir, is the total ionic content distribution of the lake waters. In Ounianga Kebir, lakes Yoa, Oma, Béver, Mijoi and Forodone are all extremely mineralized (5-197 $mScm^{-1}$). Only lake Katam, the most marginal towards the ESE, have moderate ionic content (2,600 μScm^{-1}), associated to enrichments in NO_3. In Ounianga Serir, only the sampled surface water from Lake Teli (central lake) show extreme electrical conductivities (100 $mScm^{-1}$). Otherwise, E.C. values of surface and groundwater vary between 300 and 1,000 μScm^{-1}. Similarly as for the group of lakes of Ounianga Serir, characterized by an increase of ionic content in the central lake compared to the marginal ones, the two central lakes (Oma, Bever) of Ounianga Kebir show an enrichment in Cl, compared to Lake Yoa. In Chapter 6, we showed that these two central lakes are located at slightly lower elevation, the groundwater flow being directed towards these lakes. The observed increase in ionic contents towards the central part of these groups of lakes is therefore the result of groundwater flowing from higher elevations (marginal lakes) towards lower elevations (central lakes), with progressive evaporative processes at the discharge location.

In the Southern Tibesti, the group of water points in Kouroudi-Yarda show a general bicarbonate facies with enrichments in SO_4 (Figure 7.13A). In Kouroudi, groundwater are more enriched in Na (Na-Ca-HCO_3 and Na-HCO_3–(SO_4) water types), while in Yarda, the main water types are Ca-(Mg)-Na-HCO_3 and Na-Ca-HCO_3. One sample in Yarda is particularly enriched in Na-SO_4. As previously observed for the stable isotopes, the chemical species distribution also do not show clear changes along the flow lines. Electrical conductivities vary between 420 and 1,070 μScm^{-1} and pH are slightly acidic (6.8-6.9).

In Faya-Largeau, pH values vary from 6.2 to 8.5 and conductivities from 120 to 1733 μScm^{-1}. In the center of the oasis, where most of the artesian boreholes are located, Na is dominant over Ca (water type Na-Ca-(Mg)-HCO_3), while in the upper and lower sections, Ca is slightly more enriched than Na (water types Ca-(Mg)-Na-HCO_3 and Ca-(Mg)-Na-HCO_3, Figure 7.13B). Wells tapping in the more superficial aquifer do not show a significant chemical difference from boreholes supplied from the artesian flow, when located in proximity. Bicarbonate facies is predominant, but SO_4 and Cl are also found in a certain concentration. Higher contents of SO_4 and Cl are found in the zone of higher

hydraulic heads. Additionally, all samples show a certain concentration of Mg, increasingly present in the zone of lower hydraulic heads (Kourkour, Mordangaye). The stable isotopic signature distribution showed a progressive evaporative enrichment along the flow lines, from the NE to the SW.

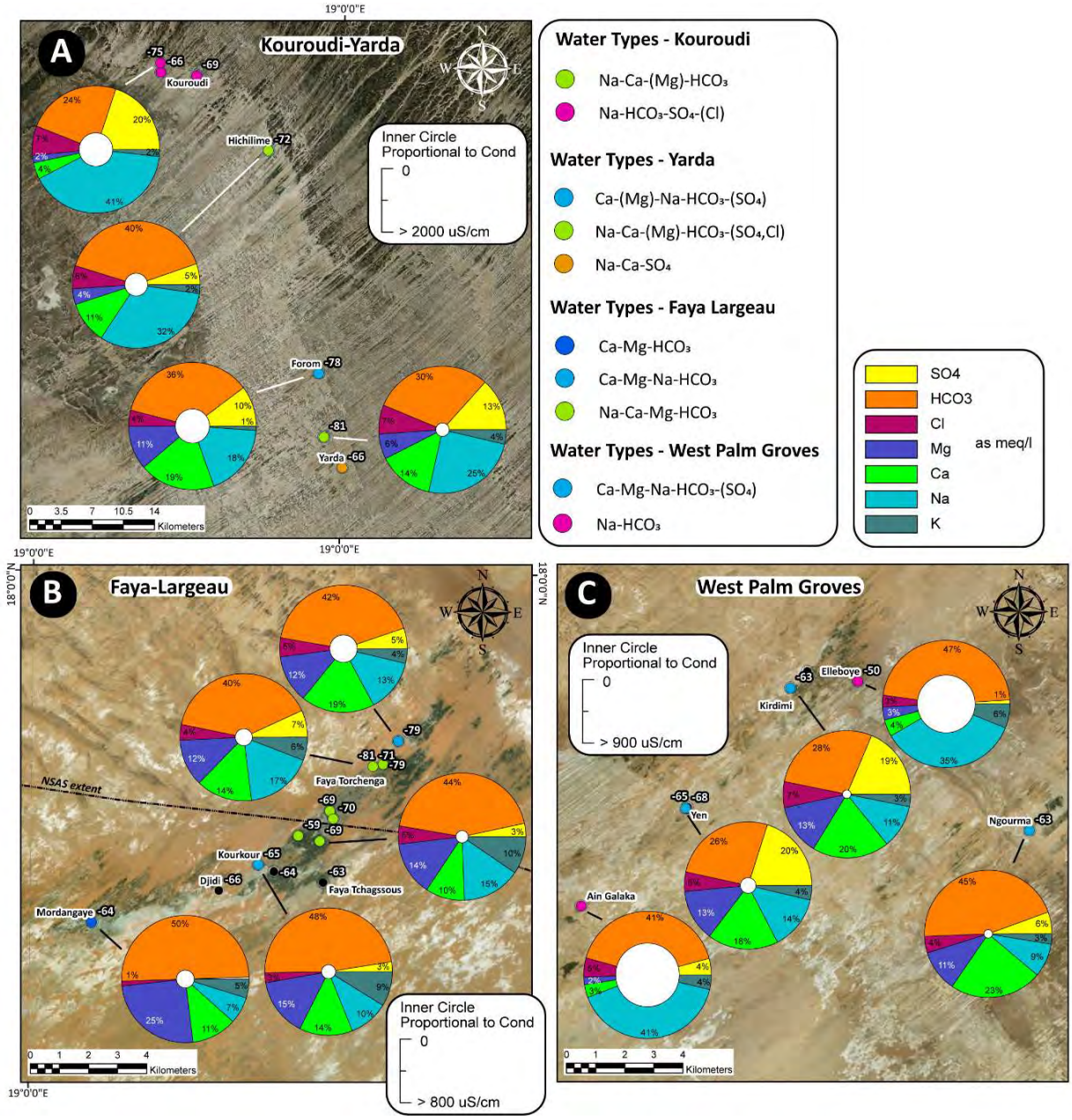

Figure 7.13: Water types and stable isotopic distribution (values are deuterium ratios) in A) Yarda-Kouroudi, B) Faya-Largeau and C) West Palm Groves.

Groundwater from the West Palm Groves (i.e. Aïn Galaka, Yen, Ngourma, Kirdimi, Elleboye) have chemical signatures varying from Ca-(Mg)-Na-HCO_3 (artesian springs of Kirdimi and Yen, well in Ngourma) and Na-HCO_3 (artesian spring of Aïn Galaka, well in Elleboye, Figure 7.13C). The artesian springs of Kirdimi and Yen have higher SO_4. Higher conductivities are associated to the well of Elleboye,

also characterized by slightly more enriched stable isotopic ratios, and to the evaporated surface water collected in Aïn Galaka.

Samples from the Lake Chad geological basin (Figure 7.11) have chemical signatures Na-Ca-HCO_3 and Na-HCO_3 with very low content of SO_4. Stable isotopic ratios are slightly more enriched than in the oases of Faya-Largeau and West Palm Groves.

7.5. Discussion

7.5.1. The Tibesti Mountains

7.5.1.1. Stable isotopic signature

The southern slopes of the Tibesti Mountains are characterized by higher rates of rainfall and a longer rainy season (May to September, Chapter 5). A generally enriched isotopic ratio is observed for groundwater located within this region. The isotopic signature is comparable to contemporary precipitation (Abouelmagd et al., 2012 ; Joseph et al., 2012), therefore indicating groundwater recharged by the current meteorological and hydrological cycle. Similar isotopic signatures are also found in water points located in the upper sections of enneris Zoumri and Yebbigué (northern slopes). These enneris are known to be active once every three years (Brunet-Moret, 1963). The enneri Zoumri-Bardangué was reported to have reached flow rates of 425 m^3s^{-1} in 1954 and 200 m^3s^{-1} in 1966 (Rodier and Roche, 1978). In such extreme events, inundated length of wadis reach 150 km north-west of Bardaï.

The northern slopes are characterized by a contracted rainy season (May and August). Rainfall rates are still high along the mountain ridges, but comparably lower in the rest of the concerned area. Stable isotopic signature of groundwater from the northern slopes are mostly depleted. Similar depleted ratios were associated by previous authors working in North-Eastern Africa, to groundwater having infiltrated during the more cooler and humid Pleistocene to Holocene periods (e.g. Sonntag et al., 1978; Edmunds and Wright, 1979; Edmunds, 2009; Sultan et al., 2011; Faitouri and Sanford, 2015). Paleohydrological deposits from the Tibesti Mountains (Jäkel, 1979) and from the Ounianga Lakes (Kröpelin et al., 2008) indicate that the region of the Tibesti has experienced a favorable climatic setting until in the least 4,300 yrs. BP.

Herczeg and Leaney (2011) critically reviewed stable isotopic fractionation processes occurring in arid climates. Very contrasted isotopic ratios could be measured in groundwater resulting from recharge occurring in different seasons (summer against winter), at different altitudes, from high-intensity or low-intensity precipitation events (amount effect), or whether located before or after the zone of major meteoric discharge. However, in the Tibesti Mountains, groundwater with distinct enriched and

depleted signatures for proximal water points proves that the depleted ratios are depleted because corresponding to recharge during a past cooler period rather than because resulting from current climatic, meteorological and topographical fractionation processes. The distinct isotopic ratios for proximal water points is therefore indicating the presence of groundwater resulting from different origins and ages. This is in agreement with dating from Jäkel (1977), which found groundwater ages of up to 10,000 yrs. BP together with a tritium content within the alluvial system of enneri Zoumri, indicating admixture with a modern component.

7.5.1.2. Chemical signature

The groundwater's chemistry of the Tibesti Mountains shows a Na-HCO_3 dominant composition. Ca and Mg are mostly subordinate. SO_4 can locally be found in high concentrations. The sodium-dominated character of groundwater was interpreted by Dalloni et al. (1934) as the result of groundwater flowing through volcanic rocks rich in dissolved salts, and discharging in areas of lacustrine deposits accumulation, containing a certain amount of sodium salts. Rhyolitic and ignimbritic deposits (40% of the rocks composing the region) cover large areas of the highest parts of the drainage systems, where precipitation rates are higher. Ryholites (and other subordinate felsic rocks, i.e. ignimbrites, phonolites, syenites, trachytes) are alkaline to subalkaline, with Na/Ca ratios varying from 1 to 9 (Dalloni et al., 1934). Associated high concentrations of K are also common. Additionally, acidic fluids related to the volcanic activity would enhance the weathering of alkaline feldspars and liberate higher amounts of Na, as suggested by Dalloni et al. (1934).

7.5.2. The Nubian Sandstone Aquifer System of Northern Chad

7.5.2.1. Stable isotopes and hydrochemical signature in the Ennedi Mountains

Similarly to the Tibesti Mountains, the spatial distribution of major ions and stable isotopic signatures in the Northern Chad's sector of the NSAS, is consistent with the distribution of the rainfall rates and with the groundwater flow directions. Where precipitations are higher (> 60 mmy^{-1}), groundwater has distinctively enriched isotopic values ($\delta^{18}O$ -6.7‰ to -2‰ and $\delta^{2}H$ -48‰ to -9‰) and a calcium-(magnesium)-sodium-bicarbonate chemical composition. In these zones, hydraulic heads are more elevated (> 600 masl) and the hydraulic gradients are higher (3-4‰).

Within the southern slopes of the Ennedi Mountains, from Bachiquele to Kondor, groundwater has a more enriched isotopic ratio ($\delta^{2}H$ > -30‰) and chemical signatures vary between Ca-(Mg)-HCO_3 and Ca-(Mg)-Na-HCO_3. Similar chemical and isotopic contents are also observed in Maya and in the downstream zone of wadis Kordi and Béméché, on the northern slopes. From Fada towards the NW, the isotopic signature progressively changes to more depleted values and the chemical composition is increasingly enriched in Na.

The changes of isotopic signature and chemical composition of groundwater are correlated to the distance from the zone of highest precipitation. Within the southern slopes and the highest plains of the mountain chain, characterized by increased precipitation, groundwater is distinctively enriched and alkali earth-bicarbonate. This compositional signature might therefore indicate the zone experiencing the highest rates of diffuse and concentrated modern recharge. With the increase of distance from the zone of highest precipitation rates, and therefore a lower direct influence of diffuse and/or concentrated recharge, hydraulic heads decrease, the stable isotopic ratios are more depleted and the groundwater chemical content changes to more alkali-bicarbonate, compatible with a longer time of rock-water interaction. The overall chemical and stable isotopic signature in the Ennedi Mountains shows that these are valuable parameters enabling to characterize: (1) where modern recharge is of increased intensity, (2) where the supply of concentrated recharge through the wadi systems contributes substantially to the groundwater signature, and (3) where groundwater discharges after a more lengthy period of percolation through the geological layers.

A zone of infiltration is undoubtedly located in the high plains of the mountain chain, characterized by increased precipitation rates. As discussed in the previous chapters (Chapters 5 and 6), the accumulation of surface water in natural ponds and subsequent infiltration is likely to be an important mechanism of recharge. Most of the water points are traditional wells located within the alluvial system of wadis, which originate in the high plains. The springs of Archeï and Bachiquele are connected through factures to the high plains.

Runoff flowing towards the north through the wadi systems is moreover the only observed mechanism capable of accumulating large volumes of surface water within the northern slopes, characterized by low rainfall rates. However, the hydraulic properties of the fractured Mid and Upper Devonian micaceous sandstone, largely devoid of vegetation, would potentially allow the infiltration of rainfall over larger areas and more specific in zones of denser fracturing.

The somehow uneven distribution of water points, densely distributed within the southern slopes and localized in the downstream of the main alluvial systems within the northern slopes, is reflecting the precipitation distribution and the increased importance of concentrated recharge versus diffuse recharge within the northern slopes. However, the few examples of water points within the northern slopes seem somehow only representing part of the flow that could result from recharge in the high plains. Part of the flow, originating from infiltration in the high plains, could potentially flow more deeply (Cambro-Ordovician and/or Lower Devonian) towards the N and NW (see Chapter 4).

7.5.2.2. Stable isotopes and hydrochemical signature in the central lowlands

Similar chemical and isotopic compositions as in the Ennedi Mountains, were also found in the Tibesti Mountains: within the eastern slopes (Bini Herdé), the southern slopes (Zouar, Misky) and in the upper parts of the main enneris (Zoumri, Yebbigué) of the northern slopes.

The central lowlands experience generally < 25 mmy^{-1} of precipitation, are situated in low-lying zones (depressions), hydraulic heads are below 500 masl, hydraulic gradients are low (0.5-1‰) and the water table is close to the surface ground (< 5 m bgl). The isotopic ratios tend to more depleted values ($\delta^{18}O$ -11.7 to -5.7 ‰, $\delta^{2}H$ -85 to -39‰) and the chemical composition shows a progressive increase in alkalis-bicarbonate contents and higher concentrations of SO_4 and Cl. pH is more alkaline and conductivities are higher in the central lowlands than in the Ennedi Mountains.

The isotopic signature distribution in the central lowlands also follows the distribution of precipitation. Intermediate values locate at the margins of the zone of influence of increased precipitation: at the foothill of the Ennedi Mountains (Bir Koraa, Mouso), of the Tibesti Mountains (Gouro, West Palm Groves) and of the Erdis plateaus (Hardjalla, Tergueshi).

The most depleted ratios are located between the oases of Faya-Largeau, Yarda-Kouroudi, Tekro, the Ounianga Lakes, Gaour, Madadi and wadi Doum. The hydrochemical and stable isotopic signatures found in this region are in agreement with the general hydochemical signatures found in oases and sebkhas in Libya (Goudarzi, 1970; Pachur and Altmann, 2007) and in the Lake Chad geological basin (Herrmann et al., 2009). These signatures were associated to groundwater recharged during the Pleistocene-Holocene pluvial periods. Ages of 9,6 – 7,5 kyr were determined for groundwater within the Paleozoic sandstone of Faya-Largeau, with associated $\delta^{18}O$ ratios varying between -9 and -10.5‰ (Schneider, 1989).

Surface water and groundwater from the oases of Ounianga and Kufra are comparably similar. The lakes of Ounianga are characterized by a general enrichment of alkalis over alkaline earths, and a bicarbonate facies (main water types Na-Ca-HCO_3 and Na-HCO_3), with relatively high amounts of sulfates and chlorine. In Kufra, groundwater has a chemical composition enriched in Na, Cl and SO_4 and alkali pH (Pachur and Altmann, 2007). In Ounianga Kebir, the isotopic ratios vary from -11.4 to -9.6‰ $\delta^{18}O$ and from -85 to -76 ‰ $\delta^{2}H$. In the Kufra oases, the shallow and deep aquifers were dated between 9,5 to 37,5 kyr (Edmunds and Wright, 1979; Swailem et al., 1983; Faitouri and Sanford, 2015), associated to depleted isotopic ratios ($\delta^{18}O$ and $\delta^{2}H$ of -11.4‰ and -84.1‰, respectively). Hydraulic heads vary between 373-383 masl in Ounianga Kebir, and 345-360 masl in Ounianga Serir. In Kufra, hydraulic heads are 375 masl. Additionally, the evaporation fractionation line of stable isotopes of

springs, lakes and shallow groundwater from Kufra (Edmunds and Wright, 1979; Swailem et al., 1983) is comparable to the evaporation line calculated for the surface water of the Ounianga Lakes.

7.5.2.3. Chemical signature of the NSAS of Northern Chad

The general signature of groundwater within the NSAS of Northern Chad is characterized by low salinity and the predominance of a Na-Ca-bicarbonate chemical composition. The aquifer is mostly composed of quartzitic sandstone and quartzwackes with high contents of quartz (SiO_2 85-96 wt%) and subordinate feldspar, plagioclase, kaolinite and biotite (< 9 wt% Al_2O_3, < 9 wt% Fe_2O_3 < 0.24 wt% CaO, < 0.1 wt% MgO and Na_2O, see Chapter 3).

Compared to the zones experiencing increased rainfall and characterized by higher hydraulic heads, thus identified as zones of recharge, groundwater in the central lowlands show increased salinities, more alkaline pH and a more sodium-bicarbonate chemical composition, with higher contents SO_4 and Cl. Chemical compositions of Ca-Na-HCO_3 or Na-Ca-HCO_3, are observed in the zones of recharge (e.g. Ennedi Mountains), changing to compositions of Na-HCO_3 and Na-HCO_3-Cl in the zones of discharge of the central lowlands.

Previous authors (e.g. Jankowski and Jacobson, 1989; Domenico and Schwartz, 1998; Cook and Herczeg, 2000; Tóth, 2009) have observed and interpreted similar chemical changes along the flowlines as resulting from a series of common chemical reactions such as dissolution-precipitation, ion exchange, redox reactions or reactions involving clay minerals. Evapotranspiration and associated precipitation of minerals is also potentially a major process determining the chemical changes of groundwater in the discharge zones of Northern Chad. Moreover, authors have observed that deposits of Trona ($NaHCO_3.Na_2CO_3.2H_2O$) and Gaylussite ($Na_2Ca(CO_3)_2.5H_2O$) are most often associated with Quaternary lake sediments such as diatomites, rich in sodium salts and widely observed in the low-lying regions of Northern Chad (Herrmann et al., 2009) and in other parts of the NSAS (Goudarzi, 1970). In Northern Chad, groundwater in proximity to diatomite deposits also shows enrichments in SO_4.

The groundwater hydrochemical signature in the central lowlands is therefore potentially the result of: (1) the chemical reactions and processes occurring from recharge to discharge, associated to the interaction with the reservoir's rocks, (2) the presence of lacustrine deposits, and (3) evaporative enrichments and associated mineral precipitation in the discharge zones.

In terms of water quality, several samples show specific contaminations of ammonia, nitrites, nitrates or fluorine. Overall 55% of the samples have a concentration in N-related species above the recommended limit for drinkable water. Values between 11 and 21 mgL^{-1} NH_4 were found in the Ennedi region. Concentrations of 785 to 844 mgL^{-1} NO_3 were found in the Ennedi region and from a minor number of samples from the Ounianga Lakes. High contents of N-related species in groundwater have

been reported in many localities from the Sahara (Herrmann et al., 2009), interpreted as the result of the degradation of vegetation, covering the Sahara during the past pluvial periods. However, variable contents were detected for several water points re-sampled at different dates, thus potentially resulting from anthropogenic contamination. In fact, most of the water points are open wells, crowded with humans and animals.

Another potential threat for human health is fluorine. 18% of the samples have a higher content of F than the recommended limit, with a maximum value of 569 mgL^{-1} for the surface water from one of the lakes in Ounianga Kebir.

7.6. Conclusions

The use of major ions and stable isotopes provided important means to characterize the groundwater system of the NSAS of Northern Chad. The hydrochemical and stable isotopic signature of groundwater, supported by data from the field (hydraulic heads, Chapter 4) and from remote sensing data analysis (precipitation and evapotranspiration maps, Chapters 5 and 6), enables to distinguish the zones experiencing modern recharge from the zones of discharge, and to assess the extent of its influence. The distribution of the signature enables to discuss about the mechanisms of recharge (diffuse, concentrated) and their regional relative predominance.

The spatial distribution of the stable isotopic and hydrochemical signatures is highly correlated to the distribution of the precipitation rates. Zones of higher precipitations have a distinct enriched isotopic ratio and a Ca-Na-bicarbonate chemical composition. The zones showing this hydrochemical characteristic are located in the Tibesti and Ennedi Mountains, also characterized by higher hydraulic heads and gradients. The regions with the highest potential for diffuse recharge correspond, unsurprisingly, to the zones of highest precipitation rates (high plains, southern slopes). Most of the water points are located along the alluvial systems of wadis and enneris, thus indicating the importance of concentrated recharge as well (see also Chapters 5 and 6). Within the northern slopes, characterized by lower rainfall rates, concentrated recharge is predominant.

Groundwater in the discharge zones of the central lowlands are characterized by more depleted stable isotopic ratios, higher ionic contents, alkali pH and increased concentrations of SO_4, Cl and Na, than in the zones of recharge. Comparable hydrochemical and stable isotopic composition were observed for groundwater and surface water from other parts of the NSAS. In particular, the similarities between the oases of Kufra (Libya) and Ounianga are remarkable. This groundwater compositional type was interpreted by previous authors as representing groundwater recharged during the past cooler pluvial periods of the late Pleistocene to Holocene.

Chapter 8

Synthesis of the results and conceptual groundwater model

8.1. Content of the chapter

The aim of this thesis is to characterize the large-scale organization of the groundwater flow system of the NSAS of Northern Chad. In the arid region of Northern Chad, groundwater constitutes the most important water resource. In order to develop a strategic plan for a sustainable use of this precious resource and given the large dimensions of the system, it is fundamental to acquire a better understanding of the aquifer's properties and of the groundwater flow organization at a regional scale.

The first section of this chapter (section 8.2) provides a synthesis of Chapters 2, 3 and 4, including a discussion of the possible origins of groundwater supplying the lakes of Ounianga and on the potential role of recharge in the regional aquifer system.

Data from the analysis of remote sensing products (precipitation, Chapter 5, and actual evapotranspiration, Chapter 6) are subsequently used to compile a preliminary surface water balance (P-ET). The volumes gained by the system through precipitation and the volumes lost by the system through evapotranspiration are discussed in section 8.3.

Finally, the integration of the chemical and stable isotopic signature of groundwater (Chapter 7) is used to develop a conceptual groundwater flow model of the Nubian Sandstone Aquifer System of Northern Chad (section 8.4).

8.2. Hydrogeology of the NSAS of Northern Chad

The analysis of the geological history of the Kufra basin has shown that the basin was shaped in several tectonic phases (Chapter 2). As a result, stratigraphic discontinuities (Silurian – Caledonian, Carboniferous – Hercynian, Cenozoic), variable thicknesses of geological formations (Paleozoic), uplifted and subsided zones, and several generations of fault directions characterize the basin.

In the Kufra basin of Northern Chad, the topography follows the geological structure of the basin. Zones of basement uplifts (Ennedi and Tibesti Mountains) are also characterized by higher elevations

(up to 1,300 masl in the Ennedi Mountains and up to 3,440 masl in the Tibesti Mountains). Topography has a direct influence on the rainfall rates and therefore on the potential for recharge (see section 8.3).

The zone between these mountainous regions ("central lowlands") lies at lower altitudes (< 500 masl). This central zone also corresponds to the subsided part of the basin, characterized by an increased sedimentary thickness. The main discharge zones of the NSAS of Northern Chad (oases of Ounianga Kebir, Ounianga Serir, Faya-Largeau) are located within this depressional and subsided zone of the basin. The zone is extending SSW-NNE from Chad to Libya and was identified as the Hercynian Borkou-Kufra Trough by Williams (1966) or the Pelusium mega shear zone by Mohamed et al. (2017). Mohamed et al. (2017) indicate this zone as characterized by increased fracturing and therefore higher hydraulic conductivities (and connectivity between aquifers).

The sedimentary sequence of the Kufra basin is composed of 950 to 1,950 m of continental sandstone with variable intergranular porosities (up to 35% for the sandstone layers, 0% for the silty interlayers). The study of the sedimentary sequence of the Kufra basin of Northern Chad (Chapters 3 and 4) shows that the multilayer aquifer system is potentially composed of three major and one minor aquifer formations: (1) Cambro-Ordovician (50-400 m), (2) Devonian (350-850 m), (3) Permo-Trias (Madadi, 50 m) and (4) Cretaceous (Ounianga, Chieun and Tekro, 500-650 m).

The sequences of continental sandstone are interrupted by sedimentary sequences of reduced intergranular porosities (up to 6%) and lower hydraulic conductivities: (1) Silurian siltstone (up to 80 m thickness), (2) Carboniferous marls and limestone (up to 350 m thickness), (3) Soeka argillite and Lakes fine sandstone (up to 400 m thickness) and (4) Cenozoic sediments (up to 70 m thickness in Faya-Largeau, BRGM, 1991).

The differential erosion of the sandstone and of the argillaceous intercalations resulted in the typical "cuesta" morphology, characteristic of the region. The sandstone layers are marked by cliffs and the more argillaceous deposits by platforms.

In Northern Chad (Chapter 4), discharge points (springs, lakes) are generally located at a topographic break, in correspondence to sandstone layers showing high intergranular porosities but in proximity to an underlying less permeable layer. Structural discontinuities and the intersection of several directions of faults and fractures are also always associated with the discharge locations. Examples are given of the springs of Archeï and Bachiquele and the oasis of Fada in the Ennedi Mountains, the spring of Madadi, the water points of Gaour, Tergueshi and Hardjalla, the lakes of Ounianga and the oases of Gouro, Faya-Largeau and West Palm Groves in the central lowlands.

The Paleozoic sedimentary sequence in the uplifted regions of the Ennedi and Tibesti Mountains is characterized by intense fracturing. The fracturing provides an increased storage capacity to the consolidated quartzitic sandstone and preferential paths for infiltration through open fractures, sinks and along wadis. In the Mountains of the Ennedi and Tibesti, wadis play a major role during the rainy season in rapidly transporting and concentrating through runoff large volumes of surface water at the foothill of the mountainous relief (see section 8.3). During the dry season wadis represent low points where groundwater, previously infiltrated within the high plains, converge, as attested by the numerous perennial water points located within the major alluvial systems. At the moment, this process secures the annual supply of water to a small group of inhabitants.

The higher hydraulic heads and gradients (3-4‰ in the Ennedi and 4-6‰ in the Tibesti), identify these mountainous regions as zones of recharge. Groundwater flows in a WNW direction from the Ennedi Mountains and in a SE and SSE direction from the Tibesti Mountains, towards the main discharge zones in Northern Chad (oases of Ounianga Kebir, Ounianga Serir and Faya-Largeau). Within the SSW-NNE central depressional zone, groundwater flows towards the SW in Chad. The lowest hydraulic heads are found in Faya-Largeau (217 masl) and more southerly in the Djourab puits 110 (198 masl). Although based on relatively few points of observation (2 water points every 1,000 km^2), hydraulic heads are generally seen to parallel the topography. Hydraulic gradients are comprised between 0.5 and 1‰. The observed hydraulic heads and gradients in Northern Chad are in general agreement with the conceptual flow model of previous authors (Ball, 1927; Sandford, 1935). These authors also observed a groundwater flow towards the NW in Libya (see Figure 1.1).

Given the hydraulic heads measured in Kufra (Libya) and in Ounianga (Chad), the groundwater divide is potentially located in the more elevated region between the Tibesti Mountains and the Erdis Plateaus, approximated by the hydrological divide between the Lake Chad and Mediterranean hydrological basins (Figure 8.1, cross-section 1). According to our analysis based on remote sensing data (Chapter 5), the origin of the groundwater corresponds to a zone where no modern recharge is likely to occur. This zone has, however, potentially experienced large amounts of recharge in the past pluvial periods, as attested by the presence of lacustrine deposits (diatomites). Previous studies have indicated that humid climatic periods have dominated the region during the late Pleistocene to mid-Holocene (from 14,000 to 8,000 yrs. BP and from 7,000 to 4,000 yrs. BP, see Chapter 4).

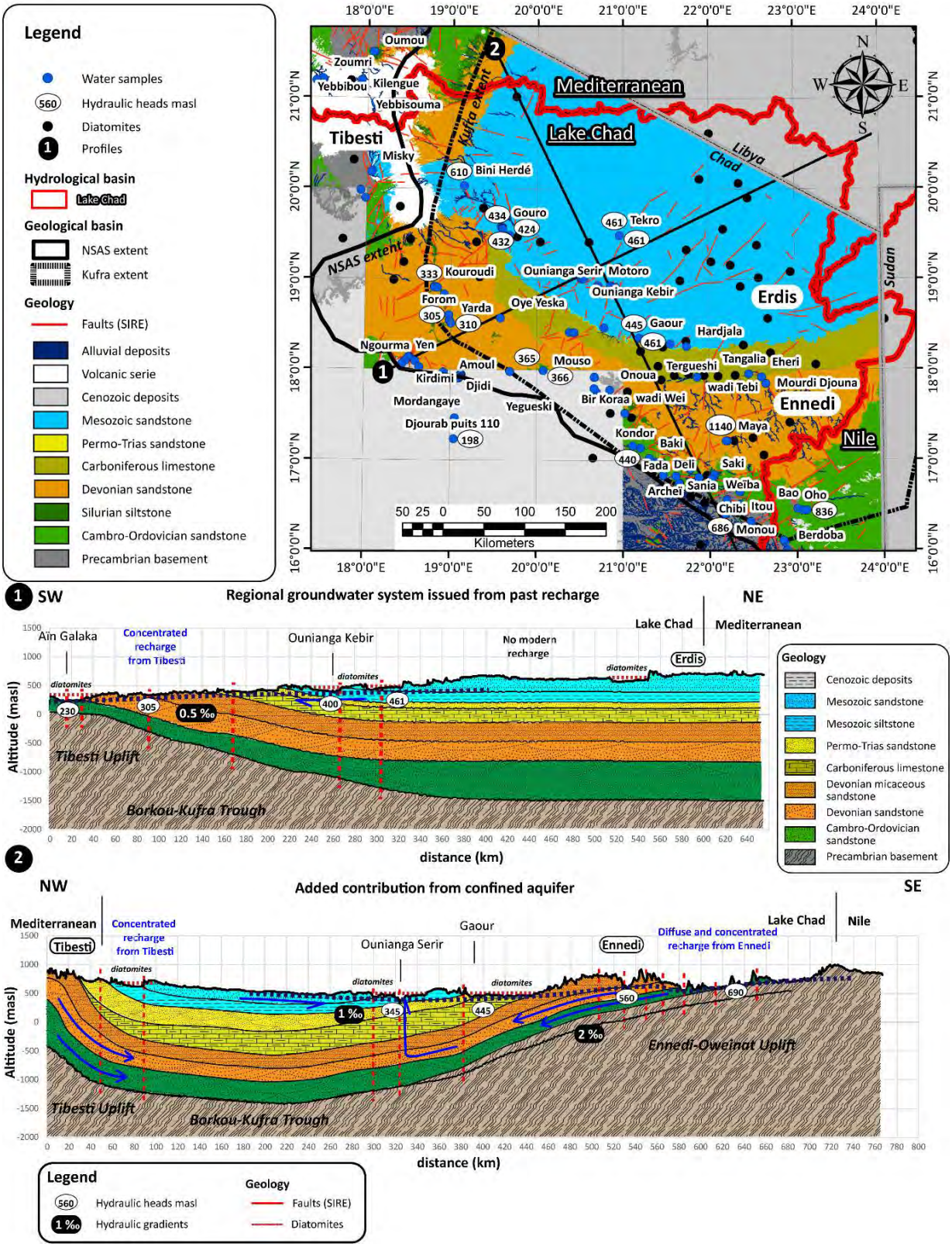

Figure 8.1: Reconstructed cross-sections, schematically representing the possible mechanisms of groundwater supply to the Ounianga Lakes.

The observed hydraulic heads in the central lowlands are therefore still indicating the zones of previous recharge during the humid periods of the late Pleistocene to mid-Holocene (Figure 8.1, cross-section 1). The high hydraulic heads observed in areas where recharge has likely been negligible for the last 4,000 years, are explained by Vasseur et al. (2015) as expressing the hydrodynamic properties of a large (horizontal and vertical) sandstone aquifer, characterized by a transient time of several thousand years.

Vasseur et al. (2015) also affirmed that modern recharge occurring in the unconfined sector of the NSAS (defined by these and previous authors as the zone south of the Post-Nubian limit, 25°N) plays a major role in maintaining higher hydraulic heads and gradients. They indicate that without the unconfined and recharged sector, the Libyan and Egyptian oases would already have disappeared. Similar conclusions were also presented by Ahmad (1983) and by Mohamed et al. (2017). Mohamed et al. (2017) concluded that the groundwater flows from the unconfined and more elevated regions of the southern Kufra basin to the northern Kufra basin. As such, these authors describe the groundwater flow configuration in a similar manner as hypothesized by the early researchers (the *allochtonous theory*, Chapter 1, Sandford, 1935; Hellström, 1940), according to which the southern borders of the NSAS, recharged and more elevated, are supplying the lower-lying areas of Libya and Egypt, where most of the oases are found.

Modern recharge occurring in the Ennedi and Tibesti Mountains is likely to be important for the Northern Chad extent of the NSAS. However, it is more challenging to assess whether this recharge plays a role for the entire aquifer system, as suggested by Vasseur et al. (2015).

For recharge occurring in the Ennedi Mountains to reach the northern Kufra basin to the NE, part of the groundwater should be confined under the Carboniferous marls and limestone (north of 18°N, see Chapters 3 and 4, Figure 4.7 cross-sections 1 and 2). All previous researchers (e.g. Sandford, 1935; Hellström, 1940; Vasseur et al. 2015) have, however, described the NSAS as unconfined south of 25°N (Figure 1.1). Confinement of the aquifer under the Carboniferous could eventually explain how recharge occurring in the Ennedi Mountains can influence the entire groundwater system of the NSAS. At the same time, groundwater flowing towards the north through the confined aquifer could eventually also contribute to the supply of the lakes of Ounianga (Figure 8.1, cross-section 2). Results from numerical modeling (Voss and Soliman, 2014) indicate that in the thickest part of the basin, such as the main discharge zones of the NSAS of Northern Chad (e.g. lakes of Ounianga), artesian flow might be an important part of the groundwater supply to the oases. Otherwise, the lakes of Ounianga are supplied by the unconfined aquifer flowing towards the SW (Figure 8.1, cross-sections 1 and 2).

8.3. Climatic and hydrological dynamics of the NSAS of Northern Chad

As shown by the analysis of remote sensing data (Chapter 5), the topography has a major influence on the distribution of precipitation rates and therefore on the potential for recharge. Increased precipitation rates (> 60 mmy^{-1}) are experienced by the mountainous reliefs of the Ennedi and Tibesti Mountains, while the central lowlands experience only limited rates of annual precipitations (< 40 mmy^{-1}). In the current climatic setting, precipitation is dominated by the summer monsoons generally occurring during the months of July to September and mostly concentrated during the month of August. Some regions also receive low rates of winter rains (mountainous Tibesti, central lowlands). The mountainous relief concentrates most of the precipitation originating in the SW, within the southern slopes and higher altitudes of these mountainous chains. Low rainfall rates occur along the northern facing slopes. Wadis play a critical role in redistributing surface water, in particular for the regions of low rainfall rates such as the northern slopes. The southern facing slopes and higher altitudes of these mountainous chains correspond to the regions with the highest potential for diffuse recharge, while the northern facing slopes are potentially only experiencing sporadic episodes of concentrated recharge (Chapters 5 and 6).

The Ennedi Mountains show higher precipitation rates and a more active annual hydrological dynamics, thus corresponding to the region of highest potential for diffuse and concentrated recharge within the Kufra basin of Northern Chad. The intensity of the hydrological response (MNDWI36) is higher in the southeast of the Ennedi Mountains (Archeï, Bachiquele, Kaoura) than in the south-west (Fada, wadi Wei), but is higher in the north-west (wadi Kordi) than in in the northeast (wadi Béméché), mirroring the distribution of precipitation rates (Figure 8.3). In particular, the zones showing the highest hydrological dynamics are located in the high plains, and along the main wadis (Kordi, Archeï, Nohi, Haouach, Sini-Chili, Sala).

In the high plains of the Ennedi Mountains, several examples of localized ponds develop during the rainy season and slowly dry out during the dry season. This indicates that these ponds are not continuously supplied with water, and are therefore attributed to surface flow. In the southern slopes, important springs such as Archeï and Bachiquele, discharge at the base of the Cambro-Ordovician sandstone, but fractures are seen to connect the system to the high plains. Most of the water points within the southern slopes are traditional wells located in the alluvial system of wadis originating in the high plains. The accumulation of rainfall in these localized ponds could therefore be an important mechanism of recharge (see also Chapters 4 and 7).

Volumes of surface water redistributed through the wadis systems are potentially large. Wadi Kordi (Ennedi north), for example, shows an annual flooding over a distance of 100 km away from the zone of increased precipitation. The analysis of LandSat8 (MNDWI36) shows a large surface covered by surface water in the downstream area of wadi Kordi (e.g. August 2014), corresponding to ten times the surface of the lakes of Ounianga Serir. Similar conclusion can also be drawn for enneris originating in the Tibesti Mountains (Gouro, Yarda-Kouroudi, West Palm Groves and Faya-Largeau), although frequencies are lower (1 event in 3 years for Gouro, 1 event every 2 years for the other localities).

The alluvial systems of wadis might also potentially represent the zones of highest losses from the system through evapotranspiration of the shallow water table. Evapotranspiration rates are expected to be higher during the rainy season as large humid surfaces will be evaporating after precipitation. However, natural losses represent potentially very low total volumes during the rest of the year, as very large areas in Northern Chad are devoid of surface water and vegetation (water-limited environment). Losses will mainly occur within the main discharge points and from phreatic evapotranspiration along the alluvial systems. However, estimated losses of phreatic evapotranspiration from the alluvial systems of wadis and enneris correspond to volumes one order of magnitude higher (705×10^6 m^3y^{-1}) than the cumulated losses from the main discharge zones located in the central lowlands (51.1 to 74.0 x 10^6 m^3y^{-1}, Chapter 6).

In synthesis, in the mountainous regions of Northern Chad, wadis are critical features because: (1) they concentrate and transport surface water from the highest altitudes to the foothill of these mountain chains, (2) they follow fracturation and constitute zones of preferential flow, linking the zone of infiltration and recharge of the high plains, to zones of discharge (springs), (3) they locally represent low points, where groundwater might converge, (4) most of the water points securing the annual water supply to the inhabitants of the region, are located within the alluvial systems of wadis and enneris, and (5) the largest natural discharge from the system potentially occurs from the alluvial systems of wadis and enneris.

To compile the preliminary water balance based on remote sensing products, the extent of the Kufra basin of Northern Chad (total surface 2.39 x10^5 km^2) was defined as follows: (1) towards the west, the limit is defined by the ridges of the Tibesti Mountains, (2) towards the south, the limit is defined by the extent of Paleozoic continental formations terminating against the Cenozoic sediments of the Lake Chad basin and against the uplifted Precambrian basement of the Ouaddai (Voss and Soliman, 2014), (3) towards the north, the limit is defined by the ridges separating the Mediterranean and Lake Chad hydrological basins and (4) towards the east, the limit is defined by the ridges separating the Nile and Lake Chad hydrological basins.

During the years 2013 to 2016, total annual volumes of precipitation detected from RFE2.0 varies between 10 to 21 x 10^9 m^3y^{-1} (Figure 8.2A). As observed in Chapters 5 and 6, 2014 shows higher precipitation rates than the other three years observed in this study.

As discussed in Chapter 5, most of the annual precipitation occurs during a few concentrated storms, closely spaced in time during the month of August. As shown by the temporal line of Figure 8.2B, for three of the four years observed by satellite images, a positive residual (P-ET volume in 10^9m^3, where ET is actual evapotranspiration extracted from LandSat8) occurs during the month of August over the Kufra basin of Northern Chad.

However, the cumulated P-ET (start: January 2013, end: December 2016, Figure 8.2C) shows that the region, during the years 2013 to 2016, experienced more losses than inputs. Similar conclusions were also drawn by previous researchers (e.g. Gossel et al., 2004), who affirmed that the total natural losses from the NSAS are several orders of magnitude higher than recharge rates.

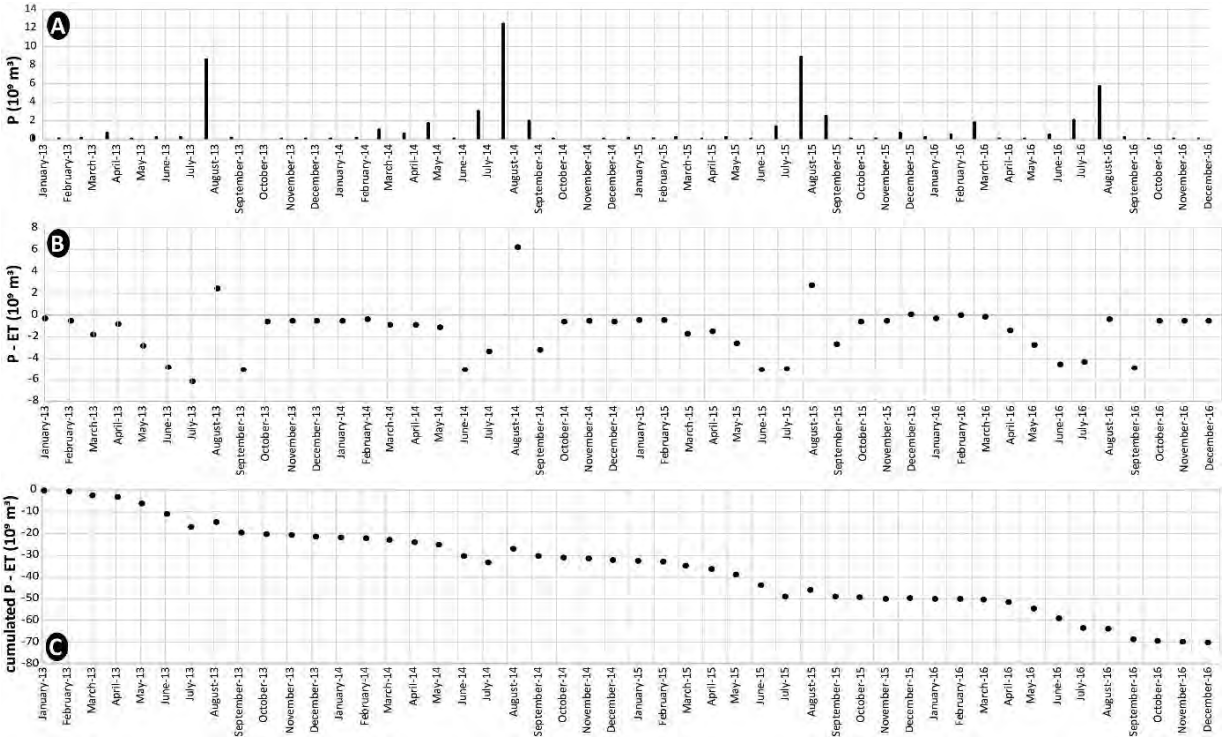

Figure 8.2: 2013 to 2016 temporal graph of A) precipitation (volumes in 10^9 m^3), extracted from RFE2.0, B) P – ET, where ET is actual evapotranspiration extracted from LandSat8 (mean value of images for the month in consideration, volumes in 10^9 m^3), C) cumulated P-ET (start: January 2013, end: December 2016, same data as (B), volumes in 10^9 m^3).

The climatic conditions prevailing over the NSAS of Northern Chad determine a very short time window over the year (month of August), during which precipitation rates overpass evapotranspiration rates. Differences from year to year are observable, but the overall pattern repeats yearly. Figure 8.3 shows the spatial distribution of potential recharge based on the average precipitation rates (RFE2.0) and

actual evapotranspiration rates (extracted from LandSat8) for the month of August (years 2013 – 2016). The image shows a high potential for recharge in the southeastern region of the NSAS (southern slopes of the Ennedi Mountains and Ouaddaï).

A relatively large area of moderated potential for recharge extends in a SW-NE direction (between Djourab puits 110 and Gouro-Hardjalla). This zone is covered by white desert sand with high reflecting properties (albedo). A high albedo decreases the net available energy and the evapotranspiration rate. Additionally, as stated by Charney et al. (1977), the decrease of net available energy resulting from the high albedo of desert sand has an overall effect of decreasing the convective clouds and precipitation. Therefore, this zone of moderate recharge potential results from low evapotranspiration rates rather than moderate precipitation rates.

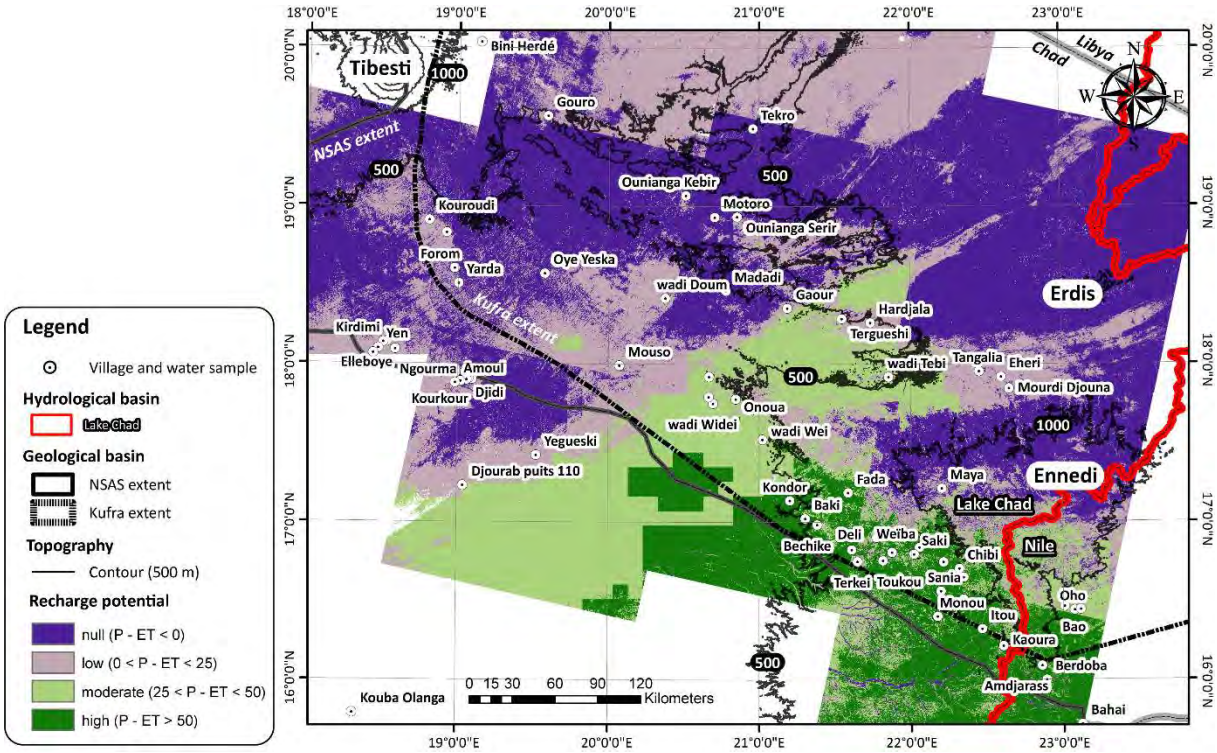

Figure 8.3: Spatially distributed residuals (P-ETa) for the month of August (mean of years 2013 to 2016), classified to represent different conditions of recharge potential in the Kufra basin of Northern Chad (P – ET). The pattern of potential recharge shows the eastern and southeastern regions, approaching the Ennedi Mountains, under an increased influence of the SW-originating monsoons.

Mohamed et al. (2016) estimate from GRACE products an annual recharge rate of 0.78 ± 0.49 x 10^9 m^3 for the southern Kufra basin (2003-2012). These authors assumed the natural losses from evapotranspiration to be negligible. Our estimates for the month of August (2013 to 2015) correspond to 3 to 8 times the volumes estimated from Mohamed et al. (2016), but mainly located in the southern margin of the NSAS (and of the Kufra basin).

8.4. Conceptual hydrogeological model

8.4.1. Groundwater flow organization in the Ennedi Mountains

Higher precipitation (> 60 mmy^{-1}), higher hydraulic heads (> 600 masl) and gradients (3-4‰), a distinct enriched isotopic ratio ($\delta^{18}O$ -6.7‰ to -2‰ and $\delta^{2}H$ -48‰ to -9‰) and a Ca-(Mg)-Na-bicarbonate chemical composition characterize the groundwater system of the Ennedi Mountains (Figure 8.4).
As shown in Chapter 7, the changes of isotopic signature and chemical composition of groundwater are correlated to the distance from the zone of highest precipitation. Within the southern slopes and the highest plains of the mountain chain, characterized by increased precipitation, groundwater is characteristically enriched ($\delta^{2}H$ > -30‰) and alkali earth-bicarbonate (Ca-(Mg)-HCO_3 and Ca-(Mg)-Na-HCO_3). From Fada towards the NW, the isotopic signature progressively changes to more depleted values and the chemical composition is increasingly enriched in Na, following the decrease of rainfall rates. The distribution of the chemical and isotopic signatures are thus indicating the zones experiencing the highest rates of diffuse and/or concentrated modern recharge. With the increase of distance from the zone of highest precipitation rates, the hydraulic heads decrease. At the same time, the stable isotopic ratios become more depleted and the groundwater chemical content changes to more alkali-bicarbonate compositions, compatible with a longer time of rock-water interaction.

Chemical and stable isotopic signatures from water points located in the downstream of wadis Kordi and Béméché, on the northern slopes of the Ennedi Mountains (wadi Tebi, Mourdi Djouna) are comparable to the chemical and stable isotopic signature of water points located in zones of increased precipitation rates. This indicates the importance of concentrated recharge in zones of low rainfall rates. In the current climatic setting, runoff through the wadi systems originating in the high plains correspond to the only mechanisms to convey surface water issued from precipitation to the localities situated south of the Mourdi depression (northern slopes).

As shown by the analysis of remote sensing (Chapters 5 and 6), the accumulation and infiltration of surface water within the high plains of the mountain chain is likely an important mechanism of recharge. The high plains of the Ennedi Mountains are covered by the Mid and Upper Devonian micaceous sandstone (Chapter 2). The area experiencing increased rainfall within the high plains and the hydraulic properties of the fractured sandstone, largely devoid of vegetation, potentially represent large volumes of recharge.

The uneven distribution of water points, densely distributed within the southern slopes and localized in the downstream of the main alluvial systems within the northern slopes is reflecting the precipitation distribution. However, the few examples of water points within the northern slopes might also only represent part of the flow resulting from recharge in the high plains. Part of the flow

could flow more deeply (Cambro-Ordovician and/or Lower Devonian) towards the N and NW (see Chapter 4). As discussed in section 8.2, if this hypothesis is confirmed, the northerly-directed groundwater flow could eventually also contribute to the supply of the Ounianga Lakes, and potentially to the northern Kufra basin of Libya.

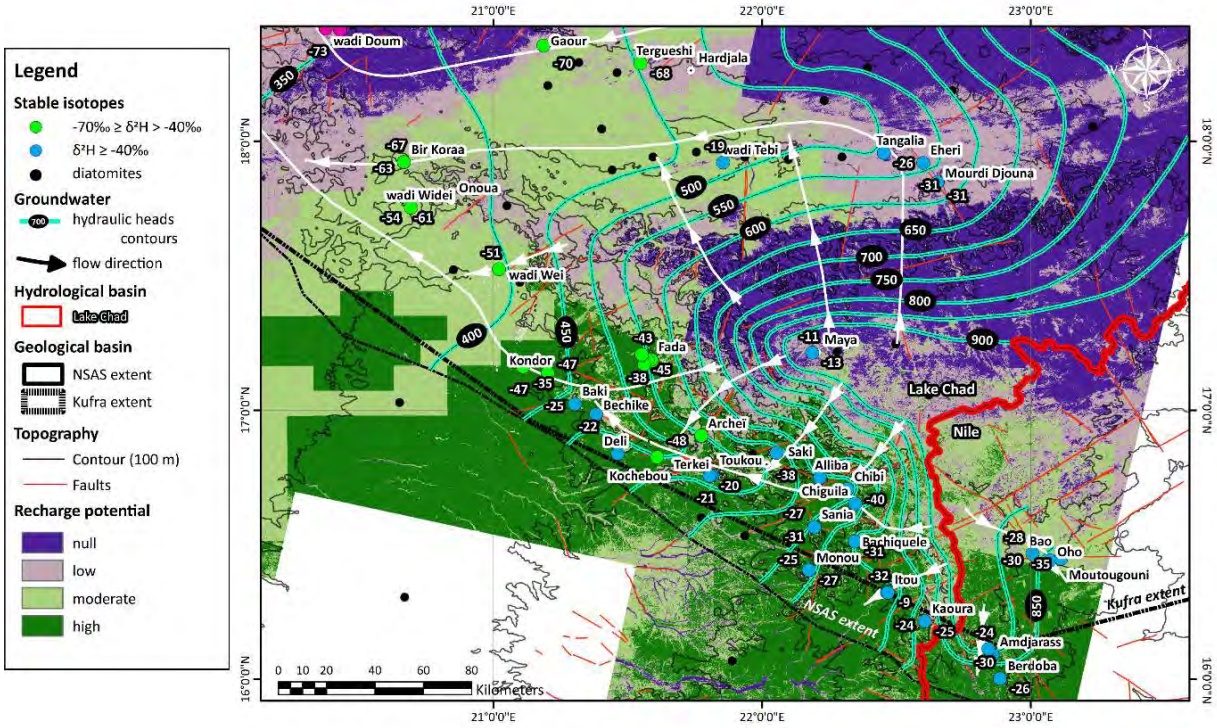

Figure 8.4: Conceptual model of the groundwater flow system of the Ennedi Mountains. Hydraulic heads contours are constructed from the water table measurements collected in the field. The flow directions follow the preferential paths (faults) identified by geological analysis (Chapter 2). The background corresponds to P-ET for the month of August (mean 2013-2016, P = precipitation from RFE2.0, ET = actual evapotranspiration from LandSat8). Are also indicated the stable isotopic ratios (deuterium values).

In synthesis, the overall chemical and stable isotopic signature of groundwater in the Ennedi Mountains of Northern Chad allowed to characterize: (1) where modern recharge is of increased intensity, (2) where the supply of concentrated recharge through the wadi systems contributes substantially to the groundwater signature, and (3) where groundwater is more likely resulting from infiltration and percolation through the geological layers before discharge.

Similar chemical and isotopic compositions as in the Ennedi Mountains were found within the southern slopes of the mountainous Tibesti (Zouar, Misky, Chapter 7) and in the upper part of the major enneris within the northern slopes (Zoumri, Yebbigué). A similar conceptual model as for the Ennedi Mountains (diffuse and concentrated recharge within the southern slopes, concentrated recharge within the northern slopes) could therefore also be applied to the Tibesti Mountains.

8.4.2. Groundwater flow organization in the central lowlands

Lower hydraulic heads (< 500 masl) and gradients (0.5–1‰), a water table close to the surface (< 5 m bgl), a chemical composition showing higher ionic content, alkali pH, increased concentrations of SO_4, Cl and Na and a general depleted stable isotopic ratio ($\delta^{18}O$ -11.7 to -5.7 ‰, $\delta^{2}H$ -85 to -39‰) characterize the groundwater in the central lowlands. In this region, precipitation rates are below 40 mmy^{-1}.

In Bini Herdé (Figure 8.5), the chemical and stable isotopic signatures are comparable to those of the Ennedi Mountains. As observed with LandSat8 images, one important flood occurred along the wadi north of the Gouro oases during August 2015 (years of observation 2013-2016). More “intermediate” isotopic ratios are found at the margins of the zone of influence of increased precipitation: at the foothill of the Ennedi Mountains (Bir Koraa, Mouso), of the Tibesti Mountains (Gouro, West Palm Groves, Faya-Largeau, Yarda-Kouroudi) and of the Erdis plateaus (Hardjalla, Tergueshi). The stable isotopic ratios are “intermediate” between the enriched isotopic signatures, which characterize the Ennedi Mountains and recognized as an indicator of modern recharge, and the more depleted isotopic ratios found in the most central zone of the Kufra basin of Northern Chad.

In this central zone (between the oases of Faya-Largeau, Yarda-Kouroudi, Gouro, Tekro, the Ounianga Lakes, Madadi and wadi Doum, Figure 8.5), the groundwater stable isotopic and hydrochemical signatures are in agreement with the general hydrochemical signatures found in oases and sebkhas in Libya (Goudarzi, 1970; Edmunds and Wright, 1979; Swailem et al., 1983; Pachur and Altmann, 2007; Faitouri and Sanford, 2015) and in the Lake Chad basin (Herrmann et al., 2009), associated to groundwater recharged during the Pleistocene-Holocene pluvial periods. Ages of 9,6-7,5 kyr were determined for groundwater within the Paleozoic sandstone of Faya-Largeau, with associated $\delta^{18}O$ ratios varying between -9 and -10.5‰ (Schneider, 1989). In the Kufra oases, the shallow and deep aquifers were dated between 9,5 to 37,5 kyr (Edmunds and Wright, 1979; Swailem et al., 1983; Faitouri and Sanford, 2015), associated to depleted isotopic ratios ($\delta^{18}O$ and $\delta^{2}H$ of -11.4‰ and -84.1‰, respectively).

The general composition of groundwater found in the main discharge zones of Northern Chad thus indicates a major component of groundwater recharged during the Pleistocene-Holocene pluvial periods. This conclusion is in agreement with the groundwater flow organization showing a SW direction originating from a zone where no modern recharge is likely to occur (Figure 8.1, cross-section 1).

In the zones of recharge, the chemical and stable isotopic changes show similar patterns. As previously stated, hydrochemistry can be a good indicator to trace the components of recharge (diffuse,

concentrated) and to differentiate groundwater resulting from percolation through the geological layers. In the discharge zones, the chemical changes do not linearly correlate with the changes of the stable isotopic signatures. As observed in Chapter 7, the groundwater hydrochemical signature in the central lowlands might be acquired within the discharge zone, through evapotranspiration and associated mineral precipitation or by the percolation of groundwater through Quaternary lake sediments such as diatomites, widely observed in the low-lying regions of Northern Chad (Herrmann et al., 2009) and in other parts of the NSAS (Goudarzi, 1970).

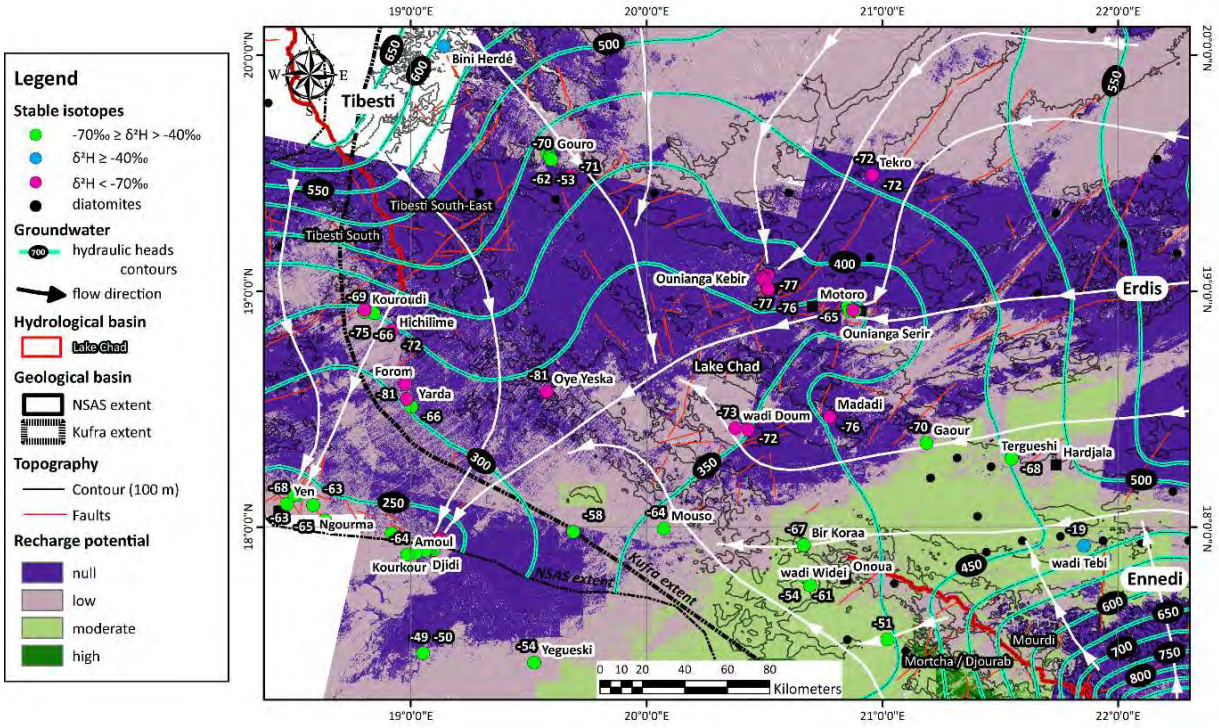

Figure 8.5: Conceptual model of the groundwater flow system of the NSAS. Hydraulic heads contours are constructed from the water table measurements collected in the field. The flow directions follow the preferential paths (faults) identified by geological analysis, by information from remote sensing and the position of paleohydrological deposits (Pachur and Altmann, 2007; SIRE database). The background corresponds to the residual P-ET (P = precipitation from RFE2.0, ET = actual evapotranspiration from LandSat8) for the month of August (mean 2013-2016). Are also indicated the stable isotopic ratios (deuterium values).

For this purpose, the example of the oasis of Faya-Largeau demonstrates the added value of combining the chemical and stable isotopic characterization to understand the relevant processes within the discharge zones of Northern Chad. In Faya-Largeau, the aquifer is confined by a layer of Cenozoic argillaceous lacustrine deposits (see Chapter 4). The artesian flow concentrates in the central part of the oasis, where increased fracturing has been observed. Groundwater in the central part of the oasis is characterized by an alkali-bicarbonate composition and by an earth alkali-bicarbonate composition in the upper and lower sections of the oasis. At the same time, the hydraulic heads distribution shows a groundwater flow directed from the NE to the SW. Stable isotopic ratios indicate a progressive enrichment through evapotranspiration along the flow lines.

8.5. Concluding remarks

The investigation of the NSAS of Northern Chad has shown that modern recharge occurs. Albeit small in quantity, it locally constitutes an important, renewable resource. Our analysis based on the hydraulic heads distribution, remote sensing data and the chemical and stable isotopic composition of groundwater, indicates that most of the modern recharge concentrates in the zones surrounding the mountainous regions. Modern recharge is likely to be important in maintaining higher hydraulic heads and gradients, thus slowing down the depletion of the NSAS. However, from the current understanding, it is not possible to conclude whether the recharge occurring in the mountainous regions of Northern Chad does only influence the Chadian sector of the NSAS or whether a part of the recharged groundwater effectively contributes to the regional flow of the NSAS in the Kufra basin. This question should be further investigated.

Previous authors (e.g. Gossel, 2004) investigating the NSAS by the use of numerical modelling, have concluded that natural losses through evapotranspiration are several orders of magnitude higher than volumes of recharge (see Chapter 1). Our preliminary water balance indicates that the system is generally experiencing more losses than gains (observation years 2013-2016). However, other methods should be employed to confirm these preliminary results. The climate of Northern Chad constitutes an extreme example, where the rainy season is characterized by few intense storms closely spaced in time. Outside this narrow window, most of the region is devoid of extended zones of surface water or vegetated areas. Moreover, the high reflecting properties (albedo) of the white desert sand of Northern Chad decreases the net available energy, the evapotranspiration rates and the overall convective fluxes and precipitation. Rates of natural losses are expected to be very low during the dry season, concentrated within the main oases. Applying a similar hypothesis, Mohamed et al. (2017) concluded from the analysis of GRACE products, that the southern Kufra basin is recharged annually. These authors provide estimates which correspond to similar orders of magnitude as estimated in this study for the month of August (P-ET).

This study has also shown the value of jointly using geology, hydrogeology and hydrochemistry in combination with remote sensing products. Although the uncertainties of precipitation and evapotranspiration rates extracted from remote sensing are difficult to estimate in a data-poor region such as Northern Chad, the methods and approaches employed in the previous chapters provide insights on the processes, dynamics and give an order of magnitude of recharge.

In the following outlook, suggestions for further research and monitoring data collection for the Nubian Sandstone Aquifer System of Northern Chad are provided.

Future lines of work

This study explored several aspects of the NSAS of Northern Chad: the structure of the basement and the sedimentary sequence composing the reservoir, the relationship between hydraulic heads, rainfall distribution and topography, the dynamics of the climate and potential for recharge, the specific chemical and isotopic signatures issued from modern recharge in the mountainous regions compared to the discharge zones in the central lowlands. Although academic, the improved knowledge gained through this research have practical implications, formulated as recommendations in this final part of the thesis.

The Ennedi Mountains correspond to a major zone of recharge. The renewable resource provided by this annual recharge should be used and managed to improve the access to water for the local population. This study identified the most active wadis where there is high potential for concentrated recharge. For example, the construction of small-scale dams in selected localities along wadis are commonly found in arid environments subject to sporadic precipitation and runoff.

The selection of the most favorable locality to manage recharge and the dimensioning of the system should be supported by studies providing a quantification of the processes. As shown by this study, there is high potential in using remote sensing data, which if properly calibrated, can provide volumes for quantification. Calibration can only be performed if a meteorological and hydrological monitoring system is capable of collecting the relevant data in the field at the time of the satellite overpass. Additionally, the meteorological stations should be equipped with components capable of measuring precipitation, solar incoming radiation (and/or actual duration of sun), air temperature, humidity and wind speed, as minimum requirements. Measurements of albedo and surface temperatures would enable to add accuracy to the extracted information from remote sensing.

In addition to a standard monitoring system, there is also a need to organize a “ground-based” observation system, through the implication of the inhabitants of the region, capable of providing qualitative and semi-quantitative information on the precipitation and runoff in wadis, by event. The interpretation of remote sensing data would benefit from such information. As shown by our analysis, the time between the precipitation event and the acquisition of the LandSat image has to be known in order to improve the interpretation of the signal. Knowing the exact date of precipitation in specific localities provides information to select the timeframe of analysis of the remote sensing data. Even if semi-quantitative, estimating the duration and intensity of the rainfall events, the number of events

per year, the timeframe between subsequent precipitation events, and observing the resulting flows in wadis, provides valuable information which can help understanding the dynamics of the system for the dates without a satellite image. Besides these information, water table depths and discharge flows from springs should also be monitored more closely.

Precipitation and actual evapotranspiration data from remote sensing could then be used in a hydrogeological model in order to quantify recharge and more generally evaluate the available resource and develop a strategy for a sustainable exploitation.

For the Nubian Sandstone Aquifer of Northern Chad, there is also a need to evaluate for how long the oases of Ounianga and of Faya-Largeau will continue existing. As shown by this study, there are still large uncertainties regarding the hydraulic properties of the aquifer system and the role of low conductive layers. Recharge occurring in the Ennedi Mountains might be flowing towards the NNW, supplying the lakes of Ounianga, and eventually the northern Kufra basin in Libya. Deep drilling should be performed between Faya-Largeau and the Kufra oases, and piezometers should be installed. The Libyan government in the past constructed few piezometers, but they have not been monitored since many years and potentially need rehabilitation. Additionally, dating of groundwater should be performed. Such information could then be used to build a numerical model to simulate the groundwater flow organization between these two oases and to make predictions of the possible future scenarios.

Bibliography

Abdelsalam, M.G., Liégeois, J.-P., Stern, R.J., 2002. The Saharan Metacraton. J. Afr. Earth Sci., 18th Colloquium of African Geology 34, 119–136. https://doi.org/10.1016/S0899-5362(02)00013-1.

Abouelmagd, A., Sultan, M., Milewski, A., Kehew, A.E., Sturchio, N.C., Soliman, F., Krishnamurthy, R.V., Cutrim, E., 2012. Toward a better understanding of palaeoclimatic regimes that recharged the fossil aquifers in North Africa: inferences from stable isotope and remote sensing data. Palaeogeogr. Palaeoclimatol. Palaeoecol. 329, 137–149.

Ahmad, M.U., 1983. A Quantitative Model to Predict a Safe Yield for Well Fields in Kufra and Sarir Basins, Libya. Groundwater 21, 58–66. https://doi.org/10.1111/j.1745-6584.1983.tb00705.x.

Albert, G., Elgargoti, J.B., 2010. Hassi Nafiou NF 34-3, Geological map of Libya 1:250,000, Explanatory booklet.

Alexandris, S., Stricevic, R., Petkovic, S., 2008. Comparative analysis of reference evapotranspiration from the surface of rainfed grass in central Serbia, calculated by six empirical methods against the Penman-Monteith formula. Eur. Water 21, 17–28.

Allen, R.G., Pereira, L.S., Raes, D., Smith, M., 1998. Crop evapotranspiration-Guidelines for computing crop water requirements-FAO Irrigation and drainage paper 56. Fao Rome 300, D05109.

Allen, R.G., Trezza, R., Tasumi, M., 2002. Surface energy balance algorithms for land. Advance training and user's manual, version 1.0.

Ball, J., 1927. Problems of the Libyan desert. Geogr. J. 70, 21–38.

Bastiaanssen, W.G., Menenti, M., Feddes, R.A., Holtslag, A.A.M., 1998. A remote sensing surface energy balance algorithm for land (SEBAL). 1. Formulation. J. Hydrol. 212, 198–212.

Baumgartner, W.C., Reichel, E., 1975. The world water balance: mean annual global, continental and maritime precipitation. Evaporation Runoff.

Beauvilain, A., 1995. Tableau de la pluviométrie dans les bassins du Tchad et de la Benoué, de la création des stations à décembre 1994.

Begg, G.C., Griffin, W.L., Natapov, L.M., O'Reilly, S.Y., Grand, S.P., O'Neill, C.J., Hronsky, J.M.A., Djomani, Y.P., Swain, C.J., Deen, T., Bowden, P., 2009. The lithospheric architecture of Africa:

Seismic tomography, mantle petrology, and tectonic evolutionThe lithospheric architecture of Africa. Geosphere 5, 23–50. https://doi.org/10.1130/GES00179.1.

Bellini, E., Massa, D., 1980. A stratigraphic contribution to the Palaeozoic of the southern basins of Libya, in: The Geology of Libya. M.J. Salem, M.T. Busrewil, London, pp. 3–56.

Beuf, S., 1971. Les grès du Paléozoïque inférieur au Sahara: Sédimentation et discontinuités; évolution structurale d'un craton. editions Technip.

BRGM, 1991. Projet de points d'eau au Salamat et au B.E.T. Volet B.E.T. Rapport no°1. Etude hydrogéologique et gàophysique de la dépression des palmeraies de Faya-Largeau. Reconnaissance hydrogéologique de trois centres: Ounianga Kebir, Fada et Gouro.

Brinkmann, P.J., Heinl, M., Hollander, R., Reich, G., 1987. Retrospective simulation of groundwater flow and transport in the Nubian Aquifer system. Berl. Geowiss Abh 75, 465–516.

Brunet-Moret, Y., 1963. Le bassin du Zoumri au Tibesti.

Brutsaert, W., 1984. Evaporation into the atmosphere: theory, history and applications. D. Reidel Publishing Company, Dordrecht, Holland.

BURGEAP, 1996. Projet d'hydraulique pastorale dans le B.E.T. Programme d'extension des travaux dans l'Ouest de l'Ennedi.

BURGEAP, 1999a. Programme d'hydraulique pastorale dans le Tibesti et le Borkou pour la réalisation de 50 points d'eau (BET II). Dossiers techniques de forages. Deuxième partie: Sud Borkou.

BURGEAP, 1999b. Programme d'hydraulique pastorale dans le Tibesti et le Borkou pour la réalisation de 50 points d'eau (BET II). Dossiers techniques de forages. Première partie: Nord - Tibesti et axes caravaniers.

BURGEAP, 2001a. Projet d'hydraulique pastorale dans le B.E.T. (BET 1). Rapport de fin de projet. Coupes des puits et caractéristiques.

BURGEAP, 2001b. Programme d'Hydraulique Pastorale dans le Tibesti et le Borkou pour la réalisation de 50 points d'eau (BET 2). Rapport de fin de projet et synthèse hydrogéologique.

Castany, G., Marcé, A., Margat, J., Moussu, H., Vuillaume, Y., Evin, J., 1974. Etude par les isotopes du milieu du regime des eaux souterraines dans les aquiferes de grandes dimensions. Isot. Tech. Groundw. Hydrol. 1.

Capot-Rey, R., 1961. Borkou et Ounianga : étude de géographie régionale, par Robert Capot-Rey. L'Université Mâcon, impr. Protat frères.

CEDARE, 2002. Regional Strategy for the Utilization of the Nubian Sandstone Aquifer System. Draft final report.

Chander, G., Markham, B., 2003. Revised Landsat-5 TM radiometric calibration procedures and postcalibration dynamic ranges. IEEE Trans. Geosci. Remote Sens. 41, 2674–2677.

Charney, J., Quirk, W.J., Chow, S., Kornfield, J., 1977. A comparative study of the effects of albedo change on drought in semi–arid regions. J. Atmospheric Sci. 34, 1366–1385.

Cook, P.G., Herczeg, A.L. (Eds.), 2000. Environmental Tracers in Subsurface Hydrology. Springer US.

Coward, M.P., Ries, A.C., 2003. Tectonic development of North African basins. Geol. Soc. Lond. Spec. Publ. 207, 61–83. https://doi.org/10.1144/GSL.SP.2003.207.4

Craig, H., 1961. Isotopic Variations in Meteoric Waters. Science 133, 1702–1703. https://doi.org/10.1126/science.133.3465.1702.

Craig, J., Rizzi, C., Said, F., Thusu, B., Luning, S., Asbali, A.I., Keeley, M.L., Bell, J.F., Durham, M.J., Eales, M.H., 2008. Structural styles and prospectivity in the Precambrian and Palaeozoic hydrocarbon systems of North Africa. Geol. East Libya 4, 51–122.

Czapla-Myers, J.S., Anderson, N.J., Biggar, S.F., 2013. Early ground-based vicarious calibration results for Landsat 8 OLI, in: Earth Observing Systems XVIII. Presented at the Earth Observing Systems XVIII, International Society for Optics and Photonics, p. 88660S. https://doi.org/10.1117/12.2022493

Dalloni, Marcel, Lacroix, A., Dalloni, Marius, 1934. Mission au Tibesti (1930-1931). Gauthier-Villars.

Dansgaard, W., 1964. Stable isotopes in precipitation. Tellus 16, 436–468.

Degens, E.T., 1963. Geochemische Untersuchungen von Wässern aus der ägyptischen Sahara 625–639.

Dembélé, M., Zwart, S.J., 2016. Evaluation and comparison of satellite-based rainfall products in Burkina Faso, West Africa. Int. J. Remote Sens. 37, 3995–4014.

Deniel, C., Vincent, P.M., Beauvilain, A., Gourgaud, A., 2015. The Cenozoic volcanic province of Tibesti (Sahara of Chad): major units, chronology, and structural features. Bull. Volcanol. 77, 74. https://doi.org/10.1007/s00445-015-0955-6.

Dinku, T., Ceccato, P., Connor, S.J., 2011. Challenges of satellite rainfall estimation over mountainous and arid parts of east Africa. Int. J. Remote Sens. 32, 5965–5979.

Direction de l'Hydraulique et de l'Assainissment, 1993. Mission d'identification de 50 points d'eau dans la préfecture du B.E.T. - Borkou-Ennedi-Tibesti (Borkou Sud and Tibesti Nord).

Domenico, P.A., Schwartz, F.W., 1998. Physical and Chemical Hydrogeology, 2nd ed. John Wiley & Sons Inc.

Dray, M., Gonfiantini, R., Zuppi, G.M., 1983. Isotopic composition of groundwater in the southern Sahara, in: Palaeoclimates and Palaeowaters: A Collection of Environmental Isotope Studies.

Du, C., Ren, H., Qin, Q., Meng, J., Zhao, S., 2015. A practical split-window algorithm for estimating land surface temperature from Landsat 8 data. Remote Sens. 7, 647–665.

Edmunds, W.M., 2005. Groundwater as an archive of climatic and environmental change, in: Isotopes in the Water Cycle. Springer, pp. 341–352.

Edmunds, W.M., 2009. Palaeoclimate and groundwater evolution in Africa—implications for adaptation and management. Hydrol. Sci. J. 54, 781–792.

Edmunds, W.M., Fellman, E., Goni, I.B., 1999. Lakes, groundwater and palaeohydrology in the Sahel of NE Nigeria: evidence from hydrogeochemistry. J. Geol. Soc. 156, 345–355. https://doi.org/10.1144/gsjgs.156.2.0345.

Edmunds, W.M., Wright, E.P., 1979. Groundwater recharge and palaeoclimate in the Sirte and Kufra basins, Libya. J. Hydrol. 40, 215–241. https://doi.org/10.1016/0022-1694(79)90032-5.

El Bakri, A., Tantawi, A., Blavoux, B., Dray, M., 1991. Sources of water recharge identified by isotopes in El Minya Governorate (Nile Valley, Middle Egypt). Proc. Isot. Tech. Water Resour.

El-Mehdi, B., Turki, S.M., Suwesi, S.K., Oweiss, K., 2004. Short notes and guidebook on the geology of Al Kufrah Basin, Al'Awaynãt area, in: Sedimentary Basins of Libya, Third Symposium, Geology of East Libya Fieldtrip. pp. 24–28.

Elsheikh, A., Abdelsalam, M.G., Mickus, K., 2011. Geology and geophysics of the West Nubian Paleolake and the Northern Darfur Megalake (WNPL–NDML): Implication for groundwater resources in Darfur, northwestern Sudan. J. Afr. Earth Sci. 61, 82–93. https://doi.org/10.1016/j.jafrearsci.2011.05.004.

Faitouri, M.A., Sanford, W.E., 2015. Stable and radio-isotope analysis to determine recharge timing and paleoclimate of sandstone aquifers in central and southeast Libya. Hydrogeol. J. 23, 707–717. https://doi.org/10.1007/s10040-015-1232-7.

Flood, N., Danaher, T., Gill, T., Gillingham, S., 2013. An Operational Scheme for Deriving Standardised Surface Reflectance from Landsat TM/ETM+ and SPOT HRG Imagery for Eastern Australia. Remote Sens. 5, 83–109. https://doi.org/10.3390/rs5010083.

Gasse, F., 2000. Hydrological changes in the African tropics since the Last Glacial Maximum. Quat. Sci. Rev. 19, 189–211.

Gee, G.W., Hillel, D., 1988. Groundwater recharge in arid regions: review and critique of estimation methods. Hydrol. Process. 2, 255–266.

Gerard, G.A., 1958. Carte geologique de l'Afrique Equatoriale francaise au 1:2.000.000: notice explicative. Impr. Typographique d'Edition.

Gindre, L., Le Heron, D., Bjørnseth, H.M., 2012. High resolution facies analysis and sequence stratigraphy of the Siluro-Devonian succession of Al Kufrah basin (SE Libya). J. Afr. Earth Sci. 76, 8–26. https://doi.org/10.1016/j.jafrearsci.2012.08.002.

Gischler, C.E., 1967. Synthèse hydrologique du bassin du lac Tchad. Nat. Ressour. 3, 10–16.

Gombert, P., 1993. Construction de cinq forages d'exploitation, trois forages de reconnaissance et un piézomètre dans la région du Borkou - Ennedi - Tibesti. Projet de points d'eau au Salamat et au B.E.T. - Volet BET. Rapport de fin de travaux.

Gonfiantini, R., Conrad, G., Fontes, J.-C., Sauzay, G., Payne, B.R., 1974. Etude isotopique de la nappe du Continental Intercalaire et de ses relations avec les autres nappes du Sahara septentrional. Isot. Tech. Groundw. Hydrol. 1, 227–241.

Gossel, W., Ebraheem, A.M., Wycisk, P., 2004. A very large scale GIS-based groundwater flow model for the Nubian sandstone aquifer in Eastern Sahara (Egypt, northern Sudan and eastern Libya). Hydrogeol. J. 12, 698–713. https://doi.org/10.1007/s10040-004-0379-4.

Goudarzi, G.H., 1970. Geology and mineral resources of Libya-a reconnaissance. US Govt. Print. Off.

Grönig, M., Sonntag, C., Suckow, A., Thorweihe, U., 1993. Isotopic evidence for the extremely low groundwater recharge in the Sahel zone of Sudan, in: Geoscientific Research in Northeast Africa. Thorweihe and Schandelmeier, pp. 671–676.

Gu, D., Gillespie, A., 1998. Topographic normalization of Landsat TM images of forest based on subpixel sun-canopy-sensor geometry. Remote Sens. Environ.

Guiraud, R., Bosworth, W., Thierry, J., Delplanque, A., 2005. Phanerozoic geological evolution of Northern and Central Africa: An overview. J. Afr. Earth Sci., Phanerozoic Evolution of Africa 43, 83–143. https://doi.org/10.1016/j.jafrearsci.2005.07.017.

Guiraud, R., Mbaigane, J.-C.D., Carretier, S., Dominguez, S., 2000. Evidence for a 6000 km length NW–SE-striking lineament in northern Africa: the Tibesti Lineament. J. Geol. Soc. 157, 897–900.

Hallet, D., 2002. Petroleum geology of Libya. Elsevier.

Hargreaves, G.H., 1975. Moisture availability and crop production. Trans. ASAE 18, 980–0984.

Hargreaves, G.L., Hargreaves, G.H., Riley, J.P., 1985. Irrigation water requirements for Senegal River basin. J. Irrig. Drain. Eng. 111, 265–275.

HCNE, ONU-DAES, PNUD, 2003. Le Schéma Directeur de l'Eau et de l'Assainissement du Tchad (SDEA). CHD98 004.

Heckendorff, W.-D., 1978. Untersuchungen zum Klima des Tibesti-Gebirges.

Heinl, M., Brinkmann, P.J., 1989. A groundwater model of the Nubian aquifer system. Hydrol. Sci. J. 34, 425–447. https://doi.org/10.1080/02626668909491350.

Heinl, M., Holländer, R., 1984. Some aspects of a new groundwater model for the Nubian aquifer system. Berl. Geowiss Abh Reihe A 50, 221–231.

Hellström, B., 1940. The Subterranean Water in the Libyan Desert. Geogr. Ann. 22, 206–239. https://doi.org/10.1080/20014422.1940.11880690.

Herczeg, A.L., Leaney, F.W., 2011. Environmental tracers in arid-zone hydrology. Hydrogeol. J. 19, 17–29.

Hermance, J.F., Sulieman, H.M., 2014. Assessing daily and seasonal satellite rainfall estimates using local gauges for the anomalous 2012 monsoon season in the African East Sahel. Int. J. Remote Sens. 35, 253–288.

Heron, D.P.L., Craig, J., 2008. First-order reconstructions of a Late Ordovician Saharan ice sheet. J. Geol. Soc. 165, 19–29. https://doi.org/10.1144/0016-76492007-002.

Heron, D.P.L., Howard, J.P., Alhassi, A.M., Anderson, L., Morton, A., Fanning, C.M., 2009. Field-based investigations of an 'Infracambrian' clastic succession in SE Libya and its bearing on the evolution of the Al Kufrah Basin. Geological Society, London, Special Publications 326, 193-210. https://doi.org/10.1144/SP326.10.

Herrmann, L., Mounkaila, M., Graef, F., 2009. Are there valuable pedological palaeoenvironmental indicators in Northern Chad?, in: Holocene Palaeoenvironmental History of the Central Sahara. CRC Press, pp. 129–148.

Herzog, U., El Ila, A., Saad, S.O., 2008. Al Kufrah basin, Libya–geological history review and refinement. Geol. East Libya 3, 3–18.

Hesse, K.H., Hissene, A., Kheir, O., Schnacker, E., Schneider, M., Thorweihe, U., 1987. Hydrogeological investigations in the Nubian Aquifer system, Eastern Sahara 397–464.

Hijmans, R.J., Cameron, S.E., Parra, J.L., Jones, P.G., Jarvis, A., 2004. The WorldClim interpolated global terrestrial climate surfaces. Version 1.3.

Hoelzmann, P., Keding, B., Berke, H., Kröpelin, S., Kruse, H.-J., 2001. Environmental change and archaeology: lake evolution and human occupation in the Eastern Sahara during the Holocene. Palaeogeogr. Palaeoclimatol. Palaeoecol. 169, 193–217.

Jäkel, D., 1979. Run-off and fluvial formation processes in the Tibesti mountains as indicators of climatic history in the central Sahara during the late Pleistocene and Holocene. Palaeoecol. Afr. 11, 13–44.

Jäkel, D., 1977. The work of the field station at Bardai in the Tibesti Mountains. Geogr. J. 61–72.

Jankowski, J., Jacobson, G., 1989. Hydrochemical evolution of regional groundwaters to playa brines in central Australia. J. Hydrol. 108, 123–173. https://doi.org/10.1016/0022-1694(89)90281-3.

Jarvis, A., Reuter, H.I., Nelson, A., Guevara, E., 2008. Hole-filled seamless SRTM data V4. Tech. rep., International Centre for Tropical Agriculture (CIAT). Int. Cent. Trop. Agric. CIAT.

Jenness, J., 2014. Polar Plots and Circular Statistics: Extension for ArcGIS. Jenness Enterprises.

Johnston, C.D., 1987. Preferred water flow and localised recharge in a variable regolith. J. Hydrol. 94, 129–142.

Joseph, A., Frangi, J.P., Aranyossy, J.F., 2012. Isotope characteristics of meteoric water and groundwater in the Sahelo-Sudanese zone. J. Geophys. Res. Atmospheres 97, 7543–7551. https://doi.org/10.1029/92JD00288.

Justice, C.O., Wharton, S.W., Holben, B.N., 1981. Application of digital terrain data to quantify and reduce the topographic effect on Landsat data. Int. J. Remote Sens. 2, 213–230.

Klitzsch, eds J.J.W. and E., 1966. South-Central Libya and Northern Chad: A Guidebook To The Geology and Prehistory. Petroleum Exploration Society of Libya.

Klitzsch, E., Sonntag, C., Weistroffer, K., Shazly, E.M.E., 1976. Grundwasser der Zentralsahara: Fossile Vorräte. Geol. Rundsch. 65, 264–287. https://doi.org/10.1007/BF01808466

Klitzsch, E., Wycisk, P., 1987. Geology of the sedimentary basins of northern Sudan and bordering areas. Berl Geowiss Abh A 75, 97–136.

Kröpelin, S., Verschuren, D., Lézine, A.-M., Eggermont, H., Cocquyt, C., Francus, P., Cazet, J.-P., Fagot, M., Rumes, B., Russell, J.M., Darius, F., Conley, D.J., Schuster, M., Suchodoletz, H. von, Engstrom, D.R., 2008. Climate-Driven Ecosystem Succession in the Sahara: The Past 6000 Years. Science 320, 765–768. https://doi.org/10.1126/science.1154913.

Kusnir, I., Schneider, J.-L., 1993. Géologie, ressources minérales et ressources en eau du Tchad. Centre national d'appui à la recherche.

Le Heron, D.P., Armstrong, H.A., Wilson, C., Howard, J.P., Gindre, L., 2010. Glaciation and deglaciation of the Libyan Desert: The Late Ordovician record. Sediment. Geol. 223, 100–125. https://doi.org/10.1016/j.sedgeo.2009.11.002.

Le Heron, D.P., Craig, J., Etienne, J.L., 2009. Ancient glaciations and hydrocarbon accumulations in North Africa and the Middle East. Earth-Sci. Rev. 93, 47–76. https://doi.org/10.1016/j.earscirev.2009.02.001.

Le Heron, D.P., Howard, J.P., 2012. Sandstones, glaciers, burrows and transgressions: The Lower Palaeozoic of Jabel az-Zalmah, Al Kufrah Basin, Libya. Sediment. Geol. 245, 63–75. https://doi.org/10.1016/j.sedgeo.2011.12.008.

Lebatard, A.-E., Bourlès, D.L., Braucher, R., Arnold, M., Duringer, P., Jolivet, M., Moussa, A., Deschamps, P., Roquin, C., Carcaillet, J., Schuster, M., Lihoreau, F., Likius, A., Mackaye, H.T., Vignaud, P., Brunet, M., 2010. Application of the authigenic 10Be/9Be dating method to continental sediments: Reconstruction of the Mio-Pleistocene sedimentary sequence in the early hominid

fossiliferous areas of the northern Chad Basin. Earth Planet. Sci. Lett. 297, 57–70. https://doi.org/10.1016/j.epsl.2010.06.003.

Legates, D.R., Willmott, C.J., 1990a. Mean seasonal and spatial variability in global surface air temperature. Theor. Appl. Climatol. 41, 11–21.

Legates, D.R., Willmott, C.J., 1990b. Mean seasonal and spatial variability in gauge-corrected, global precipitation. Int. J. Climatol. 10, 111–127.

Lestang, D., 1965. Das Paläozoikum am rande des Afro-arabischen Gondwanakontinents. Mitteilung über des Erdi-Becken (Republic Tschad). Z Dtsch. Geol Ges Jahrang 117, 479–488.

Lézine, A.-M., Hély, C., Grenier, C., Braconnot, P., Krinner, G., 2011. Sahara and Sahel vulnerability to climate changes, lessons from Holocene hydrological data. Quat. Sci. Rev. 30, 3001–3012. https://doi.org/10.1016/j.quascirev.2011.07.006.

Lloyd, J.W., 1986. A review of aridity and groundwater. Hydrol. Process. 1, 63–78.

Lüning, S., Craig, J., Fitches, B., Mayouf, J., Busrewil, A., Dieb, M.E., Gammudi, A., Loydell, D., McIlroy, D., 1999. Re-evaluation of the petroleum potential of the Kufra Basin (SE Libya, ne Chad): does the source rock barrier fall? Mar. Pet. Geol. 16, 693–718. https://doi.org/10.1016/S0264-8172(99)00013-6.

Mahamoud, A.H., 1986. Geologie und Hydrogeologie des Erdis-Beckens, NE-Tschad.

Markham, B.L., Storey, J.C., Irons, J.R., 2013. Landsat data continuity mission, now Landsat-8: Six months on-orbit, in: Earth Observing Systems XVIII. International Society for Optics and Photonics, p. 88661B.

McFeeters, S.K., 1996. The use of the Normalized Difference Water Index (NDWI) in the delineation of open water features. Int. J. Remote Sens. 17, 1425–1432. https://doi.org/10.1080/01431169608948714

McMahon, T.A., Peel, M.C., Lowe, L., Srikanthan, R., McVicar, T.R., 2013. Estimating actual, potential, reference crop and pan evaporation using standard meteorological data: a pragmatic synthesis. Hydrol. Earth Syst. Sci. 17, 1331–1363.

MEH, 2014. Données de précipitations 1995 – 2012.

MEH, 2016. Carte hydrogéologique de reconnaissance de la République du Tchad au 1:500 000, feuille NE-33-NE Pic Toussidé.

MEH, 2015. Carte hydrogéologique de reconnaissance de la République du Tchad au 1:500 000, feuille NE-34-NO Borkou Nord - Ounianga.

Ministère de l'eau, 2010. Définition nationale de l'eau potable au Tchad, décret no. 615.

Mohamed, A., Sultan, M., Ahmed, M., Yan, E., Ahmed, E., 2017. Aquifer recharge, depletion, and connectivity: Inferences from GRACE, land surface models, and geochemical and geophysical data. GSA Bull. 129, 534–546. https://doi.org/10.1130/B31460.1.

Muller, A.B., Haynes, C.V.J., 1984. Isotope hydrology of the shallow groundwaters of the western desert. Isot. Hydrol. 1983 Proc. Symp.

Münnich, K.O., Vogel, J.C., 1963. Untersuchungen an pluvialen Wässern der Ost-Sahara. Geol. Rundsch. 52, 611–624. https://doi.org/10.1007/BF01821145.

Murray, G.W., 1952. The artesian waters of Egypt.

Neev, D., Hall, J.K., Saul, J.M., 1982. The Pelusium megashear system across Africa and associated lineament swarms. J. Geophys. Res. Solid Earth 87, 1015–1030.

Nicholson, S.E., Flohn, H., 1980. African environmental and climatic changes and the general atmospheric circulation in late Pleistocene and Holocene. Clim. Change 2, 313–348.

NOAA, C., 2001. The NOAA Climate Prediction Center African Rainfall Estimation Algorithm Version 2.0.

O.N.H.P.V., 1991. Mission d'identification et d'étude de préimplantation de 20 puits dans le Tibesti ouest.

O.N.H.P.V., 1992. Réhabilitation du B.E.T. - Etude hydrogéologique en vue de la création de 50 points d'eau - deuxième partie: Tibesti Ouest.

Organisation Commune des Régions Sahariennes, 1962. Prospection par sismique refraction, Pfrefectures de Faya-Largeau, Biltine et Abéché, République du Tchad.

ORSTOM, 1973. Précipitations journalières de l'origine des stations à 1965, République du Tchad.

ORSTOM, 1962. Etudes d'hydrologie superficielle en régions subdésertiques et désertiques d'Afrique Noire. Terres Eaux 46–73.

Oursingbé, M., Tang, Z., 2011. Study of hydrogeological potential in the basement areas in eastern Chad: a case study of Ouaddaï-Biltine. Res. 3 2.

Pachur, H.-J., Altmann, N., 2007. Die Ostsahara im Spätquartär: Ökosystemwandel im größten hyperariden Raum der Erde. Springer-Verlag.

Pallas, P., 1980. Water resources of the Socialist People's Arab Libyan Republic. Geol. Libya 2.

Parodi, G.N., 2002. AHVRR Hydrological Analysis System, Algorithms and theory, Version 1.3. WRES-ITC.

Penman, H.L., 1956. Evaporation: an introductory survey. Neth J Agric Sci 4, 9–29.

Penman, H.L., 1948. Natural evaporation from open water, bare soil and grass. Proc R Soc Lond A 193, 120–145.

Priestley, C.H.B., Taylor, R.J., 1972. On the assessment of surface heat flux and evaporation using large-scale parameters. Mon. Weather Rev. 100, 81–92.

Roche, M., 1958. Etudes d'écoulement en régime désertique : massif de l'Ennedi, campagne 1958. Off. Rech. Sci. Tech. D'Outre-Mer Comm. Sci. Logone Tchad Organ. Commune Régions Sahariennes 192.

Rodier, J., Roche, M., 1978. River flow in arid regions. Hydrom. Princ. Pract. Ed. 453–472.

Roerink, G.J., Su, Z., Menenti, M., 2000. S-SEBI: A simple remote sensing algorithm to estimate the surface energy balance. Phys. Chem. Earth Part B Hydrol. Oceans Atmosphere 25, 147–157.

Roy, D.P., Wulder, M.A., Loveland, T.R., C.E., W., Allen, R.G., Anderson, M.C., Helder, D., Irons, J.R., Johnson, D.M., Kennedy, R., Scambos, T.A., Schaaf, C.B., Schott, J.R., Sheng, Y., Vermote, E.F., Belward, A.S., Bindschadler, R., Cohen, W.B., Gao, F., Hipple, J.D., Hostert, P., Huntington, J., Justice, C.O., Kilic, A., Kovalskyy, V., Lee, Z.P., Lymburner, L., Masek, J.G., McCorkel, J., Shuai, Y., Trezza, R., Vogelmann, J., Wynne, R.H., Zhu, Z., 2014. Landsat-8: Science and product vision for terrestrial global change research. Remote Sens. Environ. 145, 154–172. https://doi.org/10.1016/j.rse.2014.02.001.

Said, M.M., El-Mehdi, B.., 2000. Jabal Asbah NF 35-1, Joint geological mapping project 1:250'000.

Sandford, K.S., 1935. Sources of Water in the North-Western Sudan. Geogr. J. 85, 412–431. https://doi.org/10.2307/1785619.

Scanlon, B.R., Keese, K.E., Flint, A.L., Flint, L.E., Gaye, C.B., Edmunds, W.M., Simmers, I., 2006. Global synthesis of groundwater recharge in semiarid and arid regions. Hydrol. Process. Int. J. 20, 3335–3370.

Scaramuzza, P.L., Bouchard, M.A., Dwyer, J.L., 2012. Development of the Landsat Data Continuity Mission Cloud-Cover Assessment Algorithms. IEEE Trans. Geosci. Remote Sens. 50, 1140–1154. https://doi.org/10.1109/TGRS.2011.2164087.

Schandelmeier, H., Klitzsch, E., Hendriks, F., Wycisk, P., 1987. Structural development of north-east Africa since Precambrian times. Berl. Geowiss AbhA 75, 5–24.

Schandelmeier, H., Reynolds, P.O., Semter, A.K., 1997. Palaeogeographic-palaeotectonic atlas of North-Eastern Africa, Arabia, and Adjacent areas(late Neoproterozoic to Holocene. I, Explanatory notes. II, Plates).

Schneider, J.-L., 1989. Géologie et Hydrogéologie de la république du Tchad.

Schneider, J.-L., 1994. Le Tchad depuis 25000 ans: géologie, archéologie, hydrogéologie. Elsevier Masson.

Sefelnasr, A.M., 2007. Development of groundwater flow model for water resources management in the development areas of the Western Desert, Egypt. DSc Martin Luther Univ. Ger. Google Sch.

Sefelnasr, A., Gossel, W., Wycisk, P., 2015. Groundwater management options in an arid environment: The Nubian Sandstone Aquifer System, Eastern Sahara. J. Arid Environ. 122, 46–58. https://doi.org/10.1016/j.jaridenv.2015.06.009.

Sellers, W.D., 1964. Potential evapotranspiration in arid regions. J. Appl. Meteorol. 3, 98–104.

Sen, Z., 2008. Wadi hydrology. Crc Press.

Silva, B.B. da, Braga, A.C., Braga, C.C., de Oliveira, L.M., Montenegro, S.M., Barbosa Junior, B., 2016. Procedures for calculation of the albedo with OLI-Landsat 8 images: Application to the Brazilian semi-arid. Rev. Bras. Eng. Agríc. E Ambient. 20, 3–8.

Smith, J.A., Lin, T.L., Ranson, K.L., 1980. The Lambertian assumption and Landsat data. Photogramm. Eng. Remote Sens. 46, 1183–1189.

Soenen, S.A., Peddle, D.R., Coburn, C.A., 2005. SCS+C: a modified Sun-canopy-sensor topographic correction in forested terrain. IEEE Trans. Geosci. Remote Sens. 43, 2148–2159. https://doi.org/10.1109/TGRS.2005.852480.

Sonntag, C., 1984. Autochthonous Groundwater, in the Confined Nubian Sandstone Aquifer. Berl. Geowiss Abh 50, 217–20.

Sonntag, C., 1986. A time-dependent groundwater model for the Eastern Sahara. Berl. Geowiss Abh A 72, 124–134.

Sonntag, C., Klitzsch, E., Lohnert, E.P., Münnich, K.O., Junghans, C., Thorweihe, U., Weistroffer, K., Swailem, F.M., 1978. Paleoclimatic information from D and 18O in 14C-dated North Saharian groundwaters; groundwater formation from the past 569–580.

Sonntag, C., Neureuther, P., Kalinke, C., Münnich, K.O., Klitzsch, E., Weistroffer, K., 1976. Zur Paläoklimatik des Sahara: Kontinentaleffekt im D- 18O-Gehalt pluvialer Saharawässer 469.

Sonntag, C., Thorweihe, U., Rudolph, J., 1982. Isotopenuntersuchungen zur Bildungsgeschichte saharischer Palaowasser. Geomethodica.

Stephens, D.B., 1994. A perspective on diffuse natural recharge mechanisms in areas of low precipitation. Soil Sci. Soc. Am. J. 58, 40–48

Sturchio, N.C., Arehart, G.B., Sultan, M., Sano, Y., AboKamar, Y., Sayed, M., 1996. Composition and origin of thermal waters in the Gulf of Suez area, Egypt. Appl. Geochem. 11, 471–479. https://doi.org/10.1016/0883-2927(96)00025-X.

Suckow, A., Sonntag, C., Grönig, M., Thorweihe, U., 1993. Ground water techarge in Umm Kedada Basin, NW-Sudan, derived from environmental isotopes of soil moisture in samples collected from deep dug wells, in: Geoscientific Research in Northeast Africa. Thorweihe and Schandelmeier, pp. 677–685.

Sultan, M., Metwally, S., Milewski, A., Becker, D., Ahmed, M., Sauck, W., Soliman, F., Sturchio, N., Yan, E., Rashed, M., Wagdy, A., Becker, R., Welton, B., 2011. Modern recharge to fossil aquifers: Geochemical, geophysical, and modeling constraints. J. Hydrol. 403, 14–24. https://doi.org/10.1016/j.jhydrol.2011.03.036.

Sultan, M., Sturchio, N., Hassan, F.A., Hamdan, M.A.R., Mahmood, A.M., Alfy, Z.E., Stein, T., 1997. Precipitation Source Inferred from Stable Isotopic Composition of Pleistocene Groundwater and Carbonate Deposits in the Western Desert of Egypt. Quat. Res. 48, 29–37. https://doi.org/10.1006/qres.1997.1907.

Sultan, M., Sturchio, N.C., Gheith, H., Abdel Hady, Y., El Nabawy, M., 2000. Chemical and Isotopic Contraints on the Origin of Wadi El-Tarfa Ground Water, Eastern Desert, Egypt 743–751.

Swailem, F.M., Hamza, M.S., Aly, A.I.M., 1983. Isotopic composition of groundwater in Kufra, Libya. Int. J. Water Resour. Dev. 1, 331–341.

Swezey, C.S., 2009. Cenozoic stratigraphy of the Sahara, Northern Africa. J. Afr. Earth Sci. 53, 89–121. https://doi.org/10.1016/j.jafrearsci.2008.08.001.

Teillet, P.M., Guindon, B., Goodenough, D.G., 1982. On the Slope-Aspect Correction of Multispectral Scanner Data. Can. J. Remote Sens. 8, 84–106. https://doi.org/10.1080/07038992.1982.10855028.

Thorweihe, U., Heinl, M., 2002. Groundwater resources of the Nubian Aquifer System NE Africa. Modified synthesis submitted to Observatoire du Sahara et du Sahel (OSS, Paris).

Tóth, J., 2009. Gravitational systems of groundwater flow: theory, evaluation, utilization. Cambridge University Press.

Trabucco, A., Zomer, R.J., 2009. Global potential evapo-transpiration (Global-PET) and global aridity index (Global-Aridity) geo-database. CGIAR Consort. Spat. Inf.

Turc, L., 1961. Estimation of irrigation water requirements, potential evapotranspiration: a simple climatic formula evolved up to date. Ann Agron 12, 13–49.

USGS, 2015. Landsat 8 (L8) data users handbook. USGS 1.

Valor, E., Caselles, V., 1996. Mapping land surface emissivity from NDVI: Application to European, African, and South American areas. Remote Sens. Environ. 57, 167–184.

Vasseur, G., Rousseau-Gueutin, P., Marsily, G. de, 2015. Time constant of hydraulic-head response in aquifers subjected to sudden recharge change: application to large basins. Hydrogeol. J. 23, 915–934. https://doi.org/10.1007/s10040-015-1252-3.

Vincent, P.M., 1970. The evolution of the Tibesti volcanic province, eastern Sahara, in: African Magmatism and Tectonics. Oliver and Boyd Edinburgh, pp. 301–319.

Voss, C.I., Soliman, S.M., 2014. The transboundary non-renewable Nubian Aquifer System of Chad, Egypt, Libya and Sudan: classical groundwater questions and parsimonious hydrogeologic analysis and modeling. Hydrogeol. J. 22, 441–468. https://doi.org/10.1007/s10040-013-1039-3.

Vrbka, P., Thorweihe, U., 1993. Hydrogeology of the Wadi El Milk – Wadi Muqaddam area, northern Sudan, in: Geoscientific Research in Northeast Africa. Thorweike and Schandelmeier, pp. 693–698.

Wacrenier, P., 1958. Notice explicative de la carte géologique provisoire du Borkou-Ennedi-Tibesti au 1/1.000.000. Afrique équatoriale française, Haut Commissariat de la république, Direction des mines et de la géologie.

Williams, J.J., 1966. South-Central Libya and Northern Chad: a guidebook to the geology and prehistory. Petroleum Exploration Society of Libya.

Willmott, C.J., Matsuura, K., 1995. Smart interpolation of annually averaged air temperature in the United States. J. Appl. Meteorol. 34, 2577–2586.

Wolff, J.P., 1964. Carte géologique de la République du Tchad 1: 1 500 000. Imprimerie Moderne.

Wood, W.W., Sanford, W.E., 1995. Chemical and isotopic methods for quantifying ground-water recharge in a regional, semiarid environment. Groundwater 33, 458–468.

Wright, E.P., Benfield, A.C., Edmunds, W.M., Kitching, R., 1982. Hydrogeology of the Kufra and Sirte basins, eastern Libya. Q. J. Eng. Geol. Hydrogeol. 15, 83–103. https://doi.org/10.1144/GSL.QJEG.1982.015.02.02.

Xu, H., 2006. Modification of normalised difference water index (NDWI) to enhance open water features in remotely sensed imagery. Int. J. Remote Sens. 27, 3025–3033. https://doi.org/10.1080/01431160600589179.

Zhong, Q., Yinhai, L., 1988. Satellite observation of surface albedo over the Qinghai-Xizang plateau region. Adv. Atmospheric Sci. 5, 57–65.

WEBSITE

http://www.inseed-td.net/index.php/thematiques/statistique-demographique/population

Appendices

Annex 1 Geochemical analysis of rock samples

Annex 2 Rock samples description

Annex 3 Inspected water points

Annex 4 Hydrochemical analysis of water samples

Annex 5 Stable isotopes analysis of water samples

Annex 6 Processed LandSat8 images

Annex 1 – Geochemical analysis of rock samples

Age	Name Sample	SiO_2	Al_2O_3	CaO	Fe_2O_3	NaO	K2O	MgO	P_2O_5	MnO	TiO_2	LOI	W	Zr	Ba	Mn	Ce	Co	Cr	Sr	La	V	Nd	Y	Zn	Pb	Nb	Cu	Ni	Th	Ga	Hf	Sn	Sc	Rb	As	Sm	Cd	Sb	U	Yb	Se
							ppm																		ppb																	
Cambro-Ordovician	NO.8	94.35	2.15	0.06	0.80	0.06	0.10	0.06	0.04	0.00	0.11	1.41	201	87	44	13	117	35	201	31	62	29	49			12			17													
Cambro-Ordovician	NO.23	86.43	1.51	0.24	8.70	0.03	0.08	0.08	0.35	0.01	0.04	2.45	323	57	19	85		70	15	12		36			53			17													
Cambro-Ordovician mean		90.39	1.83	0.15	4.75	0.04	0.09	0.07	0.20	0.00	0.07	1.93	262	72	31	49	117	52	108	21	62	33	49		53	12			17	17												
Cambro-Ordovician standard deviation		3.96	0.32	0.09	3.95	0.03	0.01	0.01	0.16	0.00	0.04	0.52	61	15	12	36	0	18	93	9	0	4	0		0	0			0	0												
Silurian	NO.14A	85.08	9.92	0.03	0.30	0.01	0.05	0.01	0.04	0.01	0.58	3.77	522	463	32	23	44	68	31	17	25	30	18	31								10									
Silurian	NO.14B	97.08	0.99	0.04	0.26	0.02	0.02	0.03	0.04	0.00	0.30	0.47	390	278	27	15	68	62	22	19	27	17	24																		
Silurian mean		91.08	5.45	0.03	0.28	0.01	0.03	0.02	0.04	0.00	0.44	2.12	456	370	30	19	56	65	27	18	26	24	21	31								10									
Silurian standard deviation		6.00	4.46	0.01	0.02	0.01	0.01	0.01	0.00	0.00	0.14	1.65	66	93	3	4	12	3	5	1	1	6	3	0								0									
Lower Devonian	OHO	96.03	2.16	0.04	0.17	0.01	0.04	0.04	0.03	0.00	0.09	1.14	332	82	28		28	53	12	42	16	10	13																		
Lower Devonian	GN1401	61.14	24.45	0.02	1.17	0.40	0.65	0.04	0.15	0.00	1.17	10.27	32	378	262	16	206	11	122	293	118	71	80	31	20	90	21		11	23	31			14		12				
Lower Devonian	GN1404	66.53	7.84	0.39	20.29	0.09	0.12	0.08	0.15	0.00	0.32	4.03	294	237	116	34	44	38	77	59	23	194	18		31	20				13				11						
Lower Devonian	GB1456	96.06	1.73	0.11	0.08	0.02	0.03	0.05	0.02	0.00	0.17	0.84	425	179	36	10	38	93	38	28	21	10	15					19												
Lower Devonian	GB1408	92.85	2.23	1.19	0.22	0.11	0.04	0.06	0.07	0.02	0.10	2.92	337	69	371	224	222	59	64	143	116	10	53			126			11											
Lower Devonian	GB1412	83.21	10.41	0.30	0.77	0.04	0.13	0.04	0.03	0.01	0.59	4.35	102	1205	155	37	86	14	34	32	40	18	25	47	10	24	15		30	15	33		14						
Lower Devonian	GB1415	97.48	1.02	0.02	0.14	0.01	0.03	0.03	0.01	0.00	0.18	0.48	415	160	23	20	12	90	112			14					25													
Lower Devonian mean		84.76	7.12	0.30	3.26	0.10	0.15	0.05	0.07	0.00	0.38	3.43	277	330	142	57	91	51	68	93	56	47	34	39	20	65	18	22	11	21	20	33		14	14	11	12				
Lower Devonian standard deviation		12.40	6.10	0.28	4.86	0.09	0.14	0.01	0.05	0.01	0.14	2.94	120	264	104	56	74	26	33	79	41	49	22	8	7	43	3	3	0	7	8	0		0	0	0	0				
Upper Devonian	GN1453	74.15	2.01	0.34	14.77	0.07	0.46	0.12	0.22	0.07	0.87	4.40	337	556	26000	644		58	19	37	23	44			125		10		26	10		50		13		21	15				
Upper Devonian	GN1418	94.41	1.97	0.02	0.72	0.12	0.07	0.07	0.03	0.01	1.14	1.21	529	815	66	30	69	98	41	11	29	51	25	22		10	17	18		16		22									
Upper Devonian	NO.13	7.00	8.89	0.23	66.90	0.03	0.06	0.04	1.99	2.28	0.60	10.94	36	143	12000	13972	618	40	49	1126	227	530	423	158	318	88	10	25	65	12	12		35	50		13	78	17	11	28	13
Upper Devonian	NO.12	87.36	5.40	0.27	3.13	0.02	0.06	0.04	0.04	0.03	0.55	2.77	299	359	275	289	49	65	19	46	31	27	21	18	18	10			16			10									
Upper Devonian	NO.11	65.04	1.58	0.09	30.49	0.00	0.09	0.02	0.09	0.04	0.31	2.00	257	225	3036	248	11	19	28	13	11	66			40				12					14						
Upper Devonian	NO.10	94.91	2.59	0.05	0.13	0.02	0.03	0.03	0.02	0.00	0.35	1.05	281	217	37		69	50	17	14	38	21	36			10															
Upper Devonian mean		70.48	3.74	0.17	19.36	0.04	0.13	0.05	0.40	0.41	0.64	3.73	290	386	854	3037	163	55	29	208	60	121	126	66	125	30	12	22	30	13	12	16	42	50		13	78	19	13	28	13
Upper Devonian standard deviation		15.69	1.95	0.10	16.76	0.03	0.09	0.02	0.45	0.54	0.21	2.25	85	171	873	3645	152	16	5	262	48	116	113	46	77	23	2	2	14	2	0	4	5	0		1	0	1	1	0	0
Carboniferous	NO.21	96.45	1.49	0.11	0.16	0.01	0.03	0.07	0.01	0.01	0.41	0.76	318	630	31	35	23	50	54		13			11								15									
Carboniferous	NO.2	3.92	0.74	51.92	0.21	0.03	0.03	0.60	0.01	0.52	0.05	41.58	24	14	769	3994	11			236	20																				
Carboniferous	NO.17	49.15	6.13	20.83	1.09	1.66	0.68	0.71	0.08	0.66	1.22	17.09	89	434	5390	5417	30	25	66	352	33	54		19	16	11	14	14	10			16	21								
Carboniferous	GN1419	12.56	2.06	45.27	0.76	0.14	0.45	0.58	0.18	0.31	0.15	36.73	56	83	155	2274		13		211	19	12			11								20								
Carboniferous	GN1421	63.72	0.64	17.98	0.66	0.02	0.04	0.19	0.01	0.74	0.69	14.81	387	751	23	6390	25	55	23	73	15	19	11				10					17								
Carboniferous mean		45.16	2.21	27.22	0.57	0.37	0.25	0.43	0.06	0.45	0.50	22.19	175	382	1274	3622	22	36	46	218	20	28	11	15	14	11	12	14	10			16	16	20						
Carboniferous standard deviation		29.54	1.57	17.10	0.31	0.51	0.25	0.24	0.06	0.23	0.36	13.57	142	267	1647	1974	6	17	16	76	5	17	0	4	3	0	2	0	0			1	0	1						
Permo-Trias	NO.5	97.00	1.05	0.07	0.32	0.02	0.03	0.04	0.01	0.01	0.31	0.61	349	574	56	69	27	56		11	13		18								13									
Permo-Trias	NO.6	81.37	10.77	0.15	1.81	0.01	0.06	0.06	0.03	0.01	0.97	4.30	69	553	58	47	61	18	100	15	39	41	18	21		12	29			11	16	14								
Permo-Trias	GAOUR	87.22	7.04	0.11	1.61	0.02	0.03	0.03	0.05	0.02	0.22	3.05	140	97	78	121	113	32	66	76	70	22	33																	
Permo-Trias	MADADI	83.62	0.48	0.05	0.10	0.09	0.03	0.03	0.00	0.01	0.13	15.05	815	203	25	26	12	141	29			10																		
Permo-Trias	GB1425	90.03	6.12	0.20	0.25	0.02	0.04	0.03	0.05	0.00	0.53	2.60	286	337	152	19	155	46	41	80	97	38	89	22		18	13			13					16					
Permo-Trias	GN1427	71.63	13.89	0.05	7.02	0.06	0.19	0.03	0.06	0.01	0.96	5.39	93	285	65	61	67	29	85	40	30	88	33	45	14	22	21	22	14	14	18		10	29						
Permo-Trias	GN1428	86.39	7.31	0.12	2.30	0.03	0.07	0.04	0.05	0.01	0.53	3.02	184	202	79	41	99	32	71	80	42	62	35	20			11													
Permo-Trias	GN1436	56.54	7.95	0.03	27.93	0.00	0.26	0.07	0.44	0.04	0.42	6.20	194	107	95	189	67	67	85	23	32	40	27	16	99	22		15	50		12									
Permo-Trias mean		81.73	6.83	0.10	5.17	0.03	0.09	0.04	0.09	0.01	0.51	5.03	266	295	76	72	75	53	68	67	46	43	36	25	57	18	19	18	33	13	15	13		10	29		16				
Permo-Trias standard deviation		8.91	3.21	0.05	6.15	0.02	0.07	0.01	0.03	0.01	0.24	2.89	163	145	25	42	35	26	20	28	21	16	15	8	43	4	7	4	18	3	2	0		0	0		0				
Jurassic - Lower Cretaceous	GB1433	96.74	1.39	0.05	0.18	0.02	0.03	0.03	0.01	0.00	0.07	0.63	327	49	26	13	19	56	34	12	16		12																		
Jurassic - Lower Cretaceous	GN1437	96.02	1.80	0.12	0.17	0.02	0.02	0.04	0.01	0.00	0.24	0.80	392	197	45	12	30	66	11	18	18	10	11																		
Jurassic - Lower Cretaceous	GB1440	81.88	11.82	0.12	0.14	0.14	0.09	0.01	0.05	0.00	0.54	4.67	70	390	124	10	88	17	49	79	42	15	38	24		13	11			11											
Jurassic - Lower Cretaceous	GN1444	94.83	3.02	0.01	0.41	0.02	0.06	0.02	0.02	0.01	0.16	1.36	466	150	163	20	16	78	105	35	10	21																		
Jurassic - Lower Cretaceous	MOTORO	84.94	7.52	0.14	2.90	0.01	0.04	0.03	0.07	0.01	0.58	3.28	227	274	116	37	59	39	110	37	38	71	33	19	20	12	10		14		10									
Jurassic-Lower Cretaceous mean		90.88	5.11	0.09	0.76	0.04	0.05	0.03	0.03	0.00	0.32	2.14	296	212	95	18	32	51	61	36	25	29	24	21	20	12	11		14		10									
Jurassic-Lower Cretaceous standard deviation		5.98	3.65	0.05	0.86	0.04	0.03	0.01	0.02	0.00	0.19	1.45	119	96	47	8	25	18	37	17	13	21	12	2	0	0	1		0		1									

Age	Name Sample	SiO_2	Al_2O_3	CaO	Fe_2O_3	Na_2O	K_2O	MgO	P_2O_5	MnO	TiO_2	LOI	W	Zr	Ba	Mn	Ce	Co	Cr	Sr	La	V	Nd	Y	Zn	Pb	Nb	Cu	Ni	Th	Ga	Hf	Sn	Sc	Rb	As	Sm	Cd	Sb	U	Yb	Se
		ppm											ppb																														
Upper Cretaceous	GN1445	95.70	1.78	0.12	0.40	0.03	0.03	0.04	0.01	0.00	0.10	0.98	350	100	45	13	31	63	80	18	25	13	17					24														
Upper Cretaceous	GB1447	96.38	1.58	0.14	0.14	0.01	0.04	0.04	0.01	0.00	0.42	0.82	530	953	68	23	40	95	14	17	16	20	20	12				29				25									
Upper Cretaceous	GB1448	76.64	15.53	0.03	0.34	0.08	0.05	0.00	0.03	0.00	1.33	5.89	82	373	65	17	86	21	60	47	38	32	47	29			33		11	19		10									
Upper Cretaceous	GB1449	94.79	2.37	0.22	0.24	0.02	0.04	0.03	0.02	0.00	0.21	1.26	199	228	131	15	35	34	110	23	23	15	14																		
Upper Cretaceous mean		90.88	5.31	0.13	0.28	0.03	0.04	0.03	0.02	0.00	0.51	2.24	290	413	77	17	48	53	66	26	26	20	24	20			33	27	11	19	25	10									
Upper Cretaceous standard deviation		7.12	5.11	0.05	0.09	0.02	0.00	0.01	0.01	0.00	0.41	1.83	150	279	27	3	19	25	29	10	6	6	11	9			0	3	0	0	0	0									
Cenozoic	CT	91.05	4.30	0.20	0.56	0.09	0.25	0.08	0.01	0.01	0.26	2.46	245	65	123	50	17	50	42	30		23			13			29														
Cenozoic	GB1405	90.91	4.85	0.14	0.68	0.05	0.29	0.06	0.02	0.00	0.22	2.06	632	69	131	24	18	109	83	23	15	20		10	13			525				88									
Cenozoic	GN1406	86.16	4.20	0.03	3.15	0.04	0.05	0.03	0.06	0.01	0.40	5.34	189	213	60	17	52	39	81	30	33	48	20		19		16	149	16			26									
Cenozoic	GN1409	49.79	4.51	0.08	39.24	0.03	0.17	0.03	0.10	0.00	0.53	5.34	126	202	148	31	51		59	41	29	743	16	10	41	59		18	10	16	10					47				12
Cenozoic	GN1451	97.47	0.95	0.04	0.41	0.01	0.03	0.03	0.02	0.00	0.08	0.50	204	120	120		32	43	20	14	24		23					36													
Cenozoic	GN1455	65.81	22.27	0.00	1.20	0.14	1.34	0.22	0.14	0.00	1.08	7.39	20	179	591	26	101	13	100	200	50	113	42	45	12	25	19		11	22	28		14	50							
Cenozoic mean		80.20	6.85	0.08	7.54	0.06	0.35	0.08	0.06	0.00	0.43	3.85	236	141	196	30	45	51	64	56	30	189	25	22	19	42	17	151	12	19	19	57	14	50	47					12
Cenozoic standard deviation		14.33	5.14	0.06	10.57	0.04	0.33	0.05	0.04	0.00	0.25	2.18	135	57	132	9	23	23	24	48	9	222	8	15	8	17	1	149	3	3	9	31	0	0	0					0

Annex 2 – Rock samples description

NoID	Name Sample	Lat	Long	Yutm	Xutm	Alt	Context	Date	Age evaluation			Intergranular porosity
									Age (MEH, 2015, 2016)	Age (Wolff, 1964)	Age (this work)	
1	EN1301	16.482	22.208	1822639	628930	810	outcrop	12.02.2013	Cambrian	Cambrian	Precambrian	
2	EN1302	16.482	22.208	1822639	628930	810	outcrop	12.02.2013	Cambrian	Cambrian	Precambrian	2
3	EN1303	16.734	21.876	1850340	593395	569	outcrop	15.02.2013	Cambrian	Cambrian	Cambrian	
4	EN1304	16.566	22.197	1831973	627685	652	crumbled block	12.02.2013	Precambrian	Precambrian	Precambrian	
5	EN1305	16.900	21.777	1868631	582786	558	outcrop	16.02.2013	Cambrian	Lower Devonian	Cambrian	
6	EN1306	16.900	21.777	1868631	582786	558	outcrop	16.02.2013	Cambrian	Lower Devonian	Cambrian	
7	EN1307	16.861	21.757	1864385	580683	600	crumbled block	16.02.2013	Ordovician	Ordovician	Ordovician	
8	EN1309	16.861	21.757	1864385	580683	600	crumbled block	16.02.2013	Ordovician	Ordovician	Ordovician	
9	EN1310	16.892	21.642	1867727	568363	626	outcrop	16.02.2013	Silurian	Lower Devonian	Silurian	
10	EN1311	16.900	21.639	1868635	568103	630	outcrop	16.02.2013	Ordovician	Lower Devonian	Ordovician	
11	EN1312	16.981	21.673	1877552	571612	670	outcrop	16.02.2013	Lower Devonian	Lower Devonian	Lower Devonian	
12	EN1313	17.214	21.418	1903260	544401	528	outcrop	17.02.2013	Cambrian	Lower Devonian	Cambrian	
13	EN1314	17.213	21.417	1903113	544332	547	outcrop	17.02.2013	Ordovician	Lower Devonian	Ordovician	
14	EN1315	17.211	21.446	1902966	547415	556	outcrop	17.02.2013	Lower Devonian	Lower Devonian	Lower Devonian	6
15	EN1316	17.261	21.626	1908552	566552	606	outcrop	19.02.2013	Lower Devonian	Lower Devonian	Lower Devonian	
16	EN1317	17.343	21.606	1917619	564398	698	outcrop	19.02.2013	Upper Devonian	Upper Devonian	Upper Devonian	17
17	EN1318	17.447	21.529	1929031	556209	780	outcrop	19.02.2013	Upper Devonian	Upper Devonian	Upper Devonian	
18	EN1319	17.602	21.455	1946182	548246	730	outcrop	19.02.2013	Upper Devonian	Upper Devonian	Upper Devonian	
19	EN1320	17.770	21.469	1964846	549698	570	outcrop	19.02.2013	Upper Devonian	Upper Devonian	Upper Devonian	
20	EN1321	17.938	21.831	1983513	587984	486	outcrop	20.02.2013	Upper Devonian	Carboniferous	Carboniferous	15
21	EN1322	18.090	21.792	2000303	583776	503	outcrop	20.02.2013	Carboniferous	Carboniferous	Carboniferous	5
22	EN1323	18.090	21.792	2000303	583776	503	outcrop	20.02.2013	Carboniferous	Carboniferous	Carboniferous	
23	EN1324	18.266	21.735	2019761	577652	483	outcrop	20.02.2013	Permo-Trias	Carboniferous	Permo-Trias	
24	EN1325	18.266	21.735	2019761	577652	483	outcrop	20.02.2013	Permo-Trias	Carboniferous	Permo-Trias	20
25	EN1326	18.285	21.749	2021880	579190	503	crumbled block	20.02.2013	Permo-Trias	Permo-Trias	Permo-Trias	
26	EN1327	18.294	21.753	2022873	579536	515	crumbled block	20.02.2013	Permo-Trias	Permo-Trias	Permo-Trias	
27	EN1328	18.294	21.753	2022873	579536	515	crumbled block	20.02.2013	Permo-Trias	Permo-Trias	Permo-Trias	5.1
28	EN1329	18.294	21.753	2022873	579536	515	crumbled block	20.02.2013	Permo-Trias	Permo-Trias	Permo-Trias	4
29	EN1330	18.091	21.792	2000482	583759	503	crumbled block	20.02.2013	Carboniferous	Carboniferous	Carboniferous	
30	EN1331	17.852	21.981	1974089	603934	518	crumbled block	21.02.2013	Carboniferous	Carboniferous	Carboniferous	
31	EN1332	17.848	21.986	1973695	604489	518	outcrop	21.02.2013	Carboniferous	Carboniferous	Carboniferous	
32	EN1333	17.889	22.114	1978218	618044	496	outcrop	21.02.2013	Carboniferous	Carboniferous	Carboniferous	
33	EN1334	17.870	22.621	1976598	671713	585	outcrop	21.02.2013	Carboniferous	Carboniferous	Upper Devonian	18
34	EN1335	17.871	21.796	1976072	584342	492	outcrop	22.02.2013	Carboniferous	Carboniferous	Carboniferous	11.1
35	EN1336	17.861	21.791	1974947	583806	485	outcrop	22.02.2013	Carboniferous	Carboniferous	Carboniferous	4
36	EN1337	17.861	21.791	1974947	583806	485	outcrop	22.02.2013	Carboniferous	Carboniferous	Carboniferous	
37	EN1338	17.842	21.769	1972839	581500	507	outcrop	22.02.2013	Upper Devonian	Carboniferous	Upper Devonian	
38	EN1339	17.209	21.388	1902673	541222	518	outcrop	24.02.2013	Cambrian	Silurian	Cambrian	
39	EN1340	17.171	21.301	1898465	532052	539	outcrop	24.02.2013	Ordovician	Ordovician	Ordovician	
40	EN1341	17.129	21.292	1893847	531053	535	crumbled block	24.02.2013	Ordovician	Lower Devonian	Ordovician	
41	GN1401	17.934	19.111	1983934	299880	260	outcrop	22.01.2014	Silurian	Eocene - Miocene	Silurian	0
42	GN1402	17.913	19.100	1981610	298712	230	outcrop	22.01.2014	Holocene	Holocene	Holocene	
43	GN1403	17.974	19.169	1988299	306089	317	outcrop	23.01.2014	Ordovician	Lower Devonian	Ordovician	10
44	GN1404	17.974	19.169	1988299	306089	317	crumbled block	23.01.2014	Ordovician	Lower Devonian	Eocene - Miocene	0
45	GN1405	18.009	19.224	1992105	311920	312	outcrop	23.01.2014	Eocene - Miocene	Eocene - Miocene	Eocene - Miocene	
46	GN1406	18.047	19.247	1996299	314406	336	outcrop	23.01.2014	Eocene - Miocene	Eocene - Miocene	Eocene - Miocene	20
47	GN1407	18.045	19.247	1996022	314414	327	outcrop	23.01.2014	Eocene - Miocene	Eocene - Miocene	Eocene - Miocene	
48	GN1408	18.146	19.295	2007186	319642	341	outcrop	23.01.2014	Devonian	Lower Devonian	Lower Devonian	7
49	GN1409	18.148	19.296	2007340	319760	351	outcrop	23.01.2014	Eocene - Miocene	Eocene - Miocene	Eocene - Miocene	7
50	GN1410	18.148	19.296	2007340	319760	351	outcrop	23.01.2014	Eocene - Miocene	Eocene - Miocene	Ordovician	6
51	GN1411	18.148	19.296	2007340	319760	351	crumbled block	23.01.2014	Eocene - Miocene	Eocene - Miocene	Eocene - Miocene	
52	GN1412	18.254	19.339	2019063	324438	357	outcrop	23.01.2014	Silurian	Lower Devonian	Eocene - Miocene	0
53	GN1413	18.433	19.410	2038851	332077	388	crumbled block	23.01.2014	Eocene - Miocene	Eocene - Miocene	Eocene - Miocene	
54	GN1414	18.479	19.473	2043841	338806	403	outcrop	24.01.2014	Devonian	Upper Devonian	Upper Devonian	8
55	GN1415	18.479	19.473	2043841	338806	403	outcrop	24.01.2014	Devonian	Upper Devonian	Upper Devonian	7
56	GN1416	18.497	19.497	2045822	341368	391	outcrop	24.01.2014	Devonian	Upper Devonian	Upper Devonian	
57	GN1416A	18.497	19.497	2045822	341368	391	outcrop	24.01.2014	Devonian	Upper Devonian	Upper Devonian	
58	GN1417	18.574	19.576	2054321	349703	353	outcrop	24.01.2014	Holocene	Holocene	Holocene	
59	GN1418	18.670	19.643	2064824	356907	410	outcrop	24.01.2014	Devonian - Lower Carboniferous	Carboniferous	Upper Devonian	7
60	GN1419	18.884	19.621	2088581	354739	414	crumbled block	24.01.2014	Carboniferous	Carboniferous	Carboniferous	0
61	GN1420	19.291	19.685	2133496	361776	426	crumbled block	25.01.2014	Permo-Trias	Permo-Trias	Permo-Trias	
62	GN1421	19.289	19.685	2133373	361859	427	outcrop	25.01.2014	Carboniferous	Permo-Trias	Carboniferous	0
63	GN1421A	19.289	19.685	2133373	361859	427	outcrop	25.01.2014	Carboniferous	Permo-Trias	Carboniferous	0
64	GN1422	19.289	19.685	2133373	361859	427	crumbled block	25.01.2014	Permo-Trias	Permo-Trias	Carboniferous	
65	GN1423	19.290	19.685	2133384	361859	429	outcrop	25.01.2014	Permo-Trias	Permo-Trias	Permo-Trias	
66	GN1424	19.290	19.685	2133384	361859	429	outcrop	25.01.2014	Permo-Trias	Permo-Trias	Permo-Trias	
67	GN1425	19.290	19.685	2133429	361828	426	crumbled block	25.01.2014	Permo-Trias	Permo-Trias	Permo-Trias	3
68	GN1426	19.300	19.683	2134592	361658	462	outcrop	25.01.2014	Jurassic	Permo-Trias	Jurassic - Lower Cretaceous	
69	GN1427	19.300	19.683	2134559	361616	479	outcrop	25.01.2014	Jurassic	Permo-Trias	Jurassic - Lower Cretaceous	0
70	GN1428	19.300	19.683	2134582	361595	476	outcrop	25.01.2014	Jurassic	Permo-Trias	Jurassic - Lower Cretaceous	<1

NoID	Name Sample	Lat	Long	Yutm	Xutm	Alt	Context	Date	Age evaluation			Intergranular porosity
									Age (MEH, 2015, 2016)	Age (Wolff, 1964)	Age (this work)	
71	GN1429	19.299	19.683	2134449	361615	453	crumbled block	25.01.2014	Jurassic	Permo-Trias	Jurassic - Lower Cretaceous	0
72	GN1430	19.472	19.661	2153569	359473	441	outcrop	25.01.2014	Jurassic - Cretaceous	Jurassic - Lower Cretaceous	Eocene - Miocene	30
73	GN1431	19.862	19.300	2197086	321975	584	outcrop	26.01.2014	Miocene - Holocene	Miocene - Holocene	Miocene - Holocene	<2
74	GN1432	19.929	19.185	2204662	309980	637	outcrop	26.01.2014	Miocene - Holocene	Miocene - Holocene	Miocene - Holocene	0
75	GN1433	19.884	19.237	2199623	315392	585	outcrop	26.01.2014	Jurassic - Cretaceous	Jurassic - Lower Cretaceous	Jurassic - Lower Cretaceous	35
76	GN1434	19.582	19.564	2165904	349361	430	outcrop	25.01.2014	Holocene	Holocene	Holocene	
77	GN1435	17.913	19.100	1981610	298712	230	outcrop	22.01.2014	Holocene	Holocene	Holocene	
78	GN1436	19.297	19.678	2134254	361057	466	outcrop	25.01.2014	Jurassic	Permo-Trias	Permo-Trias	2
79	GN1437	19.602	19.584	2168100	351488	498	outcrop	27.01.2014	Jurassic - Cretaceous	Jurassic - Lower Cretaceous	Jurassic - Lower Cretaceous	25
80	GN1438	19.604	19.585	2168265	351584	521	outcrop	27.01.2014	Jurassic - Cretaceous	Jurassic - Lower Cretaceous	Jurassic - Lower Cretaceous	5
81	GN1439	19.287	19.910	2132922	385428	466	crumbled block	27.01.2014	Eocene - Miocene	Eocene - Miocene	Eocene - Miocene	
82	GN1440	19.050	20.491	2106404	446475	390	outcrop	28.01.2014	Jurassic - Cretaceous	Jurassic - Lower Cretaceous	Jurassic - Lower Cretaceous	3
83	GN1441	19.049	20.492	2106360	446517	384	outcrop	28.01.2014	Jurassic - Cretaceous	Jurassic - Lower Cretaceous	Jurassic - Lower Cretaceous	
84	GN1442	19.049	20.492	2106360	446517	384	outcrop	28.01.2014	Jurassic - Cretaceous	Jurassic - Lower Cretaceous	Jurassic - Lower Cretaceous	
85	GN1443	19.043	20.558	2105688	453512	422	outcrop	29.01.2014	Jurassic - Cretaceous	Jurassic - Lower Cretaceous	Jurassic - Lower Cretaceous	25
86	GN1444	19.043	20.558	2105688	453512	422	outcrop	29.01.2014	Jurassic - Cretaceous	Jurassic - Lower Cretaceous	Jurassic - Lower Cretaceous	5
87	GN1445	19.499	20.951	2156032	494879	494	outcrop	29.01.2014	Cretaceous	Cretaceous	Cretaceous	25
88	GN1446	19.499	20.953	2156076	495079	480	outcrop	29.01.2014	Cretaceous	Cretaceous	Cretaceous	8
89	GN1447	19.498	20.954	2155932	495163	464	outcrop	29.01.2014	Cretaceous	Cretaceous	Cretaceous	20
90	GN1448	19.499	20.955	2155988	495299	462	outcrop	29.01.2014	Cretaceous	Cretaceous	Eocene - Miocene	0
91	GN1449	19.499	20.955	2155988	495299	462	crumbled block	29.01.2014	Cretaceous	Cretaceous	Cretaceous	3
92	GN1450	18.916	20.860	2091550	485247	375	outcrop	30.01.2014	Holocene	Holocene	Holocene	
93	GN1451	18.896	20.671	2089330	465351	428	outcrop	30.01.2014	Eocene - Miocene	Jurassic - Lower Cretaceous	Jurassic - Lower Cretaceous	27
94	GN1452	18.430	20.463	2037889	443238	401	crumbled block	31.01.2014	Carboniferous	Carboniferous	Carboniferous	
95	GN1453	18.267	20.465	2019753	443459	406	crumbled block	31.01.2014	Devonian - Lower Carboniferous	Upper Devonian	Eocene - Miocene	20
96	GN1454	17.948	20.008	1984691	394896	368	outcrop	01.02.2014	Eocene - Miocene	Eocene - Miocene	Eocene - Miocene	
97	GN1455	17.948	20.008	1984691	394896	368	outcrop	01.02.2014	Eocene - Miocene	Eocene - Miocene	Eocene - Miocene	
98	GN1456	17.938	19.050	1984409	293463	232	outcrop	02.02.2014	Cambrian	Lower Devonian	Lower Devonian	7
99	GN1457	18.113	18.568	2004420	242665	256	outcrop	02.02.2014	Silurian	Lower Devonian	Lower Devonian	0
100	BK1503	17.455	19.053	1930945	293229	230	outcrop	22.01.2015	Eocene - Miocene	Eocene - Miocene	Eocene - Miocene	8
101	BK1504	17.818	19.153	1971016	304244	270	outcrop	22.01.2015	Eocene - Miocene	Eocene - Miocene	Eocene - Miocene	0
102	BK1505	17.941	19.114	1984671	300247	260	outcrop	23.01.2015	Devonian	Lower Devonian	Lower Devonian	17
103	BK1506	17.941	19.114	1984671	300247	260	outcrop	23.01.2015	Devonian	Lower Devonian	Lower Devonian	0
104	BK1507	17.945	19.116	1985112	300464	270	outcrop	23.01.2015	Devonian	Lower Devonian	Lower Devonian	
105	BK1508	17.945	19.115	1985113	300358	290	outcrop	23.01.2015	Devonian	Lower Devonian	Lower Devonian	21
106	BK1509	17.945	19.115	1985113	300358	300	outcrop	23.01.2015	Devonian	Lower Devonian	Lower Devonian	17
107	BK1510	17.938	19.102	1984352	298973	260	outcrop	23.01.2015	Cambrian	Lower Devonian	Lower Devonian	10
108	BK1512	17.885	18.993	1978607	287361	220	outcrop	24.01.2015	Silurian	Lower Devonian	Silurien	1
109	BK1513	17.886	18.971	1978743	285030	220	outcrop	24.01.2015	Cambrian	Lower Devonian	Lower Devonian	16
110	BK1514	17.914	18.896	1981931	277116	230	outcrop	24.01.2015	Cambrian	Lower Devonian	Lower Devonian	0
111	BK1515	17.917	18.891	1982269	276590	220	outcrop	24.01.2014	Silurian	Lower Devonian	Silurien	0
112	BK1517	18.097	18.586	2002590	244526	250	outcrop	25.01.2015	Silurian	Lower Devonian	Eocene - Miocene	0
113	BK1518	18.097	18.585	2002592	244420	260	outcrop	25.01.2015	Silurian	Lower Devonian	Eocene - Miocene	
114	BK1519	18.097	18.585	2002592	244420	260	outcrop	25.01.2015	Devonian	Lower Devonian	Eocene - Miocene	0
115	BK1520	18.097	18.585	2002592	244420	270	outcrop	25.01.2015	Devonian	Lower Devonian	Eocene - Miocene	10
116	BK1521	18.097	18.585	2002592	244420	270	outcrop	25.01.2015	Devonian	Lower Devonian	Lower Devonian	12
117	BK1522	18.189	18.116	2013495	194915	290	outcrop	26.01.2015	Ordovician	Lower Devonian	Ordovician	0
118	BK1523	18.189	18.116	2013495	194915	290	outcrop	26.01.2015	Ordovician	Lower Devonian	Eocene - Miocene	10
119	BK1524	19.890	17.988	2202087	812887	720	outcrop	27.01.2015	Precambrian	Cambrian	Precambrian	
120	BK1525	19.978	17.932	2211732	806848	750	outcrop	27.01.2015	Precambrian	Precambrian	Precambrian	0
121	BK1527	20.172	18.075	2233209	194262	860	outcrop	27.01.2015	Jurassic - Cretaceous	Jurassic - Lower Cretaceous	Eocene - Miocene	20
122	BK1528	20.128	18.063	2228357	192920	860	outcrop	27.01.2015	Jurassic - Cretaceous	Jurassic - Lower Cretaceous	Jurassic - Lower Cretaceous	6
123	BK1529	20.128	18.063	2228357	192920	860	outcrop	27.01.2015	Jurassic - Cretaceous	Jurassic - Lower Cretaceous	Eocene - Miocene	5
124	BK1530	20.128	18.063	2228357	192920	860	outcrop	28.01.2015	Jurassic - Cretaceous	Jurassic - Lower Cretaceous	Eocene - Miocene	0
125	BK1531	20.113	18.065	2226692	193100	930	crumbled block	28.01.2015	Miocene - Holocene	Miocene - Holocene	Miocene - Holocene	0
126	BK1532	20.007	18.115	2214859	198129	840	outcrop	28.01.2015	Jurassic - Cretaceous	Cambrian	Cambrian	15
127	BK1534	19.735	18.195	2184589	206003	810	outcrop	28.01.2015	Jurassic - Cretaceous	Cambrian	Cambrian	0
128	BK1537	19.058	18.423	2109238	228793	450	outcrop	30.01.2015	Devonian	Lower Devonian	Lower Devonian	30
129	BK1538	19.058	18.423	2109238	228793	450	outcrop	30.01.2015	Devonian	Lower Devonian	Lower Devonian	0
130	BK1539	19.058	18.423	2109238	228793	450	outcrop	30.01.2015	Devonian	Lower Devonian	Lower Devonian	0
131	BK1540	18.902	18.780	2091453	266162	350	outcrop	30.01.2015	Silurian	Lower Devonian	Eocene - Miocene	12
132	BK1541	18.879	18.858	2088805	274350	340	outcrop	31.01.2015	Devonian	Lower Devonian	Lower Devonian	16
133	BK1542	18.298	18.627	2024788	249155	360	outcrop	01.02.2015	Eocene - Miocene	Eocene - Miocene	Eocene - Miocene	0
134	BK1543	18.939	18.578	2095829	244932	410	outcrop	30.01.2015	Silurian	Upper Devonian	Upper Devonian	0
135	BK1545	20.007	18.115	2214859	198129	840	outcrop	28.01.2015	Jurassic - Cretaceous	Cambrian	Jurassic - Lower Cretaceous	0

Annex 3 – Inspected water points

Hydrological unit	ID	Locality	Sample Name	Long	Lat	Xutm	Yutm	Elevation GPS (msl) corrected	Geology (MEH 2015/16)	Geology (Wolff 1964)	Morphology
Nile hydrological basin	1A	Bao	no. 4	23.007	16.465	714259	1821449	904	Precambrian basement	Precambrian granites	alluvial system, valley low relief
	1B	Bao	BAO-PUI	23.007	16.465	714255	1821448	904	Precambrian basement	Precambrian granites	alluvial system, valley low relief
	2A	Oho	no. 6	23.073	16.442	721290	1818925	873	Cambro-Ordovician sandstone	Cambro-Ordovician sandstone	alluvial system, valley low relief
	2B	Oho	OHO-PUI	23.073	16.442	721287	1818928	873	Cambro-Ordovician sandstone	Cambro-Ordovician sandstone	alluvial system, valley low relief
	3A	Moutougouni	no. 7	23.114	16.447	725663	1819570	860	Cambro-Ordovician sandstone	Cambro-Ordovician sandstone	alluvial system, valley low relief
	3B	Moutougouni	MOUT-PUI	23.114	16.447	725664	1819585	860	Cambro-Ordovician sandstone	Cambro-Ordovician sandstone	alluvial system, valley low relief
	4	Amdjarass borehole	no. 3	22.857	16.091	698653	1779879	911	Precambrian basement	Cambro-Ordovician sandstone	alluvial system, valley low relief
	5	Amdjarass well	AMDJ-PUI	22.843	16.112	697076	1782151	925	Precambrian basement	Cambro-Ordovician sandstone	alluvial system, valley low relief
	6A	Berdoba	no. 9	22.886	16.001	701858	1769984	862	Precambrian basement	Precambrian granites	alluvial system, valley low relief
	6B	Berdoba	BERD-PUI	22.886	16.001	701859	1769985	862	Precambrian basement	Precambrian granites	alluvial system, valley low relief
	7	Bahai Kariari	Kariari	23.117	15.719	726859	1738989	778	Cambro-Ordovician sandstone	-	wide alluvial system, sandy
	8	Bahai well	BAHAI	22.926	15.534	706538	1718298	798	Precambrian basement	-	wide alluvial system, sandy
wadi Haouach	9	Kaoura borehole	Kaoura forage	22.606	16.215	671652	1793346	844	Precambrian basement	Cambro-Ordovician sandstone	alluvial system, valley low relief
	10A	Kaoura well	Kaoura puits	22.606	16.215	671652	1793346	844	Precambrian basement	Cambro-Ordovician sandstone	alluvial system, valley low relief
	10B	Kaoura well	KAOU-PUI	22.606	16.215	671657	1793338	844	Precambrian basement	Cambro-Ordovician sandstone	alluvial system, valley low relief
	11A	Itou	ITOU	22.466	16.323	656610	1805206	778	Precambrian basement	Precambrian granites	alluvial system, valley low relief
	11B	Itou	ITOU-PUI	22.468	16.321	656863	1805011	778	Precambrian basement	Precambrian granites	alluvial system, valley low relief
wadi Sala	12A	Bachiquele	BACH	22.345	16.511	643513	1825983	740	Cambro-Ordovician sandstone	Cambro-Ordovician sandstone	rock formation, tight valley
	12B	Bachiquele	BACH-MAR	22.345	16.511	643558	1825970	740	Cambro-Ordovician sandstone	Cambro-Ordovician sandstone	rock formation, tight valley
	13A	Monou	MO-1	22.174	16.404	625348	1813975	703	Precambrian basement	Precambrian granites	alluvial system, valley low relief
	13B	Monou	MONO-PUI	22.174	16.405	625384	1814118	703	Precambrian basement	Precambrian granites	alluvial system, valley low relief
	14A	Sania	SA-1	22.195	16.564	627528	1831722	671	Cambro-Ordovician sandstone	Cambro-Ordovician sandstone	alluvial system, valley low relief
	14B	Sania	SANI-PUI	22.195	16.564	627531	1831726	671	Cambro-Ordovician sandstone	Cambro-Ordovician sandstone	alluvial system, valley low relief
	15A	Chiguila	CHI-1	22.347	16.652	643617	1841506	716	Precambrian basement	Cambro-Ordovician sandstone	alluvial system, valley low relief
	15B	Chiguila	CHIG-PUI	22.347	16.652	643620	1841509	716	Precambrian basement	Cambro-Ordovician sandstone	alluvial system, valley low relief
	16A	Alliba	ALIBA	22.214	16.748	629391	1852062	670	Cambro-Ordovician sandstone	Lower Devonian	rock formation, tight valley
	16B	Alliba	ALI-SOU	22.214	16.748	629443	1852090	670	Cambro-Ordovician sandstone	Lower Devonian	rock formation, tight valley
	17	Chibi 1	CHIBI-1	22.316	16.705	640348	1847416	662	Precambrian basement	Precambrian granites	alluvial system, valley low relief
	18A	Chibi 2	CHIBI-2	22.316	16.705	640348	1847416	662	Precambrian basement	Precambrian granites	alluvial system, valley low relief
	18B	Chibi 2	CHIB-PUI	22.317	16.706	640431	1847487	662	Precambrian basement	Precambrian granites	alluvial system, valley low relief
	19	Terkei	TKD	21.646	16.751	568836	1852073	624	Cambro-Ordovician sandstone	Cambro-Ordovician sandstone	rock formation, valley low relief
	20	Welba 1	NOH-1	22.053	16.836	612222	1861693	585	Cambro-Ordovician sandstone	Cambro-Ordovician sandstone	wide alluvial system, sand-clay
	21	Welba 2	NOH-2	22.053	16.836	612193	1861662	584	Cambro-Ordovician sandstone	Cambro-Ordovician sandstone	wide alluvial system, sand-clay
	22	Welba	WEIBA--PUI	22.054	16.836	612257	1861709	580	Cambro-Ordovician sandstone	Cambro-Ordovician sandstone	wide alluvial system, sand-clay
	23	Welba 3	NOH-3	22.054	16.841	612279	1862308	605	Cambro-Ordovician sandstone	Cambro-Ordovician sandstone	wide alluvial system, sand-clay
	24	Saki	SAK-PQ-3-MAR	22.018	16.798	608532	1857491	570	Cambro-Ordovician sandstone	Cambro-Ordovician sandstone	wide alluvial system, sand-clay
	25A	Fada 3	FA3	21.591	17.183	562859	1899871	568	Silurian siltstone	Lower Devonian	alluvial system, valley low relief
	25B	Fada 3	Fad-3-PUI	21.591	17.183	562858	1899862	568	Silurian siltstone	Lower Devonian	alluvial system, valley low relief
	26A	Fada palm grove	PFO	21.587	17.187	562444	1900361	575	Silurian siltstone	Lower Devonian	alluvial system, valley low relief
	26B	Fada palm grove	Fada-PAL-MAR	21.587	17.187	562442	1900359	575	Silurian siltstone	Lower Devonian	alluvial system, valley low relief
	27A	Fada military garden	PFP	21.587	17.187	562444	1900361	575	Silurian siltstone	Lower Devonian	alluvial system, valley low relief
	27B	Fada military garden	Fada-PAL-PUI	21.587	17.187	562442	1900359	575	Silurian siltstone	Lower Devonian	alluvial system, valley low relief
	28A	Fada administrative ward	QA-FADA	21.574	17.186	561085	1900234	572	Silurian siltstone	Lower Devonian	alluvial system, valley low relief
	28B	Fada administrative ward	Fada-QA-PUI	21.574	17.186	561081	1900233	572	Silurian siltstone	Lower Devonian	alluvial system, valley low relief
	29A	Fada Ubyan borehole	FL	21.562	17.170	559733	1898417	597	Devonian sandstone	Lower Devonian	alluvial system, valley low relief
	29B	Fada Ubyan borehole	Fada-FL-FOR	21.562	17.170	559725	1898415	597	Devonian sandstone	Lower Devonian	alluvial system, valley low relief

Hydrological unit	ID	Locality	Sample Name	Long	Lat	Xutm	Yutm	Elevation GPS (masl) corrected	Geology (MEH 2015/16)	Geology (Wolff 1964)	Morphology
wadi Sala	30A	Fada Apidel 1	FSU	21.551	17.205	558628	1902286	566	Silurian siltstone	Lower Devonian	alluvial system, valley low relief
	30B	Fada Apidel 1	Fada-API-PUI	21.551	17.205	558629	1902284	566	Silurian siltstone	Lower Devonian	alluvial system, valley low relief
	31A	Fada Apidel 2	FSU-2	21.552	17.207	558686	1902532	563	Silurian siltstone	Lower Devonian	alluvial system, valley low relief
	31B	Fada Apidel 2	Fada-API2-PUI	21.552	17.207	558682	1902527	563	Silurian siltstone	Lower Devonian	alluvial system, valley low relief
	32A	Archei guelta	GAR	21.773	16.903	582346	1868964	571	Cambro-Ordovician sandstone	Lower Devonian	alluvial system, tight valley
	32B	Archei guelta	Guel-Ar-PUI	21.774	16.902	582398	1868913	571	Cambro-Ordovician sandstone	Lower Devonian	alluvial system, tight valley
	33	Archei spring	AR-SP	21.775	16.906	582507	1869300	575	Cambro-Ordovician sandstone	Lower Devonian	rock formation, tight valley
	34A	Deli	DE	21.462	16.838	549213	1861680	560	Cambro-Ordovician sandstone	Cambro-Ordovician sandstone	rock formation, valley low relief
	34B	Deli	DEL-SOU	21.463	16.838	549294	1861702	560	Cambro-Ordovician sandstone	Cambro-Ordovician sandstone	rock formation, valley low relief
	35A	Toukou 1	TUK	21.815	16.757	586895	1852815	551	Cambro-Ordovician sandstone	Cambro-Ordovician sandstone	alluvial system, valley low relief
	35B	Toukou 1	TOUK-1-PUI	21.809	16.756	586244	1852773	551	Cambro-Ordovician sandstone	Cambro-Ordovician sandstone	alluvial system, valley low relief
	36A	Toukou 2	TUK	21.805	16.756	585770	1852688	553	Cambro-Ordovician sandstone	Cambro-Ordovician sandstone	alluvial system, valley low relief
	36B	Toukou 2	TOUK-2-PUI	21.805	16.755	585777	1852676	553	Cambro-Ordovician sandstone	Cambro-Ordovician sandstone	alluvial system, valley low relief
	37	Bir Degaulle	Bir-D-PQ-3-PUI	21.874	16.810	593076	1858779	545	Cambro-Ordovician sandstone	Cambro-Ordovician sandstone	wide alluvial system, sand-clay
	38A	Kochebou	KO	21.609	16.825	564932	1860327	519	Precambrian basement	Cambro-Ordovician sandstone	wide alluvial system, sand-clay
	38B	Kochebou	KOCH-PUI	21.609	16.825	564927	1860329	519	Precambrian basement	Cambro-Ordovician sandstone	wide alluvial system, sand-clay
	39A	Bechike	BECHI	21.382	16.984	540688	1877813	523	Cambro-Ordovician sandstone	Lower Devonian	alluvial system, valley low relief
	39B	Bechike	BACHK--PUI	21.382	16.984	540686	1877814	523	Cambro-Ordovician sandstone	Lower Devonian	alluvial system, valley low relief
	40A	Baki	BAK	21.303	17.023	532284	1882069	494	Cambro-Ordovician sandstone	Cambro-Ordovician sandstone	alluvial system, valley low relief
	40B	Baki	BAK-PUI	21.303	17.023	532281	1882069	494	Cambro-Ordovician sandstone	Cambro-Ordovician sandstone	alluvial system, valley low relief
	41A	Kondor 1	KON-1	21.202	17.137	521451	1894746	478	Cambro-Ordovician sandstone	Cambro-Ordovician sandstone	alluvial system, valley low relief
	41B	Kondor 1	KON-1-PUI	21.202	17.137	521454	1894744	478	Cambro-Ordovician sandstone	Cambro-Ordovician sandstone	alluvial system, valley low relief
	42A	Kondor 2	KON-2	21.111	17.161	511758	1897381	476	Cambro-Ordovician sandstone	Cambro-Ordovician sandstone	alluvial system, valley low relief
	42B	Kondor 2	KON-2-PUI	21.111	17.161	511763	1897380	476	Cambro-Ordovician sandstone	Cambro-Ordovician sandstone	alluvial system, valley low relief
	43A	Ouadi Wei	no. 19	21.021	17.524	502191	1937533	409	Cambro-Ordovician sandstone	Cambro-Ordovician sandstone	rock formation, valley low relief
	43B	Ouadi Wei	Ouadi-W-PUI	21.021	17.524	502193	1937531	409	Cambro-Ordovician sandstone	Cambro-Ordovician sandstone	rock formation, valley low relief
	44	Onoua	Onoua--MAR	20.844	17.780	483467	1965811	380	-	Upper Devonian	rock formation, valley low relief
	45A	Ouadi Widei	no. 18	20.693	17.753	467473	1962861	370	-	Silurian siltstone	alluvial platform, white concretions
	45B	Ouadi Widei	Ouadi-WDS-MAR	20.693	17.753	467484	1962882	386	-	Silurian siltstone	alluvial platform, white concretions
	46	Ouadi Widei Adjouz	Oua-W-AD-PQ 23-MAR	20.664	17.795	464386	1967503	370	-	Lower Devonian	alluvial platform, white concretions
	47A	Bir Koraa	no. 10	20.667	17.922	464732	1981565	378	-	Upper Devonian	low relief morphology, white concretions
	47B	Bir Koraa	BIR-K-PUI	20.667	17.923	464705	1981742	378	-	Upper Devonian	low relief morphology, white concretions
	48	Mouso Libyan borehole	Forage Lybien	20.073	17.993	401837	1989701	390	-	Cambro-Ordovician sandstone	alluvial platform, sand
	49	Mouso well ONHPV	P1 - ONHPV	19.689	17.981	361168	1988596	378	-	Cambro-Ordovician sandstone	alluvial platform, sand
Mourdi	50	Guelta Maya	W966	22.205	17.214	628125	1903646	1149	Devonian sandstone	Upper Devonian	rock formation, valley low relief
	51A	Guelta Maya	W961A	22.187	17.213	626177	1903511	1140	Devonian sandstone	Upper Devonian	rock formation, valley low relief
	51B	Guelta Maya	W961B	22.187	17.213	626177	1903511	1140	Devonian sandstone	Upper Devonian	rock formation, valley low relief
	52	Mourdi Djouna	MRDJ	22.653	17.847	675138	1974057	608	Devonian sandstone	Carboniferous marine	alluvial platform, sand
	53	Eheri	ERI	22.600	17.920	669445	1982030	576	Carboniferous limestone	Carboniferous marine	alluvial platform, sand
	54	Tangalia	TANG	22.454	17.956	653994	1985902	515	Carboniferous limestone	Carboniferous marine	alluvial platform, sand
	55	wadi Tebi	TEB	21.855	17.921	590556	1981605	499	Carboniferous limestone	Carboniferous marine	alluvial platform, sand
	56	Hardjala	ARDJ	21.736	18.263	577842	2019416	497	Nubian sandstone	Carboniferous marine	alluvial platform, sand
	57	Tergueshi	TKI	21.548	18.290	557895	2022357	462	Nubian sandstone	Nubian sandstone	alluvial platform, sand
	58	Gaour	no. 13	21.186	18.356	519680	2029558	451	Nubian sandstone	Nubian sandstone	alluvial platform, sand
	59	Madadi	no. 12	20.777	18.466	476488	2041810	409	Nubian sandstone	Nubian sandstone	rock formation, valley low relief
	60	Ouadi Doum 1	no. 11	20.376	18.418	434136	2036570	338	Nubian sandstone	Carboniferous marine	alluvial platform, white concretions
	61	Ouadi Doum 2	OD - S1	20.430	18.414	439831	2036062	374	Carboniferous limestone	Carboniferous marine	alluvial platform, white concretions

Hydrological unit	ID	Locality	Sample Name	Long	Lat	Xutm	Yutm	Elevation GPS (masl) corrected	Geology (MEH 2015/16)	Geology (Wolff 1964)	Morphology
	62	Bini Herdé	Bini Herdé	19.141	20.037	305537	2216635	622	Nubian sandstone	Nubian sandstone	rock formation, tight valley
	63A	Tekro	no. 17	20.957	19.492	495519	2155224	463	Nubian sandstone	Nubian sandstone	alluvial platform, white concretions
	63B	Tekro	TEK - P1	20.957	19.492	495519	2155224	463	Nubian sandstone	Nubian sandstone	alluvial platform, white concretions
	64	Gouro Manna	GOU-Manna	19.577	19.584	350737	2166036	449	Nubian sandstone	Nubian sandstone	alluvial platform, sand
	65	Gouro Terre Rouge	Terre Rouge	19.590	19.576	352146	2165172	442	Nubian sandstone	Nubian sandstone	alluvial platform, sand
	66	Gouro Guelta du voyageur	GOU - Guelta voyageur	19.590	19.570	352120	2164542	433	Nubian sandstone	Nubian sandstone	alluvial platform, sand
	67	Gouro Hille Tchiluk	GOU - Ille Tchiluk	19.591	19.567	352222	2164164	435	Nubian sandstone	Nubian sandstone	alluvial platform, sand
	68	Gouro Houkoudoubou	GOU - Houkoudoubou	19.595	19.557	352654	2163109	434	Nubian sandstone	Nubian sandstone	alluvial platform, sand
	69	Gouro Kosh	Puits Kosh	19.675	19.489	360925	2155439	426	Nubian sandstone	Nubian sandstone	alluvial platform, white concretions
	70	Ounianga Kebir Yoa - Hoy 1	OUA - HOY S1	20.512	19.068	448627	2108467	390	Nubian sandstone	Nubian sandstone	low relief morphology, white concretions
	71	Ounianga Kebir - Lokore	OUA - LOK - P1	20.492	19.061	446500	2107688	410	Nubian sandstone	Nubian sandstone	low relief morphology, white concretions
	72	Ounianga Kebir Yoa - Ruliu	OUA - RUL S3	20.496	19.059	446993	2107443	388	Nubian sandstone	Nubian sandstone	low relief morphology, white concretions
	73	Ounianga Kebir - Djedjibre	OUA - P3	20.491	19.055	446476	2106946	410	Nubian sandstone	Nubian sandstone	low relief morphology, white concretions
	74	Ounianga Kebir Yoa S1	OUA - S1	20.493	19.050	446633	2106437	386	Nubian sandstone	Nubian sandstone	low relief morphology, white concretions
	75	Ounianga Kebir Yoa	OUA - L1	20.493	19.050	446633	2106426	386	Nubian sandstone	Nubian sandstone	low relief morphology, white concretions
	76	Ounianga Kebir - Ibechi	OUA - P2	20.503	19.042	447693	2105593	424	Nubian sandstone	Nubian sandstone	low relief morphology, white concretions
	77	Ounianga Kebir Ahmad	OUA - P1	20.512	19.009	448630	2101906	379	Nubian sandstone	Nubian sandstone	low relief morphology, white concretions
	78A	Ounianga Kebir Ahmad	OUA - L2	20.513	19.011	448778	2102160	374	Nubian sandstone	Nubian sandstone	low relief morphology, white concretions
	78B	Ounianga Kebir Ahmad	no. 16	20.516	19.010	449106	2102029	379	Nubian sandstone	Nubian sandstone	low relief morphology, white concretions
	79	Ounianga Kebir Akhdar	OUA - L3	20.517	19.010	449114	2102026	376	Nubian sandstone	Nubian sandstone	low relief morphology, white concretions
	80	Ounianga Kebir Akhdar	OUA - S2	20.516	19.010	449104	2102015	376	Nubian sandstone	Nubian sandstone	low relief morphology, white concretions
	81	Ounianga Kebir Katam 1	OUA - L4	20.536	19.008	451187	2101821	381	Nubian sandstone	Nubian sandstone	low relief morphology, white concretions
	82	Ounianga Serir Edem 1	OUS - L1	20.859	18.931	485112	2093177	348	Nubian sandstone	Nubian sandstone	low relief morphology, white concretions
	83	Ounianga Serir Edem 2	OUS - L2	20.853	18.934	484533	2093553	351	Nubian sandstone	Nubian sandstone	low relief morphology, white concretions
Ounianga	84	Ounianga Serir	no. 14	20.911	18.915	490669	2091468	360	Nubian sandstone	Nubian sandstone	low relief morphology, white concretions
	85	Ounianga Serir - Eghi	OUS - S1	20.873	18.919	486669	2091870	364	Nubian sandstone	Nubian sandstone	low relief morphology, white concretions
	86	Ounianga Serir - Eghi	OUS - L3	20.873	18.919	486669	2091870	350	Nubian sandstone	Nubian sandstone	low relief morphology, white concretions
	87	Ounianga Serir	no. 15	20.880	18.916	487405	2091583	359	Nubian sandstone	Nubian sandstone	low relief morphology, white concretions
	88	Ounianga Serir - Coop. Suisse	OUS - P1	20.860	18.916	485237	2091539	351	Nubian sandstone	Nubian sandstone	low relief morphology, white concretions
	89	Ounianga Serir Motoro	Motoro Lac 1	20.704	18.933	468701	2093396	380	Nubian sandstone	Nubian sandstone	low relief morphology, white concretions
		Ounianga Kebir - no coordinates									
	90	Yoa well	Y-Well	unknown	unknown			unknown	Nubian sandstone	Nubian sandstone	low relief morphology, white concretions
	91	Yoa	Y1	unknown	unknown			unknown	Nubian sandstone	Nubian sandstone	low relief morphology, white concretions
	92	Yoa spring	Y2	unknown	unknown			unknown	Nubian sandstone	Nubian sandstone	low relief morphology, white concretions
	93	Yoa spring	Y3	unknown	unknown			unknown	Nubian sandstone	Nubian sandstone	low relief morphology, white concretions
	94	Forodone (north)	H1	unknown	unknown			unknown	Nubian sandstone	Nubian sandstone	low relief morphology, white concretions
	95	Forodone (south)	H2	unknown	unknown			unknown	Nubian sandstone	Nubian sandstone	low relief morphology, white concretions
	96	Mijoi	M1	unknown	unknown			unknown	Nubian sandstone	Nubian sandstone	low relief morphology, white concretions
	97	Oma (east)	U1	unknown	unknown			unknown	Nubian sandstone	Nubian sandstone	low relief morphology, white concretions
	98	Oma (east)	U1b	unknown	unknown			unknown	Nubian sandstone	Nubian sandstone	low relief morphology, white concretions
	99	Oma (west)	U2	unknown	unknown			unknown	Nubian sandstone	Nubian sandstone	low relief morphology, white concretions
	100	Oma spring	US1	unknown	unknown			unknown	Nubian sandstone	Nubian sandstone	low relief morphology, white concretions
		Motoro - no coordinates									
	101	Motoro	Moltrow	unknown	unknown			unknown	Nubian sandstone	Nubian sandstone	low relief morphology, white concretions
		Ounianga Serir - no coordinates									
	102	Teli	WPS1	unknown	unknown			unknown	Nubian sandstone	Nubian sandstone	low relief morphology, white concretions
	103	Teli spring	WPS2	unknown	unknown			unknown	Nubian sandstone	Nubian sandstone	low relief morphology, white concretions
	104	Edim	Edim	unknown	unknown			unknown	Nubian sandstone	Nubian sandstone	low relief morphology, white concretions
	105	Bokou	Bokou	unknown	unknown			unknown	Nubian sandstone	Nubian sandstone	low relief morphology, white concretions

Hydrological unit	ID	Locality	Sample Name	Long	Lat	Xutm	Yutm	Elevation GPS (masl) corrected	Geology (MEH 2015/16)	Geology (Wollf 1964)	Morphology
	106	Bembéché Oye Yeska	OYE YESKA	19.576	18.574	349682	2054321	355	Devonian sandstone	Upper Devonian	alluvial platform, white concretions
	107	Kouroudi Bili Choui	Puits Bili Choui	18.804	18.920	268674	2093414	337	Devonian sandstone	Lower Devonian	alluvial system, valley low relief
	108	Kouroudi Gali	Mare Kouroudi Gali	18.804	18.911	268724	2092362	333	Silurian siltstone	Lower Devonian	alluvial platform, white concretions
	109	Kouroudi camp	Puits Kouroudi camp	18.842	18.907	272724	2091958	333	Devonian sandstone	Lower Devonian	low relief morphology, white concretions
	110	Hichilime	Puits Hichilime	18.920	18.832	280813	2083568	323	Devonian sandstone	Lower Devonian	low relief morphology, white concretions
	111	Forom	Puits Forom 2	18.976	18.606	286464	2058470	312	Devonian sandstone	Lower Devonian	low relief morphology, white concretions
	112	Yarda	Puits Yarda 1	18.982	18.542	287038	2051323	305	Devonian sandstone	Lower Devonian	low relief morphology, white concretions
	113	Yarda school	Puits Yarda 2	19.002	18.511	289112	2047868	311	Devonian sandstone	Lower Devonian	low relief morphology, white concretions
	114	Elleboye	FM Elleboy	18.529	18.138	238563	2007232	245	Silurian siltstone	Lower Devonian	alluvial platform, white concretions
	115	Kirdimi Boubou	Forage Boubou	18.513	18.141	236820	2007566	256	Silurian siltstone	Lower Devonian	alluvial platform, white concretions
	116	Kirdimi Gali	Source Gali	18.507	18.136	236241	2006998	251	Silurian siltstone	Lower Devonian	alluvial platform, white concretions
	117	Ngourma	Puits Gourouma	18.586	18.093	244467	2002093	242	Silurian siltstone	Lower Devonian	alluvial platform, white concretions
	118	Yen well	Puits Yen 1	18.474	18.098	232690	2002893	256	Silurian siltstone	Cenozoic Lake Chad	alluvial platform, white concretions
	119	Yenspring	Source Yen 2	18.474	18.098	232637	2002861	246	Silurian siltstone	Cenozoic Lake Chad	alluvial platform, white concretions
	120	Ain Galaka	Ain Galaka	18.440	18.067	229042	1999499	230	Silurian siltstone	Cenozoic Lake Chad	alluvial platform, white concretions
	121	Elleboye Hachien	Puits Hachien	18.637	18.028	249776	1994904	232	Devonian sandstone	Lower Devonian	alluvial platform, white concretions
Southern Tibesti	122	Kirdimi 1	FM Kirdimi	18.919	17.971	279593	1988235	251	-	Lower Devonian	alluvial platform, white concretions
	123	Faya Dozanga borehole	Dozanga 2 For	19.122	17.951	301148	1985758	250	-	Quaternary lake sediments	alluvial platform, clay
	124	Faya Dozanga well	Dozanga 1 Puits	19.119	17.948	300796	1985441	254	-	Quaternary lake sediments	alluvial platform, clay
	125	Faya 2	43	19.114	17.941	300268	1984649	266	-	Quaternary lake sediments	alluvial platform, clay
	126	Faya Torchenga borehole	Torchenga 1 Forage	19.111	17.940	299939	1984575	250	-	Quaternary lake sediments	alluvial platform, clay
	127	Faya Torchenga well	Torchenga 2 Puits	19.111	17.940	299918	1984575	248	-	Quaternary lake sediments	alluvial platform, clay
	128A	Faya Houchma base PNSA	Puits Base Faya	19.097	17.926	298440	1983040	235	-	Quaternary lake sediments	alluvial platform, clay
	128B	Faya Houchma base PNSA	44	19.097	17.926	298440	1983040	248	-	Quaternary lake sediments	alluvial platform, clay
	129	Faya Ribouguidina PNSA Iriboudiaga	Forage Iriboudiaga	19.098	17.924	298554	1982774	236	-	Quaternary lake sediments	alluvial platform, clay
	130	Faya 1	42	19.094	17.917	298090	1982004	247	-	Quaternary lake sediments	alluvial platform, clay
	131	Faya F2bis	Forage F2 Faya	19.087	17.918	297350	1982188	223	-	Quaternary lake sediments	alluvial platform, clay
	132	Faya Tchagssous	Forage Tchadgssous	19.095	17.904	298203	1980574	227	-	Quaternary lake sediments	alluvial platform, clay
	133	Faya F4	Forage F4 Faya	19.079	17.907	296511	1980957	225	-	Quaternary lake sediments	alluvial platform, clay
	134	Kourkour Koukourou	Puits Koukourou	19.074	17.909	295973	1981195	226	-	Quaternary lake sediments	alluvial platform, clay
	135	Djidi PNSA Amoul	Forage PNSA Amoul	19.061	17.901	294618	1980301	224	-	Quaternary lake sediments	alluvial platform, white concretions
	136	Mordangaye PNSA	Forage PNSA Martagaye	19.020	17.891	290240	1979218	221	-	Cenozoic Lake Chad	alluvial platform, clay
	137	Amoul PNSA Amouli	Forage PNSA Amouli	18.985	17.883	286511	1978395	222	-	Cenozoic Lake Chad	alluvial platform, clay
	138	Yegueski Nasara	Puits Nasara	19.523	17.426	343171	1927310	262	-	Quaternary lake sediments	alluvial platform, sand
	139A	Erg Djourab axis Kouba	P-Axe Kouba	19.052	17.465	293102	1932075	228	-	Cenozoic Lake Chad	alluvial platform, sand
	139B	Erg Djourab axis Kouba	PNSA_Kouba	19.052	17.465	293102	1932075	226	-	Cenozoic Lake Chad	alluvial platform, sand
Lake Chad basin	140	Erg du Djourab puits 110	Puits_110	19.040	17.232	291607	1906288	198	-	Quaternary lake sediments	alluvial platform, white concretions
	141	Kouba 1	45	18.351	15.808	216202	1749498	264	-	-	alluvial platform, sand
	142	Kouba Olanga	P-Kouba	18.328	15.789	213720	1747381	249	-	-	alluvial platform, sand
	143	Kouba 2	46	18.297	15.749	210373	1743072	263	-	-	alluvial platform, sand
	144	Domou	7	16.5925	20.4667	39982	39982	819	Cambro-Ordovician sandstone	Cambro-Ordovician sandstone	wide alluvial system, sandy
	145	zouar 5	5	16.5600	20.4725	36602	36602	786	Cambro-Ordovician sandstone	Cambro-Ordovician sandstone	wide alluvial system, sand-clay
	146	zouar 4	4	16.5370	20.4689	34187	34187	781	Cambro-Ordovician sandstone	Cambro-Ordovician sandstone	wide alluvial system, sandy
	147A	zouar 1	1	16.5358	20.4575	34027	34027	786	Cambro-Ordovician sandstone	Cambro-Ordovician sandstone	wide alluvial system, sandy
	147B	zouar 6	6	16.5358	20.4575	34027	34027	782	Cambro-Ordovician sandstone	Cambro-Ordovician sandstone	wide alluvial system, sandy
Zouar	148	zouar 3	3	16.5164	20.4636	32017	32017	779	Cambro-Ordovician sandstone	Cambro-Ordovician sandstone	wide alluvial system, sandy
erneri Zouarké	149	zouar 2	2	16.5136	20.4453	31669	31669	761	Cambro-Ordovician sandstone	Cambro-Ordovician sandstone	wide alluvial system, sandy
	150	Kougou	9	16.4497	20.4519	25008	25008	745	Cambro-Ordovician sandstone	Cambro-Ordovician sandstone	alluvial system, tight valley
	151	Armogo2	10	16.4581	20.4133	25768	25768	754	Cambro-Ordovician sandstone	Cambro-Ordovician sandstone	wide alluvial system, sandy
	152	Armogo	8	16.4464	20.4242	24578	24578	745	Cambro-Ordovician sandstone	Cambro-Ordovician sandstone	wide alluvial system, sandy
	153	Yigue-yeski	11	16.3253	20.4217	11905	11905	696	Cambro-Ordovician sandstone	Cambro-Ordovician sandstone	wide alluvial system, sandy
	154	Zouarké1	12	16.2308	20.4219	2022	2022	690	Cambro-Ordovician sandstone	Precambrian metasediments	wide alluvial system, sandy

Hydrological unit	ID	Locality	Sample Name	Long	Lat	Xutm	Yutm	Elevation GPS (masl) corrected	Geology (MEH 2015/16)	Geology (Wollf 1964)	Morphology
enneri Misky	155	Bini Erde Misky 2	Forage Misky 2	18.0624	20.1926	192984	192984	835	Mesozoic sandstone	Mesozoic sandstone	wide alluvial system, sandy
	156A	Bini Erde Misky 1	Puits Misky 1	18.0522	20.1798	191892	191892	825	Mesozoic sandstone	Mesozoic sandstone	alluvial system, valley low relief
	156B	Miski1	40	18.0522	20.1798	191889	191889	839	Mesozoic sandstone	Mesozoic sandstone	alluvial system, valley low relief
	157	Enneri Misky Bichira	Puits Bichira	17.9319	19.9776	178897	178897	738	-	Precambrian metasediments	alluvial system, valley
	158A	Enneri Misky Oloni	Puits Oloni	17.9877	19.8901	184567	184567	717	-	Cambro-Ordovician sandstone	alluvial system, tight valley
	158B	Miski2	41	17.9877	19.8901	184568	184568	723	-	Cambro-Ordovician sandstone	alluvial system, tight valley
Bardaï enneri Zoumri	159	Zoumri4	16	17.4731	21.1933	133756	133756	1276	volcanic serie Tibesti	Andésite (labradorite) - mid black serie	alluvial system, tight valley
	160	Zoumri3	15	17.4718	21.1933	133620	133620	1276	volcanic serie Tibesti	Andésite (labradorite) - mid black serie	alluvial system, tight valley
	161	Zoumri2	14	17.4647	21.2006	132901	132901	1275	volcanic serie Tibesti	Basalte (olivine) - lower black serie	alluvial system, tight valley
	162	Zoumri1	13	17.4619	21.2050	132620	132620	1271	volcanic serie Tibesti	Basalte (olivine) - lower black serie	alluvial system, tight valley
	163	Ouaychi	17	17.4211	21.1789	128314	128314	1302	volcanic serie Tibesti	Ignimbrite (rhyolite) - upper white serie	alluvial system, tight valley
	164	Odissi	18	17.3872	21.1833	124801	124801	1294	volcanic serie Tibesti	Andésite (labradorite) - mid black serie	alluvial system, tight valley
	165	Osouni	19	17.1756	21.3236	103180	103180	1110	Paleozoic sandstone - Bardaï fm.	Mesozoic sandstone	wide alluvial system, sandy
	166	Zoui2	20	17.0706	21.3250	92276	92276	1063	Paleozoic sandstone - Bardaï fm.	Mesozoic sandstone	alluvial system, valley low relief
	167	Bardai1	21	17.0208	21.3356	87132	87132	1033	Paleozoic sandstone - Bardaï fm.	Mesozoic sandstone	alluvial system, valley low relief
	168	Bardai2	22	17.0181	21.3308	86838	86838	1039	Paleozoic sandstone - Bardaï fm.	Mesozoic sandstone	alluvial system, valley low relief
	169	Bardai3	23	17.0022	21.3492	85239	85239	1022	Paleozoic sandstone - Bardaï fm.	Mesozoic sandstone	alluvial system, valley low relief
	170	Bardai5	25	17.0017	21.3517	85198	85198	1022	Paleozoic sandstone - Bardaï fm.	Mesozoic sandstone	alluvial system, valley low relief
	171	Bardai4	24	17.0000	21.3606	85042	85042	1027	Paleozoic sandstone - Bardaï fm.	Basalte (olivine) - plateau black serie	alluvial system, valley low relief
	172	Zougoura1	26	17.0161	21.4208	86884	86884	1044	Paleozoic sandstone - Bardaï fm.	Mesozoic sandstone	wide alluvial system, sandy
Aouzou enneri Yebbigué	173	Yeboubou2	38	18.0917	20.9267	197499	197499	1395	volcanic serie Tibesti	Basalte (olivine) - valley black serie	alluvial system, tight valley
	174	Yeboubou1	37	18.0831	20.9481	196647	196647	1384	volcanic serie Tibesti	Basalte (olivine) - valley black serie	alluvial system, tight valley
	175	yebbisouma	36	17.9556	21.1042	183708	183708	1183	volcanic serie Tibesti	Basalte (olivine) - lower black serie	alluvial system, tight valley
	176	Kilengue	35	17.9212	21.1946	180326	180326	1111	volcanic serie Tibesti	Rhyolite - lower white serie	alluvial system, valley low relief
	177	Oumou2	34	18.0689	21.5022	196307	196307	1085	Cambro-Ordovician sandstone	Mesozoic sandstone	wide alluvial system, grey clay
	178	Oumou1	33	18.0531	21.5067	194679	194679	1074	Cambro-Ordovician sandstone	Mesozoic sandstone	wide alluvial system, grey clay
	179	Aouzou6	32	17.4322	21.8133	131075	131075	929	Paleozoic sandstone - Bardaï fm.	Mesozoic sandstone	alluvial system, tight valley
	180	Aouzou5	31	17.4336	21.8164	131228	131228	927	Paleozoic sandstone - Bardaï fm.	Mesozoic sandstone	alluvial system, tight valley
	181	Aouzou2	28	17.4250	21.8167	130338	130338	914	Paleozoic sandstone - Bardaï fm.	Mesozoic sandstone	alluvial system, tight valley
	182	Aouzou4	30	17.4306	21.8194	130925	130925	919	Paleozoic sandstone - Bardaï fm.	Mesozoic sandstone	alluvial system, tight valley
	183	Aouzou3	29	17.4283	21.8197	130688	130688	918	Paleozoic sandstone - Bardaï fm.	Mesozoic sandstone	alluvial system, tight valley
	184	Aouzou1	27	17.4351	21.8673	131514	131514	892	Paleozoic sandstone - Bardaï fm.	Mesozoic sandstone	alluvial system, tight valley

Hydrological unit	ID	Locality	Sample Name	Vegetation	Water Point Type	Depth Water Point (m bgl)	Sampling campaign	Date of measure	Water table (m bgl)	Elevation water table (m asl)	Std. Dev. Hydr. Heads
Nile hydrological basin	1A	Bao	no. 4	sparse vegetation	improved well	19.8	Ennedi-Ounianga 2013	28.07.2013	14.4	890	0.3
	1B	Bao	BAO-PUI	sparse vegetation	improved well	19.8	Ennedi 2016	06.12.2016	13.8	890	
	2A	Oho	no. 6	sparse vegetation	improved well	27.2	Ennedi-Ounianga 2013	28.07.2013	25.9	847	0.3
	2B	Oho	OHO-PUI	sparse vegetation	improved well	27.2	Ennedi 2016	06.12.2016	26.4	847	
	3A	Moutougouni	no. 7	sparse vegetation	improved well	unknown	Ennedi-Ounianga 2013	28.07.2013	22.0	838	1.0
	3B	Moutougouni	MOUT-PUI	sparse vegetation	improved well	unknown	Ennedi 2016	06.12.2016	23.9	836	
	4	Amdjarass borehole	no. 3	sparse vegetation	borehole	unknown	Ennedi-Ounianga 2013	27.07.2013	unknown	unknown	
	5	Amdjarass well	AMDJ-PUI	dense vegetation	improved well	unknown	Ennedi 2016	05.12.2016	13.2	912	
	6A	Berdoba	no. 9	sparse vegetation	improved well	30.6	Ennedi-Ounianga 2013	29.07.2013	29.4	833	0.9
	6B	Berdoba	BERD-PUI	sparse vegetation	improved well	30.6	Ennedi 2016	05.12.2016	27.6	834	
	7	Bahai Kariari	Kariari	dense vegetation	lake - surface water	0.0	Grès de Nubie 2014	18.01.2014	0.0	778	
	8	Bahai well	BAHAI	dense vegetation	traditional well	8.0	Grès de Nubie 2014	18.01.2014	6.1	792	
wadi Haouach	9	Kaoura borehole	Kaoura forage	sparse vegetation	borehole	unknown	Grès de Nubie 2014	19.01.2014	7.1	837	
	10A	Kaoura well	Kaoura puits	sparse vegetation	improved well	unknown	Grès de Nubie 2014	19.01.2014	5.9	838	1.5
	10B	Kaoura well	KAOU-PUI	sparse vegetation	improved well	unknown	Ennedi 2016	04.12.2016	3.0	841	
	11A	Itou	ITOU	sparse vegetation	improved well	unknown	Grès de Nubie 2014	19.01.2014	16.6	761	1.7
	11B	Itou	ITOU-PUI	sparse vegetation	improved well	unknown	Ennedi 2016	04.12.2016	13.2	765	
wadi Sala	12A	Bachiquele	BACH	dense vegetation	spring	0.0	Ennedi 2013	13.02.2013	0.0	740	0.0
	12B	Bachiquele	BACH-MAR	dense vegetation	pond - surface water	0.0	Ennedi 2016	04.12.2016	0.0	740	
	13A	Monou	MO-1	sparse vegetation	improved well	16.4	Ennedi 2013	12.02.2013	13.9	689	1.6
	13B	Monou	MONO-PUI	sparse vegetation	improved well	16.4	Ennedi 2016	04.12.2016	17.1	686	
	14A	Sania	SA-1	sparse vegetation	traditional well	13.4	Ennedi 2013	12.02.2013	13.2	658	0.3
	14B	Sania	SANI-PUI	sparse vegetation	improved well	13.4	Ennedi 2016	04.12.2016	12.6	658	
	15A	Chiguila	CHI-1	sparse vegetation	improved well	12.3	Ennedi 2013	13.02.2013	11.8	704	1.3
	15B	Chiguila	CHIG-PUI	sparse vegetation	improved well	12.3	Ennedi 2016	04.12.2016	9.2	707	
	16A	Alliba	ALIBA	dense vegetation	spring	0.0	Ennedi 2013	13.02.2013	0.0	670	0.0
	16B	Alliba	ALLI-SOU	dense vegetation	spring	0.0	Ennedi 2016	03.12.2016	0.0	670	
	17	Chibi 1	CHIBI-1	sparse vegetation	improved well	18.3	Ennedi 2013	13.02.2013	15.0	647	
	18A	Chibi 2	CHIBI-2	sparse vegetation	improved well	12.5	Ennedi 2013	13.02.2013	11.2	651	1.4
	18B	Chibi 2	CHIB-PUI	sparse vegetation	improved well	12.5	Ennedi 2016	03.12.2016	8.4	654	
	19	Terkei	TKD	sparse vegetation	pond - surface water	0.0	Ennedi 2013	15.02.2013	0.0	624	
	20	Weiba 1	NOH-1	dense vegetation	improved well	8.9	Ennedi 2013	15.02.2013	8.1	577	
	21	Weiba 2	NOH-2	dense vegetation	improved well	11.4	Ennedi 2013	15.02.2013	11.1	573	
	22	Weiba	WEIBA--PUI	dense vegetation	traditional well	unknown	Ennedi 2016	03.12.2016	6.6	573	
	23	Weiba 3	NOH-3	dense vegetation	borehole	unknown	Ennedi 2013	15.02.2013	unknown	unknown	
	24	Saki	SAK-PO-3-MAR	dense vegetation	pond - surface water	0.0	Ennedi 2016	03.12.2016	0.0	570	
	25A	Fada 3	FA3	dense vegetation	improved well	6.3	Ennedi 2013	17.02.2013	5.1	563	0.4
	25B	Fada 3	Fad-3-PUI	dense vegetation	improved well	6.3	Ennedi 2016	29.11.2016	4.3	564	
	26A	Fada palm grove	PFO	dense vegetation	pond - surface water	0.0	Ennedi 2013	17.02.2013	0.0	575	0.0
	26B	Fada palm grove	Fada-PAL-MAR	dense vegetation	pond - surface water	0.0	Ennedi 2016	01.12.2016	0.0	575	
	27A	Fada military garden	PFP	dense vegetation	traditional well	3.6	Ennedi 2013	17.02.2013	1.1	574	0.1
	27B	Fada military garden	Fada-PAL-PUI	dense vegetation	traditional well	3.6	Ennedi 2016	29.11.2016	1.0	574	
	28A	Fada administrative ward	QA-FADA	dense vegetation	improved well	12.4	Ennedi 2013	17.02.2013	8.8	563	0.4
	28B	Fada administrative ward	Fada-QA-PUI	dense vegetation	improved well	12.4	Ennedi 2016	27.11.2016	8.0	564	
	29A	Fada Libyan borehole	FL	dense vegetation	borehole	39.0	Ennedi 2013	17.02.2013	20.9	576	0.2
	29B	Fada Libyan borehole	Fada-FL-FOR	dense vegetation	borehole	39.0	Ennedi 2016	29.11.2016	20.5	576	

Hydrological unit	ID	Locality	Sample Name	Vegetation	Water Point Type	Depth Water Point (m bgl)	Sampling campaign	Date of measure	Water table (m bgl)	Elevation water table (m asl)	Std. Dev. Hydr. Heads
wadi Sala	30A	Fada Apidel 1	FSU	dense vegetation	improved well	9.5	Ennedi 2013	17.02.2013	8.1	558	0.2
	30B	Fada Apidel 1	Fada-API-PUI	dense vegetation	improved well	9.5	Ennedi 2016	27.11.2016	7.6	558	
	31A	Fada Apidel 2	FSU-2	dense vegetation	improved well	12.1	Ennedi 2013	17.02.2013	7.6	555	0.8
	31B	Fada Apidel 2	Fada-API2-PUI	dense vegetation	improved well	12.1	Ennedi 2016	29.11.2016	6.1	557	
	32A	Archei guelta	GAR	sparse vegetation	spring	0.0	Ennedi 2013	14.02.2013	0.0	571	0.5
	32B	Archei guelta	Guel-Ar-PUI	sparse vegetation	traditional well	0.0	Ennedi 2016	02.12.2016	1.0	570	
	33	Archei spring	AR-SP	dense vegetation	spring	0.0	Ennedi 2013	14.02.2013	0.0	575	
	34A	Deli	DE	dry	spring	0.0	Ennedi 2013	15.02.2013	0.0	560	0.0
	34B	Deli	DEL-SOU	dry	spring	0.0	Ennedi 2016	02.12.2016	0.0	560	
	35A	Toukou 1	TUK	sparse vegetation	improved well	6.0	Ennedi 2013	15.02.2013	4.4	547	0.8
	35B	Toukou 1	TOUK-1-PUI	sparse vegetation	improved well	6.0	Ennedi 2016	02.12.2016	2.7	548	
	36A	Toukou 2	TUK	sparse vegetation	improved well	27.8	Ennedi 2013	15.02.2013	20.9	532	1.5
	36B	Toukou 2	TOUK-2-PUI	sparse vegetation	improved well	27.8	Ennedi 2016	02.12.2016	17.9	535	
	37	Bir Degaulle	Bir-D-PQ-3-PUI	dense vegetation	improved well	unknown	Ennedi 2016	03.12.2016	11.5	534	
	38A	Kochebou	KO	dry, white concretions	improved well	29.5	Ennedi 2013	15.02.2013	21.8	497	0.2
	38B	Kochebou	KOCH-PUI	dry, white concretions	improved well	29.5	Ennedi 2016	02.12.2016	22.3	497	
	39A	Bechike	BECHI	sparse vegetation	improved well	33.2	Ennedi 2013	23.02.2013	28.9	494	1.3
	39B	Bechike	BACHK--PUI	sparse vegetation	improved well	33.2	Ennedi 2016	02.12.2016	26.2	497	
	40A	Baki	BAK	sparse vegetation	improved well	35.6	Ennedi 2013	23.02.2013	28.9	465	0.5
	40B	Baki	BAK-PUI	sparse vegetation	improved well	35.6	Ennedi 2016	02.12.2016	29.9	464	
	41A	Kondor 1	KON-1	dry	improved well	32.2	Ennedi 2013	23.02.2013	31.7	446	2.2
	41B	Kondor 1	KON-1-PUI	dry	improved well	32.2	Ennedi 2016	01.12.2016	27.3	451	
	42A	Kondor 2	KON-2	dry	improved well	39.3	Ennedi 2013	23.02.2013	37.0	439	0.4
	42B	Kondor 2	KON-2-PUI	dry	improved well	39.3	Ennedi 2016	01.12.2016	36.2	440	
	43A	Ouadi Wei	no. 19	d	improved well	4.3	Ennedi-Ounianga 2013	02.08.2013	2.1	407	1.3
	43B	Ouadi Wei	Ouadi-W-PUI	dense vegetation	improved well	4.3	Ennedi 2016	01.12.2016	4.7	404	
	44	Onoua	Onoua--MAR	dense vegetation	pond - surface water	0.0	Ennedi 2016	30.11.2016	0.0	380	
	45A	Ouadi Widei	no. 18	dense vegetation	pond - surface water	0.0	Ennedi-Ounianga 2013	02.08.2013	0.0	370	0.0
	45B	Ouadi Widei	Ouadi-WDS-MAR	dense vegetation	pond - surface water	0.0	Ennedi 2016	30.11.2016	0.0	386	
	46	Ouadi Widei Adjouz	Oua-W-AD-PQ 23-MAR	dense vegetation	pond - surface water	0.0	Ennedi 2016	27.11.2016	0.0	370	
	47A	Bir Koraa	no. 10	sparse vegetation	traditional well	0.5	Ennedi-Ounianga 2013	30.07.2013	1.2	377	0.3
	47B	Bir Koraa	BIR-K-PUI	sparse vegetation	traditional well	0.5	Ennedi 2016	28.11.2016	0.6	377	
	48	Mouso Libyan borehole	Forage Lybien	dry	borehole	65.0	Grès de Nubie 2014	01.02.2014	24.5	366	
	49	Mouso well ONHPV	P1 - ONHPV	dry	improved well	14.9	Grès de Nubie 2014	01.02.2014	13.2	365	
Mourdi	50	Guelta Maya	W966	dense vegetation	guelta - surface water	0.0	Maya Ennedi 2016	2016	0.0	1149	
	51A	Guelta Maya	W961A	dense vegetation	guelta - surface water	0.0	Maya Ennedi 2016	2016	0.0	1140	
	51B	Guelta Maya	W961B	dense vegetation	guelta - surface water	0.0	Maya Ennedi 2016	2016	0.0	1140	
	52	Mourdi Djouna	MRDJ	sparse vegetation	improved well	5.7	Ennedi 2013	21.02.2013	5.0	603	
	53	Eheri	ERI	sparse vegetation	improved well	6.1	Ennedi 2013	21.02.2013	6.1	570	
	54	Tangalia	TANG	dry	improved well	9.2	Ennedi 2013	21.02.2013	8.7	506	
	55	wadi Tebi	TEB	sparse vegetation	traditional well	4.4	Ennedi 2013	21.02.2013	4.3	495	
	56	Hardjala	ARDJ	dry	improved well	6.3	Ennedi 2013	20.02.2013	4.2	493	
	57	Terguesht	TKI	dry	traditional well	0.0	Ennedi 2013	20.02.2013	1.2	461	
	58	Gaour	no. 13	dry	improved well	8.2	Ennedi-Ounianga 2013	30.07.2013	6.3	445	
	59	Madadi	no. 12	dense vegetation	spring	0.0	Ennedi-Ounianga 2013	30.07.2013	0.0	409	
	60	Ouadi Doum 1	no. 11	dry	spring	0.0	Ennedi-Ounianga 2013	30.07.2013	0.0	338	
	61	Ouadi Doum 2	OD - 51	dry	spring	0.6	Grès de Nubie 2014	31.01.2014	0.0	374	

Hydrological unit	ID	Locality	Sample Name	Vegetation	Water Point Type	Depth Water Point (m bgl)	Sampling campaign	Date of measure	Water table (m bgl)	Elevation water table (m asl)	Std. Dev. Hydr. Heads
	62	Bini Herdé	Bini Herdé	dry	traditional well	11.9	Grès de Nubie 2014	26.01.2014	11.8	610	
	63A	Tekro	no. 17	sparse vegetation	traditional well	3.2	Ennedi-Ounianga 2013	01.08.2013	2.4	461	0.0
	63B	Tekro	TEK - P1	sparse vegetation	traditional well	2.4	Grès de Nubie 2014	29.01.2014	2.3	461	
	64	Gouro Manna	GOU-Manna	dense vegetation	traditional well	11.6	Grès de Nubie 2014	25.01.2014	11.4	438	
	65	Gouro Terre Rouge	Terre Rouge	dense vegetation	traditional well	5.3	Grès de Nubie 2014	25.01.2014	4.9	437	
	66	Gouro Guelta du voyageur	GOU - Guelta voyageur	dense vegetation	traditional well	7.2	Grès de Nubie 2014	25.01.2014	0.0	433	
	67	Gouro Hille Tchiluk	GOU - Ille Tchiluk	dense vegetation	traditional well	3.3	Grès de Nubie 2014	25.01.2014	3.2	432	
	68	Gouro Houkoudoubou	GOU - Houkoudoubou	dense vegetation	spring	0.0	Grès de Nubie 2014	25.01.2014	0.0	434	
	69	Gouro Kosh	Puits Kosh	sparse vegetation	traditional well	3.8	Grès de Nubie 2014	27.01.2014	2.4	424	
	70	Ounianga Kebir Yoa - Hoy 1	OUA - HOY S1	dense vegetation	spring - lake	0.0	Grès de Nubie 2014	31.01.2014	0.0	390	
	71	Ounianga Kebir - Lokore	OUA - LOK - P1	dense vegetation	traditional well	16.5	Grès de Nubie 2014	31.01.2014	16.2	394	
	72	Ounianga Kebir Yoa - Rullu	OUA - RUL S3	dense vegetation	spring - lake	0.0	Grès de Nubie 2014	31.01.2014	0.0	388	
	73	Ounianga Kebir - Djedjibre	OUA - P3	dense vegetation	traditional well	10.5	Grès de Nubie 2014	28.01.2014	9.9	400	
	74	Ounianga Kebir Yoa S1	OUA - S1	dense vegetation	spring - lake	0.0	Grès de Nubie 2014	28.01.2014	0.0	386	
	75	Ounianga Kebir Yoa	OUA - L1	dense vegetation	spring - lake	0.0	Grès de Nubie 2014	28.01.2014	0.0	386	
	76	Ounianga Kebir - Ibechi	OUA - P2	dense vegetation	traditional well	28.7	Grès de Nubie 2014	28.01.2014	28.4	396	
	77	Ounianga Kebir Ahmad	OUA - P1	dense vegetation	traditional well	2.7	Grès de Nubie 2014	28.01.2014	2.1	377	
	78A	Ounianga Kebir Ahmad	OUA - L2	dense vegetation	lake - surface water	0.0	Grès de Nubie 2014	28.01.2014	0.0	374	0.0
	78B	Ounianga Kebir Ahmad	no. 16	dense vegetation	lake - surface water	0.0	Ennedi-Ounianga 2013	01.08.2013	0.0	379	
	79	Ounianga Kebir Akhdar	OUA - L3	dense vegetation	lake - surface water	0.0	Grès de Nubie 2014	28.01.2014	0.0	376	
	80	Ounianga Kebir Akhdar	OUA - S2	dense vegetation	spring - lake	0.0	Grès de Nubie 2014	28.01.2014	0.0	376	
	81	Ounianga Kebir Katam 1	OUA - L4	dense vegetation	lake - surface water	0.0	Grès de Nubie 2014	28.01.2014	0.0	381	
	82	Ounianga Serir Edem 1	OUS - L1	dense vegetation	lake - surface water	0.0	Grès de Nubie 2014	30.01.2014	0.0	348	
	83	Ounianga Serir Edem 2	OUS - L2	dense vegetation	lake - surface water	0.0	Grès de Nubie 2014	30.01.2014	0.0	351	
Ounianga	84	Ounianga Serir	no. 14	dense vegetation	lake - surface water	0.0	Ennedi-Ounianga 2013	01.08.2013	0.0	360	
	85	Ounianga Serir - Eghi	OUS - S1	dense vegetation	spring - lake	0.0	Grès de Nubie 2014	30.01.2014	0.0	364	
	86	Ounianga Serir - Eghi	OUS - L3	dense vegetation	lake - surface water	0.0	Grès de Nubie 2014	30.01.2014	0.0	350	
	87	Ounianga Serir	no. 15	dense vegetation	traditional well	0.5	Ennedi-Ounianga 2013	01.08.2013	unknown	unknown	
	88	Ounianga Serir - Coop. Suisse	OUS - P1	dense vegetation	improved well	8.0	Grès de Nubie 2014	30.01.2014	6.3	345	
	89	Ounianga Serir Motoro	Motoro Lac 1	dense vegetation	lake - surface water	0.0	Grès de Nubie 2014	30.01.2014	0.0	380	
		Ounianga Kebir - no coordinates									
	90	Yoa well	Y-Well	dense vegetation	traditional well	unknown	Ounianga 2011	12.10.2011	unknown	unknown	
	91	Yoa	Y1	dense vegetation	lake - surface water	0.0	Ounianga 2011	12.10.2011	0.0	unknown	
	92	Yoa spring	Y2	dense vegetation	spring - lake	0.0	Ounianga 2011	12.10.2011	0.0	unknown	
	93	Yoa spring	Y3	dense vegetation	spring - lake	0.0	Ounianga 2011	12.10.2011	0.0	unknown	
	94	Forodone (north)	H1	dense vegetation	unknown	unknown	Ounianga 2011	12.10.2011	unknown	unknown	
	95	Forodone (south)	H2	dense vegetation	unknown	unknown	Ounianga 2011	12.10.2011	unknown	unknown	
	96	Mijoi	M1	dense vegetation	unknown	unknown	Ounianga 2011	12.10.2011	unknown	unknown	
	97	Oma (east)	U1	dense vegetation	unknown	unknown	Ounianga 2011	12.10.2011	unknown	unknown	
	98	Oma (east)	U1b	dense vegetation	unknown	unknown	Ounianga 2011	13.10.2011	unknown	unknown	
	99	Oma (west)	U2	dense vegetation	unknown	unknown	Ounianga 2011	12.10.2011	unknown	unknown	
	100	Oma spring	U51	dense vegetation	spring - lake	0.0	Ounianga 2011	12.10.2011	0.0	unknown	
		Motoro - no coordinates									
	101	Motoro	Moltrow	dense vegetation	lake - surface water	0.0	Ounianga 2011	13.10.2011	0.0	unknown	
		Ounianga Serir - no coordinates									
	102	Teli	WPS1	dense vegetation	lake - surface water	0.0	Ounianga 2011	13.10.2011	0.0	unknown	
	103	Teli spring	WPS2	dense vegetation	spring - lake	0.0	Ounianga 2011	13.10.2011	0.0	unknown	
	104	Edim	Edim	dense vegetation	lake - surface water	0.0	Ounianga 2011	13.10.2011	0.0	unknown	
	105	Bokou	Bokou	dense vegetation	unknown	unknown	Ounianga 2011	14.10.2011	unknown	unknown	

Hydrological unit	ID	Locality	Sample Name	Vegetation	Water Point Type	Depth Water Point (m bgl)	Sampling campaign	Date of measure	Water table (m bgl)	Elevation water table (m asl)	Std. Dev. Hydr. Heads
Southern Tibesti	106	Bembéché Oye Yeska	OYE YESKA	dry	borehole	unknown	Grès de Nubie 2014	24.01.2014	unknown	unknown	
	107	Kouroudi Bili Choui	Puits Bili Choui	dry	traditional well	0.5	Borkou 2015	30.01.2015	0.2	337	
	108	Kouroudi Gali	Mare Kouroudi Gali	sparse vegetation	pond - surface water	0.2	Borkou 2015	30.01.2015	0.0	333	
	109	Kouroudi camp	Puits Kouroudi camp	sparse vegetation	traditional well	1.2	Borkou 2015	30.01.2015	0.2	333	
	110	Hichilime	Puits Hichilime	sparse vegetation	traditional well	0.7	Borkou 2015	31.01.2015	0.4	323	
	111	Forom	Puits Forom 2	sparse vegetation	improved well	2.4	Borkou 2015	31.01.2015	1.8	310	
	112	Yarda	Puits Yarda 1	sparse vegetation	traditional well	0.5	Borkou 2015	31.01.2015	0.3	305	
	113	Yarda school	Puits Yarda 2	sparse vegetation	traditional well	2.5	Borkou 2015	31.01.2015	1.5	310	
	114	Elleboye	FM Elleboy	dense vegetation	borehole	unknown	Grès de Nubie 2014	02.02.2014	3.0	242	
	115	Kirdimi Boubou	Forage Boubou	dense vegetation	borehole - artesian	122.0	Borkou 2015	25.01.2015	0.0	256	
	116	Kirdimi Gali	Source Gali	dense vegetation	spring	0.0	Borkou 2015	25.01.2015	0.0	251	
	117	Ngourma	Puits Gourouma	dense vegetation	traditional well	3.0	Borkou 2015	25.01.2015	2.2	240	
	118	Yen well	Puits Yen 1	sparse vegetation	traditional well	4.5	Borkou 2015	25.01.2015	3.0	253	
	119	Yen spring	Source Yen 2	sparse vegetation	spring	0.0	Borkou 2015	25.01.2015	0.0	246	
	120	Ain Galaka	Ain Galaka	sparse vegetation	pond - surface water/artesian	0.0	Grès de Nubie 2014	02.02.2014	0.0	230	
	121	Elleboye Hachien	Puits Hachien	dry	traditional well	0.5	Borkou 2015	25.01.2015	0.9	231	
	122	Kirdimi 1	FM Kirdimi	sparse vegetation	borehole	unknown	Grès de Nubie 2014	02.02.2014	4.0	247	
	123	Faya Dozanga borehole	Dozanga 2 For	dense vegetation	borehole	unknown	Borkou 2015	23.01.2015	4.1	246	
	124	Faya Dozanga well	Dozanga 1 Puits	dense vegetation	traditional well	4.1	Borkou 2015	23.01.2015	4.0	250	
	125	Faya 2	43	dense vegetation	borehole - artesian	unknown	Tibesti 2015	30.05.2015	0.0	266	
	126	Faya Torchenga borehole	Torchenga 1 Forage	dense vegetation	borehole	unknown	Borkou 2015	23.01.2015	unknown	unknown	
	127	Faya Torchenga well	Torchenga 2 Puits	dense vegetation	traditional well	unknown	Borkou 2015	23.01.2015	unknown	unknown	
	128A	Faya Houchma base PNSA	Puits Base Faya	dense vegetation	traditional well	16.9	Borkou 2015	24.01.2015	4.4	231	0.0
	128B	Faya Houchma base PNSA	44	dense vegetation	traditional well	5.0	Tibesti 2015	30.05.2015	4.4	244	
	129	Faya Ribouguidina PNSA Iriboudiaga	Forage Iriboudiaga	dense vegetation	borehole	18.5	Borkou 2015	02.02.2015	4.4	232	
	130	Faya 1	42	dense vegetation	borehole - artesian	unknown	Tibesti 2015	30.05.2015	0.0	247	
	131	Faya F2bis	Forage F2 Faya	dense vegetation	borehole - artesian	unknown	Grès de Nubie 2014	04.02.2014	0.0	223	
	132	Faya Tchagssous	Forage Tchadgssous	dense vegetation	borehole - artesian	unknown	Grès de Nubie 2014	04.02.2014	0.0	227	
	133	Faya F4	Forage F4 Faya	dense vegetation	borehole - artesian	unknown	Grès de Nubie 2014	04.02.2014	0.0	225	
	134	Kourkour Koukourou	Puits Koukourou	dense vegetation	traditional well	1.6	Borkou 2015	24.01.2015	0.9	225	
	135	Djidi PNSA Amoul	Forage PNSA Amoul	dense vegetation	borehole	unknown	Borkou 2015	24.01.2015	unknown	unknown	
	136	Mordangaye PNSA	Forage PNSA Martagaye	dense vegetation	borehole	20.0	Borkou 2015	24.01.2015	3.9	217	
	137	Amoul PNSA Amouli	Forage PNSA Amouli	dense vegetation	borehole	23.0	Borkou 2015	24.01.2015	4.1	218	
Lake Chad basin	138	Yegueski Nasara	Puits Nasara	dry	improved well	unknown	Grès de Nubie 2014	21.01.2014	7.9	254	
	139A	Erg Djourab axis Kouba	P-Axe Kouba	dry	borehole	unknown	Grès de Nubie 2014	05.02.2014	unknown	unknown	
	139B	Erg Djourab axis Kouba	PNSA_Kouba	dry	borehole	unknown	Borkou 2015	22.01.2015	unknown	unknown	
	140	Erg du Djourab puits 110	Puits_110	dry	improved well	4.2	Borkou 2015	22.01.2015	0.0	198	
	141	Kouba 1	45	sparse vegetation	improved well	21.2	Tibesti 2015	02.06.2015	19.5	245	
	142	Kouba Olanga	P-Kouba	sparse vegetation	improved well	19.5	Grès de Nubie 2014	05.02.2014	19.2	230	
	143	Kouba 2	46	sparse vegetation	improved well	23.6	Tibesti 2015	02.06.2015	22.2	241	
Zouar ennedi Zouarké	144	Domou	7	sparse vegetation	improved well	25.7	Tibesti 2015	19.05.2015	22.0	797	
	145	zouar 5	5	dense vegetation	improved well	13.7	Tibesti 2015	19.05.2015	10.1	776	
	146	zouar 4	4	sparse vegetation, white concretions	improved well	12.0	Tibesti 2015	19.05.2015	9.4	772	
	147A	zouar 1	1	dry, white concretions	improved well	11.4	Tibesti 2015	19.05.2015	9.6	776	
	147B	zouar 6	6	dry, white concretions	borehole	unknown	Tibesti 2015	19.05.2015	unknown	unknown	
	148	zouar 3	3	dry	improved well	10.8	Tibesti 2015	19.05.2015	9.9	769	
	149	zouar 2	2	sparse vegetation	improved well	14.5	Tibesti 2015	19.05.2015	11.2	750	
	150	Kougou	9	dry, white concretions	improved well	22.6	Tibesti 2015	19.05.2015	18.2	727	
	151	Armogo2	10	sparse vegetation	borehole	unknown	Tibesti 2015	20.05.2015	17.4	737	
	152	Armogo	8	sparse vegetation, white concretions	improved well	14.8	Tibesti 2015	19.05.2015	12.3	733	
	153	Yigue-yeski	11	sparse vegetation, white concretions	improved well	15.9	Tibesti 2015	20.05.2015	14.3	682	
	154	Zouarké1	12	dry	improved well	26.1	Tibesti 2015	20.05.2015	22.7	667	

Hydrological unit	ID	Locality	Sample Name	Vegetation	Water Point Type	Depth Water Point (m bgl)	Sampling campaign	Date of measure	Water table (m bgl)	Elevation water table (m asl)	Std. Dev. Hydr. Heads
enneri Misky	155	Bini Erde Misky 2	Forage Misky 2	dry	borehole	70.0	Borkou 2015	27.01.2015	14.0	821	
	156A	Bini Erde Misky 1	Puits Misky 1	dry	improved well	13.7	Borkou 2015	27.01.2015	12.5	813	0.2
	156B	Miski1	40	dry	improved well	14.1	Tibesti 2015	27.05.2015	13.0	826	
	157	Enneri Misky Bichira	Puits Bichira	dense vegetation	traditional well	20.1	Borkou 2015	27.01.2015	18.5	720	
	158A	Enneri Misky Oloni	Puits Oloni	sparse vegetation	traditional well	25.1	Borkou 2015	27.01.2015	24.4	693	0.1
	158B	Miski2	41	sparse vegetation	traditional well	26.3	Tibesti 2015	27.05.2015	24.6	698	
Bardaï enneri Zoumri	159	Zoumri4	16	sparse vegetation	pond	surface water	Tibesti 2015	22.05.2015	0.0	1276	
	160	Zoumri3	15	sparse vegetation	traditional well	10.9	Tibesti 2015	22.05.2015	9.3	1267	
	161	Zoumri2	14	dry, wite cocretions	borehole	50.0	Tibesti 2015	22.05.2015	9.4	1266	
	162	Zoumri1	13	dry, white concretions	traditional well	8.6	Tibesti 2015	22.05.2015	8.1	1263	
	163	Ouaychi	17	sparse vegetation	traditional well	5.7	Tibesti 2015	22.05.2015	4.4	1298	
	164	Odissi	18	sparse vegetation	traditional well	3.4	Tibesti 2015	22.05.2015	2.3	1292	
	165	Osouni	19	dense vegetation, white concretions	improved well	5.7	Tibesti 2015	22.05.2015	4.7	1105	
	166	Zoui2	20	sparse vegetation	improved well	6.3	Tibesti 2015	23.05.2015	5.9	1057	
	167	Bardai1	21	sparse vegetation	borehole	unknown	Tibesti 2015	23.05.2015	7.3	1026	
	168	Bardai2	22	sparse vegetation	traditional well	11.5	Tibesti 2015	23.05.2015	10.7	1028	
	169	Bardai3	23	dense vegetation	improved well	6.2	Tibesti 2015	23.05.2015	5.3	1017	
	170	Bardai5	25	dense vegetation	borehole	unknown	Tibesti 2015	23.05.2015	unknown	unknown	
	171	Bardai4	24	dense vegetation	borehole	unknown	Tibesti 2015	23.05.2015	unknown	unknown	
	172	Zougoura1	26	sparse vegetation	borehole	unknown	Tibesti 2015	24.05.2015	9.8	1034	
Aouzou enneri Yebbigué	173	Yeboubou2	38	dense vegetation	spring	groundwater outcrop	Tibesti 2015	27.05.2015	0.0	1395	
	174	Yeboubou1	37	dry	spring	groundwater outcrop	Tibesti 2015	27.05.2015	0.0	1384	
	175	yebbisouma	36	dense vegetation	traditional well	3.8	Tibesti 2015	27.05.2015	3.5	1180	
	176	Kilengue	35	dry, white concretions	spring	groundwater outcrop	Tibesti 2015	26.05.2015	0.0	1111	
	177	Oumou2	34	sparse vegetation	traditional well	9.3	Tibesti 2015	26.05.2015	8.2	1077	
	178	Oumou1	33	sparse vegetation	traditional well	5.9	Tibesti 2015	26.05.2015	5.8	1068	
	179	Aouzou6	32	dense vegetation, white concretions	spring	groundwater outcrop	Tibesti 2015	25.05.2015	2.0	929	
	180	Aouzou5	31	dense vegetation, white concretions	spring	groundwater outcrop	Tibesti 2015	25.05.2015	0.0	927	
	181	Aouzou2	28	dense vegetation, white concretions	traditional well	6.4	Tibesti 2015	25.05.2015	6.0	908	
	182	Aouzou4	30	dense vegetation, white concretions	traditional well	9.0	Tibesti 2015	25.05.2015	8.1	911	
	183	Aouzou3	29	dense vegetation, white concretions	traditional well	10.0	Tibesti 2015	25.05.2015	9.1	909	
	184	Aouzou1	27	sparse vegetation	spring	groundwater outcrop	Tibesti 2015	25.05.2015	0.0	892	

Annex 4 – Hydrochemical analysis of water samples

Geographical Location	ID	E.C. µ/cm	pH	Temperature °C	Alkalinity mg/l	Li mg/l	Na mg/l	NH4 mg/l	K mg/l	Mg mg/l	Ca mg/l	HCO3 mg/l	F mg/l	Cl mg/l	NO2 mg/l	Br mg/l	NO3 mg/l	SO4 mg/l	TDI meq/l	Ionic balance	Contamination	High concentration	Water Type	Water Type +
Nile hydrological basin	1A	665	6.3	29.8	121																			
	1B	627	7.2	23.9		0.0	14.8	0.7	7.5	23.7	86.9	403.0	0.8	6.6	0.0	0.0	11.0	11.8	14.4	-1%	F, NH4		Ca-(Mg)-HCO3	
	2A	525	6.7	29.9	127	0.0	14.5	0.2	2.1	21.4	58.5	261.9	0.4	4.3	0.0	0.0	8.9	4.7	10.0	7 %			Ca-(Mg)-HCO3	
	2B	423	6.9	22.9		0.0	12.3	0.6	3.1	17.7	52.2	270.8	0.4	3.3	0.0	0.0	9.4	5.9	9.5	-1%	NH4		Ca-(Mg)-HCO3	
	3A	376	6.6	29.9	106	0.0	13.3	0.0	1.2	16.0	45.9	188.4	0.4	4.5	0.0	0.0	11.7	5.4	7.8	9 %			Ca-(Mg)-HCO3	
	3B	450	6.8	22.7		0.0	13.2	0.9	5.7	18.6	56.0	292.9	0.4	4.8	0.0	0.0	0.6	8.3	10.2	0%	NH4		Ca-(Mg)-HCO3	
	4	489	7.9	33.1	82	0.0	37.7	0.4	2.5	24.1	56.6	258.8	1.7	8.6	0.1	0.1	27.7	15.6	11.9	10 %	F		Ca-(Mg)-Na-HCO3	
	5	295	6.1	26.8		0.0	11.2	0.5	10.4	10.2	26.7	101.0	0.1	10.9	0.0	0.1	33.0	24.9	6.0	-1%			Ca-(Mg)-HCO3	
	6A	529	6.8	33.5	116	0.1	63.9	0.3	7.7	6.2	44.3	190.6	3.2	24.4	0.1	0.2	22.8	30.5	10.7	7%	F		Na-Ca-HCO3	
	6B	625	7.3	25.6		0.0	72.4	2.6	8.9	7.3	50.4	230.2	3.3	30.7	0.0	0.4	37.0	40.1	13.2	0%	F, NH4		Na-Ca-HCO3	
	7	206	7.6	25.6	54																			
	8	1305	6.9	25.1	381																			
wadi Haouach	9	784	7.3	23.2	191	0.0	38.8	1.1	1.5	20.7	54.2	377.2	1.7	9.7	0.0	0.0	11.4	19.9	13.4	-7 %	F, NH4		Ca-(Mg)-Na-HCO3	
	10A	462	7.2	23.4	194	0.0	38.5	2.6	3.8	25.3	73.0	306.0	0.6	20.5	0.0	0.0	55.2	39.0	15.0	2 %	NO3, NH4		Ca-(Mg)-Na-HCO3	
	10B	354	7.2	25.0		0.0	23.2	0.9	3.2	11.8	38.0	225.8	0.9	4.1	0.0	0.0	4.8	7.8	8.1	-1%	F, NH4		Ca-(Mg)-Na-HCO3	
	11A	2633	6.7	23.2	188	0.0	30.9	0.8	22.3	94.6	389.0	143.5	0.2	127.3	0.0	0.0	975.2	226.8	55.7	5 %	NO3, NH4	E.C., Mg, K, Ca	high NO3	
	11B	901	6.9	25.0		0.0	16.0	1.1	44.7	34.5	111.7	586.9	0.3	5.3	0.0	0.0	6.6	15.0	20.5	1%	NH4	K, Ca	Ca-(Mg)-HCO3	
wadi Sala	12A	119	7.2	20.3	106																			
	12B	162	7.3	16.0		0.0	3.5	4.8	22.5	3.8	7.1	91.6	0.0	5.6	0.2	0.0	2.9	7.2	3.5	-6%	NH4	K	Ca-K-HCO3	
	13A	338	7.5	24.0	128	0.0	7.7	0.8	11.4	9.5	25.1	109.1	0.4	4.3	0.0	0.0	15.4	6.7	5.0	8 %	NH4		Ca-(Mg)-HCO3	
	13B	573	7.6	28.5		0.0	12.7	0.9	20.7	22.0	60.1	227.2	0.9	14.9	0.0	0.2	72.1	29.4	11.9	0%	NO3, F, NH4	K	Ca-(Mg)-HCO3	
	14A	298	7.9	27.3	34	0.0	7.4	0.6	24.5	4.3	13.2	68.1	0.0	12.9	0.0	0.1	0.3	14.4	3.8	5 %	NH4	K	Ca-K-HCO3	
	14B	228	6.6	26.3		0.0	6.3	1.1	27.9	4.9	15.3	79.7	0.0	9.2	0.5	0.0	14.2	15.9	4.3	2%	NH4	K	Ca-K-HCO3	
	15A	196	6.3	26.6	28																			
	15B	163	6.4	25.0		0.0	5.7	0.4	21.1	4.1	9.0	48.2	0.0	8.7	0.0	0.0	17.0	14.0	3.2	0%		K	Ca-K-HCO3	Mg
	16A	297	6.3	26.0	128																			
	16B	130	6.6	19.1		0.0	4.0	2.0	9.1	3.1	11.2	59.3	0.0	5.2	0.4	0.0	6.8	6.4	2.7	-1%	NH4		Ca-(Mg)-HCO3	
	17	265	6.7	29.0	135	0.0	6.3	0.8	6.7	3.9	19.2	33.3	0.1	11.9	1.1	0.1	23.2	17.1	3.4	4 %	NO2, NH4		high NO3	
	18A	405	7.2	28.0	68	0.0	12.4	0.5	9.3	8.7	43.5	84.7	0.1	25.2	0.0	0.3	18.7	42.8	7.0	6%			Ca-(Mg)-HCO3	SO4, Cl
	18B	1020	7.6	26.7		0.0	34.3	1.3	58.1	27.7	104.9	189.1	0.3	46.2	0.0	0.4	61.2	249.6	21.2	0%	NO3, NH4	K, Ca	Ca-(Mg)-SO4-HCO3	
	19	222	7.9	17.5	146	0.0	4.8	2.5	17.0	4.3	24.1	82.3	0.1	11.5	0.9	0.1	6.5	11.8	4.4	7 %	NO2, NH4	K	Ca-(Mg)-HCO3	
	20	428	7.3	37.0	166	0.0	3.4	3.7	9.9	6.7	35.9	104.6	0.1	10.3	1.1	0.1	5.9	15.3	5.4	9 %	NO2, NH4		Ca-(Mg)-HCO3	
	21	293	7.4	22.0	156	0.0	4.3	3.2	15.8	5.6	32.5	86.4	0.1	14.9	0.0	0.2	13.2	18.1	5.3	8 %	NH4	K	Ca-(Mg)-HCO3	
	22	451	6.9	23.0		0.0	2.4	8.2	24.0	10.2	52.5	271.6	0.1	8.1	0.0	0.1	0.3	4.1	9.4	-2%	NH4	K	Ca-(Mg)-HCO3	
	23	379	6.5		30	0.0	9.1	2.4	5.2	5.8	16.8	65.7	0.1	10.9	0.0	0.1	12.1	6.6	3.7	7 %	NH4		Ca-(Mg)-Na-HCO3	
	24	951	8.6	16.6		0.0	15.8	21.1	141.2	17.8	53.7	318.7	0.3	53.6	0.0	0.6	0.6	65.8	17.8	8%	NH4	K	Ca-K-HCO3	
	25A	395	6.7	32.3	68	0.0	28.8	1.8	27.7	4.4	18.6	56.6	0.1	29.3	1.1	0.2	63.5	29.0	6.8	-1%	NO3, NO2, NH4	K	high NO3	
	25B	389	6.1	25.7		0.0	34.3	1.2	30.4	4.5	18.3	70.0	0.0	25.0	0.0	0.2	69.5	38.2	7.4	-2%	NO3, NH4	K	high NO3	
	26A	356	7.5	21.7	173	0.0	13.1	0.6	15.4	8.7	39.9	148.4	0.1	17.7	1.2	0.1	1.6	3.5	6.8	9 %	NO2, NH4	K	Ca-(Mg)-HCO3	
	26B	111	7.3	18.1		0.0	2.7	0.0	3.2	2.6	15.0	69.8	0.1	2.2	0.0	0.0	0.0	1.5	2.4	-3%			Ca-(Mg)-HCO3	
	27A	92	6.5	24.1	65	0.0	7.1	1.6	1.5	1.5	6.9	27.2	0.0	5.4	0.0	0.0	2.9	4.2	1.6	10 %	NH4		Ca-(Mg)-Na-HCO3	
	27B	82	5.8	23.7		0.0	5.1	0.2	1.9	1.6	7.8	37.9	0.0	4.1	0.0	0.0	4.3	3.0	1.7	-4%		pH < 6	Ca-(Mg)-Na-HCO3	
	28A	1080	7.0	26.0	72	0.0	73.4	0.5	38.9	9.9	28.4	63.0	0.1	90.4	0.1	1.3	49.8	83.7	12.6	2 %		K	Na-Ca-Cl	SO4
	28B	860	7.0	26.6		0.0	100.4	3.3	44.9	12.1	35.0	137.9	0.0	122.2	0.0	1.3	16.7	119.6	16.9	0%	NH4	K	Na-Ca-Cl	SO4, HCO3
	29A	240	7.0	33.0	74	0.0	5.8	0.3	5.5	1.3	13.0	38.1	0.2	6.3	0.7	0.0	1.1	8.0	2.2	7 %	NO2		Ca-(Mg)-Na-HCO3	
	29B	307	6.2	30.4		0.0	8.5	0.3	17.9	2.2	35.7	57.2	0.1	10.6	0.0	0.0	34.4	59.0	5.8	-4%		K	Ca-(Mg)-SO4-HCO3	

Geographical Location	ID	E.C. µ/cm	pH	Temperature °C	Alkalinity mg/l	Li mg/l	Na mg/l	NH4 mg/l	K mg/l	Mg mg/l	Ca mg/l	HCO3 mg/l	F mg/l	Cl mg/l	NO2 mg/l	Br mg/l	NO3 mg/l	SO4 mg/l	TDI meq/l	Ionic balance	Contamination	High concentration	Water Type	Water Type +
	30A	306	6.9			0.0	59.6	0.6	7.8	5.8	23.0	114.4	0.4	49.2	1.0	0.5	12.7	30.4	8.6	3 %	NO2, NH4		Na-Ca-HCO3	Cl
	30B	2011	7.7	25.0		0.0	372.0	11.9	31.0	17.4	43.4	216.8	0.9	286.3	0.0	2.6	36.5	402.1	41.9	1%	F, NH4	Cl, SO4, Na, K	Na-SO4-Cl	
	31A	306	6.9	34.0	98	0.0	60.0	0.1	8.2	6.2	24.7	108.8	0.0	63.8	0.7	0.1	5.4	7.6	8.4	9 %	NO2		Na-Ca-Cl	HCO3
	31B	489	6.8	26.8		0.0	61.9	2.2	9.5	6.6	27.9	177.4	0.6	43.4	0.0	0.4	11.4	31.6	10.0	0%	NH4		Na-Ca-HCO3	Cl
	32A	93	6.5	30.0	20																			
	32B	688	6.7	24.3		0.0	52.6	10.9	63.3	8.9	36.3	264.1	0.0	21.4	0.0	0.0	24.3	55.9	13.5	4%	NH4	K	Na-Ca-HCO3	K
	33	59	6.2	29.0	12	0.0	3.0	0.2	1.5	1.1	6.1	17.3	0.0	3.5	0.0	0.0	4.9	1.3	1.1	8 %			Ca-(Mg)-Na-HCO3	
	34A	18	7.7	21.5	94																			
	34B	62	6.8	20.4		0.0	2.2	0.2	5.5	1.1	4.2	20.3	0.1	2.3	0.2	0.0	7.2	3.3	1.1	-4%			high NO3	
	35A	653	6.9	24.0	97	0.0	8.0	0.8	24.2	4.6	21.3	77.3	0.1	7.8	0.1	0.1	21.8	10.6	4.5	9 %	NH4	K	Ca-K-HCO3	
	35B	159	6.4	27.3		0.0	4.4	1.9	20.2	2.4	10.2	53.1	0.0	3.6	0.2	0.0	17.6	7.1	2.9	4%	NH4	K	Ca-K-HCO3	
	36A	844	7.2	23.0	123	0.0	6.5	2.4	23.8	5.5	19.2	63.3	0.1	9.9	0.1	0.1	26.0	16.4	4.5	7 %	NH4	K	Ca-K-HCO3	Mg
	36B	197	6.2	28.3		0.0	4.6	0.4	19.1	4.4	13.6	44.3	0.0	6.8	0.0	0.0	36.5	14.9	3.6	-2%		K	high NO3	
	37	190	7.1	27.7		0.0	6.5	0.3	10.5	6.9	16.4	100.9	0.2	5.8	0.0	0.0	7.5	4.3	4.0	-2%			Ca-(Mg)-HCO3	
	38A	583	6.7	25.0	34	0.0	14.8	1.8	6.4	2.0	9.8	51.1	0.2	9.2	0.1	0.1	6.3	4.7	2.9	9 %	NH4		Na-Ca-HCO3	
	38B	126	6.1	28.5		0.0	14.8	0.7	4.4	1.4	7.2	61.4	0.2	6.2	0.0	0.0	6.4	4.8	2.7	-5%	NH4		Na-Ca-HCO3	
	39A	478	6.8	28.0	58																			
wadi Sala	39B	346	6.5	29.3		0.0	17.9	0.8	8.4	10.7	31.0	89.2	0.1	18.8	0.2	0.2	38.2	38.6	6.9	1%	NH4		Ca-(Mg)-Na-HCO3	SO4
	40A	248	6.4	30.3	23	0.0	5.2	0.3	7.8	2.5	9.4	45.6	0.1	5.7	0.0	0.0	11.8	5.1	2.3	-4 %			Ca-(Mg)-HCO3	
	40B	163	6.9	28.4		0.0	8.5	2.6	10.1	3.3	12.9	87.7	0.1	7.1	0.0	0.0	6.1	5.7	3.5	-5%	NH4		Ca-(Mg)-Na-HCO3	
	41A	1010	7.1	28.4	307																			
	41B	827	7.5	26.8		0.0	21.6	0.8	30.5	27.4	89.2	359.0	0.5	22.0	0.3	0.2	45.7	60.5	17.0	0%	NH4	K	Ca-(Mg)-HCO3	
	42A	557	6.8	29.6	71	0.0	19.4	0.5	29.9	11.0	43.8	93.3	0.2	21.2	0.0	0.2	51.7	42.8	8.6	10 %	NO3	K	Ca-(Mg)-HCO3	SO4
	42B	507	7.0	25.8		0.0	18.8	1.0	37.0	11.0	42.1	139.1	0.2	20.7	0.4	0.2	71.3	43.1	9.8	-1%	NO3, NH4	K	high NO3	
	43A	609	6.7	34.8	84																			
	43B	302	6.2	27.1		0.0	17.0	0.6	19.2	7.2	19.0	41.4	0.0	18.7	0.0	0.2	27.9	59.6	5.7	-2%	NH4	K	Ca-Na-SO4-HCO3	Mg
	44	442	8.3	24.3		0.0	13.7	6.1	25.9	10.3	45.7	145.6	0.2	13.0	0.0	0.1	0.4	90.5	9.4	1%	NH4	K	Ca-(Mg)-HCO3	SO4
	45A	189500	7.5	32.9	412	0.3	82156.5	0.0	17101.9	4574.4	240.8	36.0	0.2	90902.6	0.0	58.7	0.0	92973.4	8900.8	-1 %		E.C., Cl, SO4, Mg, Na, K, Ca	Na-Cl-(HCO3)	SO4
	45B	1143	7.1	23.0		0.0	166.0	5.7	33.8	14.5	47.5	274.1	0.4	160.4	0.0	0.1	0.4	138.9	23.9	0%	NH4	K	Na-Cl-(HCO3)	SO4
	46	653	5.5	20.7		0.0	70.2	2.4	13.2	16.4	34.3	109.8	0.1	52.7	0.0	0.0	0.2	164.4	13.3	-1%	NH4	pH < 6, K	Na-Ca-SO4	Mg, HCO3, Cl
	47A	402	6.5	36.3	61	0.0	15.0	0.0	7.8	9.9	42.9	48.5	0.1	16.1	0.1	0.1	5.4	106.7	7.4	3 %			Ca-(Mg)-SO4-HCO3	
	47B	736	6.6	15.7		0.0	12.1	3.3	10.5	28.5	105.7	195.1	0.0	3.7	0.0	0.0	0.5	272.7	17.6	-2%	NH4	SO4, Ca	Ca-(Mg)-SO4-HCO3	
	48	151	6.9	25.7																				
	49	528	8.1	25.3		0.0	21.5	0.3	16.1	10.3	28.8	163.0	0.4	15.8	0.0	0.0	0.5	41.3	7.7	-5 %		K	Ca-(Mg)-Na-HCO3	SO4
	50	82	7.4			0.0	1.0	0.0	2.2	1.5	10.5	42.9	0.1	1.5	0.0	0.0	4.7	3.8	1.7	-9 %			Ca-(Mg)-HCO3	
	51A	112	7.1			0.0	2.6	0.0	5.0	3.1	14.8	68.8	0.1	2.3	0.0	0.0	5.2	2.5	2.6	-4 %			Ca-(Mg)-HCO3	
	51B	128	7.1			0.0	1.8	0.0	4.2	2.7	13.1	60.3	0.1	1.6	0.0	0.0	4.0	2.6	2.2	-4 %			Ca-(Mg)-HCO3	
	52	288	7.9	29.1	288	0.0	3.0	1.0	4.2	5.0	25.3	78.9	0.3	3.5	0.0	0.0	6.9	6.1	3.6	9 %	NH4		Ca-(Mg)-HCO3	
	53	478	7.9	32.2	117	0.0	14.2	0.6	8.2	8.7	42.6	124.1	0.7	8.1	0.0	0.1	11.7	29.5	6.8	9 %	NH4		Ca-(Mg)-HCO3	
	54	830	7.9		302																			
Mourdi	55	262	7.1	20.7	88																			
	56	2122	8.3	23.3	159	0.0	520.0	0.0	17.5	8.5	16.4	213.9	0.9	363.8	0.1	2.2	36.6	346.1	46.2	6 %	F	Cl, SO4, Na, K	Na-Cl-(HCO3)	SO4
	57	880	9.0	21.0	189																	pH > 9		
	58	457	6.9	35.6	57	0.0	96.8	0.1	1.2	0.3	5.8	68.8	1.1	33.2	0.1	0.1	2.5	101.5	8.8	3 %	F		Na-SO4-Cl	HCO3
	59	235	7.0	34.8	60	0.0	55.4	0.0	0.8	0.2	0.9	102.8	0.5	8.1	0.0	0.1	2.9	4.2	4.6	9 %			Na-HCO3	
	60	267	6.8	35.6	80																			
	61	250	6.8	27.6		0.0	25.4	0.4	23.8	9.6	6.5	183.5	0.3	8.2	0.0	0.0	0.5	8.2	6.3	-9 %		K	Na-Mg-HCO3	

Geographical Location	ID	E.C. µ/cm	pH	Temperature °C	Alkalinity mg/l	Li mg/l	Na mg/l	NH4 mg/l	K mg/l	Mg mg/l	Ca mg/l	HCO3 mg/l	F mg/l	Cl mg/l	NO2 mg/l	Br mg/l	NO3 mg/l	SO4 mg/l	TDI meq/l	Ionic balance	Contamination	High concentration	Water Type	Water Type +
	62	278	7.3	28.6	99	0.0	18.2	0.5	3.2	5.6	34.5	124.9	0.4	8.1	0.0	0.0	32.0	26.1	6.4	-4 %			Ca-(Mg)-Na-HCO3	
	63A	1036	6.4	35.0	30																			
	63B	1082	7.9	21.3	30	0.0	137.5	3.3	43.3	7.5	24.3	66.4	0.2	200.9	0.0	0.0	12.9	120.6	18.6	-2 %	NH4	K	Na-Cl-(HCO3)	SO4
	64	197	7.6	28.9	48	0.0	20.0	0.5	5.8	1.5	8.1	79.5	1.5	3.9	6.3	0.0	2.0	6.0	3.4	-7 %	NO2, F		Na-Ca-HCO3	
	65	481	7.6	26.0	100	0.0	38.9	1.9	8.3	4.4	28.0	163.5	1.2	7.0	0.0	0.0	12.6	48.0	7.9	-5 %	F, NH4		Na-Ca-HCO3	SO4
	66	274	6.7	29.2	83	0.0	24.1	0.9	7.4	5.1	25.9	142.0	0.6	5.3	0.1	0.0	10.5	30.5	6.3	-5 %	NH4		Ca-(Mg)-Na-HCO3	SO4
	67	521	6.9	27.2	76	0.0	36.9	0.4	10.8	9.8	46.0	123.5	0.9	12.4	0.0	0.0	12.7	144.3	10.7	-6 %	F		Ca-Na-SO4-HCO3	
	68	214	7.1	28.3	71	0.0	18.7	0.7	5.0	3.9	17.8	122.0	0.5	5.3	0.0	0.0	12.1	13.4	4.8	-9 %	NH4		Ca-(Mg)-Na-HCO3	
	69	401	7.2	24.1	154	0.0	37.3	0.5	10.6	6.8	30.8	191.8	0.4	27.6	0.0	0.0	1.1	40.6	8.8	-9 %			Na-Ca-HCO3	
	70	5501	10.3	26.9		0.0	1169.3	0.0	182.5	10.6	14.6	1631.4	1.2	556.9	0.0	0.0	0.0	912.6	118.6	-4 %	F	pH > 9, E.C., Cl, SO4, Na, K	Na-HCO3	SO4, Cl
	71	284	7.4	27.8		0.0	25.4	0.5	4.7	5.7	25.1	137.1	0.1	12.5	1.8	0.0	1.0	35.8	6.4	-7 %	NO2		Ca-(Mg)-Na-HCO3	SO4
	72	369	6.6	26.9	67	0.0	35.7	1.2	5.6	5.4	19.6	120.0	0.2	26.3	0.0	0.0	3.2	42.0	6.8	-7 %	NH4		Na-Ca-HCO3	SO4, Cl
	73	407	8.2	25.0	85	0.0	49.3	1.4	6.6	6.7	32.5	150.3	0.3	35.6	0.0	0.0	4.6	72.5	9.6	-5 %	NH4		Na-Ca-HCO3	SO4, Cl
	74	6817	10.4	24.8	> 400	0.0	1525.3	0.0	232.7	6.7	22.9	1972.9	1.5	717.4	0.0	0.0	0.0	1207.6	151.8	-3 %	F	pH > 9, E.C., Cl, SO4, Na, K	Na-HCO3	SO4, Cl
	75	36640	11.2	16.7		0.0	9983.4	0.0	1488.5	22.5	35.5	12463.5	7.8	5021.6	0.0	0.0	843.8	8136.2	1005.3	-5 %	NO3	pH > 9, E.C., Cl, SO4, Na, K	Na-HCO3	SO4, Cl
	76	290	8.7	26.1	78	0.0	25.2	2.2	8.0	4.5	12.0	126.4	0.5	10.5	0.0	0.0	5.7	13.6	5.2	-7 %	NH4		Na-Ca-HCO3	
	77	556	8.7	22.4		0.0	72.7	2.6	7.6	6.4	27.5	224.0	0.7	36.5	0.0	0.0	7.3	70.6	11.7	-8 %	NH4		Na-Ca-HCO3	SO4
	78A	160900	10.6	18.9		0.0	94668.3	0.0	8651.8	24.1	29.3	92085.5	38.1	61558.2	0.0	0.0	0.0	35291.6	8325.0	4 %	F	pH > 9, E.C., Cl, SO4, Na, K	Na-Cl-(HCO3)	
	78B	81990	10.0	33.7	140																	pH > 9, E.C.		
	79	57140	10.9	20.9		0.0	18873.1	0.0	1808.2	17.8	31.3	18444.0	8.7	13793.4	0.0	0.0	0.0	7303.0	1714.1	2 %	F	pH > 9, E.C., Cl, SO4, Na, K	Na-Cl-(HCO3)	
	80	8669	10.5	26.9		0.0	1574.3	0.0	148.8	4.5	13.0	1669.0	1.3	1188.2	0.0	0.0	0.0	638.4	147.5	-1 %	F	pH > 9, E.C., Cl, SO4, Na, K	Na-Cl-(HCO3)	
	81	2629	9.0	21.4		0.0	561.4	0.0	73.6	38.4	23.4	459.2	5.1	199.6	0.0	0.0	785.1	268.3	62.3	-2 %	F	pH > 9, E.C., Cl, SO4, Na, K	high NO3	
	82	988	8.7	22.3		0.0	144.4	1.3	25.2	19.4	34.0	359.7	0.9	45.4	0.0	0.0	0.2	157.7	20.8	-1 %	F, NH4	K	Na-HCO3	SO4
	83	642	8.5	22.4		0.0	55.6	1.0	21.3	18.2	37.4	337.2	0.9	18.1	0.0	0.0	0.5	12.3	12.7	0 %	F, NH4	K	Na-Ca-HCO3	Mg
	84	307	7.7	34.2	81																			
	85	794	8.5	27.0		0.0	251.7	0.0	77.1	4.8	8.1	386.0	0.4	167.3	0.0	0.0	8.4	95.0	26.9	2 %		Na, K	Na-HCO3	Cl
Qunlanga	86	100000	10.2	21.2		0.0	28537.9	0.0	9361.4	95.8	44.6	41309.0	18.6	21121.7	0.0	51.9	0.0	12798.9	3031.8	-2 %	F	pH > 9, E.C., Cl, SO4, Mg, Na, K	Na-HCO3	Cl
	87	232	6.9	35.4	49																			
	88	261	7.1	28.1		0.0	25.9	0.2	5.6	3.6	11.3	114.2	0.3	9.1	0.0	0.0	9.1	15.1	4.7	-10 %			Na-Ca-HCO3	
	89	75900	9.7	20.1	> 400	0.0	29574.0	0.0	1096.6	95.8	18.6	3582.4	7.1	9937.5	0.0	0.0	0.0	45535.8	2610.8	1 %	F	pH > 9, E.C., Cl, SO4, Mg, Na, K	Na-SO4-Cl	
	90	661	8.2									188.9												
	91	67800	10.0			0.0	21190.4	0.0	3317.0	12.7	0.0	27425.5	0.0	10033.6	0.0	0.0	0.0	16311.0	2079.7	-3 %		pH > 9, E.C., Cl, SO4, Na, K	Na-HCO3	SO4, Cl
	92	656	9.3																			pH > 9		
	93	451	8.3			0.0	59.8	0.0	16.2	5.3	16.9	145.9	0.0	18.5	0.0	0.0	0.0	61.5	8.5	1 %			Na-HCO3	SO4
	94	14430	9.5			0.0	3495.2	0.0	446.3	56.9	0.0	6451.4	0.0	1045.9	0.0	0.0	0.0	2040.2	345.8	-3 %		pH > 9, E.C., Cl, SO4, Mg, Na, K	Na-HCO3	SO4
	95	5170	10.6			0.0	1024.5	0.0	182.2	46.2	19.2	1603.6	7.3	457.5	0.0	0.0	0.0	525.2	104.5	3 %	F	pH > 9, E.C., Cl, SO4, Na, K	Na-HCO3	SO4
	96	155900	10.2			0.0	122820.0	0.0	39276.2	0.0	0.0	140715.0	568.7	129045.0	0.0	390.6	0.0	32122.3	12996.8	-2 %	F	pH > 9, E.C., Cl, SO4, Na, K	Na-Cl-(HCO3)	
	97	133500	10.0			0.0	53762.6	0.0	5412.9	0.0	0.0	54766.0	0.0	38786.9	0.0	0.0	0.0	21712.2	4920.7	1 %		pH > 9, E.C., Cl, SO4, Na, K	Na-Cl-(HCO3)	
	98	131300	10.0			0.0	51923.6	0.0	5202.8	0.0	0.0	54217.0	0.0	40141.6	0.0	0.0	0.0	22679.2	4884.7	-2 %		pH > 9, E.C., Cl, SO4, Na, K	Na-Cl-(HCO3)	
	99	197000	9.6			0.0	82611.9	0.0	12436.3	0.0	0.0	88352.5	63.5	104638.6	0.0	316.6	0.0	15405.9	8639.2	-9 %	F	pH > 9, E.C., Cl, SO4, Na, K	Na-Cl-(HCO3)	
	100	369	8.2			0.0	56.7	0.1	4.2	2.8	13.9	134.2	0.6	22.2	0.0	0.0	5.1	56.2	7.6	-8 %			Na-HCO3	SO4
	101	142800	8.1			0.0	66864.3	0.0	2253.1	2393.2	387.9	1183.9	0.0	46390.3	0.0	0.0	0.0	97926.9	6549.3	-3 %		E.C., Cl, SO4, Mg, Na, K, Ca	Na-SO4-Cl	
	102	105900	10.0			0.0	30070.2	0.0	9983.7	105.6	0.0	45115.5	19.1	24235.1	0.0	58.6	0.0	13163.6	3270.9	-4 %	F	pH > 9, E.C., Cl, SO4, Mg, Na, K	Na-HCO3	Cl
	103	991	9.6																			pH > 9		
	104	795	8.5																					
	105	321	8.1			0.0	13.9	0.0	2.6	6.1	42.4	162.0	0.5	9.7	0.0	0.0	0.0	25.9	6.8	-3 %			Ca-(Mg)-HCO3	

Geographical Location	ID	E.C. µ/cm	pH	Temperature °C	Alkalinity mg/l	Li mg/l	Na mg/l	NH4 mg/l	K mg/l	Mg mg/l	Ca mg/l	HCO3 mg/l	F mg/l	Cl mg/l	NO2 mg/l	Br mg/l	NO3 mg/l	SO4 mg/l	TDI meq/l	Ionic balance	Contamination	High concentration	Water Type	Water Type +
	106	504	6.4	27.2	69	0.0	23.2	2.9	17.2	5.7	17.2	144.0	0.6	8.4	0.0	0.0	0.8	28.6	6.2	-5 %	NH4	K	Na-Ca-HCO3	
	107	1050	6.8	21.1		0.0	131.1	0.0	9.9	3.3	11.7	206.3	0.0	37.3	0.0	0.0	3.8	134.2	14.1	-3 %			Na-HCO3	SO4
	108	491	6.8	21.6		0.0	82.0	0.0	7.3	2.7	10.1	178.2	0.0	23.8	0.0	0.0	1.7	60.8	9.4	-4 %			Na-HCO3	SO4
	109	675	6.8	21.1		0.0	87.4	0.0	6.7	3.1	10.6	215.7	0.0	15.4	0.0	0.0	1.3	20.8	9.2	4 %			Na-HCO3	
	110	717	6.8	19.3		0.0	108.9	0.0	13.4	7.3	31.8	360.9	1.0	30.9	0.0	0.0	0.0	38.1	14.9	-2 %	F	K	Na-Ca-HCO3	
	111	1070	6.9	24.6		0.0	62.8	0.0	6.6	20.1	57.3	323.5	0.9	21.9	0.0	0.0	0.0	73.2	14.9	-1 %	F		Ca-(Mg)-Na-HCO3	SO4
	112	420	6.9	20.7		0.0	30.7	0.1	7.8	4.2	15.1	99.6	0.5	14.2	0.0	0.0	3.9	34.6	5.5	-4 %			Na-Ca-HCO3	SO4
	113	267	6.9	25.1		0.0	28.8	0.0	4.8	3.3	11.0	26.2	0.0	20.9	0.0	0.0	0.0	67.3	4.6	-5 %			Na-Ca-SO4	Cl
	114	816	8.1	29.1		0.0	130.5	2.2	38.6	6.5	13.7	456.8	0.4	17.0	0.0	0.0	1.1	7.8	16.2	-1 %	NH4	K	Na-HCO3	
	115	75	6.1	27.0																				
	116	120	6.9	25.9		0.0	3.9	0.0	1.9	2.4	6.0	26.4	0.0	3.6	0.0	0.0	0.0	13.7	1.5	-6 %			Ca-(Mg)-Na-HCO3	SO4
	117	120	6.9	23.8		0.0	3.8	0.1	2.0	2.5	9.1	53.4	0.3	2.9	0.0	0.0	0.0	5.2	2.0	-10 %			Ca-(Mg)-Na-HCO3	
	118	560	7.0	23.3																				
	119	220	6.3	25.5		0.0	8.5	0.0	3.9	4.3	9.7	43.6	0.0	4.8	0.0	0.0	1.2	26.0	2.7	-4 %			Ca-(Mg)-Na-HCO3	SO4
	120	898	9.3	21.3		0.0	201.3	0.0	31.4	5.1	13.9	546.6	1.1	37.6	0.0	0.0	0.0	43.4	21.7	-1 %	F	pH > 9, Na, K	Na-HCO3	
	121	755	9.3	23.7		0.0	138.8	2.0	21.0	7.0	23.2	389.2	0.4	58.5	0.0	0.0	26.6	50.9	18.0	-6 %	NH4	pH > 9, K	Na-HCO3	
Southern Tibesti	122	175	6.3	28.5																				
	123	204	7.0	27.5																				
	124	345	8.0	23.0		0.0	18.5	0.0	8.8	8.8	22.4	153.5	0.3	10.3	0.0	0.0	0.6	15.1	6.0	-5 %			Ca-(Mg)-Na-HCO3	
	125	213	7.0	30.6		0.0	17.4	0.2	10.2	6.4	12.6	107.4	0.4	6.3	0.0	0.0	0.0	14.6	4.4	-2 %			Na-Ca-HCO3	Mg
	126	171	6.8	28.0																				
	127	745	8.5	26.5		0.0	46.9	0.0	10.9	8.1	23.1	127.2	0.2	33.6	0.0	0.0	39.7	42.4	8.7	-5 %			Na-Ca-HCO3	Cl, SO4
	128A	420	7.8	24.8		0.0	39.8	0.0	16.9	5.3	14.7	172.3	0.2	14.5	0.0	0.0	1.1	19.5	7.0	-5 %		K	Na-Ca-HCO3	
	128B	326	7.0	30.4		0.0	39.5	0.8	17.8	6.1	14.4	167.8	0.2	13.2	0.0	0.0	0.9	17.9	7.0	-1 %	NH4	K	Na-Ca-HCO3	
	129	244	7.0	30.6		0.0	10.7	0.2	9.9	5.0	5.5	69.7	0.1	6.2	0.0	0.0	0.5	6.5	2.9	-2%			Na-Mg-HCO3	
	130	153	6.2	29.2		0.0	8.4	0.0	9.2	4.1	4.9	65.9	0.2	4.1	0.0	0.0	0.0	4.0	2.5	-4 %			Na-Mg-HCO3	
	131	150	6.0	26.6		0.0	8.0	0.2	9.3	4.1	4.9	66.9	0.1	4.8	0.0	0.0	0.0	3.9	2.5	-6 %			Na-Mg-HCO3	
	132	139	6.1	26.7																				
	133	124	6.1	25.2																				
	134	175	6.4	22.1		0.0	5.3	0.0	7.9	4.1	6.2	66.6	0.2	2.1	0.0	0.0	0.1	2.8	2.3	-6 %			Ca-(Mg)-Na-HCO3	
	135	171	6.8	26.9																				
	136	223	7.5	27.0		0.0	7.5	0.0	9.1	14.7	11.0	147.0	0.0	2.1	0.0	0.0	0.0	1.1	4.8	-4 %			Ca-(Mg)-HCO3	
	137	131	7.0	28.0																				
	138	365	6.9	23.9	162	0.0	35.5	1.6	2.3	3.8	19.9	142.5	0.3	12.9	0.0	0.0	6.5	37.0	6.6	-9 %	NH4		Na-Ca-HCO3	SO4
	139A	685	8.5	24.7		0.0	150.3	0.0	11.9	2.7	5.2	282.6	12.6	39.3	0.0	0.0	16.6	49.0	15.0	-2 %	F		Na-HCO3	
	139B	740	8.6	27.4		0.0	125.1	0.0	8.0	2.4	4.6	270.4	8.7	18.4	0.0	0.0	8.4	26.4	12.2	0 %	F		Na-HCO3	
Lake Chad basin	140	2095	7.4	24.6		0.0	316.9	0.0	26.5	17.2	42.2	813.0	0.6	160.1	0.0	0.0	0.0	140.8	38.8	-7 %	NO3	Na, K	Na-HCO3	Cl
	141	305	7.0	28.8		0.0	66.9	0.0	6.0	0.4	1.9	164.3	0.5	7.6	0.0	0.0	1.8	13.6	6.4	-1 %			Na-HCO3	
	142	409	8.3	28.8		0.0	92.0	2.3	7.9	0.6	1.9	235.2	0.5	17.8	0.0	0.0	0.0	16.4	9.2	-3 %	NH4		Na-HCO3	
	143	455	7.0	28.9		0.0	94.5	0.0	6.5	0.7	4.2	161.3	0.5	45.8	0.0	0.0	16.9	20.7	9.2	-1 %			Na-HCO3	Cl
	144	355	6.91	32.8	0.0	51.7	0.0	5.5	5.2	19.9	0.0	204.2	1.4	9.9	0.0	0.0	3.4	12.4	7.8	-3 %	F		Na-Ca-HCO3	
	145	353	7.15	29.6	0.0	32.7	0.0	4.6	7.6	36.5	0.0	221.2	1.5	6.0	0.0	0.0	4.8	10.9	8.2	-2 %	F		Ca-Na-HCO3	
	146	303	7.47	31.6	0.0	31.5	0.0	4.6	5.3	26.6	0.0	175.3	1.5	4.8	0.0	0.0	7.3	11.8	6.7	-3 %	F		Na-Ca-HCO3	
	147A	516	7.3	30.4	0.0	91.0	0.0	5.3	4.4	27.9	0.0	281.5	4.0	19.0	0.0	0.0	12.9	20.9	11.9	-1 %	F		Na-HCO3	
	147B	1057	7.76	31.5	0.0	100.4	0.0	6.7	3.0	17.3	0.0	300.7	3.6	15.9	0.0	0.0	4.0	14.4	11.6	-2 %	F		Na-HCO3	
Zouar	148	415	7.78	28.1	0.0	73.3	0.0	7.0	4.1	17.8	0.0	256.3	3.1	9.8	0.0	0.0	2.7	11.9	9.5	-4 %	F		Na-HCO3	
enneri Zouarké	149	281	6.77	29	0.0	28.7	0.0	4.9	4.3	27.4	0.0	156.2	0.7	8.1	0.0	0.0	5.6	11.4	6.2	-1 %			Ca-Na-HCO3	
	150	824	7.58	28.6	0.0	131.4	0.0	7.0	9.0	40.3	0.0	304.5	2.5	109.3	0.0	0.0	25.8	25.2	17.8	-3 %	F		Na-HCO3-Cl	
	151	163	6.74	32.6	0.0	12.6	0.0	4.1	2.3	11.5	0.0	65.3	0.3	7.2	0.0	0.0	6.4	6.8	3.0	-4 %			Ca-Na-HCO3	
	152	1382	8.26	27.4	0.0	304.6	0.0	19.3	4.0	20.4	0.0	765.1	3.2	61.4	0.0	0.0	31.4	52.9	31.1	-3 %	F	K, Na	Na-HCO3	
	153	702	7.43	31.3	0.0	134.9	0.0	3.3	6.2	31.4	0.0	453.0	1.6	7.4	0.0	0.0	21.4	18.2	16.5	-2 %	F		Na-HCO3	
	154	352	7.4	31.5	0.0	28.3	0.0	4.6	5.6	38.3	0.0	173.2	1.3	6.7	0.0	0.0	23.2	17.3	7.5	-2 %	F		Ca-Na-HCO3	

Geographical Location	ID	E.C. µ/cm	pH	Temperature °C	Alkalinity mg/l	Li mg/l	Na mg/l	NH4 mg/l	K mg/l	Mg mg/l	Ca mg/l	HCO3 mg/l	F mg/l	Cl mg/l	NO2 mg/l	Br mg/l	NO3 mg/l	SO4 mg/l	TDI meq/l	Ionic balance	Contamination	High concentration	Water Type	Water Type +
enneri Misky	155	2110	7.1	30	0.0	146.7	0.0	24.1	65.0	142.0	0.0	400.5	0.7	62.5	0.0	0.0	0.0	590.9	40.1	-3 %	SO4	Ca, K, Mg	Ca-Na-Mg-SO4-HCO3	
	156A	1050	7	28.3																				
	156B	1017	7.37	29.9																				
	157	1539	7.2	33.5	0.0	244.7	0.0	4.9	17.3	125.2	0.0	449.3	0.4	106.4	0.0	0.0	29.2	352.6	36.6	1 %	SO4	Ca, Na	Na-HCO3-SO4	
	158A	1733	7.2	26.3	0.0	317.9	0.0	6.3	14.3	57.5	0.0	559.4	0.7	102.1	0.0	0.0	8.6	341.6	37.4	-3 %	SO4	Na	Na-HCO3-SO4	
	158B	1638	8.3	30																				
Bardaï enneri Zoumri	159	446	7.27	22.5	0.0	51.9	0.0	7.7	3.5	21.6	0.0	222.5	0.9	11.4	0.0	0.0	0.0	7.9	8.0	-5 %	F		Na-Ca-HCO3	
	160	610	7.63	26.2	0.0	101.5	0.0	12.9	6.0	29.4	0.0	343.9	1.5	24.7	0.0	0.0	3.2	24.6	13.7	-2 %	F		Na-HCO3	
	161	467	7.52	29.6	0.0	68.8	0.0	7.8	5.4	22.9	0.0	259.5	0.6	12.6	0.0	0.0	10.3	18.6	10.0	-4 %			Na-HCO3	
	162	495	7.67	24.9	0.0	74.1	0.0	8.6	5.7	26.6	0.0	287.3	0.6	14.3	0.0	0.0	4.9	21.5	10.9	-4 %			Na-HCO3	
	163	442	7.97	25.6	0.0	68.0	0.0	16.9	6.5	15.2	0.0	244.7	1.4	17.1	0.0	0.0	1.7	17.4	9.6	-3 %	F	K	Na-HCO3	
	164	957	7.84	23.9	0.0	161.5	0.0	38.5	15.2	22.0	0.0	548.1	2.0	37.4	0.0	0.0	0.0	39.8	21.3	-3 %	F	K	Na-HCO3	
	165	1429	6.86	26.7	0.0	252.9	0.0	28.7	18.2	46.5	0.0	635.0	0.0	204.6	0.0	0.0	0.0	16.2	32.1	-3 %		K, Na	Na-HCO3-Cl	
	166	546	6.08	26	0.0	49.7	0.0	6.2	13.6	24.5	0.0	200.6	0.0	50.6	0.0	0.0	3.8	15.2	9.8	-4 %			Na-Ca-HCO3-Cl	
	167	433	6.52	29.6																				
	168	377	6.44	27.5	0.0	29.2	0.0	5.8	14.9	31.8	0.0	237.9	0.4	9.8	0.0	0.0	2.9	6.3	8.6	-2 %			Ca-Mg-Na-HCO3	
	169	1172	6.84	25.4	0.0	164.9	0.0	15.2	31.9	55.6	0.0	462.0	0.0	193.2	0.0	0.0	0.0	13.8	26.3	-1 %		K	Na-HCO3-Cl	
	170	1211	6.8	30.3	0.0	184.7	0.0	14.0	24.0	49.3	0.0	414.8	0.0	206.1	0.0	0.0	0.0	15.3	25.8	0 %		K	Na-HCO3-Cl	
	171	314	7.08	34.6	0.0	24.2	0.0	5.4	11.6	22.4	0.0	149.5	0.0	14.6	0.0	0.0	5.3	20.4	6.6	-2 %			Ca-Na-Mg-HCO3	
	172	315	6.76	29.6	0.0	20.3	0.0	3.3	10.4	24.9	0.0	182.5	0.2	8.9	0.0	0.0	2.0	8.4	6.5	-6 %			Ca-Na-Mg-HCO3	
Aouzou enneri Yebbigué	173	421	8.23	30.1	0.0	40.1	0.0	7.0	13.2	29.7	0.0	181.9	0.5	22.8	0.0	0.0	14.9	35.0	9.1	-1 %			Na-Ca-HCO3	
	174	438	7.46	30.2	0.0	51.6	0.0	6.0	7.0	25.7	0.0	169.2	0.6	26.5	0.0	0.0	16.3	40.2	8.9	-4 %			Na-Ca-HCO3	
	175	531	7.98	27.4	0.0	82.1	0.0	11.5	9.8	22.0	0.0	206.9	0.0	48.1	0.0	0.0	11.2	48.6	11.7	-1 %			Na-HCO3	
	176	679	7.4	26.9	0.0	101.0	0.0	4.0	15.8	15.2	0.0	242.9	0.0	47.1	0.0	0.0	14.0	55.5	13.2	-1 %			Na-HCO3	
	177	840	6.86	29.7	0.0	88.7	0.0	13.7	30.7	50.0	0.0	268.2	0.0	42.6	0.0	0.0	0.0	189.4	18.8	-2 %		K	Na-Mg-Ca-HCO3-SO4	
	178	1332	7.07	28.2	0.0	182.9	0.0	20.7	52.2	64.1	0.0	675.6	0.0	49.6	0.0	0.0	3.7	180.6	32.3	-1 %		K, Mg	Na-Mg-HCO3	
	179	350	6.48	26.1	0.0	29.3	0.0	7.5	11.8	29.0	0.0	188.0	0.5	11.0	0.0	0.0	3.2	26.6	7.9	-2 %			Ca-Na-HCO3	
	180	225	6.78	31.6	0.0	21.4	0.0	2.8	5.1	19.3	0.0	118.6	0.2	7.8	0.0	0.0	2.9	14.9	4.9	-3 %			Ca-Na-HCO3	
	181	325	6.7	28.9	0.0	28.9	0.0	3.4	8.4	27.8	0.0	171.3	0.3	9.4	0.0	0.0	0.0	22.4	7.0	-2 %			Ca-Na-HCO3	
	182	332	6.75	32	0.0	31.3	0.0	3.2	8.5	27.6	0.0	180.2	0.3	9.4	0.0	0.0	0.8	21.2	7.2	-2 %			Ca-Na-HCO3	
	183	294	6.93	30.2	0.0	26.5	0.0	3.3	6.7	26.2	0.0	155.3	0.2	8.9	0.0	0.0	1.9	19.2	6.3	-2 %			Ca-Na-HCO3	
	184	532	6.7	22.4	0.0	53.3	0.0	8.5	11.2	43.9	0.0	238.6	0.0	20.4	0.0	0.0	0.0	64.3	11.5	-2 %			Ca-Na-HCO3	

Annex 5 – Stable isotopes analysis of water samples

Geographical Location	ID	Elevation water table (m asl)	Rainfall (mm y⁻¹)	δ^2H	$\delta^{18}O$	Standard deviation δ^2H	Standard deviation $\delta^{18}O$	Isotopic Groups
Nile hydrological basin	1A	890	72	-30	-4.9	1	0.0	Group I
	1B	890	72	-28	-4.9			Group I
	2A	847	66	-33	-5.7	3	0.6	Group I
	2B	847	66	-27	-4.5			Group I
	3A	838	66	-39	-6.2	2	0.2	Group I
	3B	836	66	-35	-5.8			Group I
	4	unknown	89	-32	-5.2			Group I
	5	912	89	-24	-4.4			Group I
	6A	833	94	-30	-5.0	2	0.3	Group I
	6B	834	94	-26	-4.5			Group I
	7	778	108					
	8	792	127	-36	-5.8			Group I
wadi Haouach	9	837	114	-33	-5.4			Group I
	10A	838	114	-24	-4.4	0	0.0	Group I
	10B	841	114	-25	-4.4			Group I
	11A	761	122	-32	-4.7	11	1.3	Group I
	11B	765	122	-9	-2.0			Group I
wadi Sala	12A	740	120	-30	-4.1	1	0.2	Group I
	12B	740	120	-31	-4.5			Group I
	13A	689	132	-25	-3.9	1	0.3	Group I
	13B	686	132	-27	-4.5			Group I
	14A	658	120	-31	-4.3	2	0.0	Group I
	14B	658	120	-27	-4.2			Group I
	15A	704	109	-40	-6.6	0	0.2	Group I
	15B	707	109	-40	-6.3			Group I
	16A	670	120	-31	-4.9	1	0.3	Group I
	16B	670	120	-28	-4.3			Group I
	17	647	114	-39	-6.0			Group I
	18A	651	114	-38	-5.8	1	0.0	Group I
	18B	654	114	-37	-5.7			Group I
	19	624	103	42	12.7			evaporated
	20	577	118	44	12.1			evaporated
	21	573	118	23	7.6			evaporated
	22	573	118	45	10.5			evaporated
	23	unknown	118	-38	-6.0			Group I
	24	570	114	91	20.1			evaporated
	25A	563	89	-42	-6.2	0	0.1	Group III
	25B	564	89	-42	-6.1			Group III
	26A	575	89	-30	-2.8	2	0.8	evaporated
	26B	575	89	-34	-4.4			Group I
	27A	574	89	-45	-6.6	0	0.0	Group III
	27B	574	89	-45	-6.6			Group III
	28A	563	89	-43	-5.9	2	0.4	Group I
	28B	564	89	-39	-5.2			Group I
	29A	576	89	-46	-6.7	1	0.2	Group III
	29B	576	89	-43	-6.4			Group III
	30A	558	89	-45	-6.4	4	1.0	Group III
	30B	558	89	-38	-4.4			Group I
	31A	555	89	-45	-6.6	1	0.3	Group III
	31B	557	89	-43	-5.9			Group I
	32A	571	104	-38	-5.4	8	1.2	Group I
	32B	570	104	-21	-3.0			Group I
	33	575	104	-43	-6.6			Group III
	34A	560	94	-10	-0.2	5	1.3	evaporated
	34B	560	94	-20	-2.7			Group I
	35A	547	107	-12	-2.2	0	0.1	Group I
	35B	548	107	-12	-2.4			Group I
	36A	532	107	-21	-3.5	1	0.1	Group I
	36B	535	107	-20	-3.3			Group I
	37	534	112	-46	-6.9			Group III
	38A	497	102	-48	-6.9	0	0.0	Group III
	38B	497	102	-48	-6.9			Group III
	39A	494	90	-36	-5.9	2	0.4	Group I
	39B	497	90	-33	-5.2			Group I
	40A	465	87	-25	-3.7	1	0.1	Group I
	40B	464	87	-22	-3.4			Group I
	41A	446	82	-38	-5.8	4	0.6	Group I
	41B	451	82	-47	-6.9			Group III
	42A	439	78	-47	-7.1	6	0.9	Group III

Geographical Location	ID	Elevation water table (m asl)	Rainfall (mm y⁻¹)	δ²H	δ¹⁸O	Standard deviation δ²H	Standard deviation δ¹⁸O	Isotopic Groups
	42B	440	78	-35	-5.3			Group I
	43A	407	57	-51	-7.1	0	0.1	Group III
	43B	404	57	-51	-7.3			Group III
	44	380	38	-45	-4.0			evaporated
	45A	370	38	1	9.5	28	7.9	evaporated
wadi Sala	45B	386	38	-54	-6.4			Group III
	46	370	38	-61	-7.9			Group III
	47A	377	32	-63	-8.1	2	0.4	Group III
	47B	377	32	-67	-8.9			Group III
	48	366	28	-64	-8.4			Group III
	49	365	24	-58	-7.2			Group III
	50	1149	94	29	5.9			evaporated
	51A	1140	94	-13	-2.1	1	0.1	Group I
	51B	1140	94	-11	-2.0			Group I
	52	603	27	-31	-4.8			Group I
	53	570	28	-31	-4.8			Group I
	54	506	28	-26	-3.5			Group I
Mourdi	55	495	35	-19	-2.5			Group I
	56	493	33	-61	-6.6			evaporated
	57	461	32	-68	-8.9			Group III
	58	445	25	-70	-8.9			Group II
	59	409	24	-76	-10.5			Group II
	60	338	23	-73	-10.3			Group II
	61	374	23	-72	-9.9			Group II
	62	610	28	-9	-2.5			Group I
	63A	461	22	-72	-9.7	0	0.0	Group II
	63B	461	22	-72	-9.7			Group II
	64	438	13	-53	-7.7			Group III
	65	437	13	-57	-8.3			Group III
	66	433	13	-62	-9.6			Group II
	67	432	13	-53	-8.2			Group III
	68	434	13	-70	-10.1			Group II
	69	424	15	-71	-10.1			Group II
	70	390	18	-76	-9.6			Group II
	71	394	18	-80	-10.0			Group II
	72	388	18	-80	-11.1			Group II
	73	400	18	-76	-9.8			Group II
	74	386	18	-79	-10.3			Group II
	75	386	18	-53	-5.2			evaporated
	76	396	18	-77	-9.9			Group II
	77	377	18	-76	-9.4			Group II
	78A	374	18	-33	0.2	6	1.6	evaporated
	78B	379	18	-44	-2.9			evaporated
	79	376	18	-49	-3.2			evaporated
	80	376	18	-77	-9.8			Group II
	81	381	18	-41	-2.9			evaporated
	82	348	22	-39	-5.7			Group I
	83	351	22	-58	-6.6			Group III
Ounianga	84	360	26	-39	-2.9			evaporated
	85	364	26	-74	-10.0			Group II
	86	350	26	-13	2.5			evaporated
	87	unknown	26	-65	-8.1			Group III
	88	345	26	-65	-9.1			Group II
	89	380	20	-26	1.1			evaporated
	90	unknown		-82	-11.1			Group II
	91	unknown		-15	2.0			evaporated
	92	unknown		-85	-11.3			Group II
	93	unknown		-85	-11.4			Group II
	94	unknown		5	7.1			evaporated
	95	unknown		-34	-0.9			evaporated
	96	unknown		-21	5.2			evaporated
	97	unknown		-42	-2.4			evaporated
	98	unknown		-32	-0.2			evaporated
	99	unknown		-19	4.3			evaporated
	100	unknown		-83	-10.9			Group II
	101	unknown		3	8.2			evaporated
	102	unknown		-13	2.8			evaporated
	103	unknown		-76	-10.1			Group II
	104	unknown		-55	-5.6			evaporated
	105	unknown		-37	-2.5			evaporated

Geographical Location	ID	Elevation water table (m asl)	Rainfall (mm y⁻¹)	δ^2H	$\delta^{18}O$	Standard deviation δ^2H	Standard deviation $\delta^{18}O$	Isotopic Groups
	106	unknown	19	-81	-11.7			Group II
	107	337	22	-75	-10.3			Group II
	108	333	22	-66	-8.0			Group III
	109	333	22	-69	-9.5			Group II
	110	323	22	-72	-9.9			Group II
	111	310	19	-78	-10.1			Group II
	112	305	19	-81	-11.0			Group II
	113	310	21	-66	-9.1			Group II
	114	242	28	-50	-6.3			Group III
	115	256	28	-65	-8.7			Group III
	116	251	28	-63	-8.3			Group III
	117	240	26	-63	-8.5			Group III
	118	253	28	-65	-8.4			Group III
	119	246	28	-68	-9.0			Group II
	120	230	31	-37	-3.3			evaporated
	121	231	26	-49	-5.9			Group III
Southern Tibesti	122	247	20	-65	-8.3			Group III
	123	246	18	-84	-11.6			Group II
	124	250	18	-79	-10.5			Group II
	125	266	18	-79	-10.7			Group II
	126	unknown	18	-81	-11.2			Group II
	127	unknown	18	-71	-9.4			Group II
	128A	231	18	-70	-9.4	1	0.0	Group II
	128B	244	18	-69	-9.3			Group II
	129	232	18	-70	-9.4			Group II
	130	247	18	-69	-9.0			Group II
	131	223	18	-59	-8.5			Group III
	132	227	18	-63	-7.9			Group III
	133	225	18	-64	-8.2			Group III
	134	225	18	-65	-8.5			Group III
	135	unknown	18	-66	-8.9			Group III
	136	217	20	-64	-8.5			Group III
	137	218	20	-64	-8.4			Group III
	138	254	35	-54	-6.6			Group III
	139A	unknown	33	-49	-6.4	1	0.1	Group III
	139B	unknown	33	-50	-6.2			Group III
Lake Chad basin	140	198	34	-25	-2.1			evaporated
	141	245	111	-7	-0.4			evaporated
	142	230	109	-55	-7.8			Group III
	143	241	109	-54	-7.1			Group III
	1	797	61	-27	-4.6			Group I
	2	776	60	-22	-3.9			Group I
	3	772	60	-29	-4.4			Group I
	4A	776	60	-32	-4.7	0	0.1	Group I
	4B	unknown	60	-31	-4.9			Group I
Zouar	5	769	60	-26	-4.4			Group I
enneri Zouarké	6	750	60	-43	-6.4			Group II
	7	727	61	-36	-5.5			Group II
	8	737	65	-32	-4.9			Group I
	9	733	65	-27	-3.5			Group I
	10	682	61	-21	-3.4			Group I
	11	667	53	-25	-4.0			Group I

Geographical Location	ID	Elevation water table (m asl)	Rainfall (mm y⁻¹)	δ^2H	$\delta^{18}O$	Standard deviation δ^2H	Standard deviation $\delta^{18}O$	Isotopic Groups
enneri Misky	12	821	64	-71	-9.5			Group III
	13A	813	64	-27	-3.9	1	0.1	Group I
	13B	826	64	-28	-4.0			Group I
	14	720	64	-28	-4.3			Group I
	15A	693	50	-32	-4.9	0	0.1	Group I
	15B	698	50	-31	-5.1			Group I
Bardaï enneri Zoumri	16	1276	44	-67	-9.2			Group III
	17	1267	44	-59	-8.2			Group III
	18	1266	44	-29	-4.9			Group I
	19	1263	43	-27	-4.7			Group I
	20	1298	43	-80	-10.9			Group III
	21	1292	43	-77	-10.2			Group III
	22	1105	50	-68	-9.3			Group III
	23	1057	50	-83	-11.2			Group III
	24	1026	50	-80	-10.8			Group III
	25	1028	50	-64	-8.9			Group III
	26	1017	50	-67	-9.1			Group III
	27	unknown	50	-73	-9.9			Group III
	28	unknown	50	-86	-11.7			Group III
	29	1034	50	-84	-11.2			Group III
Aouzou enneri Yebbigué	30	1395	44	-67	-8.6			Group III
	31	1384	43	-68	-8.8			Group III
	32	1180	45	-51	-7.1			Group II
	33	1111	44	-61	-8.3			Group III
	34	1077	45	-81	-11.1			Group III
	35	1068	45	-64	-9.3			Group III
	36	929	48	-68	-9.4			Group III
	37	927	48	-76	-10.5			Group III
	38	908	48	-77	-10.5			Group III
	39	911	48	-77	-10.6			Group III
	40	909	48	-76	-10.5			Group III
	41	892	48	-79	-10.2			Group III

Annex 6 – Processed LandSat8 images

Downloaded LandSat8 images	MNDWI36 > 0	Actual ET
Scene 180047		
LC08_L1TP_180047_20130612_20170504_01_T1		
LC08_L1TP_180047_20130628_20170503_01_T1		
LC08_L1TP_180047_20130714_20170503_01_T1		
LC08_L1TP_180047_20130730_20170503_01_T1		
LC08_L1TP_180047_20130815_20170503_01_T1	x	
LC08_L1TP_180047_20130831_20170502_01_T1		
LC08_L1TP_180047_20130916_20170502_01_T1		
LC08_L1TP_180047_20140311_20170425_01_T1		
LC08_L1TP_180047_20140327_20170424_01_T1		
LC08_L1TP_180047_20140615_20170421_01_T1		
LC08_L1TP_180047_20140701_20170421_01_T1		
LC08_L1TP_180047_20140717_20170421_01_T1		
LC08_L1TP_180047_20140802_20170420_01_T1	x	x
LC08_L1TP_180047_20140818_20170420_01_T1	x	x
LC08_L1TP_180047_20140903_20170420_01_T1	x	
LC08_L1TP_180047_20140919_20170419_01_T1	x	x
LC08_L1TP_180047_20150602_20170408_01_T1		
LC08_L1TP_180047_20150618_20170407_01_T1		
LC08_L1TP_180047_20150704_20170407_01_T1		
LC08_L1TP_180047_20150720_20170406_01_T1		
LC08_L1TP_180047_20150805_20170406_01_T1	x	
LC08_L1TP_180047_20150821_20170405_01_T1	x	x
LC08_L1TP_180047_20150906_20170404_01_T1	x	x
LC08_L1TP_180047_20150922_20170403_01_T1	x	x
LC08_L1TP_180047_20160112_20170405_01_T1		
LC08_L1TP_180047_20160128_20170330_01_T1		
LC08_L1TP_180047_20160316_20170328_01_T1		
LC08_L1TP_180047_20160401_20170327_01_T1		
LC08_L1TP_180047_20160604_20170324_01_T1		
LC08_L1TP_180047_20160620_20170323_01_T1		
LC08_L1TP_180047_20160706_20170323_01_T1		
LC08_L1TP_180047_20160722_20170323_01_T1	x	x
LC08_L1TP_180047_20160807_20170322_01_T1	x	
LC08_L1TP_180047_20160823_20170322_01_T1		
LC08_L1TP_180047_20160908_20170321_01_T1	x	x
LC08_L1TP_180047_20160924_20170321_01_T1	x	
Scene 180048		
LC08_L1TP_180048_20130612_20170504_01_T1	x	
LC08_L1TP_180048_20130628_20170503_01_T1	x	x
LC08_L1TP_180048_20130714_20170503_01_T1	x	x
LC08_L1TP_180048_20130730_20170503_01_T1	x	x
LC08_L1TP_180048_20130815_20170503_01_T1	x	x
LC08_L1TP_180048_20130831_20170502_01_T1	x	x
LC08_L1TP_180048_20130916_20170502_01_T1	x	x
LC08_L1TP_180048_20140327_20170424_01_T1		
LC08_L1TP_180048_20140412_20170423_01_T1		
LC08_L1TP_180048_20140514_20170422_01_T1		
LC08_L1TP_180048_20140530_20170422_01_T1	x	
LC08_L1TP_180048_20140615_20170421_01_T1	x	
LC08_L1TP_180048_20140701_20170421_01_T1		
LC08_L1TP_180048_20140717_20170421_01_T1	x	
LC08_L1TP_180048_20140802_20170420_01_T1	x	x
LC08_L1TP_180048_20140818_20170420_01_T1	x	x
LC08_L1TP_180048_20140903_20170420_01_T1	x	x
LC08_L1TP_180048_20140919_20170419_01_T1	x	x
LC08_L1TP_180048_20150602_20170408_01_T1	x	
LC08_L1TP_180048_20150618_20170407_01_T1	x	
LC08_L1TP_180048_20150704_20170407_01_T1	x	
LC08_L1TP_180048_20150720_20170406_01_T1	x	
LC08_L1TP_180048_20150805_20170406_01_T1	x	
LC08_L1TP_180048_20150821_20170405_01_T1	x	
LC08_L1TP_180048_20150906_20170404_01_T1	x	x
LC08_L1TP_180048_20150922_20170403_01_T1	x	
LC08_L1TP_180048_20160604_20170324_01_T1	x	
LC08_L1TP_180048_20160620_20170323_01_T1	x	
LC08_L1TP_180048_20160706_20170323_01_T1	x	x
LC08_L1TP_180048_20160722_20170323_01_T1	x	
LC08_L1TP_180048_20160807_20170322_01_T1	x	
LC08_L1TP_180048_20160823_20170322_01_T1		
LC08_L1TP_180048_20160908_20170321_01_T1	x	
LC08_L1TP_180048_20160924_20170321_01_T1	x	

Downloaded LandSat8 images	MNDWI36 > 0	Actual ET
Scene 180049		
LC08_L1TP_180049_20130612_20170504_01_T1	x	
LC08_L1TP_180049_20130628_20170503_01_T1	x	x
LC08_L1TP_180049_20130714_20170503_01_T1	x	x
LC08_L1TP_180049_20130730_20170503_01_T1	x	
LC08_L1TP_180049_20130815_20170503_01_T1	x	x
LC08_L1TP_180049_20130831_20170502_01_T1	x	x
LC08_L1TP_180049_20130916_20170502_01_T1	x	
LC08_L1TP_180049_20140514_20170422_01_T1	x	
LC08_L1TP_180049_20140530_20170422_01_T1	x	x
LC08_L1TP_180049_20140615_20170421_01_T1	x	x
LC08_L1TP_180049_20140701_20170421_01_T1	x	
LC08_L1TP_180049_20140717_20170421_01_T1	x	
LC08_L1TP_180049_20140802_20170420_01_T1	x	
LC08_L1TP_180049_20140818_20170420_01_T1	x	x
LC08_L1TP_180049_20140903_20170420_01_T1	x	x
LC08_L1TP_180049_20140919_20170419_01_T1	x	
LC08_L1TP_180049_20150602_20170408_01_T1		
LC08_L1TP_180049_20150618_20170407_01_T1	x	
LC08_L1TP_180049_20150704_20170407_01_T1	x	x
LC08_L1TP_180049_20150720_20170406_01_T1	x	
LC08_L1TP_180049_20150805_20170406_01_T1	x	x
LC08_L1TP_180049_20150821_20170405_01_T1	x	
LC08_L1TP_180049_20150906_20170404_01_T1	x	x
LC08_L1TP_180049_20150922_20170403_01_T1	x	
LC08_L1TP_180049_20160604_20170324_01_T1	x	x
LC08_L1TP_180049_20160620_20170323_01_T1	x	
LC08_L1TP_180049_20160706_20170323_01_T1	x	
LC08_L1TP_180049_20160722_20170323_01_T1	x	
LC08_L1TP_180049_20160807_20170322_01_T1		
LC08_L1TP_180049_20160823_20170322_01_T1	x	x
LC08_L1TP_180049_20160908_20170321_01_T1	x	x
LC08_L1TP_180049_20160924_20170321_01_T1	x	
Scene 181046		
LC08_L1TP_181046_20130603_20170504_01_T1		
LC08_L1TP_181046_20130619_20170503_01_T1		
LC08_L1TP_181046_20130705_20170503_01_T1		
LC08_L1TP_181046_20130721_20170503_01_T1		
LC08_L1TP_181046_20130806_20170503_01_T1		
LC08_L1TP_181046_20130822_20170502_01_T1		
LC08_L1TP_181046_20130907_20170502_01_T1		
LC08_L1TP_181046_20130923_20170502_01_T1		
LC08_L1TP_181046_20140214_20170425_01_T1		
LC08_L1TP_181046_20140318_20170425_01_T1		
LC08_L1TP_181046_20140403_20170424_01_T1		
LC08_L1TP_181046_20140419_20170423_01_T1		
LC08_L1TP_181046_20140505_20170423_01_T1		
LC08_L1TP_181046_20140521_20170422_01_T1		
LC08_L1TP_181046_20140606_20170422_01_T1		
LC08_L1TP_181046_20140622_20170421_01_T1		
LC08_L1TP_181046_20140708_20170421_01_T1		
LC08_L1TP_181046_20140724_20170421_01_T1		
LC08_L1TP_181046_20140809_20170420_01_T1		
LC08_L1TP_181046_20140825_20170420_01_T1	x	x
LC08_L1TP_181046_20140910_20170419_01_T1		
LC08_L1TP_181046_20140926_20170419_01_T1		
LC08_L1TP_181046_20150116_20170414_01_T1		
LC08_L1TP_181046_20150201_20170413_01_T1		
LC08_L1TP_181046_20150305_20170412_01_T1		
LC08_L1TP_181046_20150321_20170411_01_T1		
LC08_L1TP_181046_20150609_20170408_01_T1		
LC08_L1TP_181046_20150625_20170407_01_T1		
LC08_L1TP_181046_20150711_20170407_01_T1	x	
LC08_L1TP_181046_20150727_20170406_01_T1	x	
LC08_L1TP_181046_20150812_20170406_01_T1		
LC08_L1TP_181046_20150828_20170405_01_T1		
LC08_L1TP_181046_20150913_20170404_01_T1		
LC08_L1TP_181046_20150929_20170403_01_T1		
LC08_L1TP_181046_20160611_20170324_01_T1		
LC08_L1TP_181046_20160627_20170323_01_T1		
LC08_L1TP_181046_20160713_20170323_01_T1		
LC08_L1TP_181046_20160729_20170322_01_T1		
LC08_L1TP_181046_20160814_20170322_01_T1		
LC08_L1TP_181046_20160830_20170321_01_T1	x	
LC08_L1TP_181046_20160915_20170321_01_T1	x	

Downloaded LandSat8 images	MNDWI36 > 0	Actual ET
Scene 182047		
LC08_L1TP_181047_20130603_20170504_01_T1	X	X
LC08_L1TP_181047_20130619_20170503_01_T1	X	X
LC08_L1TP_181047_20130705_20170503_01_T1	X	
LC08_L1TP_181047_20130721_20170503_01_T1	X	X
LC08_L1TP_181047_20130806_20170503_01_T1	X	
LC08_L1TP_181047_20130822_20170502_01_T1	X	
LC08_L1TP_181047_20130907_20170502_01_T1	X	
LC08_L1TP_181047_20130923_20170502_01_T1	X	
LC08_L1TP_181047_20140318_20170425_01_T1	X	
LC08_L1TP_181047_20140403_20170424_01_T1	X	X
LC08_L1TP_181047_20140505_20170423_01_T1		
LC08_L1TP_181047_20140521_20170422_01_T1	X	
LC08_L1TP_181047_20140606_20170422_01_T1	X	X
LC08_L1TP_181047_20140622_20170421_01_T1	X	X
LC08_L1TP_181047_20140708_20170421_01_T1	X	X
LC08_L1TP_181047_20140724_20170421_01_T1	X	X
LC08_L1TP_181047_20140809_20170420_01_T1	X	
LC08_L1TP_181047_20140825_20170420_01_T1	X	
LC08_L1TP_181047_20140910_20170419_01_T1	X	X
LC08_L1TP_181047_20140926_20170419_01_T1	X	
LC08_L1TP_181047_20150609_20170408_01_T1	X	
LC08_L1TP_181047_20150625_20170407_01_T1	X	
LC08_L1TP_181047_20150711_20170407_01_T1	X	
LC08_L1TP_181047_20150727_20170406_01_T1	X	
LC08_L1TP_181047_20150812_20170406_01_T1	X	
LC08_L1TP_181047_20150828_20170405_01_T1	X	X
LC08_L1TP_181047_20150913_20170404_01_T1		
LC08_L1TP_181047_20150929_20170403_01_T1	X	
LC08_L1TP_181047_20160307_20170328_01_T1	X	
LC08_L1TP_181047_20160323_20170327_01_T1	X	X
LC08_L1TP_181047_20160611_20170324_01_T1	X	
LC08_L1TP_181047_20160627_20170323_01_T1	X	
LC08_L1TP_181047_20160713_20170323_01_T1	X	
LC08_L1TP_181047_20160729_20170322_01_T1	X	X
LC08_L1TP_181047_20160814_20170322_01_T1	X	
LC08_L1TP_181047_20160830_20170321_01_T1	X	
LC08_L1TP_181047_20160915_20170321_01_T1	X	X
Scene 181048		
LC08_L1TP_181048_20130603_20170504_01_T1		
LC08_L1TP_181048_20130619_20170503_01_T1	X	X
LC08_L1TP_181048_20130705_20170503_01_T1	X	
LC08_L1TP_181048_20130721_20170503_01_T1		
LC08_L1TP_181048_20130806_20170503_01_T1		
LC08_L1TP_181048_20130822_20170502_01_T1	X	
LC08_L1TP_181048_20130907_20170502_01_T1	X	X
LC08_L1TP_181048_20130923_20170502_01_T1	X	
LC08_L1TP_181048_20140302_20170425_01_T1		
LC08_L1TP_181048_20140318_20170425_01_T1	X	
LC08_L1TP_181048_20140505_20170423_01_T1		
LC08_L1TP_181048_20140521_20170422_01_T1	X	
LC08_L1TP_181048_20140606_20170422_01_T1		
LC08_L1TP_181048_20140622_20170421_01_T1	X	
LC08_L1TP_181048_20140708_20170421_01_T1		
LC08_L1TP_181048_20140724_20170421_01_T1	X	X
LC08_L1TP_181048_20140809_20170420_01_T1	X	
LC08_L1TP_181048_20140825_20170420_01_T1	X	X
LC08_L1TP_181048_20140910_20170419_01_T1	X	
LC08_L1TP_181048_20140926_20170419_01_T1	X	
LC08_L1TP_181048_20150609_20170408_01_T1	X	
LC08_L1TP_181048_20150625_20170407_01_T1	X	X
LC08_L1TP_181048_20150711_20170407_01_T1	X	
LC08_L1TP_181048_20150727_20170406_01_T1	X	
LC08_L1TP_181048_20150812_20170406_01_T1		
LC08_L1TP_181048_20150828_20170405_01_T1	X	
LC08_L1TP_181048_20150913_20170404_01_T1		
LC08_L1TP_181048_20150929_20170403_01_T1	X	
LC08_L1TP_181048_20160307_20170328_01_T1	X	X
LC08_L1TP_181048_20160323_20170327_01_T1	X	X
LC08_L1TP_181048_20160611_20170324_01_T1		
LC08_L1TP_181048_20160627_20170323_01_T1		
LC08_L1TP_181048_20160713_20170323_01_T1		
LC08_L1TP_181048_20160729_20170322_01_T1	X	
LC08_L1TP_181048_20160814_20170322_01_T1		
LC08_L1TP_181048_20160830_20170321_01_T1	X	
LC08_L1TP_181048_20160915_20170321_01_T1	X	

Downloaded LandSat8 images	MNDWI36 > 0	Actual ET
Scene 182046		
LC08_L1TP_182046_20130610_20170504_01_T1		
LC08_L1TP_182046_20130626_20170504_01_T1	X	
LC08_L1TP_182046_20130712_20170503_01_T1		
LC08_L1TP_182046_20130728_20170503_01_T1		
LC08_L1TP_182046_20130813_20170503_01_T1		
LC08_L1TP_182046_20130829_20170502_01_T1		
LC08_L1TP_182046_20130914_20170502_01_T1		
LC08_L1TP_182046_20130930_20170502_01_T1		
LC08_L1TP_182046_20140309_20170425_01_T1		
LC08_L1TP_182046_20140325_20170424_01_T1		
LC08_L1TP_182046_20140512_20170422_01_T1	X	
LC08_L1TP_182046_20140528_20170422_01_T1		
LC08_L1TP_182046_20140613_20170422_01_T1		
LC08_L1TP_182046_20140629_20170421_01_T1		
LC08_L1TP_182046_20140715_20170421_01_T1		
LC08_L1TP_182046_20140731_20170420_01_T1		
LC08_L1TP_182046_20140816_20170420_01_T1	X	
LC08_L1TP_182046_20140901_20170420_01_T1		
LC08_L1TP_182046_20140917_20170419_01_T1		
LC08_L1TP_182046_20150312_20170412_01_T1		
LC08_L1TP_182046_20150328_20170411_01_T1		
LC08_L1TP_182046_20150616_20170407_01_T1		
LC08_L1TP_182046_20150702_20170407_01_T1		
LC08_L1TP_182046_20150718_20170407_01_T1		
LC08_L1TP_182046_20150803_20170406_01_T1		
LC08_L1TP_182046_20150819_20170406_01_T1	X	X
LC08_L1TP_182046_20150904_20170404_01_T1		
LC08_L1TP_182046_20150920_20170404_01_T1		
LC08_L1TP_182046_20160314_20170328_01_T1		
LC08_L1TP_182046_20160330_20170327_01_T1		
LC08_L1TP_182046_20160602_20170324_01_T1		
LC08_L1TP_182046_20160618_20170323_01_T1		
LC08_L1TP_182046_20160704_20170323_01_T1		
LC08_L1TP_182046_20160720_20170324_01_T1	X	
LC08_L1TP_182046_20160805_20170322_01_T1		
LC08_L1TP_182046_20160821_20170322_01_T1		
LC08_L1TP_182046_20160906_20170321_01_T1		
LC08_L1TP_182046_20160922_20170321_01_T1		
Scene 182047		
LC08_L1TP_182047_20130610_20170504_01_T1	X	X
LC08_L1TP_182047_20130626_20170504_01_T1	X	
LC08_L1TP_182047_20130712_20170503_01_T1	X	X
LC08_L1TP_182047_20130728_20170503_01_T1	X	X
LC08_L1TP_182047_20130813_20170503_01_T1	X	X
LC08_L1TP_182047_20130829_20170502_01_T1	X	
LC08_L1TP_182047_20130914_20170502_01_T1	X	X
LC08_L1TP_182047_20130930_20170502_01_T1	X	X
LC08_L1TP_182047_20140309_20170425_01_T1	X	X
LC08_L1TP_182047_20140325_20170424_01_T1		
LC08_L1TP_182047_20140512_20170422_01_T1		
LC08_L1TP_182047_20140528_20170422_01_T1	X	X
LC08_L1TP_182047_20140613_20170422_01_T1	X	X
LC08_L1TP_182047_20140629_20170421_01_T1	X	X
LC08_L1TP_182047_20140715_20170421_01_T1	X	
LC08_L1TP_182047_20140731_20170420_01_T1	X	X
LC08_L1TP_182047_20140901_20170420_01_T1	X	
LC08_L1TP_182047_20140917_20170419_01_T1	X	
LC08_L1TP_182047_20150616_20170407_01_T1	X	X
LC08_L1TP_182047_20150702_20170407_01_T1	X	
LC08_L1TP_182047_20150718_20170407_01_T1	X	
LC08_L1TP_182047_20150803_20170406_01_T1	X	
LC08_L1TP_182047_20150819_20170406_01_T1	X	X
LC08_L1TP_182047_20150904_20170404_01_T1	X	
LC08_L1TP_182047_20150920_20170404_01_T1	X	X
LC08_L1TP_182047_20160314_20170328_01_T1		
LC08_L1TP_182047_20160330_20170327_01_T1	X	
LC08_L1TP_182047_20160602_20170324_01_T1	X	X
LC08_L1TP_182047_20160618_20170323_01_T1	X	
LC08_L1TP_182047_20160704_20170323_01_T1	X	X
LC08_L1TP_182047_20160720_20170324_01_T1	X	
LC08_L1TP_182047_20160805_20170322_01_T1	X	
LC08_L1TP_182047_20160821_20170322_01_T1	X	X
LC08_L1TP_182047_20160906_20170321_01_T1	X	
LC08_L1TP_182047_20160922_20170321_01_T1	X	

Downloaded LandSat8 images	MNDWI36 > 0	Actual ET
Scene 182048		
LC08_L1TP_182048_20130610_20170504_01_T1	X	
LC08_L1TP_182048_20130626_20170504_01_T1	X	
LC08_L1TP_182048_20130712_20170503_01_T1	X	
LC08_L1TP_182048_20130728_20170503_01_T1	X	
LC08_L1TP_182048_20130813_20170503_01_T1	X	
LC08_L1TP_182048_20130829_20170502_01_T1	X	
LC08_L1TP_182048_20130914_20170502_01_T1	X	
LC08_L1TP_182048_20130930_20170502_01_T1	X	X
LC08_L1TP_182048_20140309_20170425_01_T1		
LC08_L1TP_182048_20140325_20170424_01_T1		
LC08_L1TP_182048_20140512_20170422_01_T1		
LC08_L1TP_182048_20140528_20170422_01_T1	X	X
LC08_L1TP_182048_20140613_20170422_01_T1	X	
LC08_L1TP_182048_20140629_20170421_01_T1	X	
LC08_L1TP_182048_20140715_20170421_01_T1	X	
LC08_L1TP_182048_20140731_20170420_01_T1	X	
LC08_L1TP_182048_20140901_20170420_01_T1	X	
LC08_L1TP_182048_20140917_20170419_01_T1	X	
LC08_L1TP_182048_20150616_20170407_01_T1		
LC08_L1TP_182048_20150702_20170407_01_T1		
LC08_L1TP_182048_20150718_20170407_01_T1		
LC08_L1TP_182048_20150803_20170406_01_T1	X	
LC08_L1TP_182048_20150819_20170406_01_T1	X	
LC08_L1TP_182048_20150904_20170404_01_T1	X	
LC08_L1TP_182048_20150920_20170404_01_T1		
LC08_L1TP_182048_20160602_20170324_01_T1		
LC08_L1TP_182048_20160618_20170323_01_T1	X	X
LC08_L1TP_182048_20160704_20170323_01_T1	X	X
LC08_L1TP_182048_20160720_20170324_01_T1	X	
LC08_L1TP_182048_20160805_20170322_01_T1	X	
LC08_L1TP_182048_20160821_20170322_01_T1	X	
LC08_L1TP_182048_20160906_20170321_01_T1		
LC08_L1TP_182048_20160922_20170321_01_T1		

Downloaded LandSat8 images	MNDWI36 > 0	Actual ET
Scene 183047		
LC08_L1TP_183047_20130414_20170505_01_T1	X	X
LC08_L1TP_183047_20130430_20170505_01_T1	X	X
LC08_L1TP_183047_20130601_20170504_01_T1	X	X
LC08_L1TP_183047_20130703_20170503_01_T1	X	X
LC08_L1TP_183047_20130719_20170503_01_T1	X	X
LC08_L1TP_183047_20130804_20170503_01_T1	X	X
LC08_L1TP_183047_20130820_20170502_01_T1	X	
LC08_L1TP_183047_20130905_20170502_01_T1	X	
LC08_L1TP_183047_20140503_20170423_01_T1		
LC08_L1TP_183047_20140519_20170422_01_T1	X	X
LC08_L1TP_183047_20140604_20170422_01_T1	X	X
LC08_L1TP_183047_20140620_20170421_01_T1	X	
LC08_L1TP_183047_20140706_20170421_01_T1	X	X
LC08_L1TP_183047_20140722_20170421_01_T1	X	
LC08_L1TP_183047_20140807_20170420_01_T1	X	X
LC08_L1TP_183047_20140823_20170420_01_T1	X	
LC08_L1TP_183047_20140908_20170419_01_T1	X	
LC08_L1TP_183047_20140924_20170419_01_T1	X	X
LO08_L1TP_183047_20150303_20170412_01_T1		
LC08_L1TP_183047_20150319_20170412_01_T1	X	X
LC08_L1TP_183047_20150607_20170408_01_T1		
LC08_L1TP_183047_20150623_20170407_01_T1	X	
LC08_L1TP_183047_20150709_20170407_01_T1	X	
LC08_L1TP_183047_20150725_20170406_01_T1		
LC08_L1TP_183047_20150810_20170406_01_T1	X	
LC08_L1TP_183047_20150826_20170405_01_T1	X	
LC08_L1TP_183047_20150911_20170404_01_T1	X	
LC08_L1TP_183047_20150927_20170403_01_T1	X	X
LC08_L1TP_183047_20160305_20170328_01_T1	X	X
LC08_L1TP_183047_20160321_20170327_01_T1	X	X
LC08_L1TP_183047_20160609_20170324_01_T1	X	X
LC08_L1TP_183047_20160625_20170323_01_T1	X	X
LC08_L1TP_183047_20160711_20170323_01_T1	X	
LC08_L1TP_183047_20160727_20170322_01_T1	X	
LC08_L1TP_183047_20160812_20170322_01_T1	X	
LC08_L1TP_183047_20160828_20170321_01_T1	X	
LC08_L1TP_183047_20160913_20170321_01_T1	X	
LC08_L1TP_183047_20160929_20170321_01_T1	X	X